Synthesis, Photophysical and Theoretical Studies of Molecular Architecture Based on Excited State Intramolecular Proton Transfer

A dissertation as partial fulfillment for the Degree of
Doctor of Philosophy in Chemistry
by

Aastha Palta

(Roll No. 901709002)

Under the Supervision
Of

Dr. Vijay Luxami
Professor

DEPARTMENT OF CHEMISTRY & BIOCHEMISTRY
THAPAR INSTITUTE OF ENGINEERING AND TECHNOLOGY,
Patiala-147004

THAPAR INSTITUTE
OF ENGINEERING & TECHNOLOGY
(Deemed to be University)

Thapar Institute of Engineering and Technology
Patiala
Department of Chemistry and Biochemistry

STATEMENT

I hereby declare that matter embodied in this thesis is the result of investigations carried out by me in the Department of Chemistry and Biochemistry, Thapar Institute of Engineering and Technology, Patiala, India, under the supervision of Prof. Vijay Luxami. This thesis has been submitted by me to the Department of Chemistry and Biochemistry, TIET, for the award of the degree of Doctor of Philosophy

In keeping with the general practice of reporting scientific observations, due acknowledgments have been made wherever the work described is based on the findings of other investigations. I further declare that this work has not been submitted anywhere else for any degree, diploma, associateship, etc., of any Institute or University to the best of my knowledge.

Aastha Palta Aastha Palta
Reg. No. 901709002
Department of Chemistry and Biochemistry,
Thapar Institute of Engineering and Technology
Patiala-147004, Punjab, India

Vijay Luxami
Dr. Vijay Luxami
Professor
Department of Chemistry and Biochemistry,
Thapar Institute of Engineering and Technology,
Patiala-147004, Punjab, India

Thapar Institute of Engineering and Technology

Patiala

Department of Chemistry and Biochemistry

CERTIFICATE

It is certified that the work contained in the thesis entitled "**Synthesis, Photophysical and Theoretical Studies of Molecular Architecture Based on Excited State Intramolecular Proton Transfer**" by Aastha Palta in fulfillment of the degree of Doctor of Philosophy is an authentic record of the candidate's own independent and original research work carried out under my supervision in the Department of Chemistry and Biochemistry, Thapar Institute of Engineering and Technology, Patiala, Punjab, India. The material embodied in this thesis has not been submitted in part or full to any other University or Institute for the award of any degree.

Dr. Vijay Luxami
Professor
Department of Chemistry and Biochemistry,
Thapar Institute of Engineering and Technology
Patiala-147004, Punjab, India

Prof. Manmohan Chhibber
(Head, DCBC)
Department of Chemistry and Biochemistry,
Thapar Institute of Engineering and Technology
Patiala-147004, Punjab, India

DEDICATED TO MY BELOVED FAMILY

Acknowledgment

I may halt for a while to place on record my gratefulness to all those who have made a contribution towards the successful completion of this thesis. Above all, I express my gratitude to the family members for their blessings and support. I am acknowledging the gratitude towards my respected supervisor Dr. Vijay Luxami, Professor, Department of Chemistry and Biochemistry (DCBC), Thapar Institute of Engineering & Technology, Patiala (Punjab, India) for the opportunity to work in her group. Her inspiring guidance, intellectual support encouragement and motivation for working on new research problems are what made this work possible. I thank her for her help in writing this dissertation, other research articles and improving me at scientific communication and style. Her wisdom and continuous optimism helped me maintain my focus and enthusiasm.

I express my gratitude to Director, Thapar Institute of Engineering & Technology, Patiala, Dr. N. Tejoprakash, Dean of Research and Sponsored Projects (RSP), Dr. Rafat Siddique, former Dean RSP, Dr. Manmohan Chhibber (Head of DCBC) for all facilities which have been immensely helpful in completing my work.

I am also thankful to all my respected teachers of the Department of Chemistry and Biochemistry (DCBC) and my doctoral committee members Dr. R.K. Gupta, Dr. Davinder Kumar for their valuable suggestion and motivation at each and every step during my whole thesis work.

During my PhD studies, I had the opportunity to work in close collaborations with other research groups. I would like to express my sincere thanks to Dr Kamaldeep Paul for his continuous support and inspiration throughout my journey. I learned a great deal about a conformational analysis problem. I would like to extend my thanks to Dr. Priya Vashisht for her collaboration.

I would also like to thank Dr. Gulshan Kumar, Dr. Iqubal Singh, Dr. Ruhi, Dr. Sudesh Rani and Dr. Sukhwinder Dhiman for scientific and non-scientific help during the PhD studies. Time flew by in the company of good friends and therefore, a special thanks to Priyanka Gautam. I would also like to extend the expression of thanks to other colleagues Dinesh Singla, Rekha Thakur, Rohini Gupta, Saurabh Gupta, Palak Sharma, Shifali, Sonia Rani, Anmol Jain, Tanya, Priya Thakur, Abhinav. Abhishek, Anju and Amrit for creating a great work atmosphere and help at different stages during my course study. I extend my gratitude to other research scholars of department: Pooja Soam, Priya Kamboj, Parmjeet Kaur, Kirti Singh, Abinash, Anshu Tyagi and

others who are not mentioned by name for their support and encouragement. I now have a forever collection of stories and a lot of everlasting memories to tell.

A special thanks to Mr. Sahil Bhardwaj for his constant motivation and support. Another round of thanks for friends away from here; Pranshu Kansal, Abhilasha Sharma, Anurag Kamboj, Richa Bansal, Geetika Bansal for a laugh whenever possible.

I acknowledge the help of Mr. Mayank Sharma, office staff and Chander Singh Thakur, Chandar Shekhar, Hemant Sharma, and Vishwanath Dass, technical staff of Department of Chemistry and Biochemistry for their support in various aspects.

I extend my thankful acknowledgement to SAI Labs, Thapar Institute of Engineering & Technology, Patiala; SAIF Lab, Panjab University, Chandigarh; CIL, IIT Ropar for providing experimental instrumentation. I extend my gratitude to Mr. Mukesh Aggarwal and Mr. Pardeep Bhatia SAI Labs, Thapar Institute of Engineering & Technology, Patiala, for their cooperation during NMR/CHN data collection. Mr. Ajeeth Singh, Department of Physics and Material Sciences, TIET for his support during FESEM data collection.

I thankfully acknowledge Thapar Institute of Engineering & Technology, Patiala for providing me teaching assistantship during my course. I am also thankful to DST-SERB, New Delhi (EMR/2016/002464) for financial assistant.

Finally, none of this would have been possible without the constant love, support, guidance and patience of all my family members. I owe my gratitude to my respected father, Mr. Mukesh Raj Palta, my mother, Mrs. Renu Palta whose blessings, belief and encouragement have shown me the path to pursue goals in my life. I thank my sister Dr. Prachi Palta for everything she has done for me. They all have been amazing and always been there for me. I cannot thank them enough. Thank you for your everlasting love and support.

Besides this, I am thankful to all those people who have knowingly/ unknowingly helped me in successfully completing my work.

Aastha Palta

Abstract

Over the past few years, excited state intramolecular proton transfer (ESIPT) has gained significant interest in the optoelectronics field due to its unique photophysical properties. These properties make ESIPT fluorophores potential candidates for various applications, including fluorescence probes, luminescent materials, molecular logic gates and OLEDs. The combination of ESIPT with intramolecuar charge transfer phenomenon offers advantages as they exhibit large Stokes shift which make them suitable for chemical and biological sensing, imaging and other applications. The research investigations presented in this thesis shed light on the impact of dual - ESIPT process on hydroxyl aryl benzimidazole and benzothiazole based Schiff bases. Also, effect of electron donating and conjugation on one of the ESIPT site was studied through experimental and theoretical methods. It was found that the presence of electron donating unit induce both excited state intramolecular charge transfer (ESICT) and proton transfer mechanism. In some cases, electron donating unit may even dominate over the ESIPT phenomenon. The torsional flexibility around C=N caused the aggregation induced emission in some of the probes. Hydroxyl aryl benzimidazole and benzothiazole Schiff bases exhibited ESIPT, ICT and AIE phenomenon while 8-hydroxyquinoline based Schiff bases demonstrated ICT phenomenon along with ESIPT. In conclusion, the synthesized probes showed interplay of different phenomenons ie. ESIPT, AIE, ESICT and have great potential in bio-imaging, sensing and in the development of optoelectronic devices.

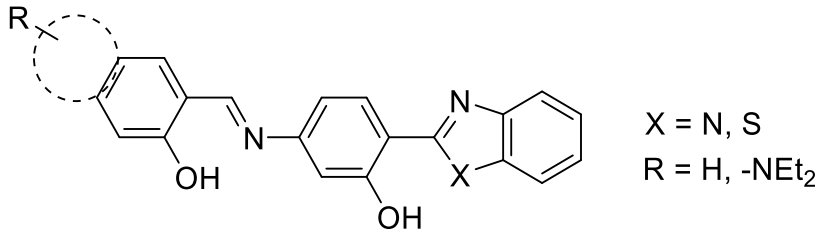

Table of Content

Abbreviations

AIE	Aggregation-induced emission
ALP	Alkalinephosphotase
CHEF	Chelation-enhanced fluorescence
Cys	Cysteine
DCP	Diethylchlorophosphate
DFT	Density Functional Theory
DLS	Dynamic light scattering
DMF	N,N-Dimethylformamide
DMSO	Diethyl sulphoxide
EDX	Energy dispersive X-ray spectroscopy
ESICT	Excited state intramolecular charge transfer
ESIPT	Excited state intramolecular proton transfer
FESEM	Field-emission scanning electron microscope
HB	Hydrogen bonding
HEPES	(4-hydroxyethyl)-1-piprazineethanesulfonic acid
HOMO	Highest occupied molecular orbital
ICT	Intramolecular charge transfer
IEFPCM	Integral equation of formalism polarized continuum model
IraHB	Intramolecular hydrogen bonding
IPA	Isopropyl alcohol
IraPT	Intramolecular proton transfer
LEDs	Light emitting diodes
LMCT	Ligand to metal charge transfer

LOD	Limit of detection
LUMO	Lowest unoccupied molecular orbital
MeOH	Methanol
MLCT	Metal to ligand charge transfer
m.pt.	Melting point
OLEDs	Organic light emitting diodes
PET	Photo-induced electron transfer
PPi	Pyrophosphate
PT	Proton transfer
TBAX	Tetrabutyl ammonium halide
TDDFT	Time-dependant density functional theory
THF	Tetrahydrofuran
TICT	Twist intramolecular charge transfer
TLC	Thin-layer chromatography

Symbols

K	Binding constant
H	HOMO (Highest occupied molecular orbital)
L	LUMO (Lowest unoccupied molecular orbital)
ϕ	Quantum yield
μM	Micromolar
nM	Nanomolar

λ_{ex}	Absorption peak
λ_{em}	Emission peak
λ_{calc}	Calculated absorption peak

Chapter 1

Introduction and review of literature

1.1. General introduction

Proton transfer is a natural process occurring everywhere and is the basis of many biological control mechanisms in living things and it has also been used in molecular material sciences to create a responsive material.[1-4] Proton transfer reactions can occur in the ground or excited states adiabatically or non-adiabatically in variety of ways. Molecular compounds exhibiting the ESIPT process have been utilized as potential candidates for optoelectronics, molecular probes, sensing and biomedical materials, and in various laser dyes.[5-10] Due to its large number of applications, ESIPT based fluorescence sensors has received a great deal of attention.[11, 12]

ESIPT is one of the most important and fundamental phenomenon in chemistry that involves the transfer of proton in tautomers of different electronic structures from original excited state i.e. the protons are transferred from proton donor to proton acceptor group through existing hydrogen bond (H-Bond).[13-19] The ESIPT phenomenon is a four level process from enol→enol*→Keto*→Keto, (E→E*→K*→K), that can occur either adiabatically or non-adiabatically. ESIPT is an extremely fast process that can even occur at very low temperature and also in a rigid glass.[20-23]

The ESIPT process occurs in molecules having hydrogen bond between proton donor groups (−OH group and $-NH_2$ group) and proton acceptor groups (–C=O, –N= etc.) present in close proximity to each other.[24-27] The properties for ESIPT chromophores are dual emission, large Strokes shift and sensitivity towards surrounding medium. The rate of ESIPT process is dependent on surrounding medium and donor/acceptor groups. At ground state the ESIPT tautomers generally exists in cis- enol from with intramolecular hydrogen bonding.[28-31] Upon photo excitation, the excited singlet state enol form is populated in accordance with Franck-Condon principle without any geometrical relaxation. Then excited singlet cis-keto form is formed (stabilized by intramolecular hydrogen bonding) by an ultrafast ESIPT phenomenon with geometrical relaxation. These electronic changes result the proton transfer from the proton donor to the proton acceptor, leading to a tautomeric transformation from the excited enol form to the excited keto form.[32-37] The excited singlet keto form is transformed into excited triplet keto form by intersystem crossing. Most of ESIPT chromophores exhibit dual emission, the one at shorter wavelength due to excited state enol form, and other at longer wavelength due to excited state keto form. ESIPT phenomenon is affected by its environment and the fluorescent properties can

be tuned by changing its surrounding environment. The spectral properties of ESIPT fluorophores are dependent on acidity/basicity of surrounding medium, hydrogen bonding and substituents on donor/acceptor groups etc.[38-43]

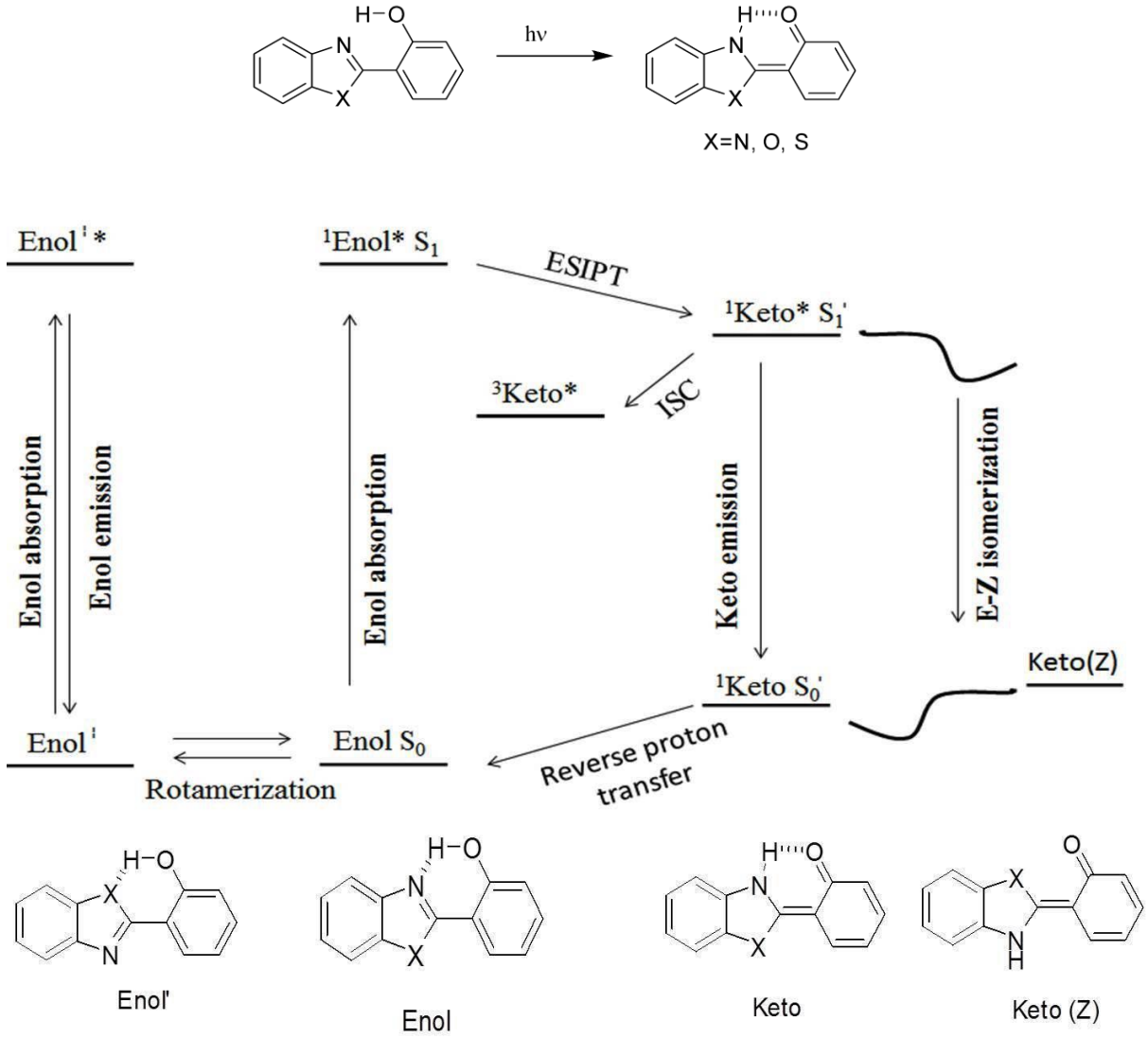

Figure 1: Photophysical process of ESIPT

The environmental sensitivity of ESIPT fluorescence makes it unique. Once the molecule absorbs a photon of light and is excited, enol emission is favored in protic solvents due to intermolecular hydrogen bonding to the solvent which disfavors ESIPT. In aprotic solvents, on the other hand, keto emission is preferred. Due to the dual emission propensity of ESIPT dyes, ratiometric outputs are possible, increasing measurement sensitivity.[44-50] Many researchers are interested in chromophore development, majority of dyes are derived from a core set of

scaffolds. These scaffolds are stitched together to form fluorescent probes used to study the localization of biological therapeutics and cell membrane potential in neurons, to name a few applications. There are several types of molecules that can go through ESIPT.

1.2. Literature Survey

ESIPT phenomenon has been a center of attraction in the last few decades due to its outstanding large Stokes shift and strong fluorescence and high quantum yield. These properties of ESIPT based sensors can be enhanced by incorporating another ESIPT site within the molecule. Based on the structural composition, the survey of literature is done on the basis of ESIPT based Schiff base sensors for metal ions, anions and enzyme.

1.2.1. Single ESIPT based sensors

Wang and coworkers synthesized compound **1**, a D-A type quinoline derivative. Compound **1** showed excited state intramolecular proton transfer (ESIPT) by forming five membered rings through O-H---N hydrogen bond which was supported by theoretical studies.[51] The removal of the hydroxyl proton from **1** by coordination with Zn^{2+} led to the suppression of ESIPT. The compound **1**.Zn^{2+} complex exhibited aggregation induced emission (AIE) behavior in THF/H_2O. Structure studies revealed that the J-aggregate formation and restriction of intramolecular rotations were the cause of the AIE characteristics. ESIPT combined with AIE can be used for the detection of Zn^{2+} in aqueous medium via fluorescence turn-on mode. Compound **1** was successfully used to create test strips for quick detection of Zn^{2+}.

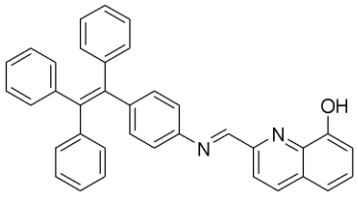

1

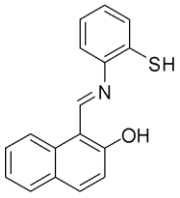

2

Callan and his coworkers developed a simple ESIPT based compound **2** for the ratiometric detection of Mg^{2+}.[52] A keto tautomer is produced by ESIPT on Schiff base of probe allowing effective Mg^{2+} binding. For the detection of low quantities of Mg^{2+} (2 μM) in a THF/H_2O (9:1) solvent system, probe was shown to have good selectivity and high sensitivity. It was demonstrated that it could bind to Mg^{2+} with a 2:1 stoichiometry and an association constant of

1.4×10^4 M^{-2}. The obtained results suggested that it might be utilized as a diagnostic probe for hypermagnesaemia (high level of Mg^{2+} in the blood).

Santra and coworkers synthesized an unsymmetrical ligand compound **3** which works as a selective "turn-on" fluorescence sensor for Al^{3+} ions in mixed aqueous medium.[53] Compound **3** was reversible with EDTA and was used as a molecular logic gate. The lowest detection limit for Al^{3+} ions using compound **3** was found out to be 72.6 nM. The compound **3**.Al^{3+} complex generated *in-situ* has been observed to detect inorganic and biological phosphates such as ATP and ADP sequentially via "turn-off" fluorescence. Filter paper strips were utilized to test its practical applicability as a real-time sensor.

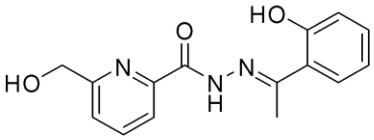

3

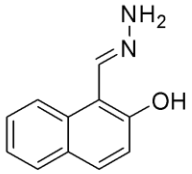

4

Bhardwaj and coworkers designed and synthesized an easy to prepare Schiff base **4**, whose AIE behavior was studied in DMSO/HEPES medium.[54] Compound **4** showed weak fluorescence in pure DMSO whereas the fluorescence was enhanced at 532 nm as the fraction of HEPES rise to 70% owing to the tendency to self-aggregate and ESIPT property of compound **4**. Compound **4** could detect Al^{3+} ions in HEPES buffer at 10 mM concentration. The fluorescence intensity at 435 nm of compound **4** was enhanced in the presence of Al^{3+} ions due to chelation enhanced fluorescence effect (CHEF). The LOD of compound **4** for detection of Al^{3+} ions were found to be 20 nM. Compound **4** was further used for the detection of Al^{3+} ions in river and tap water.

Yang and team reported a Schiff base **5** based on 4-cyanobiphenyl that could detect Cd^{2+} ions through fluorescence.[55] Compound **5** can detect Cd^{2+} ion by fluorescence turn-on response in CH_3CN/H_2O (3:2, v/v) solvent. Compound **5** binds to Cd^{2+} ions in 1:1 ratio which blocks the C=N isomerization and inhibits ESIPT whereas the fluorescence enhancement was due to CHEF. Compound **5** could detect Cd^{2+} ions with lowest detection limit of 10.5 nM. The analytical applicability of compound **5** for Cd^{2+} has been evaluated on test paper strips. Compound **5** was also used to detect Cd^{2+} in zebrafish and HeLa cells.

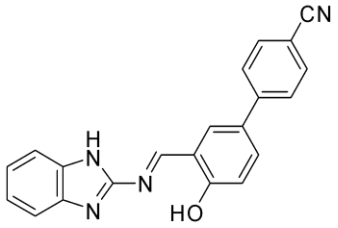

5

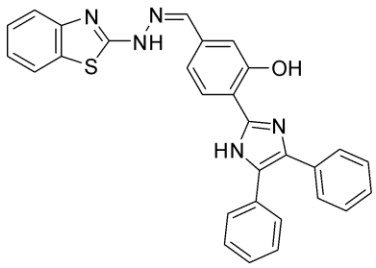

6

Kumar and coworkers designed and synthesized highly emissive compound **6** based on imidazole.[56] Compound **6** could detect Cu^{2+} ions with high selectivity and sensitivity. The LOD for the detection of Cu^{2+} ions using compound **6** was found out to be 7.84 nM. With the addition of Cu^{2+} ion to the solution of compound **6**, fluorescent and colorimetric changes were observed. Compound **6** was used for the detection of Cu^{2+} ions in real water samples and living cells and was also used as a paper strip. The potential detection method was verified using DFT simulations.

Liu and team reported the fluorescent compound **7** for the detection of Al^{3+} and Cu^{2+} ions.[57] Compound **7** exhibited three absorption maxima at 288 nm, 301 nm and 355 nm and the band at 355 nm showed a large red shift to 402 nm with Al^{3+} and to 415 nm with Cu^{2+} ion. The emission peak of compound **7** was observed at 425 nm and enhancement in the emission intensity was observed with the addition of Al^{3+} ion and quenching was observed with Cu^{2+} ion. The compound **7**-Al^{3+} complex and compound **7**-Cu^{2+} complex sensed F^- ion and S^- ion. The fluorescence emission for F^- ion in compound **7**-Al^{3+} complex shifted from 485 nm to 428 nm and for S^- ion the emission peak at 428 nm was observed in compound **7**-Cu^{2+} complex which were due to the formation of AlF_3 and CuS.

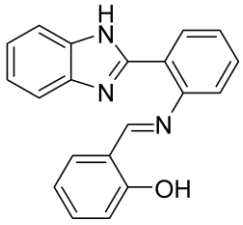

7

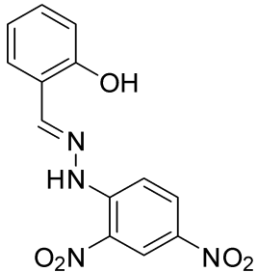

8

Behura and group synthesized and characterized a dinitrophenyl based Schiff base **8** to detect Zn^{2+} ions selectively.[58] Compound **8** showed very weak fluorescence in DMSO: H_2O owing to ESIPT phenomenon. The Job's plot showed the 1:1 stoichiometry for Zn^{2+} ions. DFT studies supported the binding modes. The detection limit and binding constants were 1.1×10^{-8} M and 6.35×10^{7} M^{-1}, respectively. Compound **8**.Zn^{2+} complex showed reversibility with the addition of EDTA. Moreover, compound **8** was used to selectively sense Zn^{2+} in the solid phase and to detect Zn^{2+} in living HeLa cells.

Kaur and team reported a simple Schiff base **9** synthesized via single step condensation of 1-aminoanthracene and 2-hydroxynaphthaldehyde.[59] Compound **9** can detect Al^{3+} and F^- ions in a dual mode via UV-vis and fluorescence "off-on" spectroscopy that cause 640-fold increases in fluorescence in the presence of F^- ions in CH_3CN. In the presence of Al^{3+} and F^- ions, compound **9** can change color from yellow to colorless and dark yellow. The in-situ complex is capable of sensing Cu^{2+} ions with an on-off fluorescence response. The limit of detection for Al^{3+}, F^- and Cu^{2+} ions were determined to be 1.48, 1.44 and 2.04 μM, respectively.

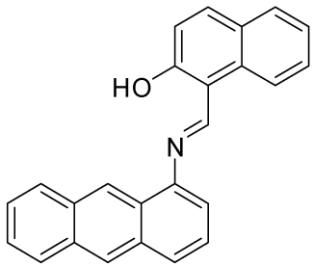

9

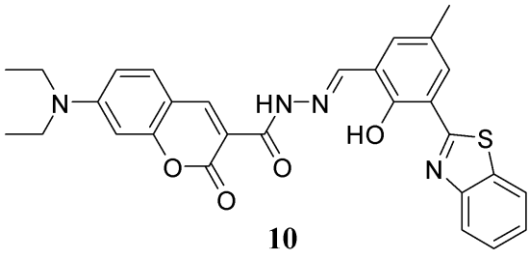

10

Li and group synthesized a novel sensor **10** and its photophysical properties were studied with sequential addition of Al^{3+} and PPi.[60] Compound **10** demonstrated significant fluorescence enhancements for Al^{3+} ions, and its complex compound **10**.Al^{3+} could detect PPi sequentially by demetallizing and turning off the fluorescence. The detection limit of compound **10** for Al^{3+} and PPi was 0.16 M μand 0.18 μM, respectively. Furthermore, the sensor was used to detect Al^{3+} and PPi in living cells.

Pan and team reported a highly selective and sensitive Schiff base fluorescence chemosensor **11**.[61] Compound **11** demonstrated excellent Cu^{2+} ion selectivity at pH 7.0 in EtOH-PBS (1:1, v/v) mixed solution. The binding mode of compound **11** and Cu^{2+} was validated using Job's plot

and FTIR. DFT theory was used to validate the binding ability of compound **11** and its quenching mechanism with Cu^{2+} ions. Furthermore, compound **11** has practical applicability as a paper strip with high selectivity for Cu^{2+} ions.

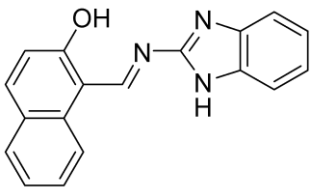

11

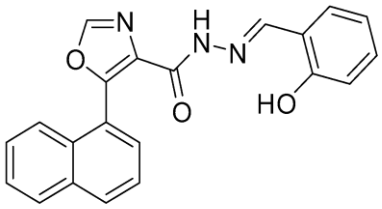

12

Guo and team designed and synthesized a novel Schiff base, **12** that contains oxazole joined to naphthalene unit.[62] Compound **12** was able to detect Al^{3+} ions in CH_3OH/H_2O with high sensitivity and very low LOD of 3.26×10^{-8} M. Further, the complex of compound **12** with Al^{3+} ions was used to detect Cu^{2+} ions with fluorescence quenching. Theoretical calculations, Job's plot and mass spectrometry supported the 1: 2 stoichiometry of compound **12** with both the ions. Compound **12** was able to detect both the ions in tap water.

Su and team reported a Schiff base **13** for the detection of Hg^{2+} ions.[63] Compound **13** showed weak emission at 415 nm on excitation at 349 nm in CH_3CN: H_2O (9:1, v/v) mixture. The fluorescence intensity at 415 nm increased in the presence of Hg^{2+} ions and a new band was formed at 473 nm. The coordination of Hg^{2+} with compound **13** through nitrogen atom and sulphur atom of the imine group and the thiophenyl moiety, respectively, forming a five membered ring structure may be attributed to the sensing mechanism as the suppression of the ESIPT process and C=N isomerization. According to results obtained from the Benesi-Hildebrand equation, the binding constant was found out to be 4.48×10^{5} M^{-1}. The lowest detection limit of compound **13** for the detection of Hg^{2+} ion was 22.68 nM.

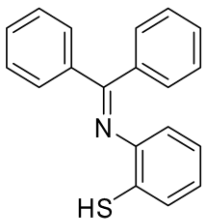

13

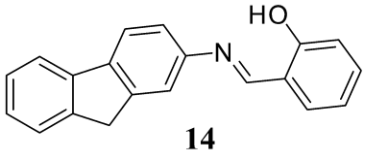

14

Tajbakhsh and group synthesized the fluorine based fluorescence turn-on Schiff base **14** for the sensing of Al^{3+} and Cr^{3+} ions.[64] Compound **14** displayed an emission at 536 nm on excitation at 333 nm in CH_3CN solution. Compound **14** demonstrated fluorescence increase at 536 nm in the presence of Al^{3+} and Cr^{3+} ions. The binding ratio was 2:1 and the binding constant for Al^{3+} and Cr^{3+} ions were found to be 5.44×10^4 M^{-1} and 8.33×10^4 M^{-1}, respectively. For Al^{3+} and Cr^{3+}, the lowest detection limit was 0.31 µM and 0.25 µM, respectively. Compound **14** was chelated with Al^{3+} and Cr^{3+}, which inhibited C=N isomerization and the ESIPT phenomenon and the fluorescence increased.

Zhu and his team synthesized Schiff base sensors **15a** and **15b** based on carbazoles to detect Fe^{3+} and Cr^{3+} ions in CH_3CN solution.[65] When exposed to Fe^{3+} and Cr^{3+} ions, compound **15a** showed considerable fluorescence enhancement that was caused by the inhibition of the ESIPT process and C=N isomerization. Without the *o*-OH group, compound **15a** has poor selectivity for the metal ion. The lowest detection limit for Fe^{3+} and Cr^{3+} ions were 4.57 µM and 2.75 µM, respectively. Fe^{3+} and Cr^{3+} ions had a binding stoichiometry of 2:1 and their respective binding constants were 4.67×10^4 M^{-1} and 5.97×10^4 M^{-1}, respectively.

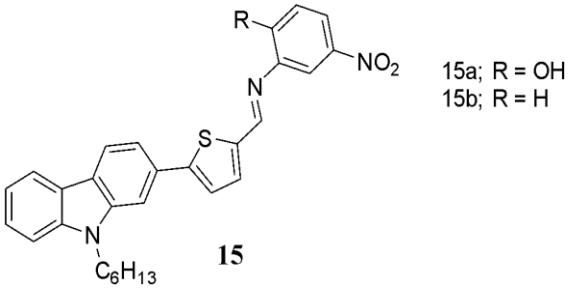

15

15a; R = OH
15b; R = H

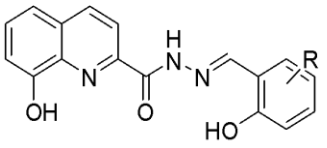

16

16a = H
16b = C_6H_5

Fu and coworkers developed Schiff base sensors **16a** and **16b** based on 8-hydroxyquinoline for the detection of Al^{3+} ions.[66] Both the compounds **16a** and **16b** are non-fluorescent in DMSO-H_2O (1:2, v/v) solution. The compound **16a** showed 270-fold and **16b** showed 460-fold increases in the fluorescence intensity at 505 nm and 509 nm, respectively in the presence of Al^{3+} ions. Inhibiting the ESIPT and C=N isomerization phenomenon through the complexation of compound **16a** and **16b** with Al^{3+} ion led to the fluorescence enhancement due to CHEF. The limit of detection for **16a** and **16b** with Al^{3+} was 14.8 nM and 42.3 nM, respectively, while the binding constant was 9.40×10^4 M^{-1}. The stoichiometry of compound **16a** and **16b** with Al^{3+} ions

were 1:1. Additionally, the complex of both the ions with Al^{3+} ions showed selective fluorescence quenching with F^- ions. Both the compounds were used in the bio-imaging of Al^{3+} and F^- ions in living cells as well as in the detection of these ions using paper strips.

Patra and coworkers synthesized a Schiff base **17** for the sensing of Zn^{2+} ions.[67] Compound **17** displayed weak yellow emission at 555 nm on excitation at 315 nm in CH_3OH: H_2O (3:1, v/v/) solution, which was attributed to the ESIPT and PET processes. Compound **17** showed fluorescence enhancement by 240-fold and a blue shift of the emission maxima from 555 nm to 512 nm in the presence of Zn^{2+} ions, which can be due to inhibition of ESIPT and PET phenomenon. The binding ratio of compound **17** with Zn^{2+} ions was 1: 1 with the binding constant of 6.49×10^4 M^{-1}. In contrast to other anions, the complex of compound **17** with Zn^{2+} ions demonstrated selective ATP-induced fluorescence quenching. The lowest detection limit for Zn^{2+} ions and ATP was found out to be 0.078 μM and 6.6 μM. Compound **17** was used in the bio-imaging and intracellular Zn^{2+} ion detection.

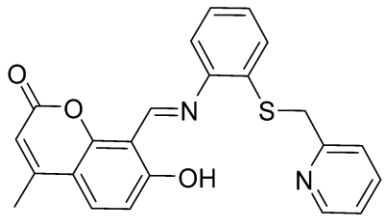

17

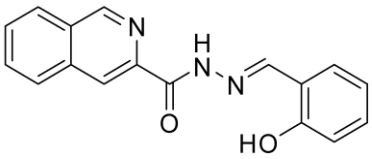

18

Huang and team reported Schiff base **18** based on isoquinoline as a turn-on sensor for Al^{3+} ions.[68] The fluorescence intensity at 458 nm was enhanced with the addition of an increasing concentration of Al^{3+} ions in ethanol solution. For Al^{3+} ions, the limit of detection was 1.11 nM. The binding stoichiometry was 2:1 and the binding constant was 2.78×10^6 M^{-1}. Al^{3+}ions in coordination with compound **18**, the ESIPT process was inhibited. Compound **18** could be used for the detection of intracellular Al^{3+} ions in living cells.

Naskar and team reported a benzophenone based Schiff base **19** for fluorimetric detection of Al^{3+} ions.[69] The compound **19** showed fluorescence at 450 nm upon excitation at 321 nm in ethanol-HEPES buffer solution. The fluorescence of compound **19** was enhanced at 450 nm when Al^{3+} ions were added. The stoichiometry of the complex was 1:2 and the binding constant was 10.18×10^3 M^{-1}. For Al^{3+}, the lowest detection limit was 4.61×10^{-7} M. The complexation of

compound **19** with Al^{3+} ions led to CHEF and inhibition of ESIPT and C=N isomerization. The MTT experiment revealed that compound **91** has no cytotoxicity upto 40 µM. Compound **19** showed blue fluorescence towards HepG2 cells when bound to intracellular Al^{3+} ions.

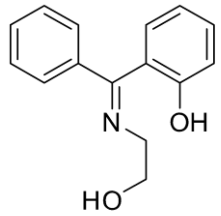

19

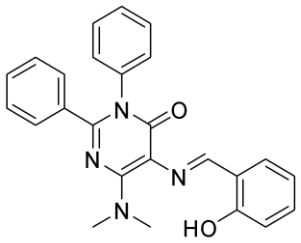

20

Singh and team reported a compound **20**, which exhibited ESIPT, linked AIE with bright green fluorescence in both aqueous and solid state.[70] Compound **20** could detect Cu^{2+} ions in HEPES buffer-CH_3CN (99:1, v/v) with high selectivity and sensitivity. It can detect Cu^{2+} ions in drinking water with a detection limit of 0.261 ppb. DLS, SEM and TEM studies revealed that the interaction of Cu^{2+} ions and the Schiff base unit of compound **20** disturbed the self-assembled aggregates. Compound **20** was also used to detect Cu^{2+} in blood serum, environmental materials and for cell imaging of HeLa cells with low cytotoxicity.

Peng and coworkers synthesized two pyridine derived Schiff bases **21a** and **21b** to serve as fluorescence sensor for Al^{3+} ion using PET and ESIPT mechanisms.[71] In DMF-H_2O (1:9, v/v) solution both the compounds displayed a rapid fluorescent response to Al^{3+} ions with 1:1 binding stoichiometry. Compound **21a** and **21b** both showed high selectivity and sensitivity to Al^{3+} ions with a color change from colorless to aquamarine. Furthermore, both were successfully used for the detection of Al^{3+} ions in real water samples.

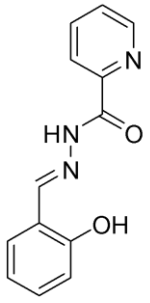

21a

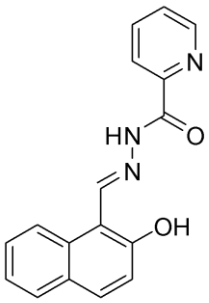

21b

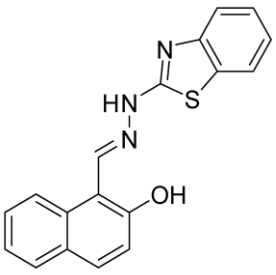

22

Paul and team reported a naphthalene-benzothiazole base Schiff base **22** for selective detection of Zn^{2+} and Cd^{2+} ions.[72] Compound **22** showed visible color change from colorless to pale yellow after the addition of Zn^{2+} ions whereas only fluorogenic response was observed for Cd^{2+} ions. It can also detect CN^- ions colorimetrically with fluorescence enhancement. ESIPT, PET, C=N isomerization, CHEF and ICT phenomenon reveal sensing mechanisms. Different techniques like ^1H NMR titration, FESEM and EDX (Energy dispersive X-ray spectroscopy) were used to show analytic interaction. Compound **22** had practical application as molecular logic gate, cell imaging and as sensor in natural sources.

Kim and group developed a Schiff base **23** for the fluorescent detection of Fe^{3+} ions.[73] After the addition of Fe^{3+} ions the fluorescence of compound **23** was enhanced at 550 nm due to inhibition of ESIPT. Compound **23** showed very high sensitivity towards Fe^{3+} ions in aqueous medium and the lowest detection limit was found out to be 0.8 ppb. It was also used to detect Fe^{3+} ions cancer cells with low cytotoxicity.

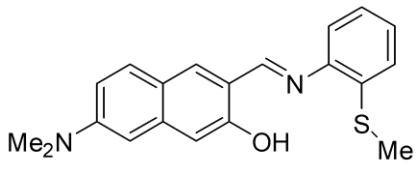

23

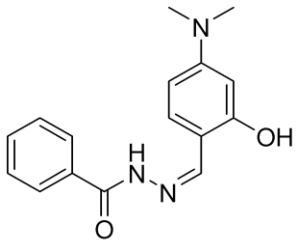

24

Yan and coworkers reported salicylaldehyde hydrazine derivative **24** based on ESIPT and C=N isomerization for the detection of Al^{3+} ions in aqueous solution.[74] Compound **24** has photochromic characteristics that are reversible due to isomerization and ESIPT phenomenon. Compound **24** binds with Al^{3+} in water at a molar ratio of 2:1 resulting in enhanced. The absorption peak of compound **24** at 367 nm was decreased with simultaneous increase in the peak at 41 nm and 438 nm after irradiation at 365 nm. The color of the compound **24** was also changed from colorless to yellow. Compound **24** was used for the detection of Al^{3+} ions in living cells and water samples.

Zhang and group developed a high-performance fluorescent compound **25** for in vitro and in vivo Al^{3+} detection.[75] The synthesized compound **25** from 2-hydroxynaphthalene that can detect Al^{3+} ion with high selectivity and sensitivity and it also exhibits "off-on" mode in methanol

solution. The detection limit for Al^{3+} ion is as low as 10^{-7} M. the inhibition of ESIPT is responsible for **25**'s high selectivity and sensitivity. They used compound **25** for in vivo detection of Al^{3+} ions in living zebrafish larvae.

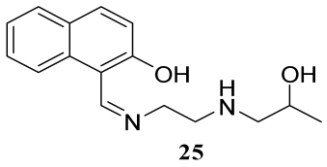

25

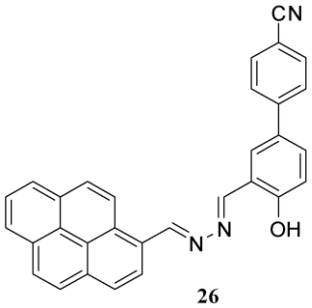

26

Bai and team designed and synthesized a compound **26** based on ESIPT-AIE mechanism, which was used to detect CN^- ions with large Stoke shift, high selectivity and low LOD.[76] Compound **26** could efficiently detect CN^- ions demonstrated through fluorescence imaging in plants. Additionally, it showed that compound **26** can also be used as a fluorescence sensor for CN^- ions in biological systems. Compound **26** exhibits significant Stokes shift, good selectivity and rapid detection of CN^- ions and AIE effects owing to restriction of intramolecular. The limit of detection (LOD) was found to be 1.32×10^{-7} M.

Shu and coworkers demonstrated the multi stimuli responsive behavior of an Et_2N substituted salicylaldehyde Schiff base compound **27**.[77] From the photophysical characteristics of compound **27** revealed that it is an ESIPT and AIE active molecule. Compound **27** exhibits reversible mechanochromism and thermochromism due to structural flexibility of salicylaldehyde Schiff base. The XRD studies demonstrated that mechanochromism in compound **27** was due to crystalline to amorphous transition whereas thermochromism was due to crystalline to crystalline transition. Moreover, with HCl, the $-NEt_2$ group in compound **27** protonated leading to acid chromism. Compound **27** was able to distinguish $CHCl_3$ from organic solvents using this property since $CHCl_3$ could produce HCl when exposed to UV light.

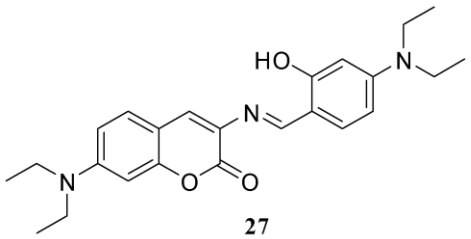

27

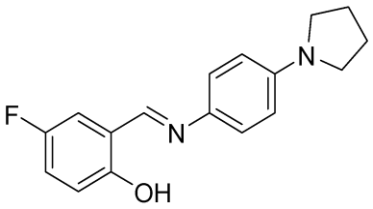

28

Xie and team developed a simple salicylaldehyde Schiff base **28** with AIE and ESIPT phenomenon for the sensing of N_2H_4 and ClO^- ions.[78] Compound **28** showed rapid turn on of blue fluorescence on detecting N_2H_4 with very high selectivity and sensitivity whereas for ClO^- ions a rapid turn off of the weak green fluorescence was observed. The mass spectrum revealed that compound **28** disintegrated when exposed to N_2H_4, but forms complex with ClO^- ions and hinder ESIPT. Compound **28** provides a useful tool for exploring N_2H_4 and ClO^- ions in live cells.

Ali and colleagues illustrated the sensing properties of **29**, which sensed F^- ion and CN^- ion.[79] This molecule showed fluorescence "Turn-On" in partially aqueous DMSO with both the ions. The absorption maximum for NTS was found to be 340 nm, 454 nm and 481 nm due to ESIPT and a weak emission band at 418 nm was observed on excitation at 340 nm. As the polarity of the solvent was increased the absorption band due to enol form diminished and keto form increased. With the addition of F^- ion the absorption band at 340 nm, 454 nm and 481 nm disappeared and a new absorption band at 492 nm emerged and similarly with CN^- ion the band at 340 nm shifted to 355 nm and from 481 nm to 42 nm. The F^- ion showed enhanced dual emission at 416 nm and 590 nm and the CN^- ion showed strong emission at 414 nm and 594 nm.

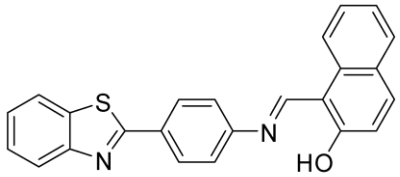

29

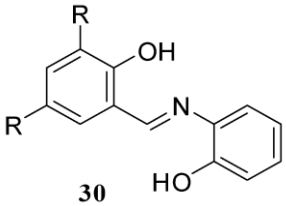

30

30a = H
30b = CH_3
30c = Cl

Nakwanich and team synthesized three salicylidene based Schiff base as colorimetric sensors **30**.[80] All the derivatives demonstrated high selectivity for colorimetric detection of F^- ions in CH_3CN. The binding stoichiometry for compound **30** and F^- ions was 1:1. Colour of compound **30** changes from pale yellow to orange red in the presence of F^- ions. The LOD for F^- ions with

compound **30** was found to be in the range of 7×10^{-5} M to 21×10^{-5} M. DFT and TDDFT studies provided confirmation of the optimized structure and electronic transitions.

Ghosh and coworkers reported a benzothiazole based Schiff base **31**.[81] Compound **31** showed fluorescence turn-on behavior with CN^- ions in CH_3OH/HEPES buffer medium at pH 7.5. the binding mechanism for CN^- ions with compound **31** was analyzed using ^1H NMR titration, IR and MS analysis. The DFT studies were also done to support the nucleophilic attack of CN^- ions on the imine bond of compound **31**. MDA-MB 231 cells have been used to test the cytotoxicity of compound **31** and fluorescence cell imaging was also performed for the sensing of CN^- ions.

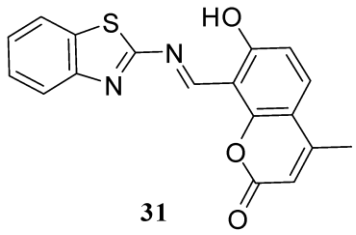

31

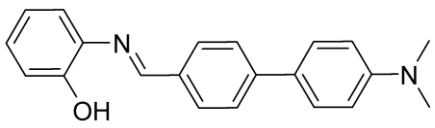

32

Gupta and team synthesized ESIPT based compound **32** that demonstrated good photophysical behavior towards CN^- ions with high selectivity and sensitivity.[82] Compound **32** acts as a chemodosimeter for CN^- ions with lowest detection limit of 24 ppb. Furthermore, the visible color change was observed for compound **32** after the addition of CN^- ions. The optical behavior of compound **32** was linked to the intramolecular charge transfer (ICT) phenomenon. The ^1H, ^{13}C NMR and HRMS spectral data analysis validated the binding mechanism. The compound **32** was used to detect CN^- ions on paper strips.

Helal and coworkers synthesized compound **33** that was used for the detection of F^- ions.[83] Compound **33** showed emission bands at 369 and 506 nm. Both the emission bands vanished in the presence of F^- ions and a new band emerged at 453 nm. The shift in the emission band was due to the inhibition of the ESIPT phenomenon caused by the deprotonation of the phenolic group.

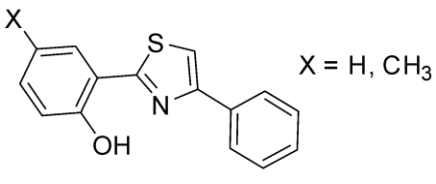

33

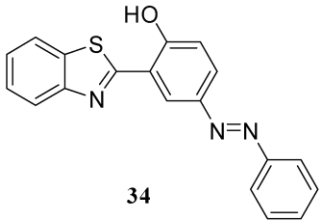

34

Pan and team reported a simple ESIPT based sensitive fluorescent compound **34** for the detection of HClO in neutral aqueous solution under physiological conditions.[84] Compound **34** showed excellent selectivity and sensitivity towards HClO with the lowest detection limit of 13.2 nM. Compound **34** was used as a ROS sensor for a wide range of chemical and biological applications.

Gil and coworkers reported a reversible colorimetric compound **35** for the detection of F^- ions.[85] Compound **35** showed color change from colorless to yellow upon interaction with F^- ions and the lowest detection limit for F^- ions was found to be 12.1 μM. Job's plot, ^1H NMR titration, DFT calculations, and ESI-MS were used to demonstrate the binding behavior and sensing mechanism of compound **35** with F^- ions.

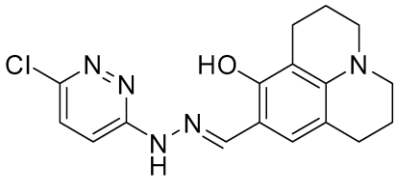

35

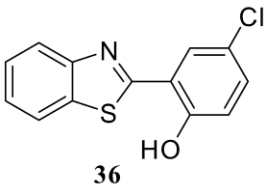

36

Bhattacharyya and team synthesized hydroxybenzothiazole derivative **36** to study its photophysical properties towards different anions.[86] Steady state, time resolved spectroscopic studies, FESEM and DLS studies showed that ESIPT and AIE in compound **36** were coupled. Compound **36** was used for the detection of S^{2-} and CN^- ions in aqueous medium colorimetrically. By observing the change in the color under UV light, paper strips coated with compound **36** were used for the detection of both the ions.

Tohora and coworkers developed a benzoxazole based Schiff base **37** for selective detection of CN^- ions in H_2O: DMSO (1:1, v/v) solvent.[87] Compound **37** showed blue fluorescence "turn-on" with CN^- ions, which was due to inhibition of ESIPT phenomenon by deprotonation of hydroxyl proton. The binding ratio of compound **37** and CN^- ions was found to be 1:1 with binding constant of 0.55×10^4 M^{-1}. The lowest detection limit for CN^- ion detection was 23 nM. It was also used as paper strips for the sensing of CN^- ions.

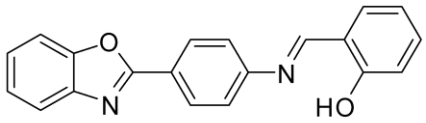

37

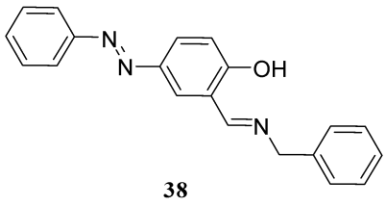

38

Kamali and team reported azo Schiff base **38** via condensation reaction.[88] Compound **38** acts as a colorimetric sensor for HSO_4^- and CN^- ions in CH_3CN: H_2O (4:1, v/v). The binding stoichiometry of compound **38** with HSO_4^- and CN^- ions was 1:1 and 1:2 with the binding constant of 2.25×10^5 M^{-1} and 2.64×10^4 M^{-1}, respectively. the lowest detection limit (LOD) for the detection of HSO_4^- and CN^- ions was found to be 1.01×10^{-10} M and 5.24×10^{-6} M, respectively.

Li and team designed and synthesized an ESIPT based ratiometric fluorescent Schiff base **39** for the sensing of HClO in MeOH: PBS (1:4, v/v) solution.[89] Over a wide range of pH, compound **39** demonstrated good selectivity for the detection of HClO. The binding mechanism was identified using MS and HPLC. The detection limit for HClO using compound **39** was 14.6 nM. Compound **39** was used to detect HClO spiked in real samples and the results revealed the potential for use in analytical and bioanalytical applications.

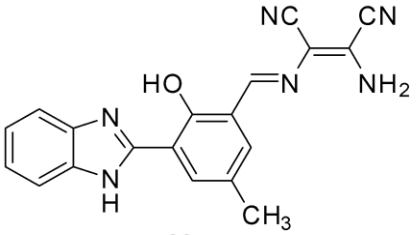

39

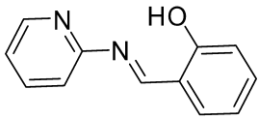

40

Alam and team synthesized an ESIPT based Schiff base **40** and its solid-state emission characteristics were investigated.[90] Compound **40** exhibited bright emission which can be due to the AIE phenomenon occurring in the compound. Further, compound **40** was used for the detection of F^- ions with very high selectivity and sensitivity. The lowest detection limit for F^- ions was found out to be 14.0 pM. UV-vis and ^1H NMR spectroscopy were used to support the 1:1 binding of the F^- ions with compound **40**. DFT and TDDFT calculations also supported the experimental results.

Chen and colleagues developed an ESIPT based fluorescent Schiff base **41** for the detection of $HOCl/ClO^-$ ions.[91] Compound **41** undergoes hydrolysis mediated by $HOCl/ClO^-$ ions that lead to enhancement in fluorescent intensity. Additionally, it demonstrated excellent sensitivity towards $HOCl/ClO^-$ ions with lowest detection limit of 0.08 μM. Compound **41** was used for the endogenous formation of $HOCl/ClO^-$ ions in living cell and tissues.

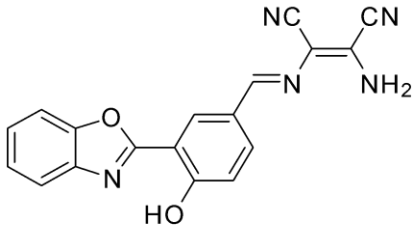

41

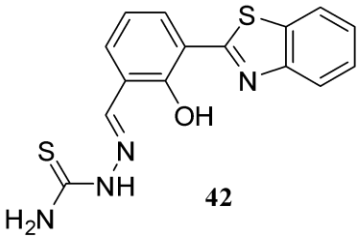

42

Manna and coworkers synthesized a thiosemicarbazide based fluorescent compound **42** for the ratiometric detection of $HOCl/ClO^-$ ions.[92] The ESIPT phenomenon taking place in compound **42** was hindered as $HOCl/ClO^-$ ions might damage the hydrogen bonding. When exposed to $HOCl/ClO^-$ ions compound **42** displayed good selectivity and sensitivity accompanied by color change from orange to blue. Compound **42** was capable of detecting $HOCl/ClO^-$ ions in tap water, demonstrating its potential use in keeping track of the purity of drinking water.

Chang and team developed a dithiolane functionalized fluorescent compound **43** for the detection of $HOCl/ClO^-$ ions.[93] The fluorescence intensity of compound **43** was enhanced with the color change from yellow to blue after the addition of $HOCl/ClO^-$ ions. Compound **43** showed high selectivity and sensitivity towards $HOCl/ClO^-$ ions with lowest detection limit of 8.9 nM. In HeLa cells, it was demonstrated that compound **43** was cell permeable and can detect both $HOCl/ClO^-$ ions.

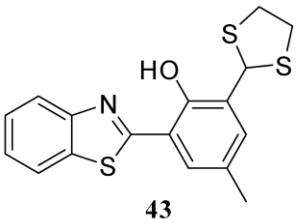

43

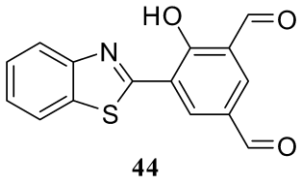

44

Goswami and colleagues reported a hydroxybenzothiazole based ratiometric compound **44** for the sensing of CN^- ions.[94] Compound **44** was selective for CN^- ions and yields a cyanohydrin that

inhibits the ESIPT process. The lowest detection limit for compound **44** to detect CN^- ions was 1.6 μM. The experimental results were supported by DFT and TDDFT calculations.

Bera and team reported a salicylaldehyde functionalized ESIPT compound **45** for CN^- ions sensing.[95] Compound **45** formed a stable cyanohydrin product and the fluorescence intensity was significantly enhanced owing to the inhibition of ESIPT process. Compound **45** was utilized for cell imaging in living SH-SY5Y cells with the LOD value of 0.06 ppm and a very low cytotoxicity. As a result, compound **45** had application in a variety of chemical and biological processes.

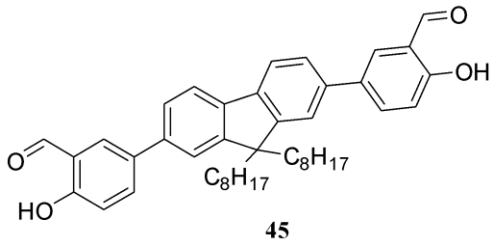

45

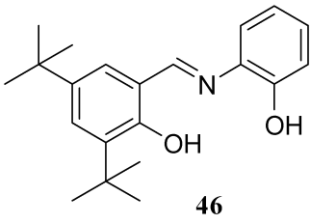

46

Liang and coworkers reported an ESIPT and AIE facile Schiff base **46** for the sensing of CN^- ions selectively and sensitively.[96] Compound **46** showed weak fluorescence due to ESIPT phenomenon and the fluorescence was enhanced after the addition of CN^- ions in aqueous medium. The lowest detection limit for the detection of CN^- ions was found to be 5.92×10^{-7} M. Compound **46** was used as a test paper strip for the detection of CN^- ions.

Pundi and team developed fluorescent and colorimetric turn-on sensor compound **47** for the detection of CN^- ions with good selectivity and sensitivity.[97] Compound **47** undergoes nucleophilic addition towards imine group with CN^- ions that resulted in the color change and decrease in the fluorescence intensity. The ^1H NMR titration and mass spectrum were used to confirm the binding mechanism. The detection limit for the sensing of CN^- ions was found out to be 0.80 μM. Further, compound **47** was used for the cell imaging for the detection of CN^- ions in living cells.

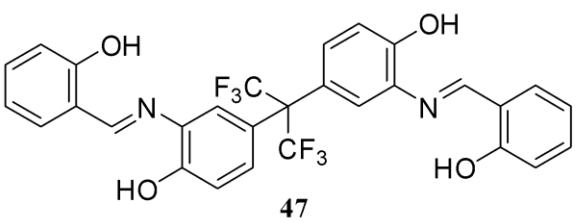

47

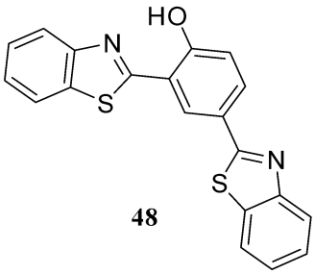

48

Liu and team investigated the two-novel fluoride sensor compound **48**.[98] The absorption spectra of compound **48** showed two peaks at 296 nm and 310 nm and with addition of fluoride from 2-20 μM these two peak intensities decreased and new peaks were observed at 377 nm and 432 nm with an isosbestic point 350 nm. The fluorescence spectra showed peaks at 386 nm (enol form) and 548 nm (keto form) which disappeared with the addition of fluoride ion and a new peak emerged at 477 nm. Compound **48** exhibited two absorption peaks at 296 nm and 315 nm and an emission at 379 nm and with the addition of fluoride ion the emission peak at 379 nm decreased and a new peak was observed at 477 nm.

1.2.2. Double ESIPT based sensors

Wang and coworkers synthesized a water soluble benzimidazole based Schiff base **49**.[99] Compound **49** was highly selective and sensitive in the aqueous solution in the pH range of 8 to 12 and it showed good reproducibility. It is a fluorescence turn off sensor for Cu^{2+} ions with lowest detection limit of 7.70×10^{-8} mol L^{-1}. Additionally, compound **49** can detect Cu^{2+} ions in real field samples with good recoveries. The job's plot and HRMS revealed that compound **49** binds to Cu^{2+} ions in 1:1 stoichiometry.

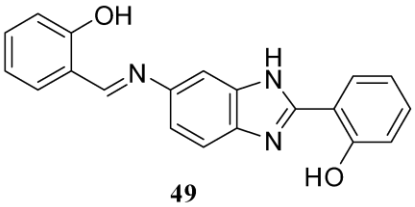

49

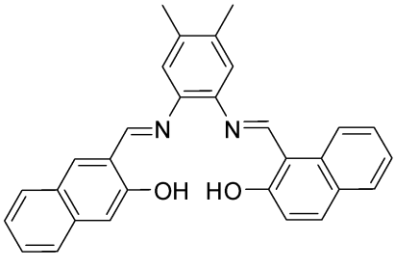

50

Sidqi and coworkers developed an effective fluorescent compound **50** for the recognition of Al^{3+} ions.[100] Compound **50** could detect Al^{3+} ions with high selectivity and sensitivity through inhibition of ESIPT and C=N isomerization phenomenon. DFT calculations were used to predict

the binding behavior of compound **50** towards Al^{3+} ions. With an association constant of 2.18×10^{5} M^{-1}, compound **50** coordinated with Al^{3+} ions in 1:1 stoichiometry. Compound **50** can detect Al^{3+} ions with the lowest detection limit of 7.05×10^{-9} M. The living HeLa cell imaging revealed that compound **50** exhibited good cell membrane permeability and was also used for fluorescence imaging.

Suman and team designed and synthesized two benzimidazole/benzothiazole (**51**) based azomethines.[101] These fluorophores showed solvatochromic behavior in solvents of varying polarity and showed Stokes shift of 134-210 nm. Time-resolved fluorescence measurements revealed the dynamics of the fluorophore in excited state. Aggregation induced emission studies showed that the molecules in the aggregated form are emissive. Significant absorption and emission changes as well as good selectivity and sensitivity were observed with Al^{3+}/Zn^{2+} ions. The binding stoichiometry was determined using electrospray ionization mass spectrometry (ESI-MS) and the binding mechanism was investigated using density functional theory.

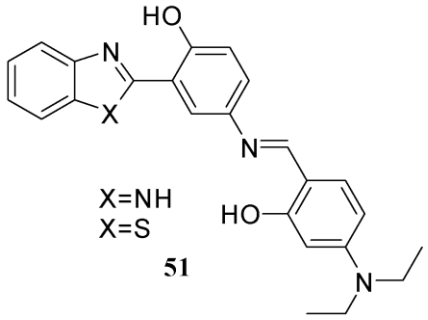

51

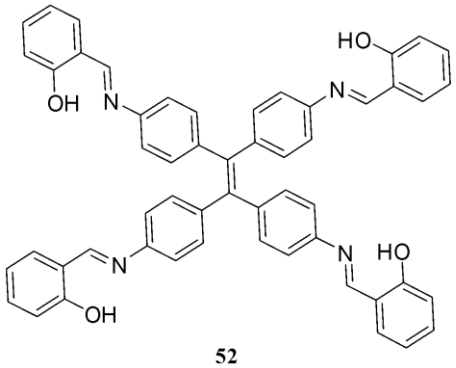

52

Puri and coworkers developed a Schiff base **52** with AIE feature for fluorescence based Al^{3+} ion sensing in methanol.[102] Compound **52** showed emission at 548 nm after excitation at 360 nm, accompanied by a Stokes shift of 188 nm, which was attributed to the ESIPT phenomenon. The addition of Al^{3+} ions to compound **52** solutions resulted in an increase in the emission intensity at 476 nm with Stokes shift of 116 nm, which was attributed to metal-template aggregation.

Sun and coworkers synthesized an AIE and ESIPT facile Schiff base **53** via one pot reaction.[103] Compound **53** can be used as a dual channel colorimetric and fluorescent sensor for Zn^{2+} ions in H_2O with good selectivity, sensitivity and low detection limit of 38.9 nM. An eco-friendly inkless rewritable paper with tremendous potential application in information security was

developed. Furthermore, compound **53** has very low cytotoxicity and has been employed for Zn^{2+} ion sensing on living cells.

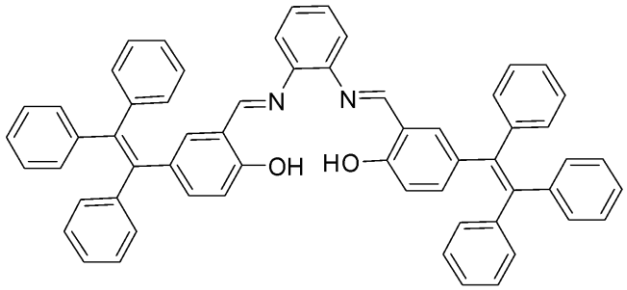

53

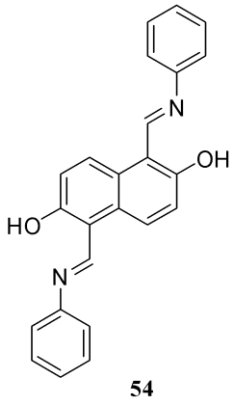

54

Zhang and team synthesized and characterized a Schiff base **54** with AIE characteristics and demonstrated sensitivity and selectivity towards Cu^{2+} ions in aqueous media with a fluorescence "Turn-off" phenomenon.[104] Compound **54** has a detection limit of 1.64×10^{-8} mol L^{-1}. Furthermore, 1:2 stoichiometry was determined using the UV-vis/fluorescence titration, Job's plot method and ^{1}H NMR titrations. The binding constant between compound **54** and Cu^{2+} ions was calculated to be 1.22×10^{3}. Compound **54** was used for detection of Cu^{2+} ions in real water samples with good recoveries.

1.2.3. ESIPT based sensors for enzymes

Liu and team designed ESIPT based compound **55** which showed excitation and emission maxima at 410 nm and 550 nm.[105] Compound **55** was used to designed enzyme responsive fluorescent probe that targeted alkaline phosphate (ALP) as a model enzyme and was designed by protecting phenolic hydroxyl group of HTPQ that resulted in ESIPT "Off" which upon interaction with enzyme resulted in ESIPT "On" of compound **55**. It was also used to visualize different levels of ALP in cells and tissues thus demonstrating its interest for diagnosis of this type of cancer.

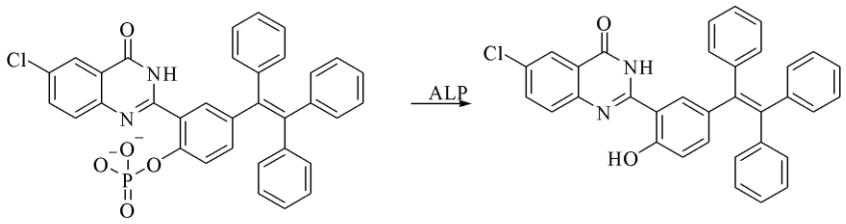

55

Yang and team synthesized compound **56** with blocked salicylaldehyde quinazoline derivative which showed weak fluorescence due to intramolecular hydrogen bonding restricted intramolecular rotation.[106] Compound **56** showed ESIPT and AIE when it detected β-galactosidase selectively. The fluorescence intensity for compound **56** for detecting β-galactosidase increased at 495 nm with the incubation time.

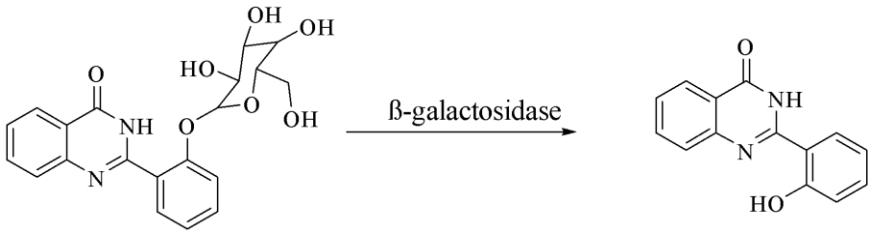

56

Sheng and team synthesized compound **57** for the selective detection of cysteine based on ESIPT.[107] Compound **57** used acrylate group as blocking and recognition site for cysteine. Compound **57** upon detecting cysteine showed fluorescent enhancement of 85-folds and large Stokes shift of 166 nm. Compound **57** showed absorption peak at 303 nm and upon treatment with cysteine the peak was red shifted by 6 nm and also fluorescence emission at 495 nm gradually increased upon adding cysteine.

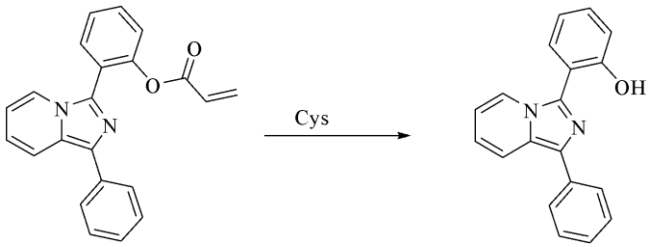

57

Sheng and group synthesized ESIPT and AIE based compound **58** with two acrylate groups for selective detection of cysteine.[108] Compound **58** showed strong fluorescence enhancement and

large Stokes shift of 162 nm upon treatment with cysteine. Compound **58** was also used to detect cysteine in living cells and it could detect cysteine with high selectivity and sensitivity.

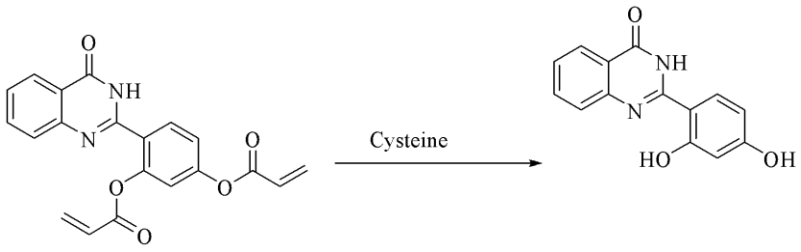

58

Yu and coworkers designed fluorescent turn-on compound **59** for the detection of cysteine.[109] Compound **59** showed high selectivity and sensitivity to cysteine as compared to other amino acids including those which have similar structure that of cysteine. Compound **59** showed absorption peak at 315 nm and after addition of cysteine the absorption peak shifted to 335 nm.

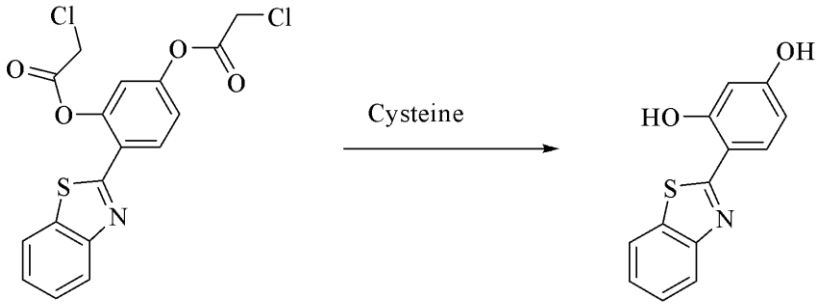

59

Liu and coworkers synthesized a highly sensitive and selective compound **60** for cysteine.[110] Compound **60** showed weak blue fluorescence but after addition of cysteine the acrylate group was hydrolyzed and the ESIPT was enabled to shift from weak blue fluorescence to strong green fluorescence. After the addition of cysteine, the absorption band at 350 nm increased with time and band at 390 nm decreased. This was successfully used for fluorescent imaging of intracellular cysteine.

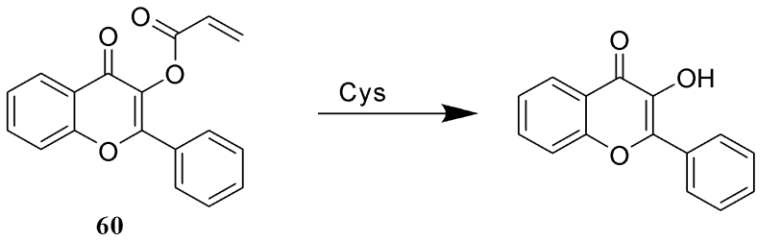

60

Tang and team developed compound **61** for the selective detection of HCys over other amino acids, including Cys and GSH.[111] Compound **61** was capable of distinguishing between HCys and Cys. As a result of compound **61** demonstrating excellent selectivity, compound **61** was used in cellular imaging experiments. Compound **61** was shown to detect intracellular HCys, leading to the suggestion that it might find utility in biological applications.

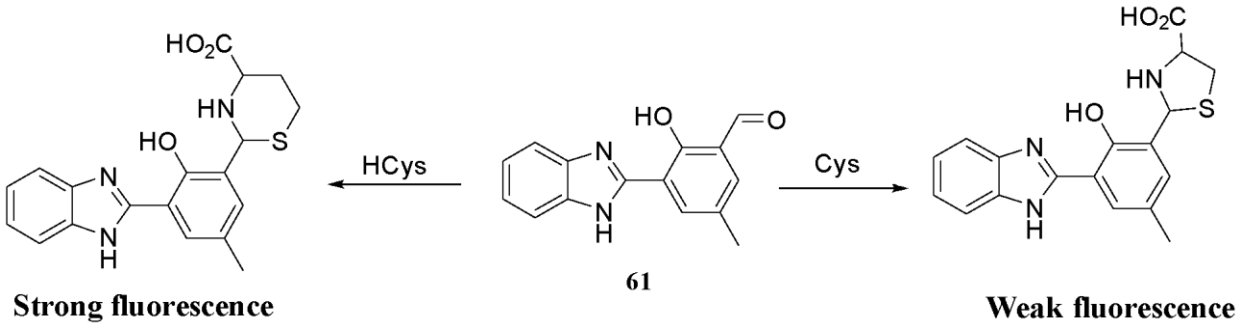

Strong fluorescence

61

Weak fluorescence

Tian and group developed compound **62** that is capable of discriminating between live and dead cells.[112] Its efficacy depends on the fact that cellular esterases are normally inactive inside dead cells. In dead cells compound **62** showed blue fluorescence peaked at 440 nm with blocked ESIPT while in live cells it showed orange emission peaked at 570 nm with recovered ESIPT. Compound **62** was capable of detecting dead tumor cells that had been killed via pre-treatment with H_2O_2 and UV.

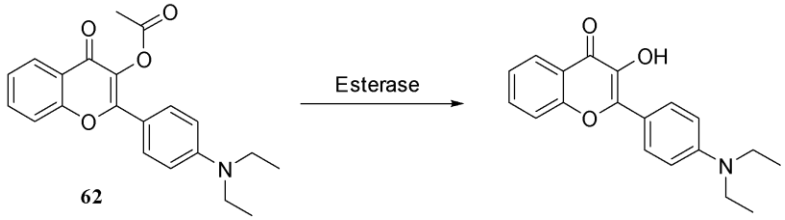

62

Hu and colleagues synthesized an ESIPT based fluorescent compound **63** for the detection of ALP.[113] Compound **63** demonstrated high selectivity and quick detection. The lowest detection

limit of compound **63** for the detection of ALP was found out to be 0.032 U/L and the binding affinity was 1.84×10^7 L/mol. Compound **63** has very low cytotoxicity and is used for the cell imaging for detection of ALP.

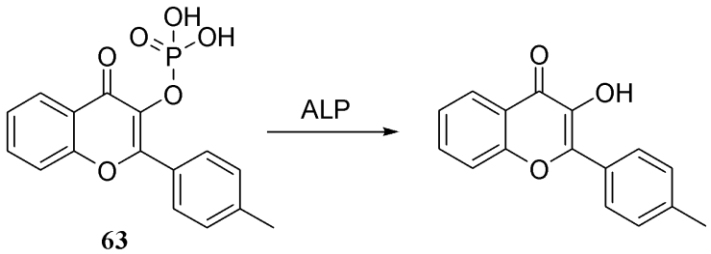

63

Zhang and team developed an ESIPT and AIE facile fluorescent compound **64** for detecting lipase enzyme in homogenous systems.[114] Compound **64** exhibited high selectivity, sensitivity, low cytotoxicity and outstanding biocompatibility. The lowest detection limit for the detection of lipase using compound **64** was found out to be 0.01 mg/mL using compound **64** in linear range of 0.2-1.3 mg/mL. Detecting exogenous lipase in HeLa cells further revealed the in vivo bioimaging capabilities of compound **64**.

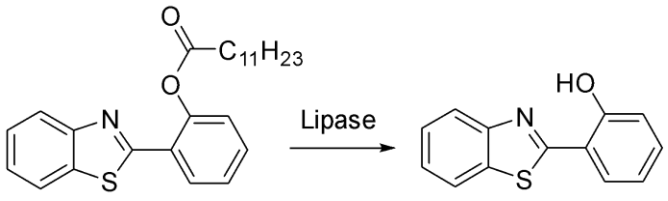

64

Zhang and team reported novel mitochondria targeted ratiometric compound **65** for ALP detection and visualization.[115] Due to the blocking of ESIPT, compound **65** had good solubility in H_2O and produced green fluorescence in aqueous buffer. Phosphate ester hydrolysis and restoration of the ESIPT process occurred in the presence of ALP, changing the fluorescence from green to red. With a LOD of 0.072 mU/mL, compound **66** was able to quantitatively detect ALP between 0 to 60 mU/mL. Compound **65** was used for measuring ALP activity in vitro and in vivo due to its low cytotoxicity.

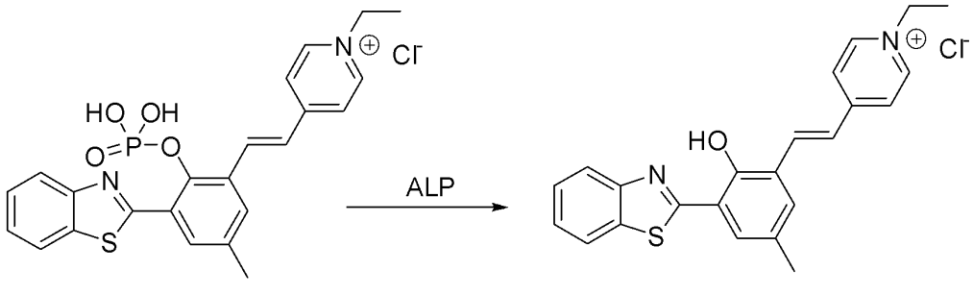

65

Peng and colleagues group synthesized compound **66** with AIE and ESIPT properties for the detection of β-galatosidase.[116] The fluorescence of compound **66** was enhanced after the breakage of the β-galactopyranoside group in the presence of β-galatosidase. The hydrolysis product readily accumulated in living cells and exhibited a potent fluorescence emission. As a result, compound **66** was used to detect intracellular β-galatosidase activity in living cells, such as HeLa and C6/LacZ cells.

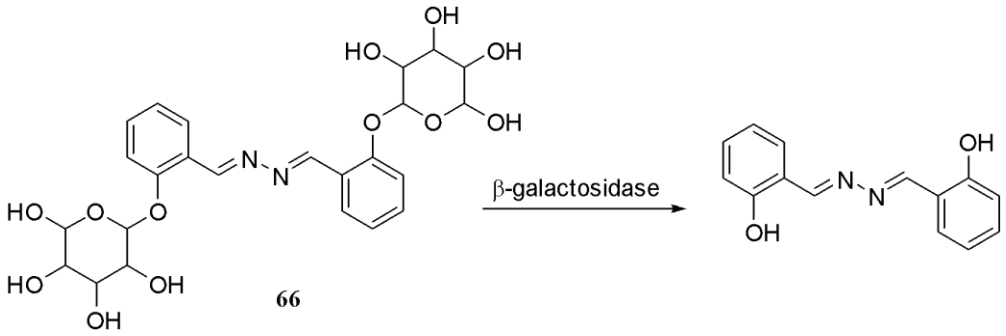

66

Tain and team designed and reported compound **67** for the detection of galatosidase.[117] The ESIPT process was turned-off in compound **67** but after the addition of β-galatosidase the ESIPT was turned-on. Compound **67** showed red shift of 140 nm with β-galatosidase and it very selective and sensitive. Compound **67** was used in diagnostic and drug screening procedure, such significant Stokes shift made it easier to analyse glycosidase activity.

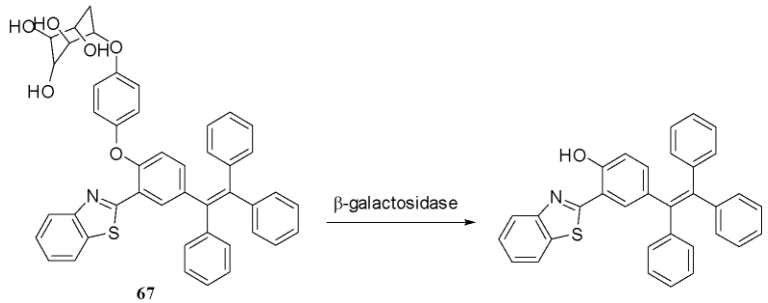

67

During the literature survey, we have found reports based on compounds which exhibited the AIE phenomenon while the Schiff base linkage allows the ESIPT phenomenon. The interplay of two phenomena has been studied by experimental and theoretical methods. Additionally, the compounds were successfully utilized for detection of common metal ions with approach of real-world applications. Despite the potential applications, the literature reports limit the theoretical insight of phenomena. The literature limits an experimental and theoretical study on the phenomenon of ESIPT/ESIDPT phenomenon.

1.3. Research Gap and Objective

1.3.1. Research Gap

Molecular systems containing double intramolecular hydrogen bonds have been scarcely studied for sensing of cations and anions. Only a very few reports are available in literature where double sites (double pair of proton donor and acceptor) for ESIPT phenomenon are available on single platform.[99-104] Furthermore, the sensing properties of these molecular systems has been less explored. Therefore, the motivation of this thesis was to gain theoretical insight into the ESIPT phenomenon in different molecular architecture.

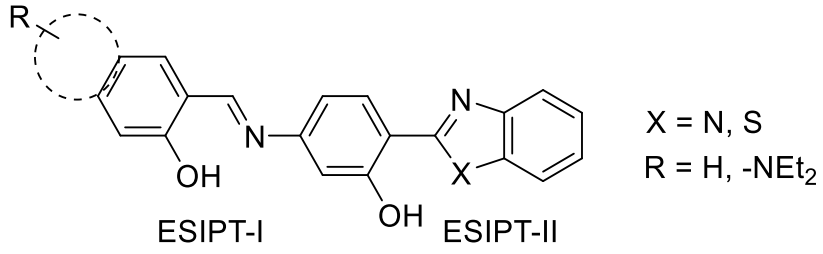

1.3.2. Objectives

1. Synthesis, characterization and stability studies of aza-heterocycle molecular architecture vulnerable for the demonstration of ESIPT.

2. To explore the sensing properties of various ESIPT based moieties towards enzymes, metal ions and anions.

3. Computational studies to detect the mechanistic pathway for ESIPT phenomenon.

Chapter 2

Materials and Methods

Chemicals, reagents and solvents used in the current investigations are described in detail. Additionally, a brief description of the approach for theoretical calculations, data analysis and experimentation was provided. This chapter also goes into detail about the equipment used in the course.

2.1. Materials

The details of chemicals and solvents used are listed below:

2.1.1. Chemicals

- ✔ 4-aminosalicylic acid (Sigma-Aldrich)
- ✔ *o*-phenylenediamine (Spectrochem India)
- ✔ 2-aminothiophenol (Spectrochem India)
- ✔ Salicylaldehyde (Spectrochem India)
- ✔ N, N-Diethylamino salicylaldehyde (Sigma-Aldrich)
- ✔ 2-hydroxy naphthaldehyde (Sigma-Aldrich)
- ✔ 2-methyl-8-quinolinol (Sigma-Aldrich)
- ✔ Selenium dioxide (Sigma-Aldrich)
- ✔ Polyphosphoric acid (Spectrochem India)
- ✔ Nitrobenzene (AR grade, Loba Chemie, India)
- ✔ Sulphuric acid (AR grade, Loba Chemie, India)
- ✔ Silica gel (60-120, 120-240) (Merck, India)
- ✔ Silica gel GF-256 (Spectrochem Inida)
- ✔ Sodium sulfate (Loba Chemie Inida)

2.1.2. Metal ions

- ✔ Sodium perchlorate monohydrate, $NaClO_4.H_2O$; (Sigma Aldrich)
- ✔ Potassium perchlorate, $KClO_4$; (Sigma Aldrich)
- ✔ Magnesium perchlorate hexahydrate, $Mg(ClO_4)_2.6H_2O$; (Sigma Aldrich)
- ✔ Calcium perchlorate tetrahydrate, $Ca(ClO_4)_2.4H_2O$; (Sigma Aldrich)
- ✔ Barium perchlorate, $Ba(ClO_4)_2$; (Sigma Aldrich)
- ✔ Aluminium perchlorate nonahydrate, $Al(ClO_4)_3.9H_2O$; (Sigma Aldrich)

- ✔ Lead perchlorate hydrate, $Pb(ClO_4)_3.xH_2O$; (Sigma Aldrich)
- ✔ Iron perchlorate hydrate, $Fe(ClO_4)_3.xH_2O$; (Sigma Aldrich)
- ✔ Cobalt perchlorate hexahydrate, $Co(ClO_4)_3.6H_2O$; (Sigma Aldrich)
- ✔ Nickel perchlorate hexahydrate, $Ni(ClO_4)_3.6H_2O$; (Sigma Aldrich)
- ✔ Copper perchlorate hexahydrate, $Cu(ClO_4)_3.6H_2O$; (Sigma Aldrich)
- ✔ Zinc perchlorate hexahydrate, $Zn(ClO_4)_3.6H_2O$; (Sigma Aldrich)
- ✔ Cobalt perchlorate hexahydrate, $Co(ClO_4)_3.6H_2O$; (Sigma Aldrich)
- ✔ Mercury perchlorate hydrate, $Hg(ClO_4)_3.xH_2O$; (Sigma Aldrich)
- ✔ Silver perchlorate, $Ag(ClO_4)_3$; (Sigma Aldrich)

2.1.3. Anions

- ✔ Tetrabutylammonium chloride $(n\text{-}Bu)_4N^+Cl^-$; (Sigma Aldrich)
- ✔ Tetrabutylammonium bromide $(n\text{-}Bu)_4N^+Br^-$; (Sigma Aldrich)
- ✔ Tetrabutylammonium iodide $(n\text{-}Bu)_4N^+I^-$; (Sigma Aldrich)
- ✔ Tetrabutylammonium cyanide $(n\text{-}Bu)_4N^+CN^-$; (Sigma Aldrich)
- ✔ Tetrabutylammonium thiocyanate $(n\text{-}Bu)_4N^+SCN^-$; (Sigma Aldrich)
- ✔ Tetrabutylammonium fluoride $(n\text{-}Bu)_4N^+F^-$; (Sigma Aldrich)
- ✔ Tetrabutylammonium sulfate $((n\text{-}Bu)_4N)_2{}^+SO_4{}^{2-}$; (Sigma Aldrich)
- ✔ Tetrabutylammonium hydrogen sulfate $(n\text{-}Bu)_4N^+HSO_4{}^-$; (Sigma Aldrich)
- ✔ Tetrabutylammonium acetate $(n\text{-}Bu)_4N^+CH_3COO^-$; (Sigma Aldrich)
- ✔ Tetrabutylammonium nitrate $(n\text{-}Bu)_4N^+NO_3{}^-$; (Sigma Aldrich)
- ✔ Tetrabutylammonium dihydrogenphosphate $(n\text{-}Bu)_4N^+H_2PO_4{}^-$; (Sigma Aldrich)
- ✔ Tetrabutylammonium pyrophosphate $((n\text{-}Bu)_4N)_4{}^+P_2O_7{}^{4-}$; (Sigma Aldrich)

2.1.4. Solvents

- ✔ 1,4-dioxane (HPLC grade, Spectrochem India)
- ✔ 2-propanol (HPLC grade, Spectrochem India)
- ✔ Acetonitrile (HPLC grade, Spectrochem India)
- ✔ Cyclohexane (HPLC grade, Spectrochem India)
- ✔ Chloroform (HPLC grade, Spectrochem India)
- ✔ Dimethylformamide (HPLC grade, Spectrochem India)

- ✔ Dimethylsulfoxide (HPLC grade, Spectrochem India)
- ✔ Diethyl ether (HPLC grade, Spectrochem India)
- ✔ Ethanol (HPLC grade, Spectrochem India)
- ✔ Ethyl acetate (HPLC grade, Spectrochem India)
- ✔ Glycerol (AR grade, Rankem India)
- ✔ Methanol (HPLC grade, Spectrochem India)
- ✔ Tetrahydrofuran (HPLC grade, Spectrochem India)
- ✔ Toluene (HPLC grade, Spectrochem India)
- ✔ Water (Millipore)
- ✔ Deuterated chloroform (99.8 atom % D, contains 0.03 % (v/v) TMS) (Sigma Aldrich)
- ✔ Deuterated Dimethylsulfoxide (99.9 atom % D) (Sigma Aldrich)
- ✔ Deuterated Acetonitrile (≥ 99.8 atom % D) (Sigma Aldrich)
- ✔ Deuterated Methanol (99.8 atom % D) (Sigma Aldrich)

As the solvents were clear and transparent in the spectral area, they were used exactly as received.

2.2. Experimental study

2.2.1. General procedure for synthesis

Clean, dry vessels were used for the all of the reactions. Reactions were monitor using thin-layer chromatography (TLC), which was performed on silica plates coated with silica gel GF-254. Chloroform –methanol or ethyl acetate-hexane mixtures were used as mobile phase for carrying out the TLC depending upon the polarity of the probe. TLCs were seen with UV light (254 or 365 nm) or I_2 staining. Purifications were carried out by column chromatography using SiO_2 (60-120 mesh). When all of the reactants were consumed, the reaction was stopped and the desired products were extracted using aqueous-organic solvent or filtered out.

2.2.2. Characterization of the probes

^1H and ^{13}C NMR spectra were recorded on JEOL ECS-400MHz spectrometer (^1H NMR at 400 MHz or 500 MHz, ^{13}C NMR at 100 MHz or 126 MHz). Chemical Shifts were expressed in parts per million with TMS as internal reference and residual peaks for deuterated solvents are ($CDCl_3$

at 7.26 ppm, and DMSO-d_6 at 3.33 ppm or 2.50 ppm). Following abbreviations are used to represent the NMR data (s, singlet; d, doublet; t, triplet; q, quartet; dd, doublet of doublets; m, multiplet). Electrospray ionization high resolution mass spectrometry was performed on XEVO G2-XS QTOF spectrometer of Waters.

2.2.3. Preparation of stock solutions

The stock solutions of compounds were prepared in CH_3CN/DMSO at 10^{-3} M concentration. Additionally, a dilution approach was used to generate the needed concentration solution in various solvent media. The stock solutions were of 10^{-1} M concentration. With the appropriate solvent, the stock solutions were further diluted to necessary concentration.

2.2.4. Absorption and emission studies

The diluted solutions with strength of μM were used to measure photophysical properties in variety of solvents. The spectra were recorded in quartz cuvettes with path length of 1 cm and temperature of 25.0 ± 0.1 °C. The absorption spectra were taken on a SHIMADZU-2600 spectrophotometer with a 1.0 nm slit width, while the emission spectra were taken on Varian Carey Eclipse fluorescence spectrophotometer at the specified excitations. All absorption and emission spectra were stored as ASCII files and analyzed using Microsoft Excel. The time-resolved studies were performed on DeltaFlex Modular Fluorescence Life-time Spectrofluorimeter (HORIBA Scientific). The quantum yield was calculated *via* absolute method on HORIBA fluorolog 3 spectrophotometer in solution form by using quantum yield analyzer. For some of the probes the quantum yield was calculated *via* relative method by using the following equation:

$$Q.Y_S = Q.Y_R\,(I_S/I_R)\;[(1-10^{-AR})/(1-10^{-AS})]\;(n_S/n_R)^2$$

Where the subscripts S and R denote the sample and reference, respectively. $Q.Y_R$ is the known quantum yield of the reference standard (quinine sulphate), I is the integral fluorescence spectrum intensity, A is the absorbance of the solution at the excitation wavelength, and n is the refractive index of the solvents.

2.2.5. DLS sample preparation

Stock solution of all the probes were prepared and filtered with the help of 0.02 µM filter to eliminate suspended particles. Additionally, solutions with strength of 20 µM were made for DLS analysis. The solutions were then processed with the detected analytes at 25 °C and the size of the particles was measured. The DLS was performed on Zeta potential analyzer (ZEN 3600) instrument.

2.2.6. FESEM measurement

The effect of aggregation was explored by measuring change in particle size and surface morphology using FESEM imaging. FESEM imaging was used to investigate metal induced aggregation. The compound solution was placed on a copper grid or cover slip by drop cast method and allowed to dry for 24 hours. The dried samples were subsequently plated with gold spray and FESEM analysis was performed. The samples were analyzed at Central University of Punjab, Bathinda and Thapar Institute of Engineering and Technology, Patiala. FESEM was performed on a ZEISS MERLIN Compact field emission-scanning electron microscope.

2.2.7. Calculation of binding constants and detection limits

The binding constants were calculated using Benesi-Hildebrand method using equation (1) where I_0, is the absorption or emission intensity of the compound in the absence of the analyte, I, is the absorption or emission intensity of the compound in the presence of the analyte and I_{max} is the absorption or emission intensity of the compound on achieving plateau on titration with the analyte (completion of titration)

$$\frac{1}{I-I_0} = \frac{1}{K_a(I_{max}-I_0)[C]^n} + \frac{1}{I_{max}-I_0} \quad \text{..... (1)}$$

The Limit of detection (LOD) is determined from the following equation (2):

$$DL = \frac{3\times Standard\ deviation\ of\ the\ blank\ solution}{slope\ of\ calibration\ curve} \quad \text{.....(2)}$$

2.2.8. Job's plot analysis

In order to ascertain the stoichiometries of complexes, a series of solutions containing probes and analytes with varying mole fractions (X) of analytes ranging from 0.1 to 1.0 were prepared. The

absorption and emission spectra were recorded. Further, according to Job's plot method, a plot of the intensity against the molar fraction of the analytes solution was examined. The complexation ratios of the analytes and probes were calculated using Job's plot.

2.2.9. NMR titration procedure

The ^{1}H NMR titrations of Probes against detected ions was carried out at 5mM concentration using JEOL ECS-400MHz spectrophotometer. The corresponding medium of detection was used to quantify the ^{1}H NMR titration of probes with their detected analytes. NMR spectra were measured with and without analytes and the measurements were repeated 24 hours later. All the recorded data was then processed in Mestronova software to draw the stacking data of probes.

2.2.10. Methodology for pH titrations

The pH was set and adjusted using an Equiptronics pH meter between 2 and 13, after which the spectra were recorded. We looked into how pH changes affected the UV-Vis and fluorescence spectra of the probes and their complexes with the ions. pH titrations were carried out, where 20 µM solutions of the probes and their complexes were prepared in various solvents, to evaluate the impact of altering pH on the probes and their complexes. In order to record the absorption and emission spectra, 3 mL of each solution was poured out using a 1000 mL pipette. The starting pH of each solution was then recorded on a pH meter. With the use of a capillary, 0.1 M NaOH solution was added in order to conduct the studies in basic medium. The mixture was mixed to preserve the homogeneity after each addition and left alone for two to three minutes. After that, along with the pH of the solutions, the UV-Vis and emission spectra were once again recorded.

Similar to this, experiments at an acidic pH were conducted by adding 0.1 M HCl with a capillary into 20 µM solutions of the probes/complexes that were prepared in the appropriate solutions in order to achieve selectivity. After each addition, the solutions were mixed and kept undisturbed for two to three minutes and after a pH adjustment of 0.2-0.3, the UV-Vis and fluorescence spectra of the solutions were recorded by placing a 3 mL of the solutions into cuvettes.

The data for absorption and emission were converted and saved n Microsoft Excel. To determine the effect of changing pH on probes/complexes, a plot between changing pH and intensity changes of absorption maximum and emission maximum at specified wavelengths was investigated.

2.2.11. Detection of analytes in real time samples

The probe's applicability for sensing analytes in real samples was tested by collecting sample water and spiking the sample with different concentrations of analytes, and then recording the AAS (Atomic Absorption Spectroscopy) of the samples. These samples were then introduced to the probe of a specific concentration, and the real concentration was determined using UV-Vis and fluorescence studies. The UV-Vis spectra of the spiked sample were then compared to the AAS (Atomic Absorption Spectroscopy) spectra as well as the probe spectra obtained by adding the same concentration of standard analyte. The concentration of the spiked samples was estimated by comparing the absorption and emission intensity graph at same wavelengths.

2.2.12. Cell viability assay

The cytotoxicity of probe and NaOCl was checked using MTT assay where A549 Lung cancer cell line (ATCC No. CCL-185) was cultured in Ham's F-12 media and supplemented with 10% Fetal Bovine Serum (FBS), antibiotics, and anti-fungal. These cells were maintained at 37 ℃ with 5 % CO_2 and humidified conditions in T25 cell culture flasks. Later these cells were seeded in a 96 well plate at a cell density of 3 x 10^4 cells/well and incubated with different concentrations of probe (1, 5, 10, 25, 50 μM) and NaOCl (1, 10, 25, 50, 100 μM) alone or in combination for 24 h. For combination, various concentrations of probe (10, 25, and 50 μM) were incubated in combination with sodium hypochlorite (5, 10, 25, 50 μM). After incubation, 10 μl of MTT solution was added to each well at a concentration of 0.2 mg/ml and incubated for another 3 h. The purple-colored formazan crystals formed were then dissolved in DMSO, and the absorbance was measured using an ELISA plate reader (PowerWave XS2, BioTek) at 570 nm. All the data were taken from the mean of 3 independent experiments, and % cell viability was calculated using the equation (3).

$$\%\ Cell\ viability = \frac{OD\ of\ treated\ cells}{OD\ of\ untreated\ cells}\ X\ 100\ \% \qquad \text{.....(3)}$$

2.2.13. *In-vitro* bio-imaging

The *in-vitro* bio-imaging for sensing of hypochlorite was done using the A549 cell line. To start with, A549 cells were seeded on sterile glass coverslips on 35 mm cell culture dishes at a cell density of 5 x 10^5 cells/ ml and incubated overnight in Ham's F12 media. NaOCl was used as extrinsic hypochlorite (ClO^-) source, and different concentrations of hypochlorite (1.0, 2.5, 5.0, 7.5, 10.0 μM) were treated with probe (30 μM). The experiment was performed in triplets and the incubation was done for 3 h at 37 ℃. The cells were later washed with 1X PBS buffer and fixed in 2 % formaldehyde solution. The change in fluorescence was checked under the microscope using violet and green excitation light at 20X magnification. Images were captured using a Dwinter Inverted Fluorescence Microscope, Italy. The pixel intensity of green and red fluorescence obtained was calculated using Image J software, and further processing was done using Microsoft Excel. Repeated measures ANOVA followed by Tukey's HSD posthoc test were performed to where 10 X 10-pixel area of the image was measured and used the pixel intensity values for the repeated measures to check the change in fluorescence pattern. Two measurements were considered statistically significant if the corresponding p-value was <0.01.

2.3. Theoretical calculations

Geometrical optimization and prediction of all photophysical properties were performed in order to provide conclusive remarks on the experimental results for the probes. The theoretical results at the S_0 state were estimated using density functional theory (DFT) and different functional levels of basis set such as B3LYP/cam-B3LYP and 6-31+g(d,p) level. The absence of imaginary frequency was used to validate all of the optimized structures. TDDFT methods were used to extend the calculations to excited state (S_n) geometry optimizations.

2.3.1. Solvent effect

To include the solvent effect in our results, we used to integrate equation of formalism polarized continuum model (IEFPCM) for all tautomeric forms and transition states in the S_0 and S_n states.

2.3.2. Electronic spectra

Furthermore, three Franck-Condon vertical excitations on the S_0 geometry were predicted using time dependent DFT (TDDFT). The excitation with the highest oscillation strength was studied for frontier molecular orbitals. The nature of electronic excitation was quantified using the hole-electron idea.

2.3.3. Establishment of intramolecular proton transfer or charge transfer

We were curious about the nature of excited state intramolecular proton transfer. As a result, the preconditions of intramolecular hydrogen bonding were explored using geometrical factors and FTIR in S_0 and S_n states.

2.3.4. Tautomeric preference

To predict the tautomeric conversion in S_0 and S_1 states, the free energy change ($\Delta G = G(S)-G(K)$; where S and K are the typical enol and keto tautomers) was used. The higher the ΔG value, the more stable the conventional enol form was and tautomeric conversion via PT was not permitted. The negative ΔG value, on the other hand, denoted the stabilization of keto tautomeric state and so implies tautomeric conversion via PT mechanism, implying an increase in emission.

The theoretical study involved the following steps:

1. Structural optimization and geometrical analysis at S_0 and S_n states.
2. Electronic spectra and charge distribution to the determined contributing excited state.
3. Structural optimization and geometrical analysis at S_n states.
4. FTIR spectra for the establishment of IraHB.
5. Energy profile of PT pathways.

2.3.5. Software used

- ✔ Gaussian 03, 09 and 16 version: For Quantum Chemical calculations
- ✔ Gauss view and Chemcraft: To visualization of the results
- ✔ MS Excel and Origin 8: For plotting the results

Chapter 3

Investigation of excited state intramolecular proton transfer process and charge transfer process in hydroxy aryl benzimidazole based Schiff bases

1. Introduction

The ESIPT based fluorophores has been extensively studied due to their strong fluorescence, high quantum yield and large Stokes shift. Further with the introduction of another proton transfer site to the single ESIPT moieties the fluorescence, quantum yield and Stokes shift can be enhanced. The hydroxy benzimidazole is well known for ESIPT phenoemnon.[118-123] The benzimidazole-based Schiff bases were employed as possible candidates for chemosensing properties.[101, 124-126] This chapter covered the synthesis and photophysical studies of benzimidazole based Schiff bases **1-4**. The Schiff bases of benzimidazole based systems displayed significant Stokes shift. Herein, the designed benzimidazole based Schiff base have two ESIPT sites, one on hydroxyl aryl Schiff base and other on hydroxyl aryl benzimidazole site. The main objective of this chapter was to discuss the effect of different substituent on the ESIPT properties of the probes and its sensing behavior towards different ions. The dual ESIPT pathways and sensing behavior of probes has been explored through experimental and theoretical studies. As a result, the photophysical properties of benzimidazole-based Schiff bases **1, 3,** and **4** were examined using experimental and theoretical studies. All the probes have proton donor groups (−OH) and proton acceptor groups (–C=O, –N= ,etc.,) present in close proximity to each other. Probes **(1, 3,** and **4)** contain unsymmetrical double proton transfer sites, one with imine bond (-C=N-) and a hydroxyl group (-OH) and the other with benzimidazole (=N) and hydroxyl group. The substituent effect surrounding the ring is employed to examine the photophysical properties of the molecules. Probe **2** with only one ESIPT sight is synthesized to check the sensing mechanism of probe **1** and to evaluate its effect on ESIPT phenomenon. This chapter has been divided into three sections based on a systematic study of effect of electron donating group and conjugation on the ESIPT phenomenon and results from experimental and theoretical studies.

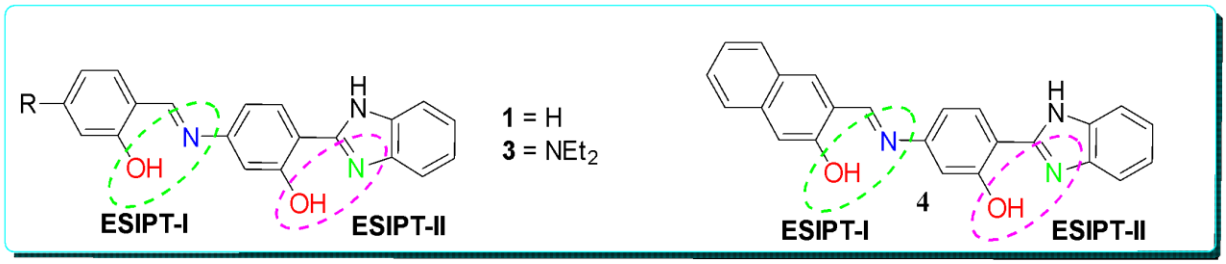

Figure 3.1: The different derivative of benzimidazole based Schiff base.

Here, we addressed a systematic analysis of ESIPT, the effect of various substituents and their photophysical behavior towards common metal ions and anions. It has been expected that substituents will modify the selectivity and sensitivity towards metal ions and anions. This chapter has been divided into three sections based on the type of the substituents and their sensing behavior.

3.1. Investigation of excited state intramolecular proton transfer process for hydroxy aryl benzimidazole based Schiff base**.**

3.2. Effect of electron donating group (–NEt_2) on excited state intramolecular proton transfer process of hydroxy aryl benzimidazole based Schiff base**.**

3.3. Effect of conjugation on excited state intramolecular proton transfer process in hydroxy aryl benzimidazole based Schiff base.

3.1.

Investigation of excited state intramolecular proton transfer process for hydroxy aryl benzimidazole based Schiff base

3.1.1. Abstract

In this section, dual ESIPT efficient benzimidazole based Schiff-base probe **1** possessing multiple binding sites, undergoing ESIPT and AIE phenomenon was studied through theoretical and experimental methods. Probe **1** showed an absorption peak at 340 nm and an emission peak at 450 nm with a large Stokes shift of 110 nm, which originated from the ESIPT phenomenon. The presence of dual intramolecular hydrogen bonding was confirmed theoretically by geometrical parameters and FTIR analysis. We confirmed the concomitant existence of the probe in two geometrical forms at the S_0 state. An energy barrier of 1 kcal mol^{-1} was calculated for probe **1**-I→probe **1**-II conversion, which was lower than thermal energy indicating that both configurations can coexist and were interconvertible at the S_0 state. All the calculations were carried out using density functional theory (DFT) at B3LYP/6-31+g(d,p) level. To complement the experimental setup, the solvation effect of acetonitrile was taken into account using the IEFPCM model. The geometrical parameter and FTIR analysis at the ground and excited state show a significant charge transfer at the proton acceptor site and therefore, facilitate the ESIPT process. The PECs also established the small barrier of ~1 $kcalmol^{-1}$ for forwarding proton transfer at the S_1 state. The dynamical nature of intramolecular H-bonding at S_1 state facile the single or/and double proton transfer and thus, contribute to the establishment of four tautomeric forms. The ESIPT process was explored through concerted proton transfer (PT I) and sequential proton transfer (PT II) mechanism. Further, probe **1** behaves as a fluorescence "turn-on" chemosensor, showing interactions with Pb^{2+} and Al^{3+} ions in H_2O-CH_3CN solvent at pH≈7. The binding constant and detection limit for all the ions was calculated. The binding properties of probe **1** with all the ions were checked by Job's plot and the ^1H NMR titration method. Thus, high selectivity and sensitivity and fast response time was achieved for simultaneous detection of Pb^{2+} and Al^{3+} ions using a simple single platform.

3.1.2. Experimental section

3.1.2.1. Synthesis of compound 1a

The mixture of 4-aminosalicylic acid (600 mg, 4 mmol) and *o*-phenylenediamine (430 mg, 4 mmol) in PPA was refluxed in 50 ml round bottom flask for 18 h **(Scheme 3.1)**. The reaction was monitored by TLC. After completion of the reaction aqueous ammonia solution was added to get purple coloured solid and was filtered and washed with water to get compound **1a** in 85% yield. m. p. 207-210 °C. ^{1}H NMR (DMSO-d_6, 400MHz): δ (ppm) 7.70 (d, 1H, *J* = 8.0 Hz, ArH), 7.57-7.55 (q, 2H, *J* = 8.0 Hz, ArH), 7.23-7.21 (q, 2H, *J* = 8.0 Hz, ArH), 6.26-6.23 (m, 1H, ArH) 6.18 (d, 1H, *J* = 2.0 Hz, ArH). ^{13}C NMR (DMSO-d_6, 100 MHz): δ (ppm) 159.9, 153.1, 152.8, 127.7, 127.6, 122.8, 122.5, 106.9, 106.6, 100.7, 100.3.

3.1.2.2. Synthesis of probe 1

The compound **1a** and salicylaldehyde were refluxed in ethanol for 12 h **(Scheme 3.1)**. On completion of reaction, the mixture was cooled and the obtained solid was filtered and washed with ethanol to get yellow colored solid of probe **1** in 60% yields. m.p. 265-267 °C; ^{1}H NMR (DMSO-d_6, 400 MHz): δ (ppm) 9.04 (s, 1H, ArH), 8.13 (d, 1H, *J* = 9.2 Hz, ArH), 7.73 (m, 3H, ArH), 7.46 (m, 1H, ArH), 7.28 (s, 2H, ArH), 7.11 (d, 2H, *J* = 4.8 Hz), 7.03 (m, 2H, ArH) **(Figure A1)**. ^{13}C NMR (DMSO-d_6, 100 MHz): δ (ppm) 192.3, 160.9, 159.9, 153.3, 152.8, 136.8, 133.9, 133.1, 129.7, 127.4, 122.3, 119.9, 119.4, 117.5, 116.9, 113.6, 109.5, 106.6, 101.1, 100.3 **(Figure A2)**. HRMS (ESI-TOF): (m/z) $[M+H]^+$ calcd for $C_{20}H_{16}N_3O_2$: 330.1258, found: 330.1278 **(Figure A3)**.

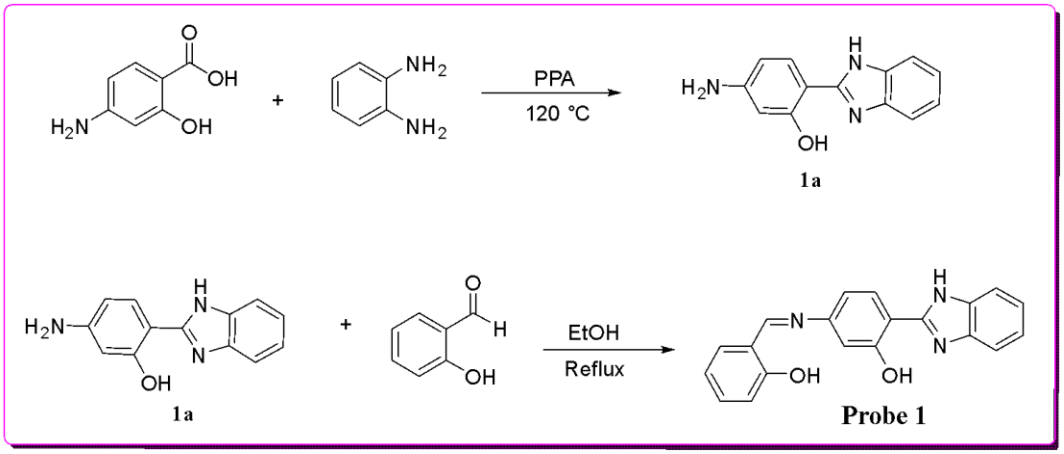

Scheme 3.1: Synthesis of probe 1.

3.1.2.2. Synthesis of probe 2

The compound **1a** and benzaldehyde were stirred at 70 °C in ethanol for 12 h **(Scheme 3.2)**. On completion the reaction mixture was cooled and solid was filtered and washed with ethanol to get yellow colored solid of probe **2** in 75% yields. m.p. 257-262 °C. ^{1}H NMR (DMSO-d_6- 400 MHz,) δ 8.98 (s, 1H, C=N), 8.23 (d, 1H, *J* = 8 Hz, ArH), 8.12 (d, 1H, *J* = 8 Hz, ArH), 8.03 (d, 1H, *J* = 8 Hz, ArH), 7.68 (d, 1H, *J* = 4 Hz, ArH), 7.51-7.39 (m, 3H, ArH), 7.06-6.94 (m, 5H, ArH) **(Figure A5)**. ^{13}C NMR (100 MHz, DMSO-d_6) δ 168.1, 167.2, 161.3, 155.3, 142.7, 142.5, 139.3, 135.6, 133.8, 132.5, 128.6, 128.3, 126.3, 126.1, 125.6, 123.5, 123.0, 120.1 **(Figure A6)**. HRMS (ESI-TOF): (m/z) [M+H+18] $^{+}$ calcd for $C_{20}H_{15}N_3O$: 330.1258, found: 330.1254 **(Figure A7).**

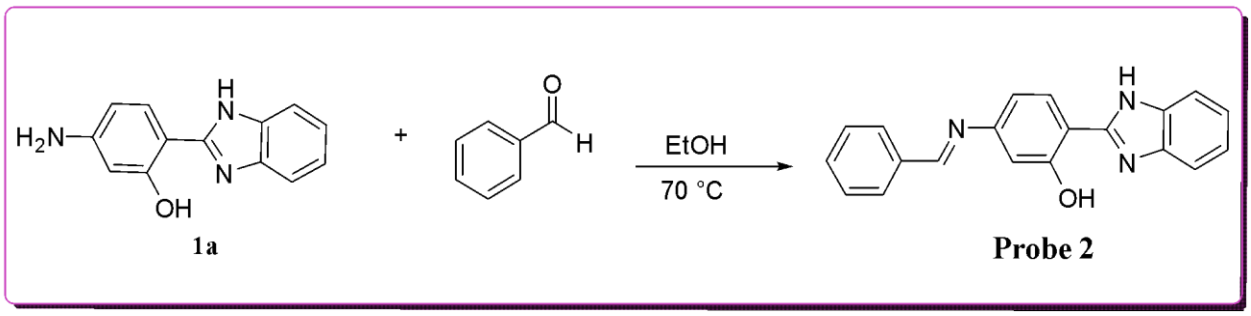

Scheme 3.2: Synthesis of probe 2.

3.1.3. Results and discussion

3.1.3.1. Photophysical behavior of Probe 1

Probe **1** (20 μM, CH_3CN) shows two absorption peaks at 340 nm and 330 nm. On photoexcitation at 340 nm, probe **1** exhibited an emission band at 450 nm accomplished by Stokes shift of 110 nm. The probe **1** showed large Stokes shifted (>100 nm) emission characteristics of the excited state intramolecular proton transfer (ESIPT) process in probe **1**. Further, the absorption spectra of probe **1** shows feeble dependency on the solvent environment and showed the absorption peaks at 340 nm and 330 nm only **(Figure 3.2a)**. Upon photoexcitation, dual emissions with low and high Stokes shifts are observed, depending upon the environment. In low polarity environments such as cyclohexane, chloroform, acetonitrile, dioxane, tetrahydrofuran, and ethyl acetate, only high Stokes shifted emission was observed at 450 nm. However, in polar environments, emission moves towards the low Stokes shift at 390 nm **(Figure 3.2b)**. It is noteworthy that the intensity ratio of low and high Stokes shifted

emission increases with the polarity of the environment. This signifies that the low Stokes shift emission at 390 nm in high polarity environment is from the enol form, while the high Stokes shift emission, which shows a negative solvatochromism effect, is ascribed due to tautomeric keto form emission.

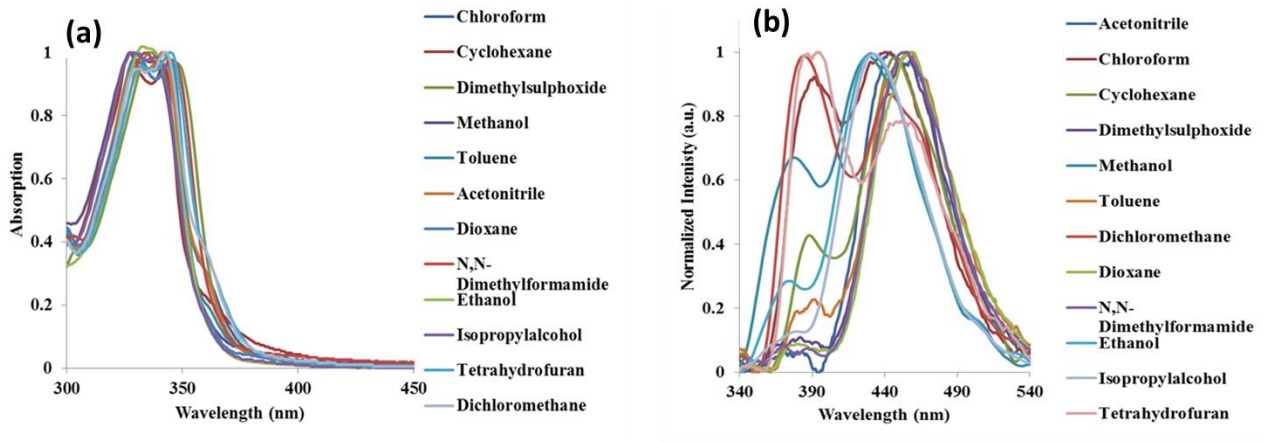

Figure 3.2: (a) Normalized absorption spectra and (b) emission spectra of probe 1 in different polarity solvents.

Probe **1** has two proton donor and acceptors sites in the form of O—H···N labeled as I and II. Therefore, proton transfer could be taken place from the phenolic unit [OH (I) and OH (II)] to nitrogen [N (I)] of the Schiff base unit and benzimidazole unit [NH (II)], respectively. The medium affects the intramolecular hydrogen bonding and thus the emission behavior of probe **1**. The proton transfer could raise different tautomeric forms at the S_1 state. To confirm the number of tautomeric forms, lifetimes were measured at the 450 nm emission peak **(Figure 3.3)**. Probe **1** showed three lifetimes of 0.57 ns (51 %), 1.83 ns (12 %) and 17.29 ns (36 %). The average lifetime for probe **1** comes out to be 1.02 ns. The emission lifetime results indicated the existence of three tautomeric forms in an excited state.

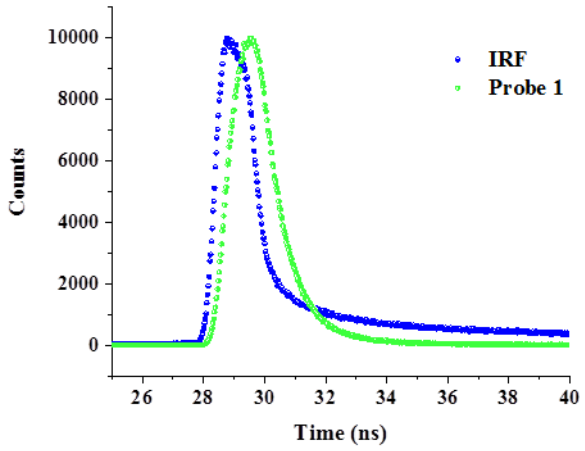

Figure 3.3: Time resolved fluorescence decay of probe 1.

3.1.3.2. Ground state structure calculation

Probe **1** has torsional flexibility to single bonds such as C–C rotation at benzimidazole unit connection and C–N rotation at imine center connection. These torsional rotations result in different conformations (**Figure 3.4**). These plausible configurations were optimized at the S_0 state and calculation suggests that Probe **1**-I and Probe **1**-II conformer are relatively stable due the formation of strong intramolecular hydrogen bonding and have a considerable population of 55 % and 45 %, respectively. These outcome shows that the probe could exist in two forms (probe **1**-I and probe **1**-II) at S_0 state.

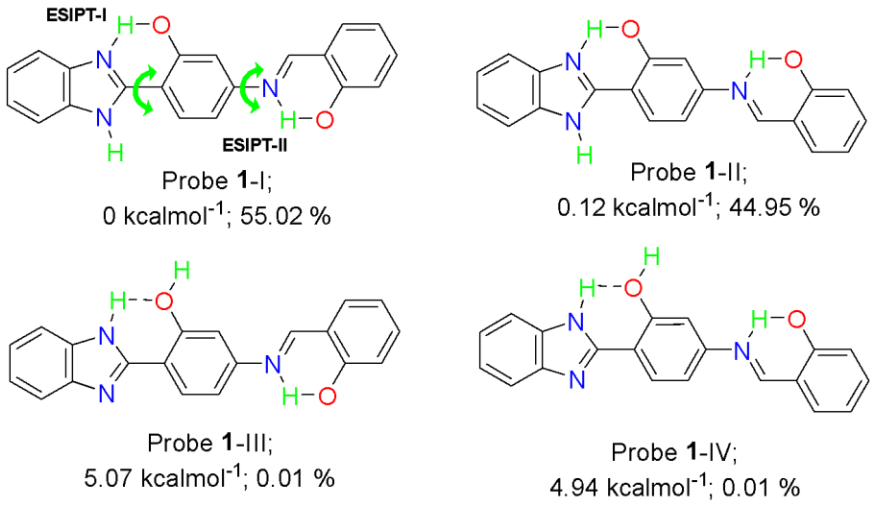

Figure 3.4: Possible tautomeric forms of probe 1 along with relative energies and population.

Both of these configurations of probe **1** have slightly twisted geometry at the S_0 state with no imaginary frequency. To check the mutual transformation of Probe **1**-I and Probe **1**-II configuration at S_0 state in acetonitrile, we constructed the potential energy curves (PECs) starting from Probe **1**-I form as a function of torsional rotation at C(Ph) –N(imine) center. An energy barrier of 1.72 kcalmol^{-1} is calculated for probe **1**-I → probe **1**-II conversion, which is lower than thermal energy and thus, shows that both configurations can coexist and are interconvertible at the S_0 state.

3.1.3.3. Electronic spectra and charge distribution

To explore the photoexcitation process, three low-lying excitations of Probe **1**-I and Probe **1**-II are calculated corresponding to S_0 geometry. The calculated excitations are tabulated in Table **3.**. For probe **1**-I, the TDDFT calculation demonstrates 82 % orbital transition contribution from the highest occupied molecular orbital (HOMO) to lowest unoccupied molecular orbital (LUMO) with oscillation strength of 1.4300 at 340 nm for $S_0 \rightarrow S_1$ excitation, which agrees with the experimental absorption peak at 340 nm. On the other hand, for probe **1**-II, $S_0 \rightarrow S_1$ excitation is calculated at 325 nm with oscillation strength of 1.3918 and orbital contribution of 80% from HOMO to LUMO transition, which agrees with the experimental absorption peak at 330 nm. The calculated $S_0 \rightarrow S_2$ and $S_0 \rightarrow S_3$ excitation have low oscillations strength for both configurations and thus, we consider only $S_0 \rightarrow S_1$ excitation for further analysis for both the conformer **(Table 3.1)**.

Table 3.1: Summary of excitation spectra of probe 1-I and probe 1-II

Probe 1-I				**Probe 1-II**			
Excitation	□ (nm)	f	MO	Excitation	□ (nm)	f	MO
$S_0 \rightarrow S_1$	340.58	1.4300	H→L (82 %)	$S_0 \rightarrow S_1$	325.76	1.3918	H→L (80 %)
$S_0 \rightarrow S_2$	298.36	0.0477	H-1→L (72 %)	$S_0 \rightarrow S_2$	291.49	0.0256	H-1→L (70 %)
$S_0 \rightarrow S_3$	279.70	0.0791	H-3→L (59 %)	$S_0 \rightarrow S_3$	277.22	0.0807	H-3→L (54 %)
□= calculated excitation wavelength (nm); MO = molecular orbitals contributing to excitations; H = HOMO; L = LUMO, f = oscillator strength							

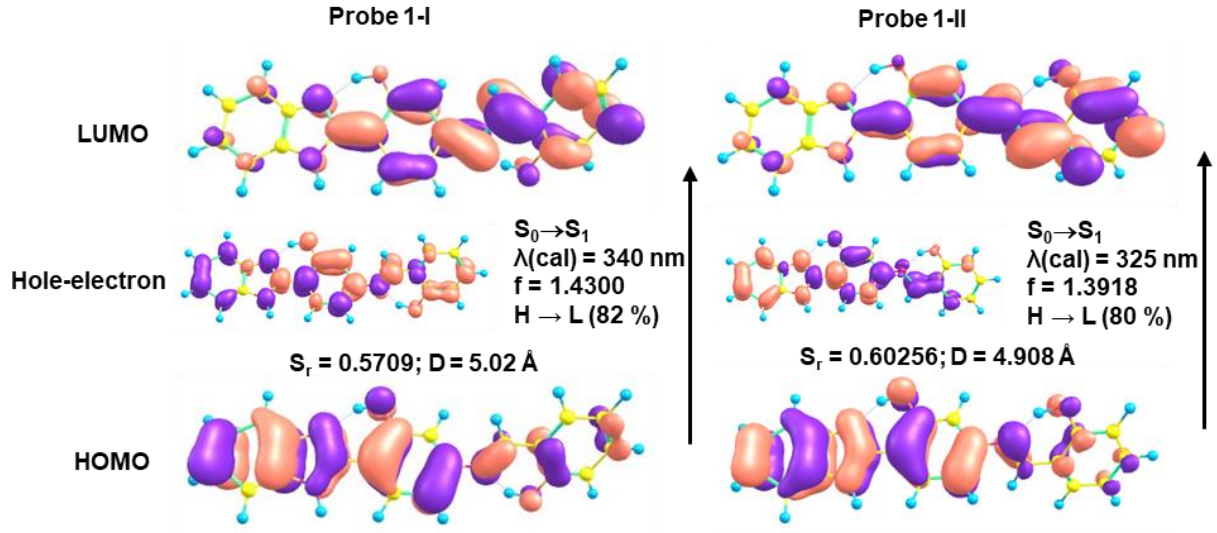

Figure 3.5: Frontier molecular orbitals and hole/electron distribution for $S_0 \rightarrow S_1$ excitation.

It is well known that upon photoexcitation, electronic distribution over the molecule could be significantly altered, that plays vital roles in excited state dynamical behaviors. Therefore, the alteration in electronic distribution is evaluated qualitatively and quantitatively. The involved molecular orbitals displayed a shift in the electron density from the benzimidazole unit (in HOMO) to the Schiff base unit (in LUMO) for both configurations probe **1**-I and probe **1**-II **(Figure 3.5)**. The subsequent hole-electron analysis shows a low overlap integral (S_r = 0.5709

for probe **1**-I and S_r = 0.6026 for probe **1**-II) of hole/electron distribution and a large distance of electron/hole centroid (D = 5.02 Å for probe **1**-I and 4.908 Å for probe **1**-II) and thus, establish an intramolecular charge transfer process in probe **1** for both configurations.

3.1.3.4. Intramolecular hydrogen bonding

In order to reveal the prerequisite condition of strengthening of intramolecular hydrogen bonding for the ESIPT process, we compared the structural variation and FTIR spectra at S_0 and S_1 states. For better understanding, geometrical parameters involved in the ESIPT process are labeled with involved atoms **(Figure 3.6)**. Probe **1** contained two kinds of asymmetrical intramolecular hydrogen bonding (IraHB) in the form of $O_1H_2\cdots N_3$ and $O_4H_5\cdots N_6$ with a short interaction distance (less than the sum of Vander Waal radii of hydrogen and nitrogen) and angles. For probe **1**-I, on photoexcitation to S_1 state, the intramolecular distances for $O_1H_2\cdots N_3$ decreased by 0.098 Å to 1.607 Å, while the bond angle increased by 3.2^o to 150.85^o. On the other hand, the $O_4H_5\cdots N_6$ distance decreased by 0.008 Å to 1.674 Å, while the bond angle increased by 0.57^o to 148.72^o. A similar trend is observed for probe **1**-II conformer too. Further, we investigate the FTIR signals of O_1H_2 and O_4H_5 of Probe **1**-I and probe **1**-II at S_0 and S_1 states. The comparative FTIR view specifies that $O_1H_2\cdots N_3$ IraHB shows the redshift of 444 cm^{-1} to 2717 cm^{-1} for both probe **1**-I and probe **1**-II conformer; while $O_4H_5\cdots N_6$ IraHB shows a redshift of 18 cm^{-1} to 3114 cm^{-1} for probe **1**-I and 3 cm^{-1} to 3143 cm^{-1} for probe **1**-II confomer. The FTIR spectral changes endorsed the variation in the geometrical parameter of intramolecular hydrogen bonding. Also, it is noted that significant molecular planarity is achieved with a decrease in the dihedral angle of the Schiff base unit for both the conformers at the S_1 state.

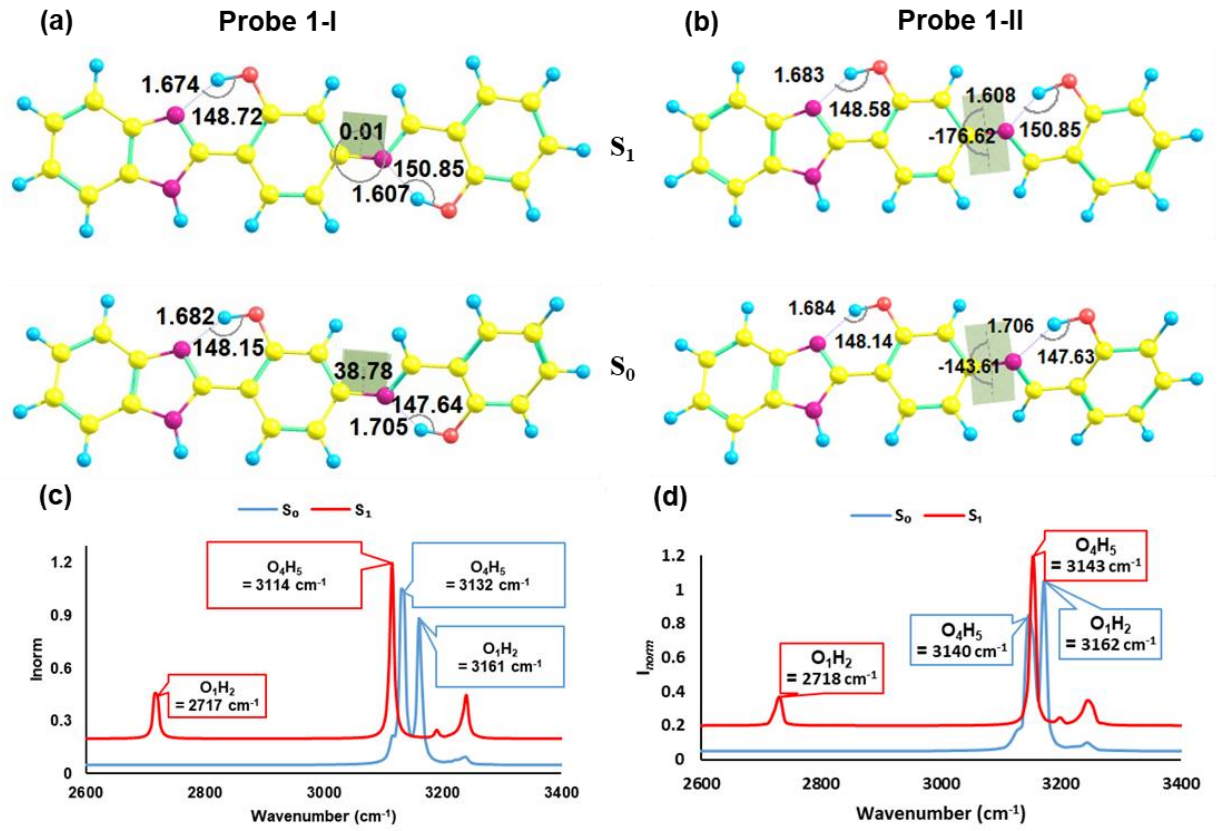

Figure 3.6: (a) and (b) Optimized structure of probe 1-I and probe 1-II; (c) and (d) FTIR spectra of probe 1-I and probe 1-II, respectively at S_0 and S_1.

Furthermore, it is noted that the atomic contribution of O_1 and H_2 decreases (1.97 % → 1.57 % for O_1 and 0.12 % → 0.05 % for H_2 **(Table 3.)**, while N_3 increases from 4.58 % to 11.50 % for probe **1**-I on HOMO→LUMO transition. On the other hand, a significant decrease is noted for the atomic contribution of O_4, H_5, and N_6 of probe **1**-I on the HOMO→LUMO transition (Table 3.). A similar trend is observed for probe **1**-II configuration. The increased electron density at N_3 signifies the strengthening of $O_1H_2\cdots N_3$ IraHB, while, a decreased atomic contribution indicates the weakened of $O_4H_5\cdots N_6$ IraHB at the S_1 state. Therefore, based on variation in geometrical parameters, FTIR spectra, and atomic contribution of HOMO/LUMO, we have reason to believe that the $O_1H_2\cdots N_3$ IraHB is strengthened significantly, while the $O_4H_5\cdots N_6$ IraHB is affected insignificantly. Thus, these results signify that the strengthened $O_1H_2\cdots N_3$ IraHB will prompt the ESIPT process.

Table 3.2: Atomic contribution of HOMO and LUMO at ESIPT sites for probe 1-I (probe 1-II).

Atom	HOMO	LUMO	Atom	HOMO	LUMO
O_1	1.97 % (1.42 %)	1.57 % (1.34 %)	O_4	6.14 % (4.37 %)	0.33 % (0.34 %)
H_2	0.11897 % (0.14364 %)	0.05317 % (0.07105 %)	H_5	0.00028 % (0.03584 %)	0.00518 % (0.00284 %)
N_3	4.58 % (3.92 %)	11.50 % (10.92 %)	N_6	6.64 % (6.17 %)	1.76 % (1.70 %)
Values in parenthesis are of probe **1-II** configuration					

3.1.3.5. Proton transfer mechanism

The short interaction distances and FTIR analysis established double IraHB for probe **1** and the comparison of FTIR spectra at S_0 and S_1 state established the alteration in IraHB strength. Further, the dynamical nature of IraHB at S_1 state facile the single or/and double proton transfer and thus, contribute to the establishment of four tautomeric forms. Therefore, there could be two pathways for intramolecular proton transfer **(Scheme 2)**. The path I involved the proton transfer from the O_1—H_2 to N_3 resulting in the tautomeric conversion of Probe **1** → SPT1 followed by proton transfer from O_4—H_5 to N_6 for the tautomeric conversion of SPT1 → DPT. **Figure 3.7** represents the two-dimensional proton transfer of probe **1** at S_0 and S_1 state and suggests only one minimum at both states. The PECs suggest that the enol form of probe **1** is only stable conformer at S_0 state, while SPT1 conformer stabilized at S_1 state. The SPT2 and DPT conformer has high relative high energies at S_1 state and thus, neglect ESIPT pathways through Probe **1**□SPT2□DPT. The calculated energy barrier for forwarding ESIPT is 1.17 kcalmol^{-1}, while for reverse proton transfer is 6.12 kcalcmol^{-1}.

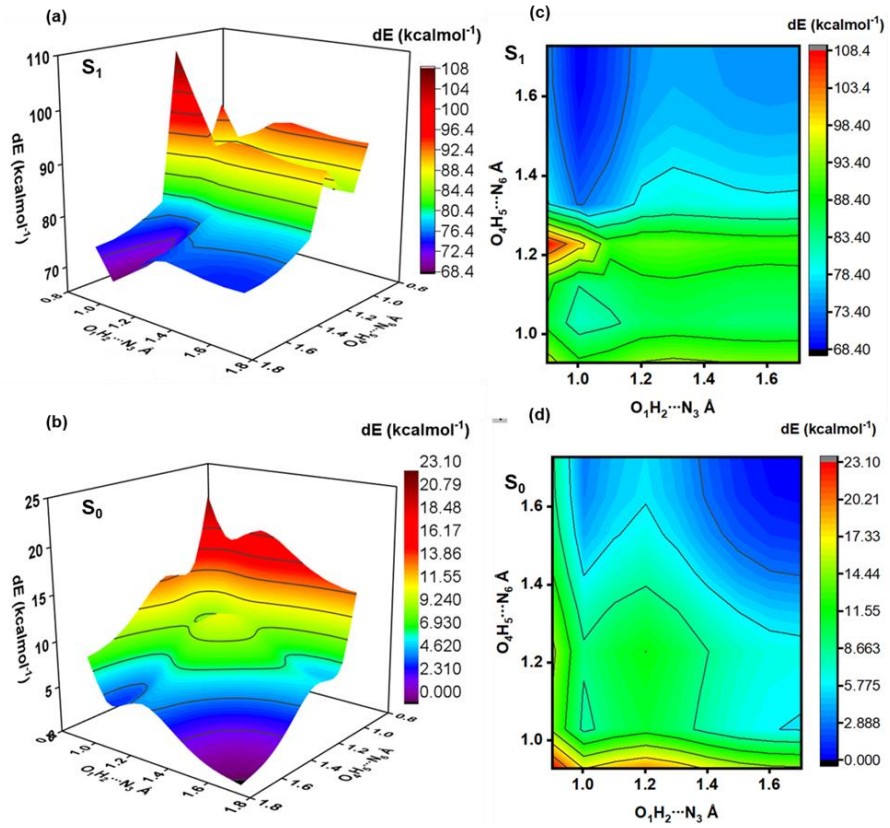

Figure 3.7: Potential energy curves the proton transfer for probe 1 at S_0 and S_1.

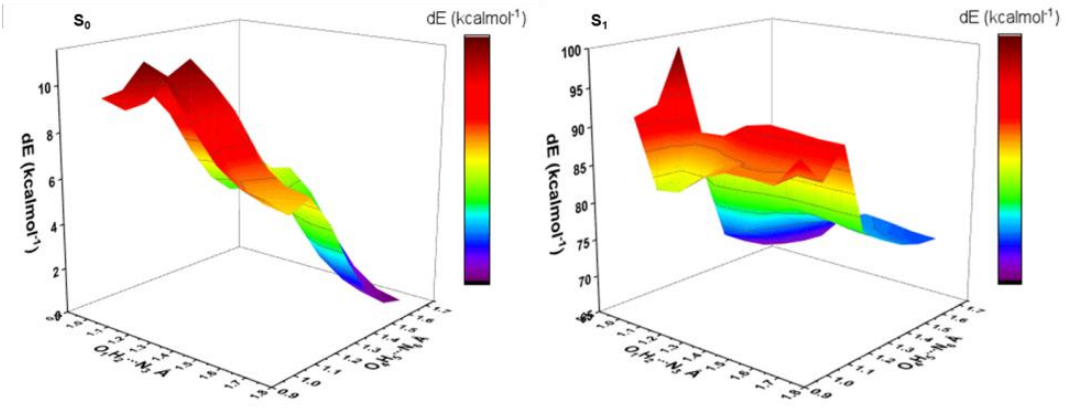

Figure 3.8: Potential energy curves the proton transfer for probe 1-II at S_0 and S_1.

The determined low barrier facile the ESIPT pathway process. In a similar way, PECs with proton transfer cordinate for probe **1**-II geometrical form are shown in **Figure 3.8**. An analysis of PEC shows a barrier of only enol form exist at S_0 state, which convert to SPT1 (Probe **1**-II,

Scheme 3.3) through ESIPT process. The determined energy barrier for forwarding ESIPT process was 1.08 kcalmol^{-1}, which very low relative reverse proton transfer process (6.20 kcalmol^{-1}) and thus facilitate the ESIPT process in a similar way as described for probe **1**-I geometry **Figure 3.9**.

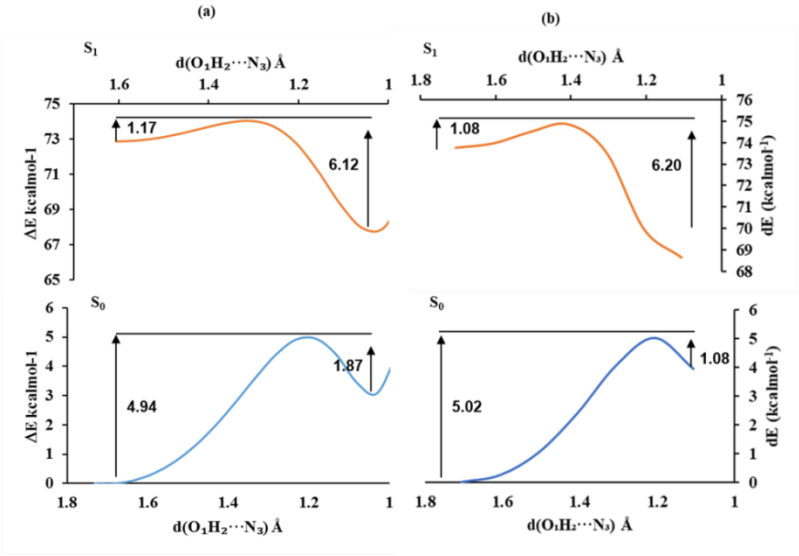

Figure 3.9: Potential energy curve for proton transfer at Schiff based site ($O_1H_2N_3$) of probe 1-I (a) and probe 1-II (b).

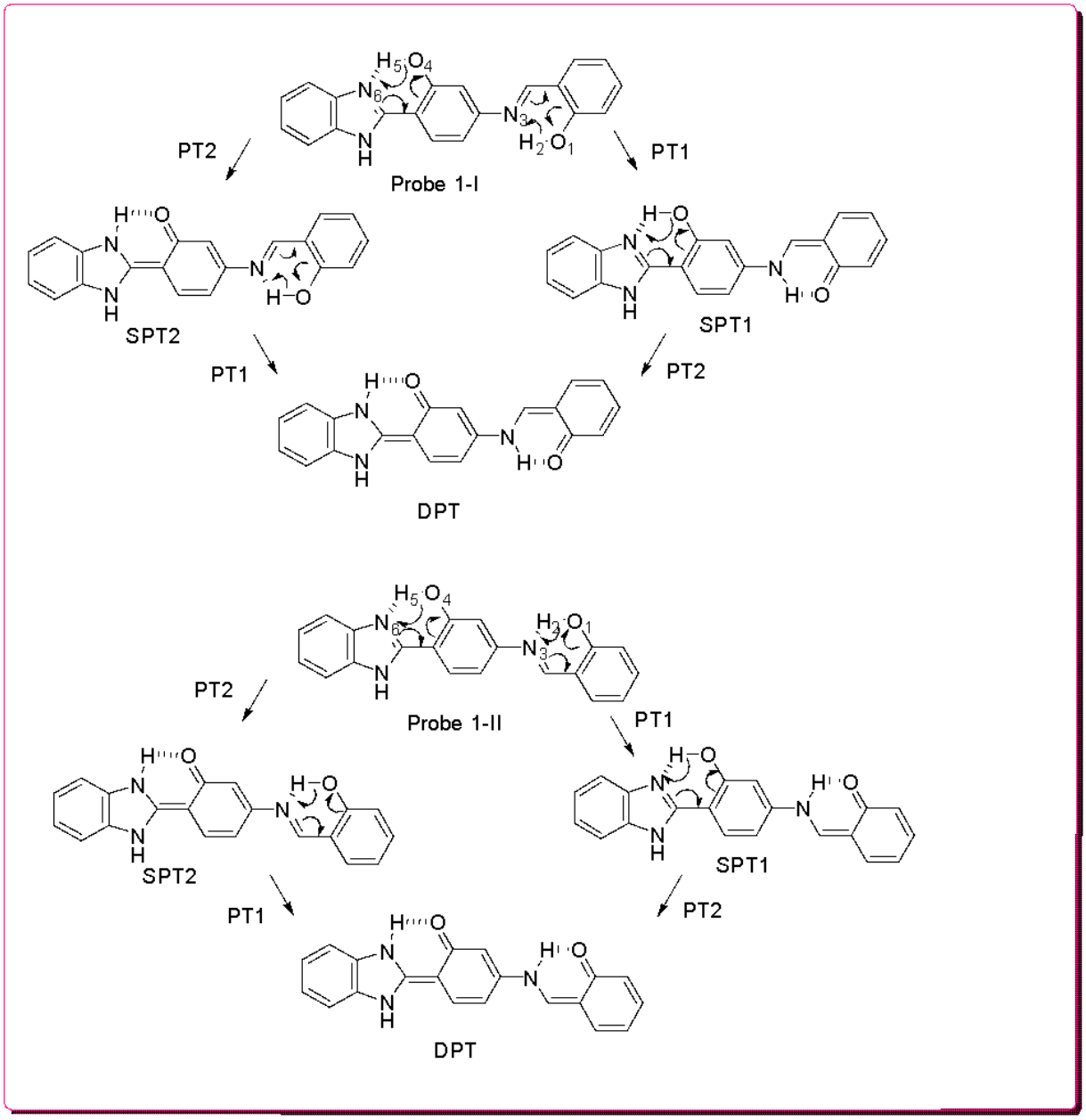

Scheme 3.3: Possible pathways of proton transfer.

3.1.3.6. Aggregation-induced emission (AIE) characteristic of probe 1

As discussed earlier, probe **1** has torsional flexibility with respect to C=N rotations at imine centre. The torsional flexibility around the C=N bond can induce aggregation in the molecule. So to confirm that experimentally we performed the Aggregation Induced Emission (AIE) studies. AIE features of probe **1** were studied by absorption and emission spectra in good solvent

(CH_3CN) with the incremental addition of poor solvent (H_2O). The solution of probe **1** (5 μM, CH_3CN) showed absorption maxima at 340 nm. Upon incremental addition of H_2O to probe **1** (5 μM, CH_3CN), decrease in the absorption intensity at 340 nm was observed with level-off tailing at 750 nm wavelength **(Figure 3.10a)**. The tailing of absorption spectra was proposed to be originated from Mie scattering due to the formation of aggregates in the medium. The emission spectrum of probe **1** (5 μM, CH_3CN, λ_{ex}= 340 nm) showed weak emission at 445 nm. Upon addition of H_2O to the solution of probe **1,** the emission intensity at 445 nm increased up to 40% H_2O: CH_3CN (v/v). On increasing the H_2O content to 50–80% two bands were observed one at 390 nm and the other at 445 nm **(Figure 3.10b)**. The emission of probe **1** at 390 nm increased with a simultaneous decrease at 445 nm from 50-80% H_2O: CH_3CN (v/v). Further, increasing the H_2O content to 90% only band at 390 nm was observed. Therefore, the emission at 390 nm in aggregated form would be due to restriction in intramolecular rotation around the C=N bond as the molecules are closely packed in aggregated form.

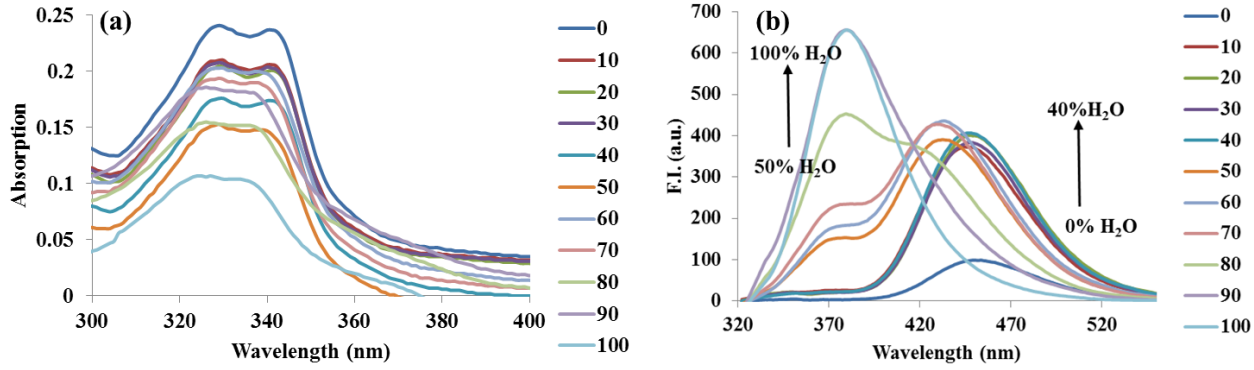

Figure 3.10: (a) Absorption and (b) emission spectra of probe 1 (5 μM) upon increasing the ratios of H_2O in CH_3CN (λ_{ex}= 340 nm).

To investigate the aggregation behaviour of probe **1** dynamic light scattering (DLS) and field emission scanning electron microscopy measurement (FESEM) were performed. The FESEM images clearly showed the increase in particle size with the increase in the H_2O ratio. The FESEM image of the sample in pure CH_3CN does not show any definite morphology whereas 90 % H_2O: CH_3CN spherical particles were observed. To further confirm the aggregation DLS experiment was performed **(Figure 3.11)**. DLS experiment supported the aggregation formation and determined the particle size for probe **1** in different H_2O: CH_3CN ratio. The size of probe **1**

(20 µM) in pure CH_3CN was found out to be 150-350 nm approximately with the average size of 250 nm whereas the particle size of probe **1** in 90 % H_2O: CH_3CN was found to be between 1000-3500 nm with the average size of 1700 nm. FESEM and DLS results were in coherence with each other **(Figure 3.12)**.

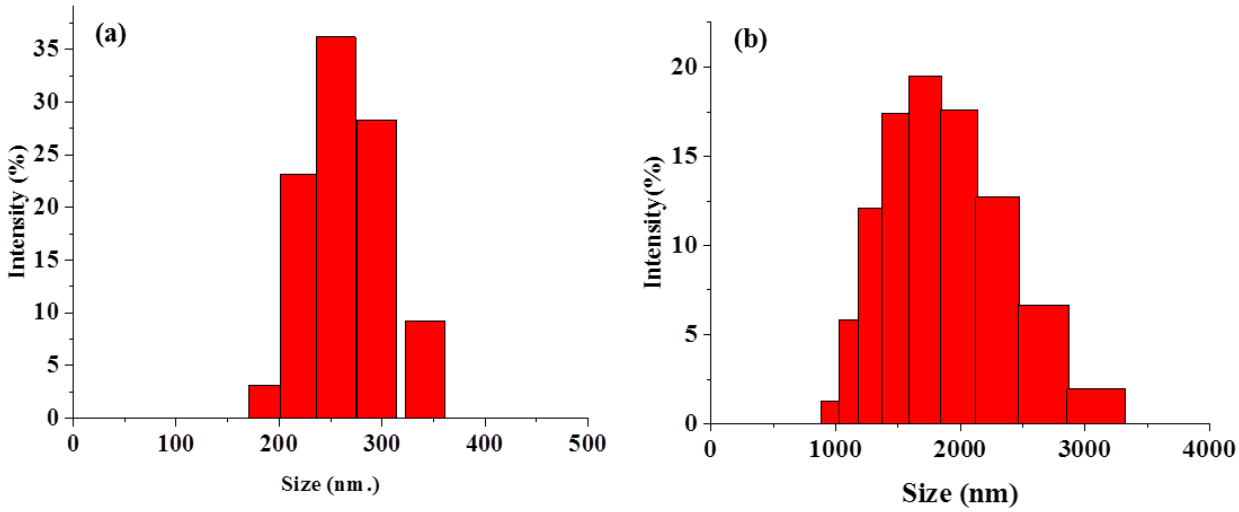

Figure 3.11: DLS of probe 1 (20 µM) in (a) pure CH_3CN and (b) 90% H_2O: CH_3CN (v/v).

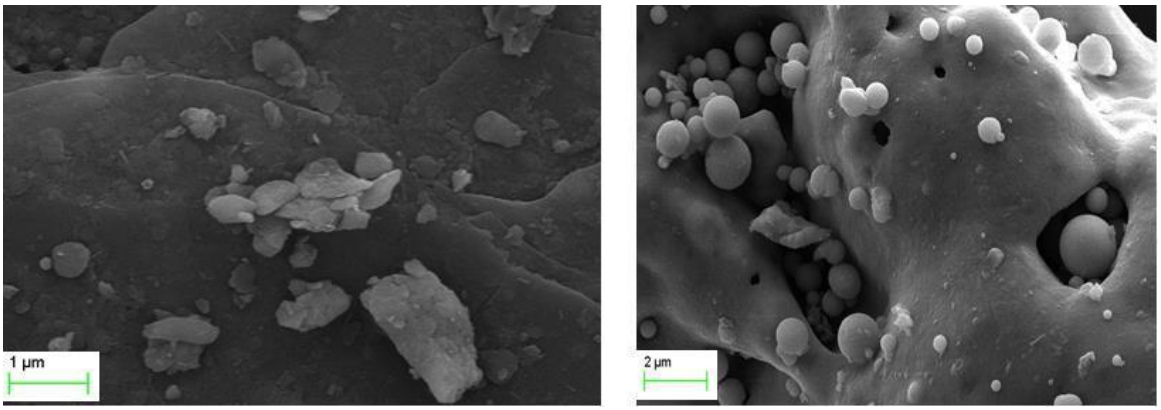

Figure 3.12: FESEM images of probe 1 (20 µM) in (a) CH_3CN and (b) 90% H_2O:CH_3CN (v/v).

3.1.3.7. The effect of metal ions on absorption properties of probe 1

The presence of two binding site on probe **1** encourages us to explore the behavior of Schiff base towards the metal ion sensing. We selected common metal ions including Na^+, K^+, Mg^{2+}, Ca^{2+}, Ba^{2+}, Al^{3+}, Pb^{2+}, Co^{2+}, Ni^{2+}, Cu^{2+}, Cr^{3+}, Hg^{2+} and Zn^{2+} (5 µM) to determine the metal ions

detected by the probe **1** in H_2O: CH_3CN (1:9 [v/v]) solution at pH≈7 with probe **1** (5 µM). As probe **1** showed aggregation induced emission in organic solvent with ≥ 50% H_2O content, it can also show aggregation which will interfere in the metal ion sensing. So, to eliminate the scope of AIE effect we performed the experiment in H_2O: CH_3CN in 1:9 organic-aqueous medium where probe **1** itself did not show AIE effect. The absorption spectra showed that, except for Pb^{2+} and Al^{3+} ions other ions added under the same conditions did not produce any obvious change in the absorption spectra **(Figure 3.13a)**. The appearance of new absorption peak at 360 nm with Pb^{2+} and Al^{3+} ions indicates the complexation of probe **1** with these ions. The systematic growth of absorbance maximum at 360 nm and simultaneous decrease of absorption at 330 nm was observed upon incremental addition Pb^{2+} and Al^{3+} ions to probe **1** solution at 5 µM concentrations. **(Figure 3.13b, c)** Distinct isosbestic point at 335 nm for Pb^{2+} and Al^{3+} implied the formation of only one active complex in the receptor.

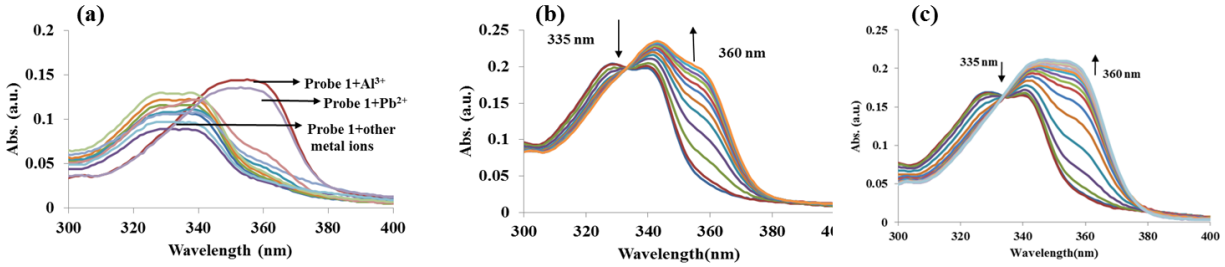

Figure 3.13: Absorption spectra of probe 1 (5 µM) in H_2O:CH_3CN (1:9, [v/v]) (a) in presence of different metal ions (1000 µM), (b) upon incremental addition of 0-35 µM of Pb^{2+} ions and (c) with the incremental addition of 0-20 µM of Al^{3+} ions.

3.1.3.8. The effect of metal ions on fluorescence spectra of probe 1

The metal ion sensing property of probe **1** (5µM) was also investigated by monitoring the changes in emission properties upon addition of several metal ions such as Na^+, K^+, Mg^{2+}, Ca^{2+}, Ba^{2+}, Al^{3+}, Pb^{2+}, Co^{2+}, Ni^{2+}, Cu^{2+}, Cr^{3+}, Hg^{2+} and Zn^{2+} (5 µM) in mixed solvent medium H_2O: CH_3CN (1:9 [v/v]). No metal ion produced fluorescence upon addition to probe **1** except for Pb^{2+} and Al^{3+} ions, which give blue emission under UV light **(Figure 3.14)**. The emission spectrum of probe **1** showed weak band with emission maxima centered at 445 nm on excitation at 340 nm. Among all the tested metal ions only Pb^{2+} and Al^{3+} ions enhanced the fluorescence intensity **(Figure 3.15a)**. The fluorescence enhancement may be derived from the formation of more

widespread π-conjugation system in probe **1** after binding with metal ions. When probe **1** was titrated with Pb^{2+} and Al^{3+} ions, the fluorescence intensity of probe **1** increased remarkably at 390 nm which can be due to inhibition of ESIPT **(Figure 3.15b, c)**.

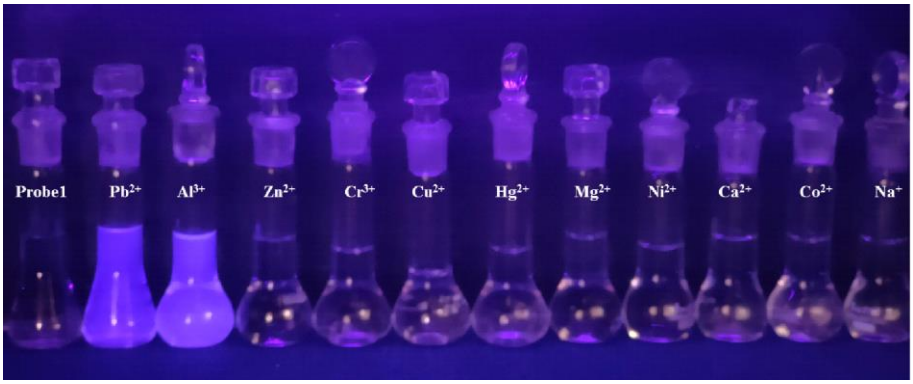

Figure 3.14: Effect of different metal ions on solution of probe 1 (20 µM, H_2O-CH_3CN, (1:9, [v/v]), pH≈7) under UV light.

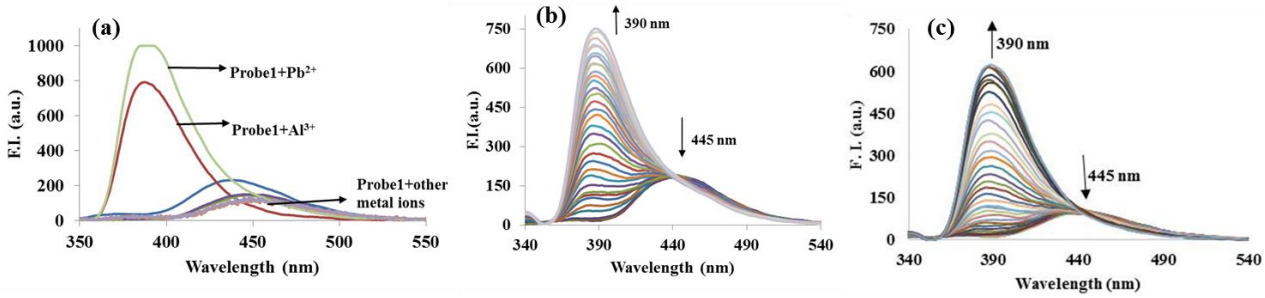

Figure 3.15: Fluorescence spectra of probe 1 (5 µM) in H_2O:CH_3CN (1:9, [v/v]) (a) in presence of various metal ions (1000 µM), (b) on incremental addition of 0-20 µM of Pb^{2+} ions and (c) with the incremental addition of 0-50 µM of Al^{3+} ions.

To further study the binding efficiency of probe **1** with metal ions the binding constant for the complexes were determined. The binding constants for the complexes were obtained by linear fitting of 1/ $(I-I_0)$ to 1/ $[M^{n+}]$ according to the Benesi-Hildebrand equation. The binding constant for probe **1**-Pb^{2+} and probe **1**-Al^{3+} complexes were 7.0×10^4 M^{-1} and 1.7×10^4 M^{-1} with lowest detection of 2.7 nM and 33 nM respectively. Fluorescence spectrum and UV-Vis spectrum were used to determine the coordination ratio between probe **1** and Pb^{2+} and Al^{3+}. The stoichiometry of probe **1** and Pb^{2+} and Al^{3+} ions complexes were found to be 1:1 **(Figure A8)**. Interferences studies for the Pb^{2+} ion complex with probe **1** were performed in the presence of other

competitive metal ions. To perform this we took probe **1** and Pb^{2+} (5 μM) in H_2O: CH_3CN (1:9 [v/v]) and added 5 μM of other competitive metal ions. The presence of other metal ions had no interference in the detection of Pb^{2+} at 390 nm (**Figure 3.16)**. Hence, the probe **1** revealed a good practical ability to recognize Pb^{2+} ions in the presence of other cations.

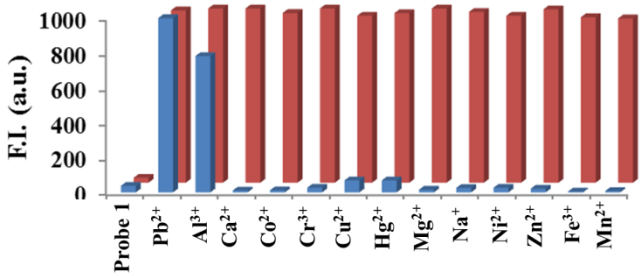

Figure 3.16: Relative emission intensity of probe 1 (5 μM) in H_2O: CH_3CN, 1:9 [v/v] (λ_{ex}= 340 nm) with different competing metal ions in the absence and presence of Pb^{2+} at λ_{em}= 390 nm, where blue bars represent the emission intensity change of probe 1 with different metal ions (5 μM) and red bars represent probe 1+ Pb^{2+} in the presence of different relevant competing metal ions (5 μM).

3.1.3.10. Plausible mechanism

In order to find the possible mechanism for the interaction of probe **1** with Pb^{2+} and Al^{3+} ions, ^1H NMR titrations were carried out in CD_3CN-d_3. In the ^1H spectrum of probe **1** peak at 8.83 ppm is the characteristic peak of imine proton (-C=N-) represented by H_b and phenolic hydrogen at 9.92 ppm represented by H_a. Upon the addition of 1.0 eq. of Pb^{2+} to 5 mM solution of probe **1** in CD_3CN-d_3 the two proton peaks at 8.83 ppm and 9.92 ppm were shifted downfield due to electron deficiency on probe **1** and a new peak at 8.99 ppm was observed on binding with Pb^{2+} ions. The noticeable downfield shifting of the imine proton signal indicates the binding of imine N atom of Schiff base in complexation. Also, the peaks at 9.92 ppm got broad after downfield shift which can be due to the interaction of phenolic hydrogens with metal ion. **(Figure 3.17)** The shifting in the protons can be due to the change in the electron density after the interaction with Pb^{2+} ions. The aromatic region peaks were merged to some extent which can imply that the structure of metal complex is more rigid than the free ligand. After the addition of D_2O to the metal complex the peaks at 10.84 ppm, 8.99 ppm and 8.01 ppm were disappeared which clearly indicated that these peaks are of phenolic and amine hydrogens **(Scheme 3.4)**. Similarly, we performed ^1H NMR titrations for Al^{3+} and after the addition of 1.0 eq. of Al^{3+} ion to the probe **1**

the peaks at 9.92 ppm, 8.83 ppm and 8.01 ppm were shifted downfield and on the addition of D_2O two peaks at 10.84 ppm and8.99 ppm were disappeared.

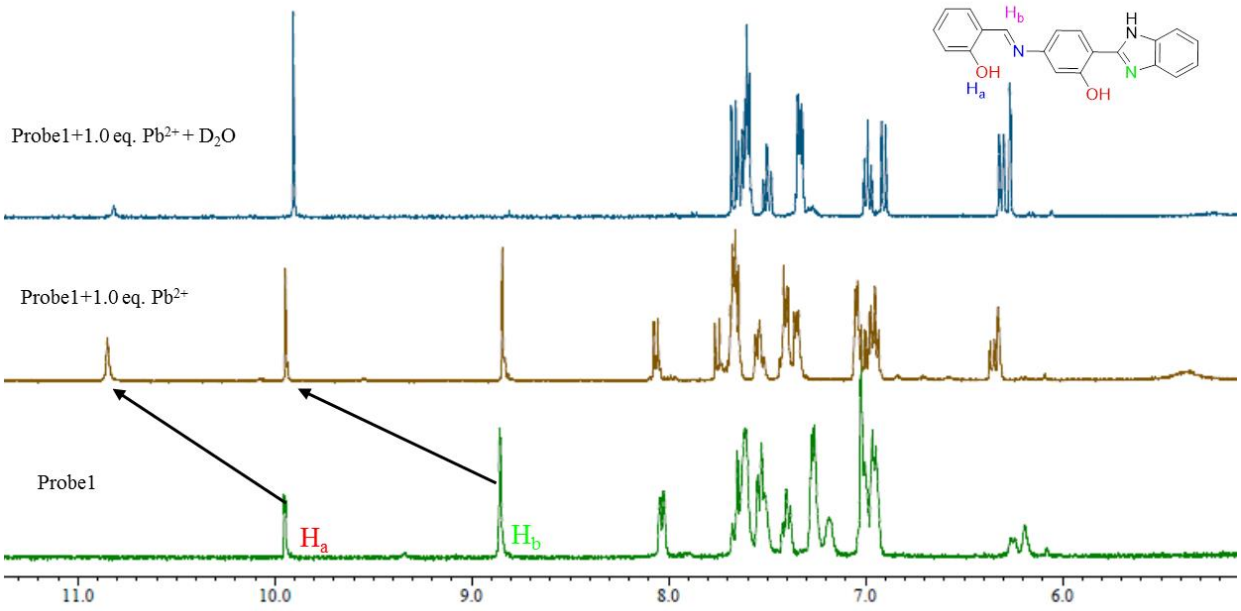

Figure 3.17: ^{1}H NMR spectra of probe 1 (5× 10^{-3} M) upon addition of 1.0 equiv. of Pb^{2+} ions in CH_3CN-d_3.

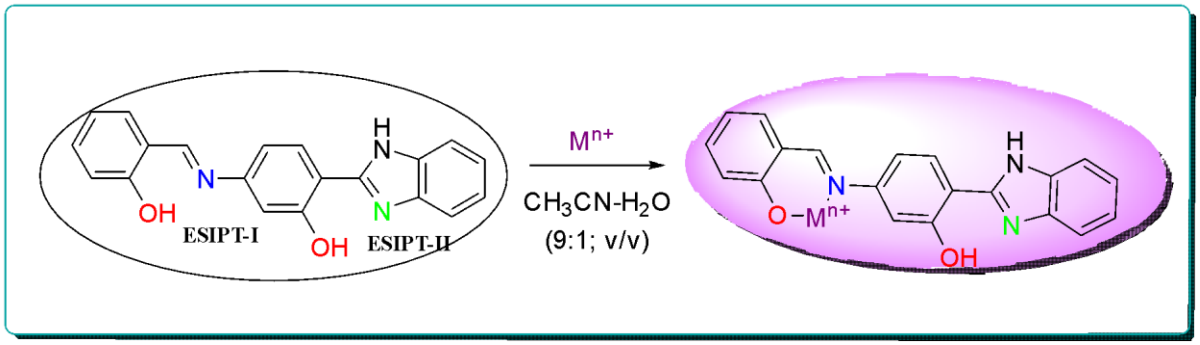

Scheme 3.4: Plausible mechanism for probe 1 and Pb^{2+} and Al^{3+} ions binding.

To prove our mechanism we synthesized Schiff base probe **2** with ESIPT-I sight missing **(Scheme 3.4)** and evaluated the sensing ability towards different metal ions in the same solvent system i.e. H_2O: CH_3CN (1:9 [v/v]). Probe **2** does not show any change in the absorption and

emission spectrum upon the addition of different metal ions **(Figure 3.18)**. This indicated that probe **1** binds with Pb^{2+} from ESIPT-I site.

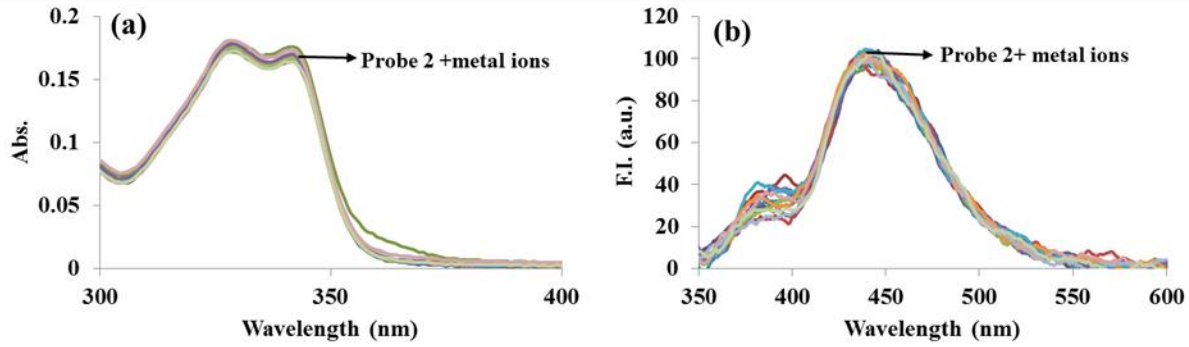

Figure 3.18: (a) Absorption and (b) emission spectra of probe 2 with different metal ions.

As the probe **1**, has flexible imine bond and that site is responsible for binding with Pb^{2+} ions, thus in order to know the binding behavior in terms of aggregation, DLS experiment was performed in the presence of Pb^{2+} ions. The probe **1** showed size of 295 nm in 10% H_2O-CH_3CN through DLS. However, upon addition of Pb^{2+} ions the size of the particles increases to 925 nm which supports the formation of aggregates on chelation with Pb^{2+} ion **(Figure 3.19)**. FESEM images showed change in morphology of probe **1** on addition of Pb^{2+} ion which confirmed the binding of probe **1** with Pb^{2+} ion **(Figure 3.20)**. Both the FESEM and DLS are in correlation with each other. The emission enhancement of probe **1** after binding with Pb^{2+} ion can be due to the formation of aggregates.

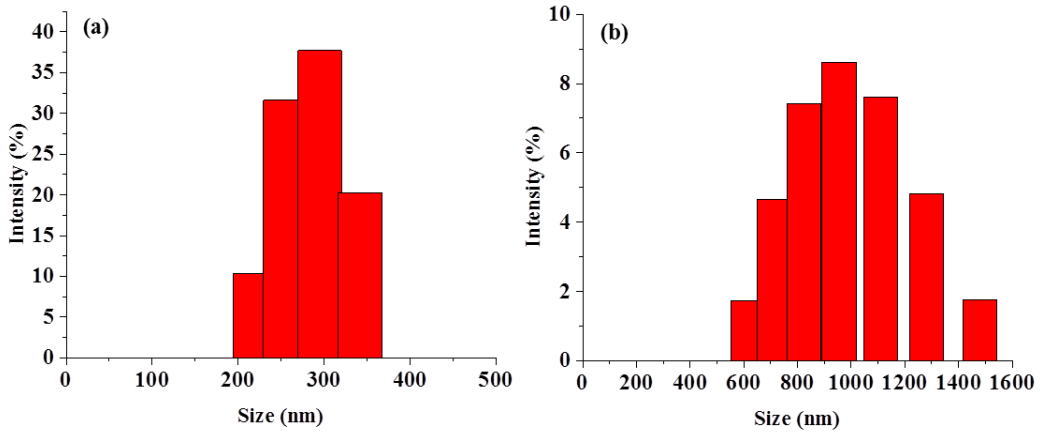

Figure 3.19: DLS profile of probe 1 (20 µM) in (a) H_2O: CH_3CN (1:9, [v/v]) (b) after the addition of Pb^{2+} ion.

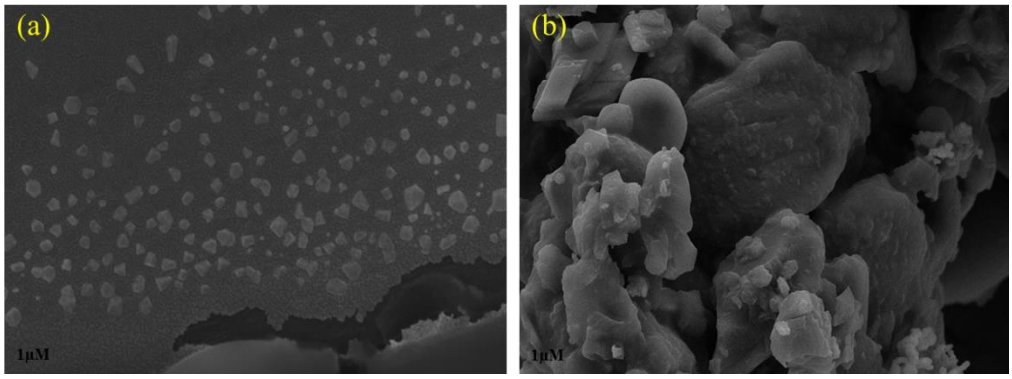

Figure 3.20: FESEM images of (a) probe 1 and (b) after addition of Pb^{2+} ion in H_2O:CH_3CN (1:9, [v/v]).

Further, the experimental results were supported with theoretical results. We optimized the both conformation of probe **1** with Pb^{2+} ions using preliminary information of NMR outcomes. The Pb^{2+} ion shows interaction with Schiff base unit with contact distance of Pb-N of 2.32 Å and Pb-O of 2.07 Å **(Figure 3.21)**. The calculated charges on nitrogen of imine and phenolic oxygen were found to be -0.232 and -0.565, respectively, while Pb^{2+} has charge of +1.078 illustrated the dipolar interaction and thus, showed the coordination. Further, first three low-lying vertical excitation peaks were summarized in **Table 3.3**. The calculated absorption peak for probe **1-I**.Pb^{2+} at 326.5 nm and probe **1-II**.Pb^{2+} at 332.4 nm were resulted from HOMO→LUMO, HOMO-1→LUMO, and HOMO-1→LUMO+1, respectively **(Figure 3.22)**. The electron density

distribution of majorly contributing frontier molecular orbital transition of probe **1**.Pb^{2+} demonstrating charge transfer from Pb^{2+} to probe **1**, further triggering the appearance of color.

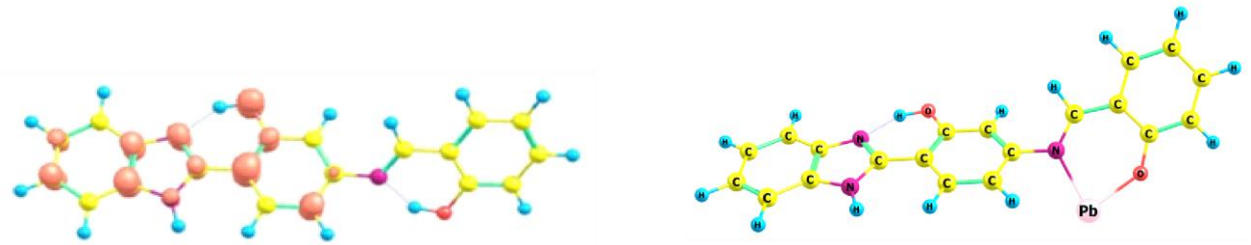

Figure 3.21: Optimized structures of probe 1 and probe 1 with Pb^{2+}.

Table 3.3: Summary of excitation spectra of probe 1 for probe 1-I.Pb^{2+} and probe 1-II.Pb^{2+} configuration.

Probe 1-I.Pb^{2+}				**Probe 1-II.Pb^{2+}**		
$S_0 \rightarrow S_n$	**□ (nm)**	**f**	**MO**	**□ (nm)**	**f**	**MO**
$S_0 \rightarrow S_1$	326.47	0.5625	H→L (20 %) H-1→L (21 %) H-1→L+1 (38 %)	332.39	0.7675	H→L (33 %) H-1→L (30 %) H-1→L+1 (12 %)
$S_0 \rightarrow S_2$	303.96	0.4456	H-1→L (30 %) H→L+1 (35 %)	307.44	0.3156	H-1→L (42 %) H→L+1 (22 %)
$S_0 \rightarrow S_3$	296.08	0.0891	H→L (44 %) H-1→L+1 (37 %)	297.73	0.0749	H→L (24 %) H-1→L+1 (47 %)
□= calculated excitation wavelength (nm); MO = molecular orbitals contributing to excitations; H = HOMO; L = LUMO, f = Oscillator strength						

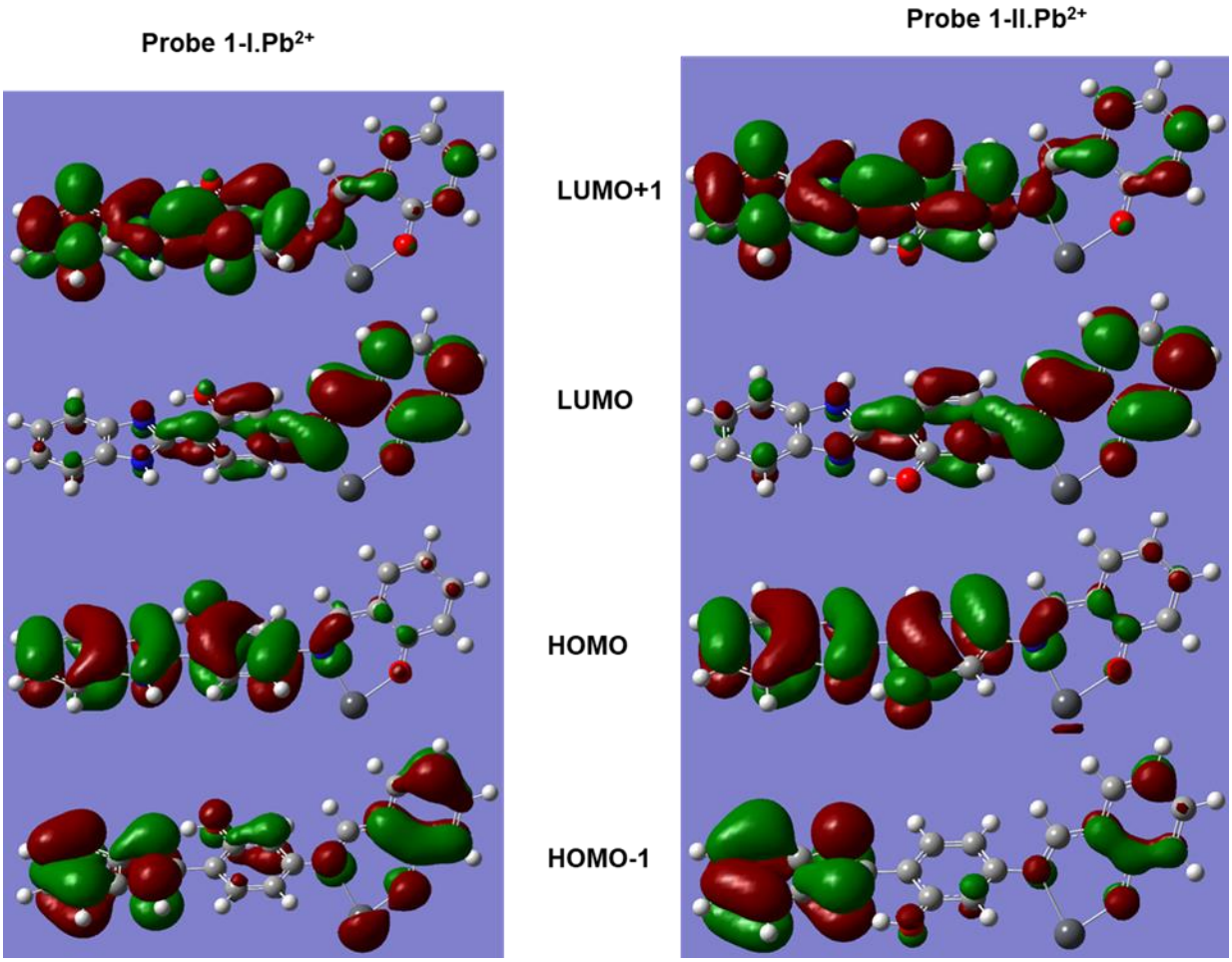

Figure 3.22: DFT computed HOMO and LUMO diagrams of probe 1 and probe 1 with Pb^{2+}.

3.1.3.11. Effect of pH on probe 1

From the ^{1}H NMR titrations it is clear that probe **1** showed deprotonation after the addition of metal ions. So, to confirm the deprotonation of probe **1**, pH titrations were performed. The charge distribution on a molecule can be affected by changing the pH of the solution which can further alter the absorption and emission properties of the molecule. The presence of aldimine (-C=N-) and hydroxyl group (-OH) can lead to the protonation or deprotonation of probe **1** under acidic or basic medium. So, the effect of pH on probe **1** in H_2O:CH_3CN (1:9, [v/v]) was also observed. It has been observed that the probe **1** was stable in pH range 6.4- 8.3. In pH 8.3 to 2.7 the absorption band at 340 nm disappeared with the appearance new band at 360 nm whereas in alkaline medium (8.2-11.3 pH) caused the decrease in the absorption intensity at 340 nm. Similarly, the emission spectra of probe **1** showed hardly any change in the fluorescence

intensity in the pH range 6-10. Below pH 6 a sharp increase in the fluorescence intensity at 390 nm was observed which can be due to deprotonation of hydroxyl O atom and imine N atom preventing the ESIPT process **(Figure 3.23)**. ESIPT is more dominant relaxation process than the fluorescence. So when the ESIPT process stops the relaxation occurs through fluorescence, hence increase in the fluorescence intensity was observed.

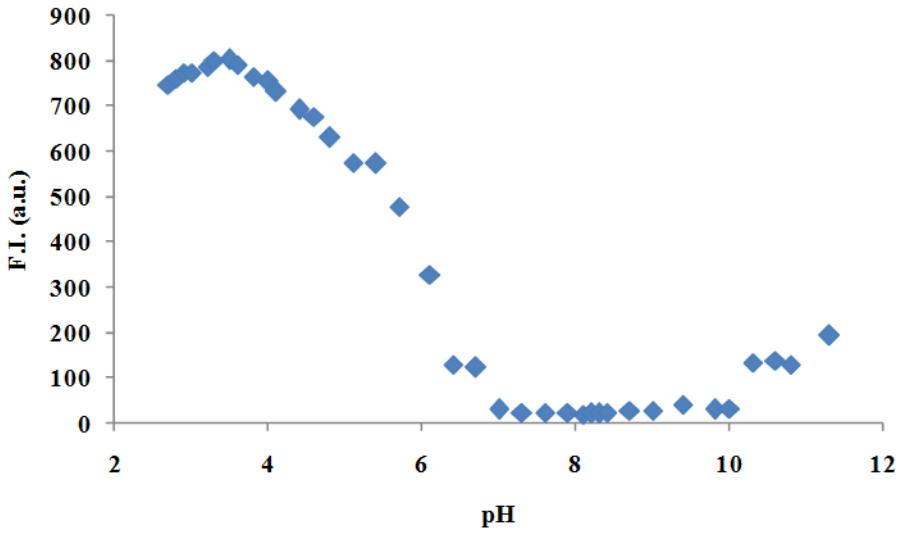

Figure 3.23: Effect of pH on probe 1 in H_2O:CH_3CN (1:9, [v/v]) at λ_{em} = 390 nm.

3.1.3.12. Time-correlated single photon counting (TCSPC) study

The enhancement in the fluorescence on binding with the Pb^{2+} and Al^{3+} ions has been supported by the results obtained from fluorescence decay measurement, using the TCSPC study. The decay behavior of probe **1** and its metal ion complexes is best fitted in third exponential function. Probe **1** showed three components having lifetimes of 0.57 ns, 1.83 ns and 17.29 ns respectively. The population of all the components was 0.51, 0.12 and 0.36 % respectively. The average life time for probe **1** comes out to be 1.02 ns. Upon the addition of Pb^{2+} to the solution of probe **1**, again three components were obtained with life time of 0.79 ns, 1.18 ns and 8.07 ns. The population of all the components was 0.60, 0.25 and 0.14 % respectively. The average life time was calculated to be 1.00 ns. Similarly, after the addition of Al^{3+} the average life time were 0.92 ns. The average lifetime of probe **1** on interaction with M^{n+} do not show much variation **(Table 3.4)**. Hence, we can say that probe **1** binds with metal ions in purely static manner.

Table 3.4: Fluorescence lifetime measurements for Probe 1 and its metal ion complexes in H_2O: CH_3CN (1:9, [v/v], 5 µM).

H_2O:CH_3CN (1:9, [v/v])	τ_1 (ns)	τ_2 (ns)	τ_3 (ns)	α_1	α_2	α_3	χ^2	τ_{av} (ns)
Probe **1**	0.57	1.83	17.29	0.51	0.12	0.36	1.45	1.02
Probe **1**+ Pb^{2+}	0.79	1.18	8.07	0.60	0.25	0.14	1.35	1.00
Probe **1**+Al^{3+}	0.64	1.60	10.36	0.63	0.15	0.21	1.30	0.92

3.1.3.13. Practical applicability of probe 1

To demonstrate the accuracy and practical applicability of probe **1** for the detection of Pb^{2+} ions in water sample taken from the drains of Thapar Institute of Engineering and Technology campus. To check the presence of Pb^{2+} ions in the water sample, we spiked certain amount (20 µM and 40 µM) of Pb^{2+} ions into the water sample and the samples were given for Atomic Absorption Spectroscopy (AAS). The amount we added and the amount obtained from AAS report were then compared and the results are listed in **Table 3.5**. The percentage recoveries of 98% and 105.5% were calculated by spiking with different concentrations of Pb^{2+} ion with RSD value of 0.23 and 0.71%.

Table 3.5: Probe 1 for analyzing Pb^{2+} in real water samples.

S. No.	Added (ppm)	Found (ppm) (through AAS)	Recovery (%)	RSD (%)
1	20	19.6	98	0.23
2	40	42.2	105.5	0.71

3.1.3.14. Reversibility and Logic gate construction of probe 1

Development of reversible chemosensor with high selectivity and sensitivity for the detection of various ions is very desirable. The reversibility of a chemosensor is also an important aspect for its practical application. Addition of EDTA, being a strong complexing agent, resulted in disappearance of the emission band of probe **1** and metal ions complexes at 390 nm. The

disappearance of emission band can be due to demetallation from Probe **1**-M^{n+} complex. The turned-on property of probe **1** was again regained upon the addition of metal ions. The result was recreated by sequencial addition of EDTA and metal ions that depicted that probe **1** reversibly recognized metal ions **(Figure 3.24)**. The response of our probe towards multiple metal ions inspired us to check its reversibility and construct a double input and single output logic gate. The INHIBIT logic gate is constructed in the emission maximum of metal ions at 390 nm, with metal ions as one input and EDTA as another input. The absence and presence of input are with basic theory of Boolean algebra where "1" represents YES/ON state and "0" represents NO/OFF state. In the absence of both the inputs i.e. metal ions and EDTA, the output was zero indicating OFF state. In variation 2, when only metal ions were present without EDTA maximum emission intensity was observed at 390 nm pointing 1 or ON state. Similarly in third variation, when metal ions were absent and only EDTA was present the output was 0 i.e. OFF state. For variation 4, when both the chemical entity were present again the output was 0 i.e. OFF state **(Table 3.6)**. Therefore, input 1 satisfies the condition for OR gate and input 2 satisfy the criteria for NOT gate. Considering all the results our truth table matches the truth table of INHIBIT logic gate.

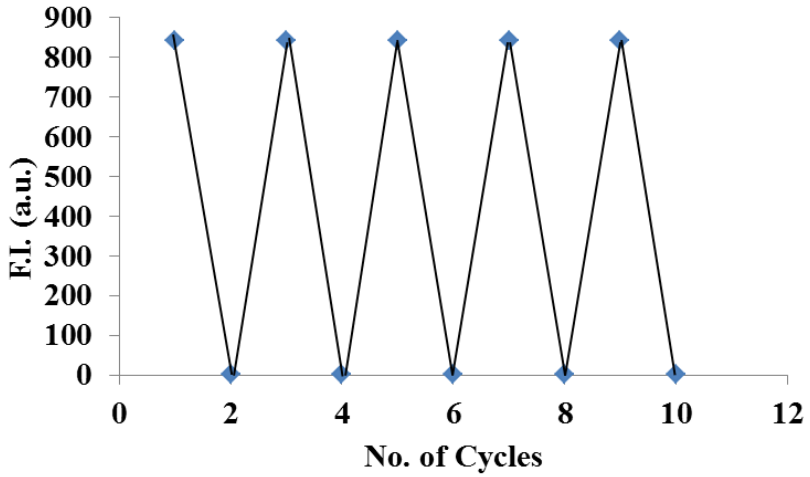

Figure 3.24: The reversible and reproducible emission signal at 390 nm (λ_{ex}=340 nm, 5μM) in H_2O:CH_3CN (1:9, [v/v]) on repetitive addition of metal ions and EDTA.

Table 3.6: Truth table for INHIBIT and IMPLICATION logic gate.

Truth Table			
INPUT		OUTPUT	
		INHIBIT	IMPLICATION
Input 1 (M^{n+})	Input 2 (EDTA)	λ_{em} = 390 nm	λ_{em} = 450 nm
0	0	0	1
1	0	1	0
0	1	0	1
1	1	0	1

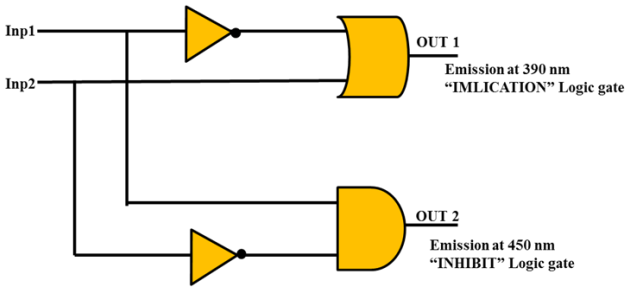

IMPLICATION gate was also obtained where the output was emission at 450 nm. There were four different states of absence and/or presence of both the inputs which were (0, 0), (1, 0), (0, 1) and (1, 1). Only in the case where metal ions were present and EDTA was absent the output was 0 i.e. OFF state due to specific combining between probe **1** and metal ions. Now this truth table matches the truth table of IMPLICATION logic gate.

3.1.4. Conclusion

On concluding remark, we have synthesized a Schiff base, from 5-amino-2-(1H-benzo[d]imidazol-2-yl) phenol and salicylaldehyde (probe **1**) by a very simple synthetic route. Probe **1** shows excellent photo physical properties such as pH dependency, solvatochromism and aggregation induced emission phenomenon. We confirm the concomitant two geometrical form probe **1**-I and probe **1**-II at S_0 state, with barrier of 1.17 kcalmol-1. Further geometrical parameter and FTIR analysis established the presence of dual intramolecular hydrogen bonding. Exploring the photoexcitation process, established a charge transition and increased charge density at proton acceptor sites, which facilitate the ESIPT process. Probe **1** could only proceed single ESIPT process, which we verified by calculating PECs with respect to proton transfer coordinate. Probe **1** was used as a chemosensor for Pb^{2+} and Al^{3+} ions in H_2O:CH_3CN (1:9, [v/v]) medium. In UV-Vis spectra, probe **1** showed changes with Pb^{2+} and Al^{3+} ions with formation of new band at 360 nm. In fluorescence spectra, probe **1** showed changes with Pb^{2+} and Al^{3+} with new band formation at 390 nm and respectively. Probe **1** was used to construct

dual logic gates by controlling the chemical inputs. Unlike single-selective system, recoginization of Pb^{2+} and Al^{3+} ions by a single probe is more desirable owing to its low synthesis cost and operational efficiency. There upon the design and synthesis of this probe developed new possibilities for synthesis of probe that can detect multiple ions.

3.2.

Effect of electron donating group ($–NEt_2$) on excited state intramolecular proton transfer process of hydroxy aryl benzimidazole based Schiff base

3.2.1. Abstract

In this section, the effect of $–NEt_2$ group as an electron donating group on photophysical behavior of benzimidazole based Schiff base **(3)** was studied. The benzimidazole moiety is an appealing building block for fluorescent chemosensors because of the multifunctionality of its heteroaromatic conjugated planar structures. The benzimidazole moiety acts as good electron acceptor due to its electron withdrawing nature and the $–NEt_2$ unit acts as a charge transferring unit and induces dipole moment in the chemosensor and resulting in the intramolecular charge transfer phenomenon. Probe **3** has functional variety in terms of hydrogen donor units and hydrogen acceptor units and NEt_2 as electron donating unit, which could result in excited state intramolecular proton transfer and excited state intramolecular charge transfer mechanism. Probe **3** displayed two absorption peaks at 325 nm and 340 nm and an emission band at 435 nm accompanied by Stokes shift of 110 nm. The electron density tends to be pushed towards the electron loving centre by the presence of the $–NEt_2$ group in probe **3**. Thus, it will facilitate the intramolecular charge transfer (ICT). Intramolecular H-bonding and ICT can tune the photophysical properties based on ESIPT or ICT phenomenon. Further, the PEC's confirmed the coexistence of two confomers of probe **3** in S_0 state. All the calculations were based on integral equation formalism polarization contiinum model (IEFPCM) connected to a long range hybrid functional theory (cam-B3LYP), which imitated the mechanistic understanding of the photophysical response. Probe **3** displayed intramolecular charge transfer and acts as a potential sensor for Al^{3+} and HSO_4^- ions. Probe **3** behaved as a fluorescence "*turn-on*" chemosensor for both Al^{3+} and HSO_4^- ions in H_2O-CH_3OH solvent system. The proposed method allowed the determination of Al^{3+} and HSO_4^- ions up to 39 nM and 23 nM at emission wavelength 385 nm and 390 nm, respectively. The binding behavior of probe **3** towards these ions is determined by the Job's plot method and ^1H NMR titrations. Probe **3** was used to construct a molecular keypad lock where the absorbance channel can be opened only in the presence of the correct sequence of chemical input. Further, it was used for the quantitative determination of HSO_4^- ion in different real-field water samples.

3.2.2. Experimental section

3.2.2.1. Synthesis of probe 3

The compound **1a** and N, N-Diethylamino salicylaldehyde were stirred at 70 °C in ethanol for 10 h **(Scheme 3.5)**. The reaction mixture was cooled on completion of the reaction and the separated solid was filtered and washed with ethanol to get yellow coloured solid of probe **3** in 75% yield. m. p. 270-275 °C; ^{1}H NMR (DMSO-d_6, 400 MHz): δ (ppm) 8.45 (s, 1H, -C=N), 7.96 (d, 1H, J = 8 Hz, H_a), 7.89 (d, 1H, J = 8 Hz, H_d), 7.67 (d, 1H, J = 8 Hz, H_f), 7.51 (t, 1H, J = 16 Hz, H_b), 7.40 (t, 1H, J = 16 Hz, H_c), 7.17 (d, 1H, J = 8 Hz, H_g), 6.93 (d, 1H, J = 4 Hz, H_h), 6.85 (dd, 1H, J_1 = 4 Hz, J_2 = 8 Hz, H_i), 6.27 (dd, 1H, J_1 = 4 Hz, J_2 = 8 Hz, H_j), 6.18 (d, 1H, J = 4 Hz, H_e), 3.43-3.37 (m, 4H, eth-CH_2), 1.22-1.19 (m, 6H, eth-CH_3) **(Figure A9)**. ^{13}C NMR (DMSO-d_6, 100 MHz): δ (ppm) 159.9, 153.1, 152.8, 127.7, 127.6, 122.8, 122.5, 106.9, 106.6, 100.7, 100.3 **(Figure A10)**. **HRMS** (ESI-TOF): (m/z) $[M+H]^+$ calcd for $C_{24}H_{25}N_4O_2$: 401.1978, found: 401.1988 **(Figure A11)**.

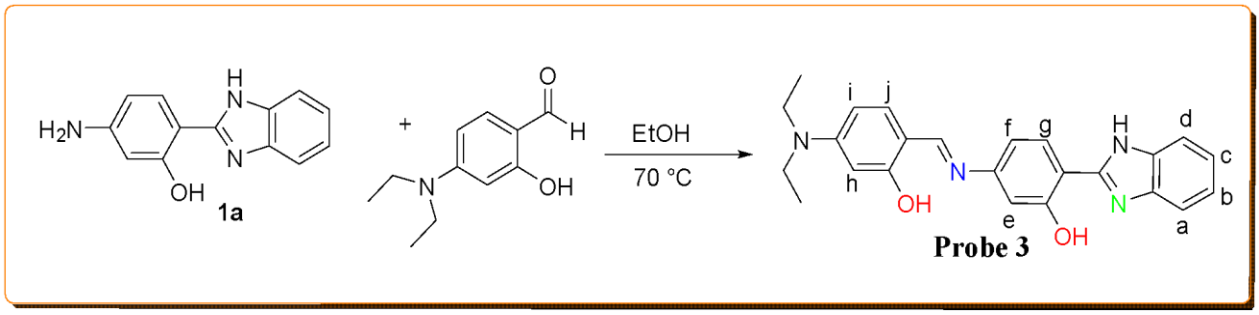

Scheme 3.5: Syntheis of probe 3.

3.2.3. Results and discussion

The synthesized benzimidazole based probe **3** contains hydroxyl group at *o*-position and N, N'-diethyl group at *p*-position to the –CH=N moiety. An essential condition for excited state intramolecular proton transfer (ESIPT) process is that the molecule must possess an electron donor group (-OH and -NH_2) and an electron acceptor group (=N- and >C=O) present in close vicinity to each other. The position of these groups in probe **3** is in such a way that there should have intramolecular hydrogen bonding.

3.2.3.1. Photophysical properties of Probe 3

Absorption and emission spectroscopic techniques were used to observe the photophysical properties of probe **3**. Absorption spectrum of probe **3** (20 μM, CH_3CN) showed two absorption

peaks at 325 nm and 340 nm. Upon excitation at 340 nm, probe **3** (20 μM, CH_3CN) showed weak emission band at 435 nm accomplished by Stokes shift of 110 nm. Probe **3** contains functional variety in terms of hydrogen donor units as O_1H_2; O_4H_5 and hydrogen acceptor units as N_3 and N_4, and NEt_2 as electron donating unit, which could result in excited state intramolecular proton transfer and excited state intramolecular charge transfer mechanism. To get insight about aforementioned mechanism, we investigated the absorption and emission spectra in different polarity medium. On increasing the polarity, a shift of 10 nm was noted for parent absorption peaks (from 325 nm to 340 nm and from 340 nm to 350 nm) **(Figure 3.25a)**. The red shift observed in the absorption spectra can be due to intramolecular charge transfer process occurring in probe **3**. A similar observation was noted for emission spectra, where the emission band shifts from 435 nm to 450 nm in high polarity medium **(Figure 3.25b)**. In protic polar solvent, a blueshift was noted of 50 nm from 440 nm to 390 nm, which could be due to interaction of protic solvent with basic imine nitrogen.

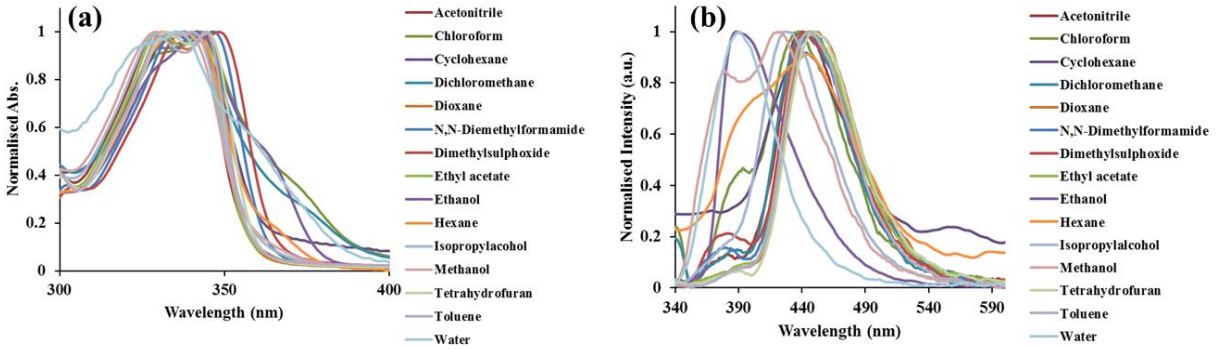

Figure 3.25: (a) Absorption and (b) emission spectra of probe 3 (20 μM) in different polarity solvents.

3.2.3.2. Ground state structure and electronic distribution

The presence of molecular flexibility around -C=N- results in different configurations. Therefore, we optimized the probe **3** and examined the possibilities of different configurations, as performed in probe **1**. Potential energy curves were constructed for C-N rotation (imine center connection). Torsional rotation around C-N unit has energy barrier of 2.18 $kcalmol^{-1}$ at S_0 state, which is less than thermal energy 5 $kcalmol^{-1}$ and thus, signifies the coexistence of probe **3**-A and probe **3**-B configurations that can be interconvertible at S_0 state **(Figure 3.26a).** The Boltzmann populations were determined to be 49 %, and 51 % for probe **3**-A, and probe **3**-B configurations, respectively. Probe **3**-A and probe **3**-B have no imaginary frequencies and

slightly twisted geometry at the S_0 state. The interconvertible natures of configurations were also determined through PEC at S_1 state and it was found that energy barriers have high values at S_1 state and thus, could not allow the interconversion.

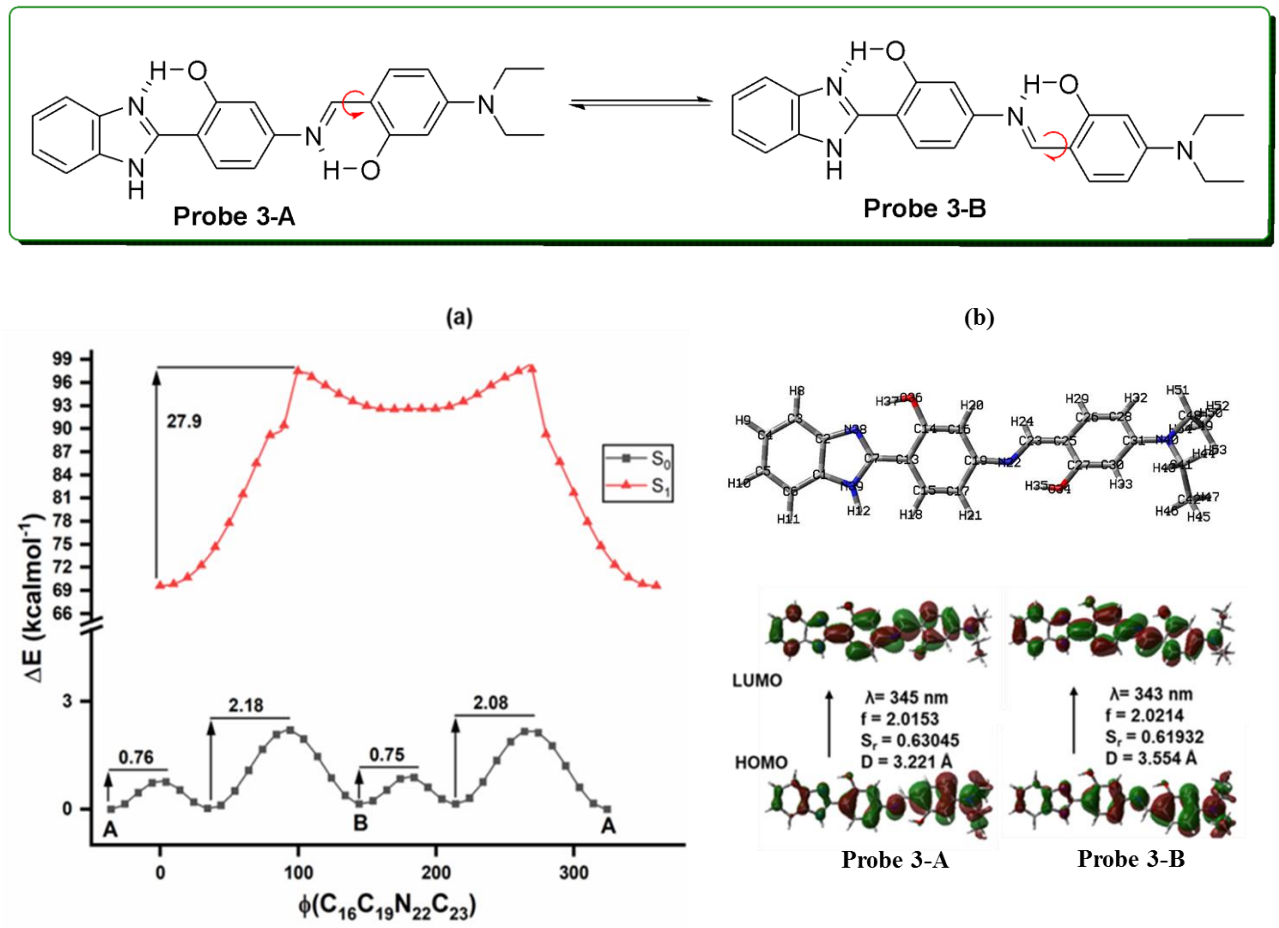

Figure 3.26: (a) Energy profile of probe 3 for torsional rotation optimized structure and (b) their frontier molecular orbitals for $S_0 \rightarrow S_1$ excitation.

Additionally, three low-lying excitations of probe **3**, correspond to S_0 geometry were calculated to investigate the source of absorption spectra. **Table 3.7** contains the summary of the computed excitations. For $S_0 \rightarrow S_1$ excitation determines 84 % orbital transition contribution from HOMO (highest occupied molecular orbital) to LUMO (lowest unoccupied molecular orbital) with oscillation strength of 2.0153 at 345 nm for probe **3**-A, which is consistent with the experimental absorption peak at 325 nm. Additionally, the $S_0 \rightarrow S_2$ and $S_0 \rightarrow S_3$ excitations were determined at 288 nm and 272 nm with oscillation strength of 0.0206 and 0.045, respectively. We considered

$S_0 \rightarrow S_1$ excitation for study because the second and the third excitations have weak oscillation strength **(Table 3.7)**. The electron density in the relevant molecular orbitals changed from Schiff base and diethylamino units (HOMO) to the benzimidazole unit (LUMO) **(Figure 3.26b)**. The subsequent orbital composition also supported the electron density shift from HOMO (majorly localized over N_{40} (28.79 %), C_{25} (15.16 %) and C_{28} (12.05 %) to LUMO (majorly localized over C_{23} (18.97 %), C_{19} (9.40 %), and N_{22} (6.51 %), evoking intramolecular charge transfer from diethylamino unit to benzimidazole unit. Additionally, the hole-electron analysis shows that the hole/electron distribution has a small overlap integral (S_r = 0.63045) and that the electron hole centroid is significantly distant (D = 3.221). Therefore, the above results suggest that the probe **3**-A is undergoing an intramolecular charge transfer process. Probe **3**-B configuration showed a similar pattern of behavior, and the findings are shown in **Figure 3.26b** and **Table 3.7**.

Table 3.7: Summary of excitation spectra of probe 3 for probe 3-A and probe 3-B configuration.

	Probe 3-A			**Probe 3-B**		
$S_0 \rightarrow S_n$	**□ (nm)**	**f**	**Molecular orbital**	**□ (nm)**	**f**	**Molecular orbital**
$S_0 \rightarrow S_1$	345.68	2.0153	H→L (84 %)	343.32	2.0214	H→L (84 %)
$S_0 \rightarrow S_2$	288.98	0.0206	H-1→L (62 %)	287.88	0.0387	H-1→L (58 %)
$S_0 \rightarrow S_3$	272.66	0.045	H-2→L (56 %)	272.40	0.0528	H-2→L (54 %)
□= Estimated excitation wavelength (nm); H = HOMO; L = LUMO, f = Oscillator Strength						

3.2.3.3. Intramolecular proton transfer or charge transfer

We established the necessary condition of intramolecular hydrogen bonding strengthening at S_0 and S_1 states to understand the probe's behavior towards ESIPT process. $O_{34}H_{35}\cdots N_{22}$ and $O_{36}H_{37}\cdots N_{38}$, two types of asymmetrical intramolecular hydrogen bonding (IraHB) with short interaction distance and angle, were present in probe **3 (Figure 3.27a)**. Further, $O_{34}H_{35}\cdots N_{22}$ IraHB exhibited a 201 cm^{-1} redshift from 3175 cm^{-1} to 2974 cm^{-1}; while $O_{36}H_{37}\cdots N_{38}$ IraHB exhibited 10 cm^{-1} redshifts to 3169 cm^{-1}, on photoexcitation to S_1 state **(Figure 3.27b)**. It was also mentioned that significant molecular planarity is attained with a reduction in the Schiff base unit's dihedral angle from 146.140 to 179.820 at the S_1 state.

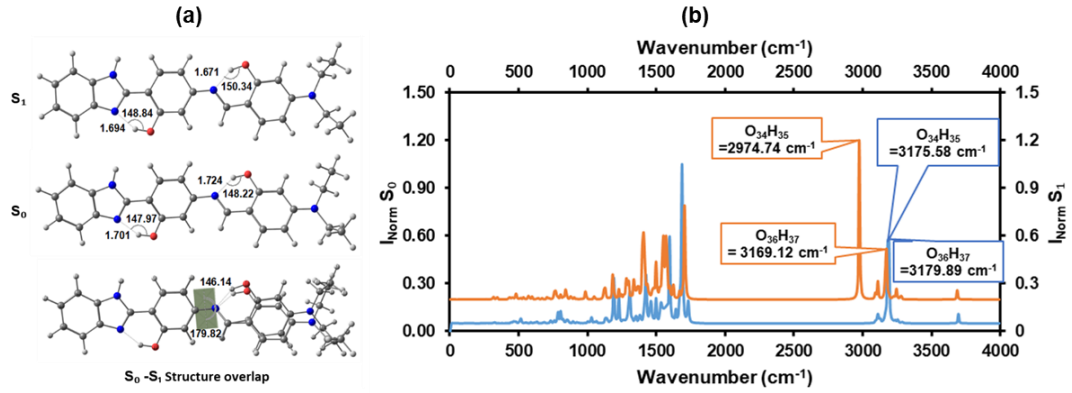

Figure 3.27: (a) Optimized structure of probe 3; (b) FTIR spectra of probe 3, respectively at S_0 and S_1.

These factors favor the excited state intramolecular proton transfer phenomenon. Therefore, PECs were constructed **(Figure 3.28)** with respect to proton transfer (PT) coordinate *via* single proton transfer (SPT) and double proton transfer (DPT) i.e. probe **3**→SPT1→DPT (Path I) and probe **3**→SPT2→DPT (Path II) **(Scheme 3.6)**. According to the PECs, the enol form of probe **3**-A is only a stable conformer in the S_0 and S_1 state and establish a relationship of probe **3** (0 kcalmol^{-1}) > SPT1 (1.44 kcalmol^{-1}) > SPT2 (6.18 kcalmol^{-1}) > DPT (7.04 kcalmol^{-1}) in S_0 state and probe **3** (69.56 kcalmol^{-1}) < SPT1 (70.66 kcalmol^{-1}) < SPT2 (75.28 kcalmol^{-1}) < DPT (75.51 kcalmol^{-1}) in the S_1 state **(Figure 3.29)**. A similar observation was noted for probe **3**-B configuration. Although FTIR analysis favors the occurrence of ESIPT process, however, the energy relationship rejects the existence of ESIPT process for probe **3**. The non-existence of ESIPT process was measured due to increase of atomic contribution of O_{34} and H_{35} (0.22 % □ 1.05 % for O_{34} and 0.008 % □ 0.07 % for H_{35}), and decrease of N_{22} (10.06 5 □ 6.51 %) on HOMO→LUMO transition, that do not allow N_{22} to hold H_{35} efficiently.

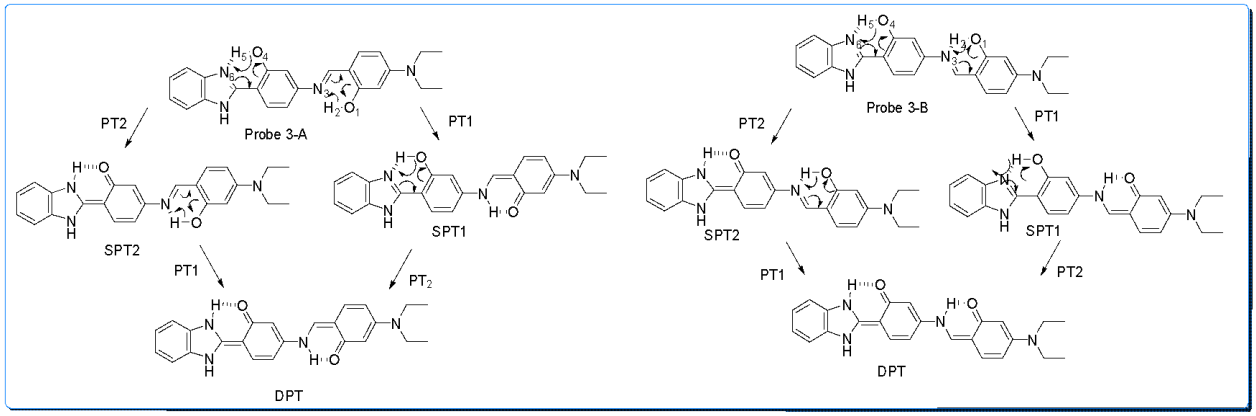

Scheme 3.6: Possible pathways of proton transfer.

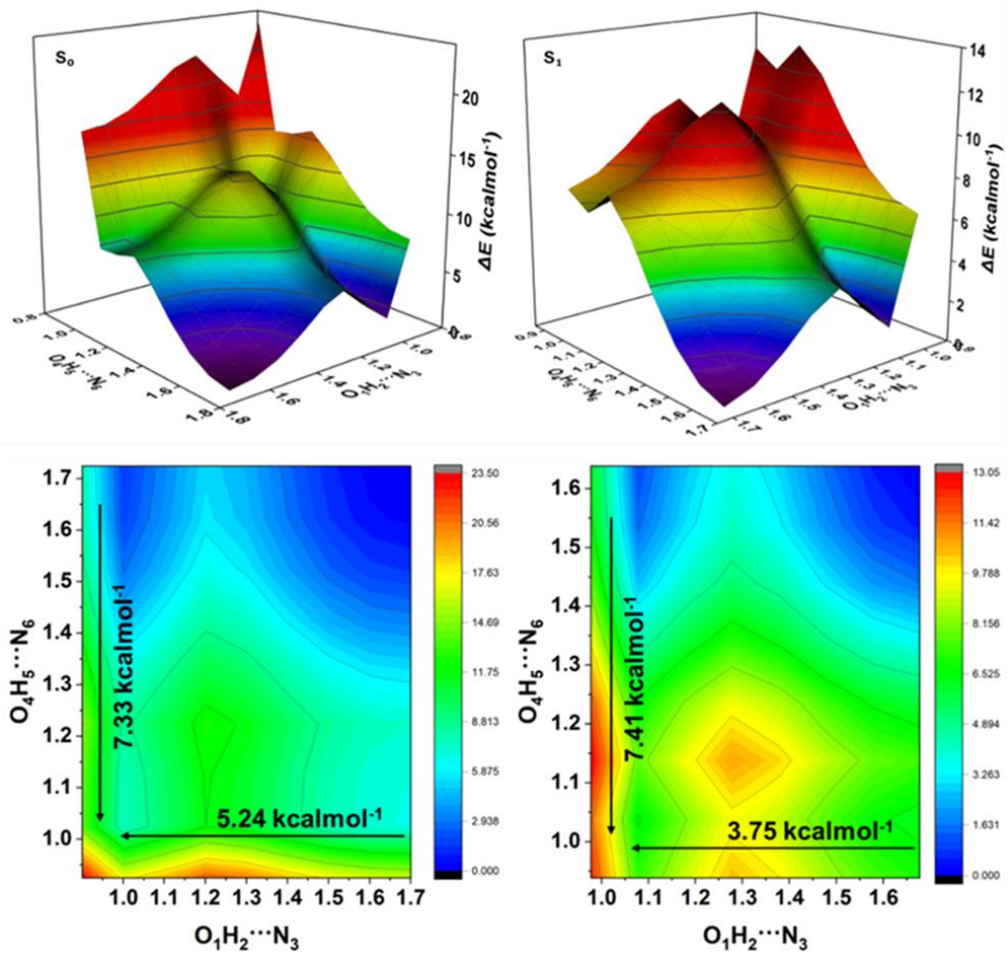

Figure 3.28: Potential energy curves the proton transfer for probe 3-A at S_0 and S_1.

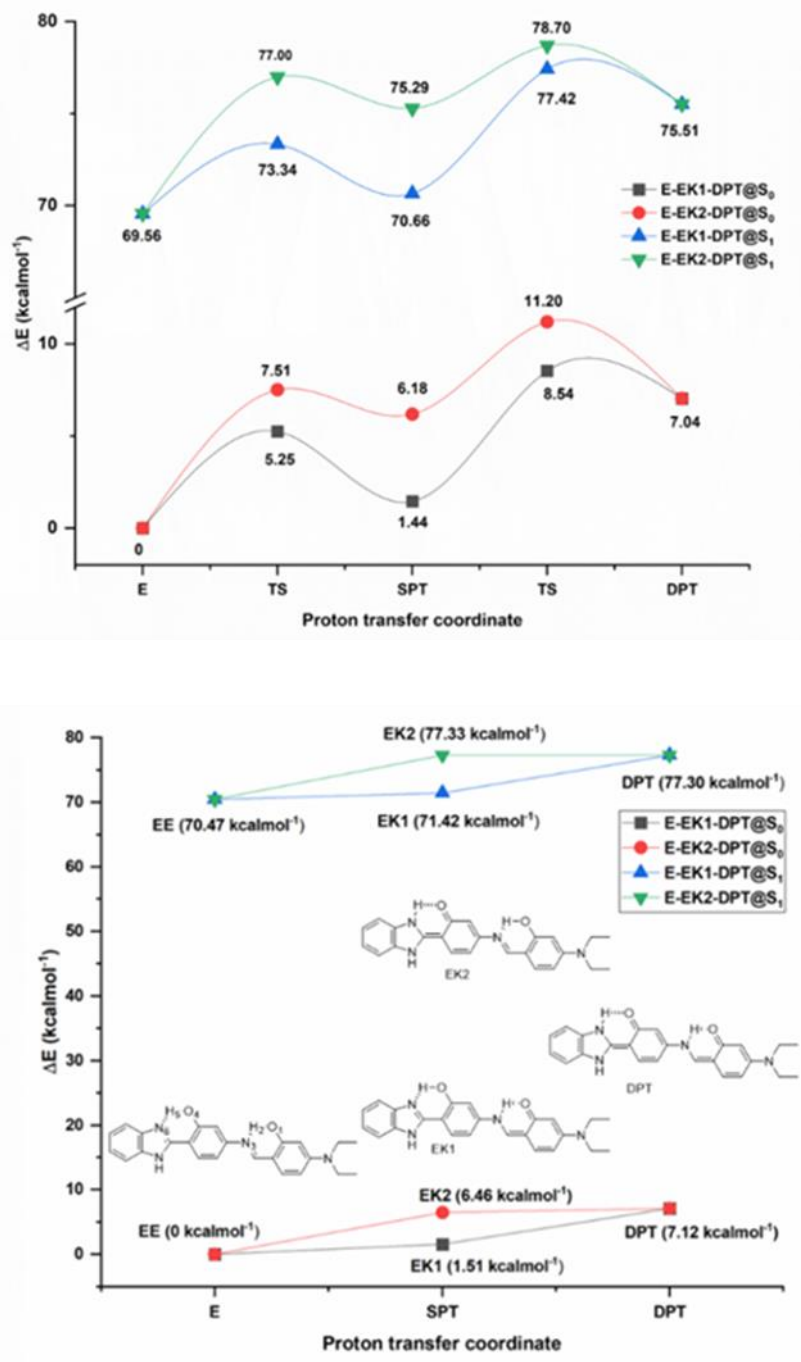

Figure 3.29: Energy profile of proton transfer for probe 3.

As discussed in the previous section, probe **3** showed intramolecular charge transfer characteristics due to presence of diethylamino unit. This process could occur *via* planar intramolecular charge transfer or twisted intramolecular charge transfer. Therefore, the

possibility of twisted intramolecular proton transfer process was also determined through PECs *via* torsional rotation at C-N rotation (at diethylamino unit connections) **(Figure 3.30a)** and C-C rotation (at benzimidazole unit connection) **(Figure 3.30b)**. The twisted forms have high energy and require energy as barrier for conversion and thus, allow planar intramolecular charge transfer process only.

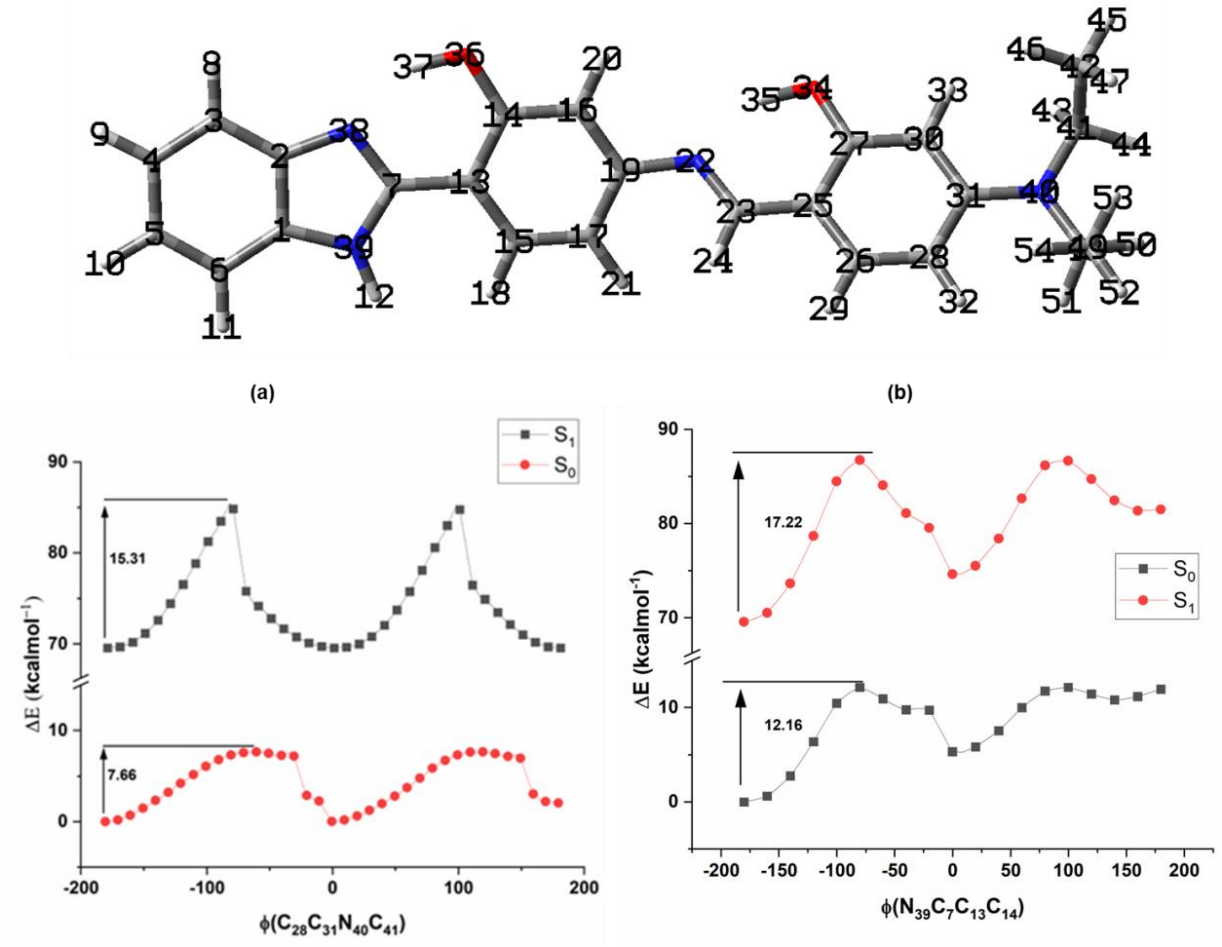

Figure 3.30: Energy barrier diagram of probe 3 (a) at diethylamino unit and (b) at benzimidazole unit.

3.2.3.4. Sensing ability of probe 3 towards metal ions

The sensing properties of probe **3** were performed in many solvents like CH_3CN, CH_3OH and CH_3CN/H_2O as well as CH_3OH/H_2O mixtures but maximum selectivity and sensitivity were observed in the case of H_2O: CH_3OH (1:1, v/v) solvent. So, preliminary study was accomplished in solution phase using H_2O: CH_3OH (1:1, v/v) solvent. The cation binding affinity of probe **3**

was investigated in the presence and absence of different metal ions such as Na^+, K^+, Mg^{2+}, Ca^{2+}, Ba^{2+}, Al^{3+}, Pb^{2+}, Co^{2+}, Ni^{2+}, Cu^{2+}, Cr^{3+}, Hg^{2+} and Zn^{2+} by recording the UV-visible spectra and fluorescence spectra at 20 µM concentration. Probe **3** showed absorption peak at 340 nm which upon interaction with Al^{3+} ion, the peak shifts to 355 nm **(Figure 3.31a)**. On the other hand, no significant change in the absorption spectrum was observed on addition of other metal ions. To further investigate the binding properties, a solution of probe **3** (20 µM) was titrated with Al^{3+} ion in H_2O: CH_3OH (1:1, v/v) solvent. With the incremental addition of Al^{3+} ion (0-133 µM) to probe **3**, the absorption band intensity at 330 nm gradually decreased and a new absorption band at 355 nm with a bathochromic shift progressively formed **(Figure 3.31b)**.

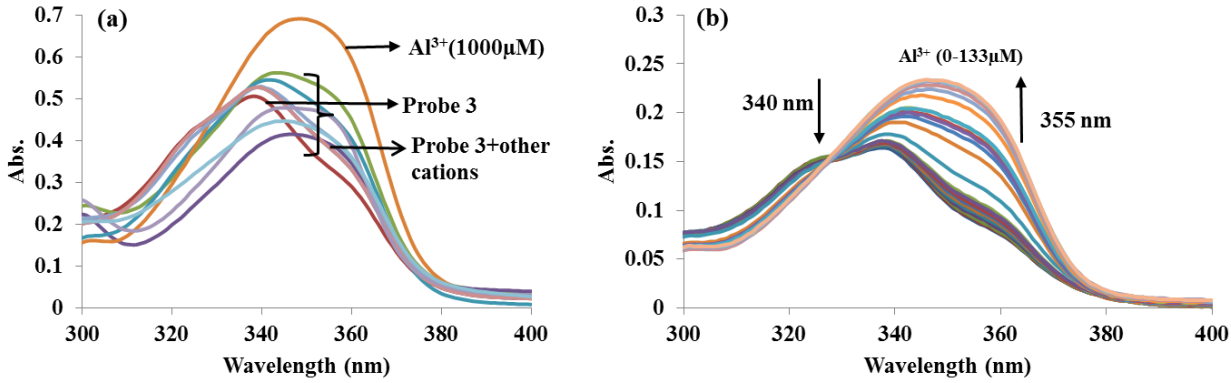

Figure 3.31: Absorption spectra of probe 3 (20µM), H_2O: CH_3OH (1:1, [v/v]), (a) in presence of different metal ions (20 µM) and (b) with incremental addition of 0- 133 µM of Al^{3+} ion.

In order to inspect the fluorescence behavior of probe **3** towards the above examined metal ions, the fluorescence spectra of probe **3** (20 µM) was recorded on photoexcitation at 340 nm in H_2O: CH_3OH (1:1, v/v) solvent. Probe **3** showed weak emission at 385 nm but the emission intensity increased after the addition of Al^{3+} ions to the solution **(Figure 3.32a)**. The addition of other metal ions does not disturb the fluorescence spectrum of probe **3**. In the case of probe **3**.Al^{3+} complex, the fluorescence intensity was increased by 3-folds at 385 nm. The fluorescence enhancement of probe **3** by Al^{3+} ions can be due to strong binding of Al^{3+} ion with probe **3** and that would impose rigidity and hence, this could lead to decrease in radioactive decay constant of the excited state probe **3**.

The steady variation in fluorescence response of probe **3**.Al^{3+} complex was recorded by spectrofluorimetric titration. The incremental addition of Al^{3+} ions (0-117 µM) into probe **3** leads

to change in emission intensity **(Figure 3.32b)**. The limit of detection (LOD) and the limit of quantification (LOQ) for Al^{3+} ion using probe **3** was calculated through the calibration curve achieved from fluorescence titration. The LOD and LOQ for Al^{3+} ions by using probe **3** were found to be 39 nM and 1.32×10^{-7} M, respectively.

The stoichiometry of probe **3** and Al^{3+} complex was determined by Job's plot method. It shows that the maximum fluorescence intensity was observed at 0.5 mole fractions that confirmed the formation of 1: 1 complex of probe **3** with Al^{3+} **(Figure A13a)**. The binding constant of probe **3** with Al^{3+} ion was calculated by using Benesi-Hildebrand equation. From the fluorescence titration data, the plot of 1/ $[I-I_0]$ v/s 1/ $[Al^{3+}]$ is linear with $R^2 = 0.9219$ and the binding constant was 4.9×10^3 M^{-1}. Further, the stability of probe **3** and Al^{3+} complex was tested in the presence of other metal ions. The results showed that the probe **3** and Al^{3+} ion complex is stable and no other metal ion interfere in the complex.

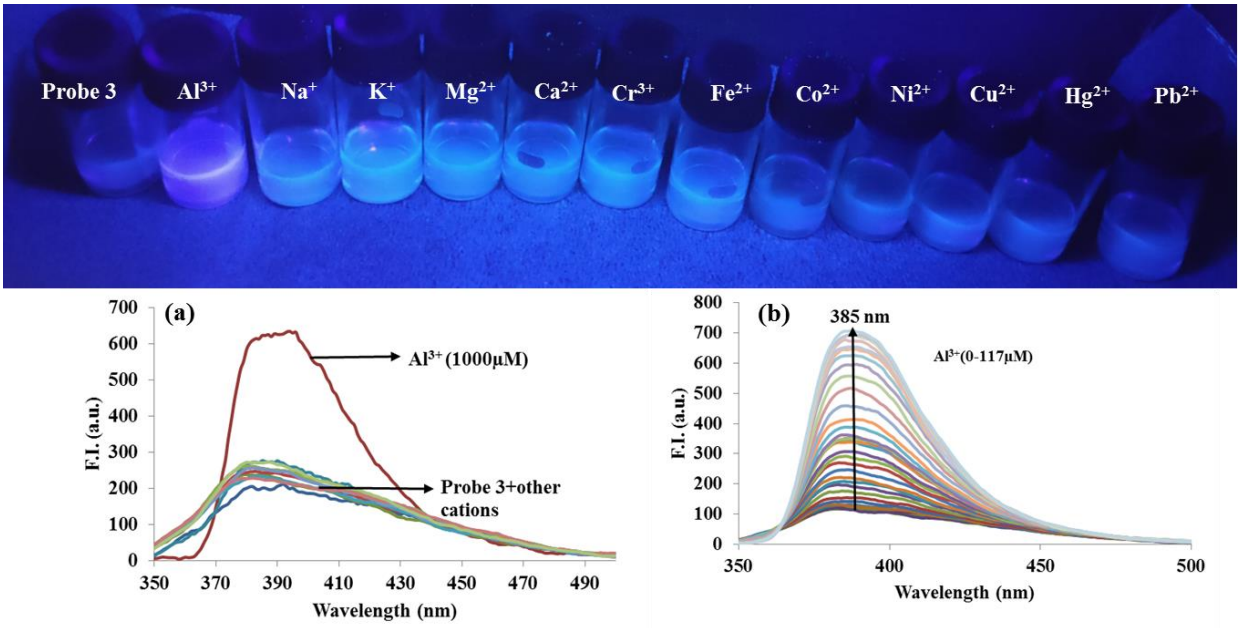

Figure 3.32: Effect of different metal ions on solution of probe 3 (20 µM, H_2O-CH_3OH, (1:1, [v/v]) under UV light, emission spectra of probe 3 (20 µM), H_2O: CH_3OH (1:1, [v/v]), (a) in presence of different metal ions (1000 µM), and (b) with incremental addition of 0-117 µM of Al^{3+} ion.

3.2.3.5. Spectral characteristics of probe 3 towards anions

The anion recognition study of probe **3** (20 µM) was investigated by monitoring the UV-vis absorption spectra and fluorescence spectra in H_2O: CH_3OH (1:1, v/v) upon addition of various

anions at 20 µM concentration. Probe **3** showed intense absorption peak centered at 340 nm. Among various anions examined, probe **3** showed selectivity only for HSO_4^- ion in H_2O: CH_3OH (1:1, v/v) at 20 µM. Upon the interaction of probe **3** with the various anions, only HSO_4^- showed bathochromic shift and shifted the absorption band at 355 nm whereas no meaningful change in the absorption spectra was observed on interaction with the other anions *viz.*, F^-, Cl^-, Br^-, I^-, $H_2PO_4^-$, NO_3^-, AcO^-, ClO^-, SO_4^{2-}, $P_2O_7^{4-}$, CN^-, SCN^- **(Figure 3.33a)**. With increase in the HSO_4^- concentration, gradually up to 120 µM, the absorption band at 355 nm was enhanced with a slight bathochromic shift **(Figure 3.33b)**.

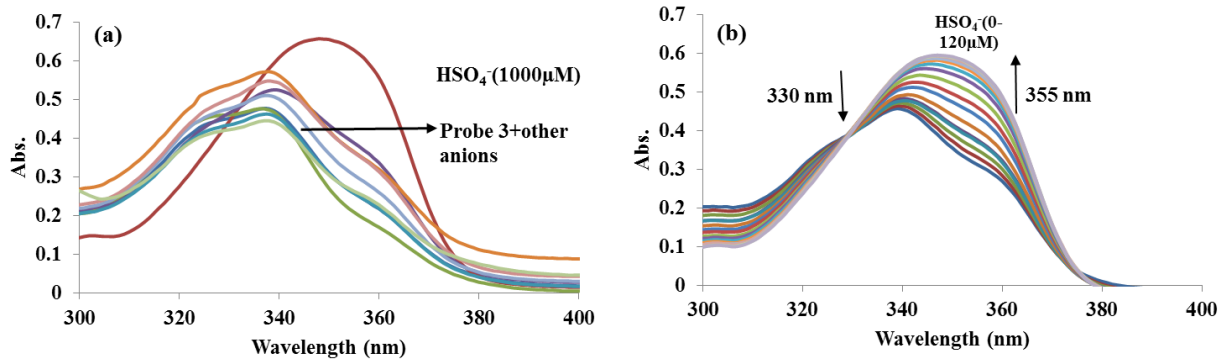

Figure 3.33: Absorption spectra of probe 3 (20 µM), H_2O:CH_3OH (1:1, [v/v]), (a) in presence of different anions (1000 µM) and (b) with incremental addition of 0-120 µM of HSO_4^- ion.

To observe the fluorescence properties of probe **3** towards HSO_4^- ion, the fluorescence spectra of probe **3** was taken in H_2O: CH_3OH (1:1, v/v) at 20 µM concentration. The fluorescence spectra were taken by excitation at 340 nm. Among the various anions, probe **3** showed selectivity towards HSO_4^- anion **(Figure 3.34a)**. Probe **3** showed enhancement in fluorescence intensity after the interaction with HSO_4^- anion at 390 nm whereas all other anions showed negligible change in fluorescence intensity of probe **3**. The increase in fluorescence intensity can be due to the formation of more widespread π-conjugation system in probe **3** after binding with HSO_4^- ion. A plateau in the fluorescence spectra was observed after the addition of 100 µM of HSO_4^- ions **(Figure 3.34b)**. As the change in emission intensity was quite noteworthy so it may be considered that the fluorescence was firstly in "switched off" state for free probe **3** and then the "switched on" after the addition of HSO_4^- ions. To further test that whether probe **3** can selectively sense HSO_4^- ion even in the presence of other anions, competitive experiment was

carried out. Probe **3** was treated with other anions in the presence of HSO_4^- ion. The results indicated that the other ions do not lead to any significant change in the fluorescence intensity and HSO_4^- ion showed the same spectral change even in the presence of other competitive anions. These results directed the selectivity of probe **3** towards HSO_4^- ion and not affected by the presence other anions.

The detection limit of probe **3** towards HSO_4^- ion was calculated based on fluorescence titration method. Under the optimal conditions, the calibration curve was drawn for the determination of HSO_4^- ion. The lowest detection limit for HSO_4^- ion was found out to be 23×10^{-9} M. Also, the binding constant (k_a) for probe **3** and HSO_4^- ion was calculated by using Benesi-Hildebrand equation. The measured fluorescence intensity $1/ [I-I_0]$ was varied as a function of $1/ [HSO_4^-]$ in a linear relationship with $R^2 = 0.9838$, indicating the 1:1 stoichiometry between probe **3** and HSO_4^- ion. From the fluorescence titration data, the binding constant was found out to be 1.0×10^4 M^{-1}. To determine the stoichiometry between probe **3** and HSO_4^- ion, Job's plot analyses was done. The maximum fluorescence intensity was found out to be at 0.5, indicating the formation of 1:1 stoichiometry **(Figure A13b)**.

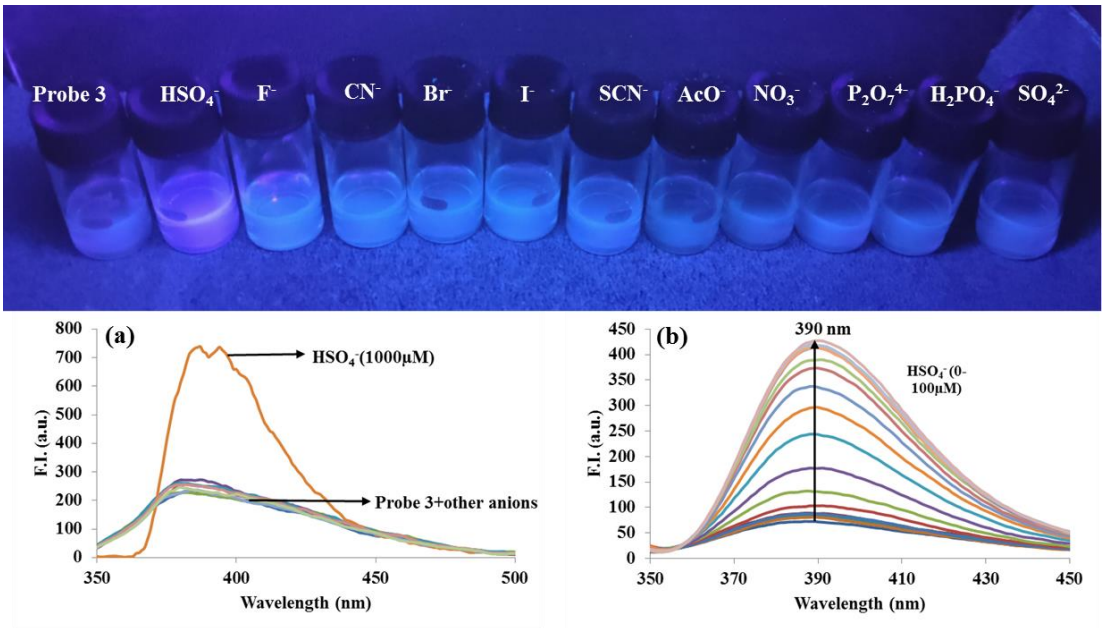

Figure 3.34: Effect of different anions on solution of probe 3 (20 µM, H_2O-CH_3OH, (1:1, [v/v]) under UV light, emission spectra of probe 3 (20 µM), H_2O:CH_3OH (1:1, [v/v]), (a) in presence of different anions (1000 µM); and (b) with incremental addition of 0-100 µM of HSO_4^- ion.

3.2.3.6. Effect of pH on probe 3

In order to check the practical applicability of probe **3** in wide pH range, pH titrations of probe **3** and its complex with the Al^{3+} and HSO_4^- ions were performed. From the acid-base titration, it is clear that probe **3** was stable in the pH range from 3.5-11. The stability of probe **3** in the pH range 3-11 establishes its benefit for rapid monitoring in environmental and biological backgrounds. The complexes of probe **3** with Al^{3+} as well as HSO_4^- ions were also stable in pH range from 7-9, so the detection of these ions using probe **3** could be well performed in this pH range **(Figure 3.35)**.

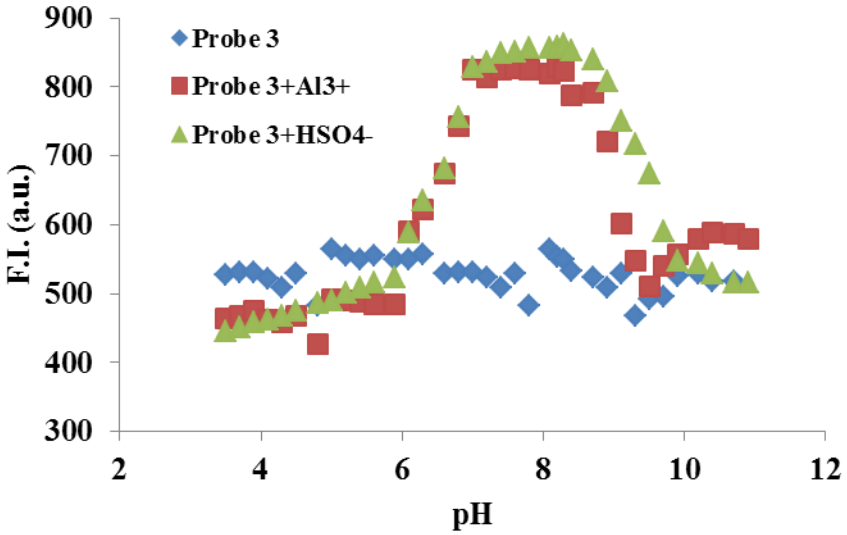

Figure 3.35: Effect of pH on probe 3 in H_2O-CH_3OH, (1:1, [v/v]) at λ_{em} = 390 nm.

Furthermore, it is possible to comprehend that the probe **3** could adopt the protonation and deprotonation in acidic and basic medium, respectively. Probe **3** contains three fundamental basic sites in the form of benzimidazole unit, imine unit, and NEt_2 unit for protonation process and phenolic units for deprotonation. To further understand the protonation process, all feasible conformations were optimized (**Figure 3.36**).

The relative energies of these configurations confirmed that protonation occurs preferentially at the imine center (N=C) position due to its low energy and high stability. These results also signify that HSO_4^- ions interacted through the imine center and phenolic protons through intramolecular bonding shown in **Scheme 3.7**.

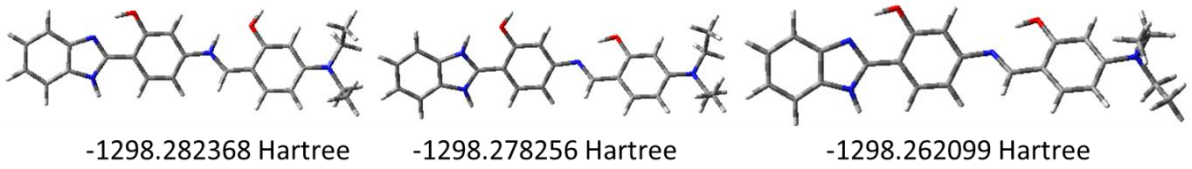

Figure 3.36: Possible optimized structure of probe 3 in low pH medium.

3.2.3.7. ^{1}H NMR of probe 3 with Al^{3+} and HSO_4^- ions

In order to investigate the binding behavior of probe **3** towards Al^{3+} and HSO_4^- ions, we have performed the ^{1}H NMR titrations in CD_3OD. Upon the addition of 1.0 eq. of Al^{3+} to the solution of probe **3** the imine peak at δ 9.36 ppm upfield shiftedto δ 8.40 ppm, supporting the binding of Al^{3+} through Schiff base site. The aromatic protons also showed downfield shift upon addition of 1.0 eq. of Al^{3+} ion with slight splitting of the signals. The doublets at 7.36 and 7.25 ppm due to respective H_b and H_c protons splits into double doublets at 7.41 and 7.21 ppm after the addition of 1.0 eq. Al^{3+} ions. The ^{1}H NMR titrations clearly showed that fluorescence enhancement of probe **3** is due to the binding of Al^{3+} through the Schiff base unit of the molecule **(Scheme 3.7)**. Probe **3**.Al^{3+} complex formation was confirmed through the HRMS analysis which shows peak at 458.9199. On the other hand, the addition of HSO_4^- ion showed completely different peak profile. The signals due to the phenolic hydrogen (-OH) were not observed in the spectra of free probe **3.** Upon the addition of HSO_4^- to probe **3** no change was observed in the signals and only slight splitting of aromatic protons H_b at 7.36 and H_c at 7.25 ppm were observed, indicating the hydrogen bonding between HSO_4^- and probe **3 (Figure 3.37)**. The HRMS peak at 536.1657 confirms the formation of probe **3** and HSO_4^- complex.

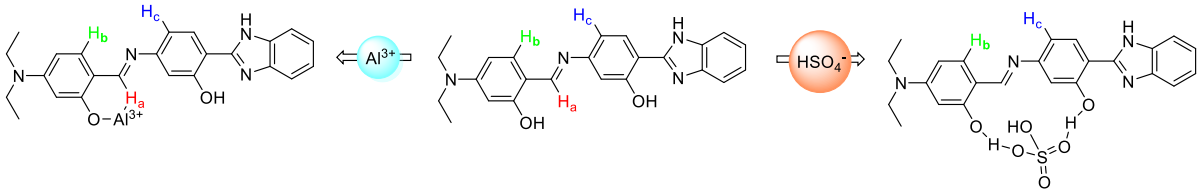

Scheme 3.7: Plausible binding mechanism for probe 3 and Al^{3+} and HSO_4^- ions.

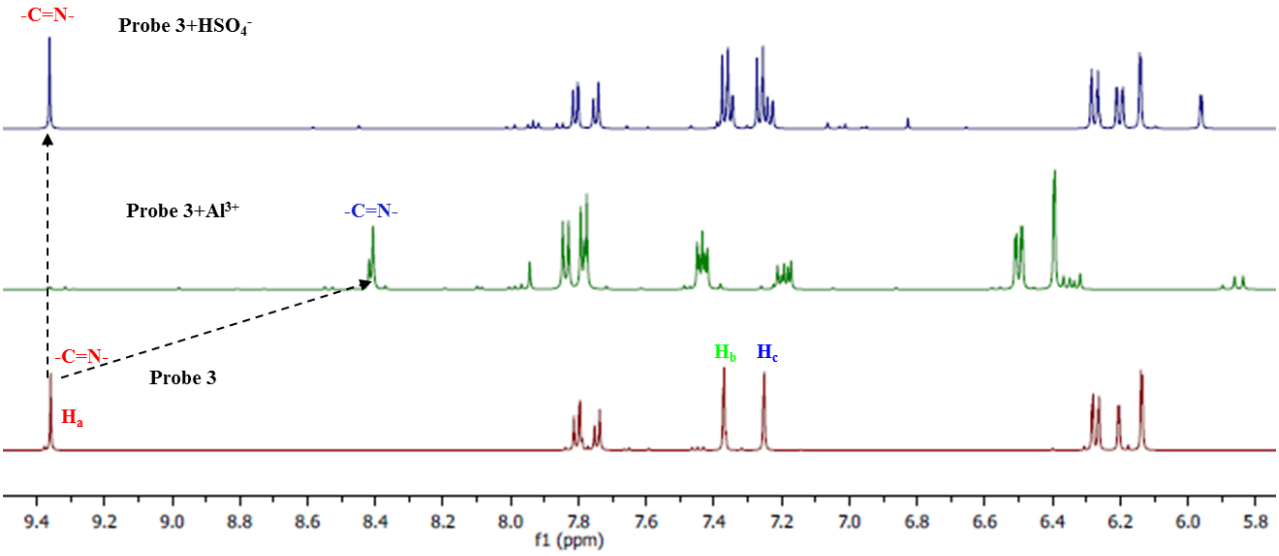

Figure 3.37: ^{1}H NMR spectra of probe 3 in the presence of Al^{3+} and HSO_4^- ions.

3.2.3.8. Time-correlated single photon counting (TCSPC) study

The results of fluorescence decay measurement using the TCSPC study have confirmed that the fluorescence is enhanced upon interaction with metal ions **(Figure 3.38)**. The bi-exponential function provides the best fit to decay behavior of probe **3** and its complexes. Probe **3** has two components with lifetime values of 0.67 ns and 1.47 ns and population of both the components was 0.98 % and 99.02%, respectively. The average life time for probe **3** was found to be 1.45 ns. Upon adding Al^{3+} to the solution of probe **3**, two components were obtained with lifetime of 0.66 and 1.86 ns with a population of 92.83% and 7.17%, respectively. The average lifetime was calculated to be 0.69 ns. Similarly, after adding HSO_4^-, the average lifetime was 0.59 ns. The decrease in average life time of probe **3** after binding with Al^{3+} and HSO_4^- ions suggests the dynamic quenching behavior.

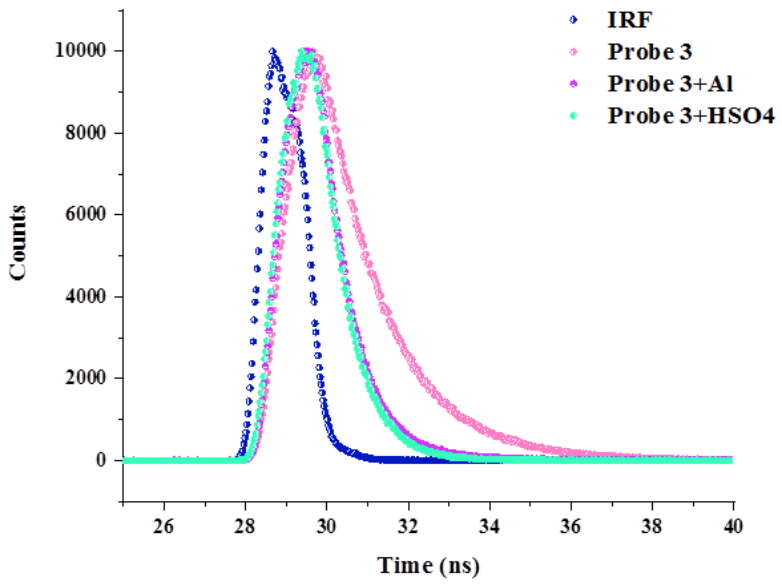

Figure 3.38: Time resolved fluorescence decay of probe 3 and its complexes with Al^{3+} and HSO_4^- ions at λ_{em}= 385 nm in H_2O: CH_3OH (1:1, [v/v], 20 µM).

Table 3.8: Fluorescence lifetime measurements for probe 3 and complexes in H_2O: CH_3OH (1:1, [v/v], 20 µM).

H_2O:CH_3OH (1:1, [v/v])	τ_1 (ns)	τ_2 (ns)	α_1	α_2	χ^2	τ_{av} (ns)
Probe **3**	0.67	1.47	0.98	99.02	1.04	1.46
Probe **3**+Al^{3+}	0.66	1.86	92.83	7.17	1.17	0.69
Probe **3**+HSO_4^-	0.45	0.63	17.7	82.3	1.05	0.59

3.2.3.9. Application of probe 3 as molecular keypad lock

It is highly desirable to develop a reversible chemosensor with good selectivity and sensitivity for detecting diverse ions. A chemosensor's reversibility is also a crucial consideration for practical implication. Probe **3**'s reversible behavior towards Al^{3+} and HSO_4^- ions can be used to stimulate and construct Boolean logic gates that can perform molecular level mathematical calculations thoroughly. The chemical inputs received from spectroscopic results constitute the

basis of molecular logic gate development. Table **3.9** summarizes the spectroscopic results of probe **3** with Al^{3+} and HSO_4^- ions.

The results of the emission measurements revealed that the developed chemosensor is capable of simulating a large variety of logic gate assembly operations involving two chemical inputs: probe **3** (In_1), Al^{3+}/ HSO_4^- (In_2). One output Y1 was produced, which denoted probe **3**'s emission peak at 390 nm. From the above results, it can be seen that adding Al^{3+} and HSO_4^- ions to probe **3**, would generate a peak at 390 nm. Probe **3** produced a molecular keypad lock involving two inputs: Probe **3** as input 1, Al^{3+}/ HSO_4^- as input 2. The emission band appeared at 390 nm after the addition of Al^{3+}/ HSO_4^- to probe **3 (Figure 3.39)**.

Two inputs, probe **3** and Al^{3+}/ HSO_4^-, are referred to as "A", and "S" correspondingly to simplify the sequence of the inputs as a secret code of molecular keypad locks. "R" is the output at 390 nm. The letter "O" denotes the keypad lock's "ON" state. The emission band at 390 nm was observed by the system on adding the input "S" to the input "A". As a result, the lock remained in the "ON" position. The system created the keypad lock's secret code as "ASR", which could only be used to access the lock. Any other sequential arrangements, on the other hand, could not lead to the simultaneous formation of the emission band at 390 nm. As a result, any other arrangement would be unable to unlock the molecular lock. Hence, the created technique may particularly useful for safeguarding molecular level information, as just the correct sequence of inputs is necessary to break the secret code.

Table 3.9: Truth table for logic gate with Al^{3+} and HSO_4^- ions as input and emission at 390 nm as output.

In_1 (Probe 3)	**In_2 (Al^{3+}/ HSO_4^-)**	**OUT Y1 (λ_{em} = 390 nm)**
0	0	0
1	0	0
0	1	0
1	1	1

Figure 3.39: Emission profile of probe 3 at 390 nm with different outputs.

3.2.3.10. Real field applications

3.2.3.10.1. Application in real field water samples

The presence of several interfering agents in real field water sample makes it challenging to detect the target analytes in real samples. As a result, the presence of Al^{3+} and HSO_4^- in different real field samples was tested using developed chemosensor probe **3**, as Al^{3+} and HSO_4^- released from various industrial sectors may contaminate natural resources. In this case, simulated contaminated samples were made by externally spiking known Al^{3+} and HSO_4^- concentrations in various real water samples like river water (from Bhakra canal), RO water (collected from department) and tap water (collected from lab). The water samples were then spiked externally with different concentrations of Al^{3+} and HSO_4^- like 10, 20, 40, 60 and 80 µM by standard addition method. The water samples were then exposed to 20 µM of probe **3** in H_2O: CH_3OH (1:1, [v/v]) and the emission intensity was measured at 390 nm. The results demonstrated that probe **3** has the capability of monitoring the level of Al^{3+} and HSO_4^- in a wide range of water samples. The samples were given for atomic absorption spectroscopy (AAS) and the results were in coherence with the amount detected. Furthermore, the satisfied Al^{3+} **(Table 3.10)** and HSO_4^- **(Table 3.11)** recoveries obtained from variable concentration of different real field water samples indicating the practical applicability of probe **3** in real world scenarios.

Table 3.10: The percentage recovery of Al^{3+} in real field water samples.

Water Samples	Spiked amount (µM)	Recovered amount (µM)	Recovery (%)
River water	10	9.7	97
	20	19.4	97

	40	40.8	102
	60	61.5	102.5
RO water	10	10.1	101
	20	20.3	101.5
	40	40.1	100.1
	60	59.8	99.6
Tap water	10	10.7	107
	20	20.1	100.5
	40	40.9	102.3
	60	60.1	100.2

Table 3.11: The percentage recovery of HSO_4^- in real field water samples.

Water Samples	Spiked amount (µM)	Recovered amount (µM)	Recovery (%)
River water	10	9.9	99
	20	18.2	91
	40	40.5	101.3
	60	62.3	103.8
RO water	10	10.3	103
	20	20.7	103.5
	40	41.5	103.8
	60	60.6	101
Tap water	10	11.4	114
	20	19.8	99
	40	41.1	102.7
	60	60.3	100.5

3.2.4. Conclusion

In the present work, we developed a Schiff base chemosensor probe **3** that can simultaneously detect Al^{3+} and HSO_4^- ions with high selectivity and sensitivity in aqueous medium. The lowest detection limits for Al^{3+} and HSO_4^- ions were found to be 39 nM and 23 nM, respectively. Furthermore, the intramolecular hydrogen bonding in water can be used to produce strong fluorescence response on binding to organic compounds. Probe **3** binds with Al^{3+} ions through imine N and O of hydroxyl to form strong complex and the HSO_4^- ion binds through hydrogen bonding mechanism. Probe **3** can be used for fabricating molecular keypad lock. Only the correct password will result in an absorption band at two different wavelengths of 355 nm and 330 nm, allowing the molecular keypad lock to open, whilst incorrect password will result in an alert signal signaling, a password mismatch. As a result, this molecular keypad lock has the ability to safeguard sensitive documents at molecular level; however it would require an authentic user to

commence the procedure. Probe **3** was used to detect Al^{3+} and HSO_4^- ions in real field water samples.

3.3.

Effect of conjugation on excited state intramolecular proton transfer process in hydroxy aryl benzimidazole based Schiff base

3.3.1. Abstract

In this section, the effect of conjugation on photophysical behavior of benzimidazole based Schiff base **(3)** was studied. Two ESIPT sites were available in the molecule and we want to check the effect of conjugation on the ESIPT phenomenon between Schiff base unit and hydroxy unit. With the increase in the conjugation the Intramolecular charge transfer (ICT) and Aggregation induced emission (AIE) phenomenon can be induced. The delocalized electronic structure of highly conjugated probe enables the strong absorption and emission properties along with the increased sensitivity towards ions. Hydroxy naphthaldehyde is very adaptable fluorescent building block for the design and development of a wide range of sensors for variety of analytes. Further, due to increase in the bulkiness the intramolecular rotations in a molecule can be restricted. Herein, a hydroxy naphthaldehyde-benzimidazole based Schiff base (probe **4**) was synthesized successfully and characterized using ^{1}H, ^{13}C NMR and HRMS spectroscopy. Probe **4** demonstrated fluorescence "*turn-on*" with comparatively high selectivity in the presence of CN^- ions as compared to other anions in H_2O:CH_3CN (1:9, v/v). The lowest detection limit (LOD) for CN^- ions using probe **4** was calculated to be 1.9×10^{-7} M. Job's plot method was used to determine the binding stoichiometry of probe **4** with CN^- ions which was found to be 1:1. Additionally, probe **4** exhibits intramolecular charge transfer (ICT) and aggregation induced emission (AIE) phenomenon.

3.3.2. Experimental section

3.3.2.1. Synthesis of probe 4

The compound **1a** and 2-hydroxy-1-naphthaldehyde were stirred at 70 °C in ethanol for 3 h **(Scheme 3.8)**. The reaction mixture was cooled on completion of reaction and the solid formed was filtered and washed with ethanol to obtain orange coloured solid of probe **4** in 85% yield. m. p. 270-275 °C; ^{1}H NMR (DMSO-d_6, 400 MHz): δ (ppm) 8.95 (s, 1H, -C=N), 8.44-8.43 (m, 1H), 8.28 (d, 2H, J = 8 Hz), 8.13 (d, 1H, J = 8 Hz), 8.11 (s, 1H), 8.09 (d, 1H, J = 4 Hz), 8.00 (d, 1H, J = 8 Hz), 7.90-7.86 (m, 2H), 7.81-7.75 (m, 2H), 7.60-7.59 (m, 2H) **(Figure A14)**. ^{13}C NMR

(DMSO-d_6, 100 MHz): δ (ppm) 173.1, 165.4, 157.9, 155.4, 151.9, 147.1, 138.4, 134.5, 133.7, 130.3, 129.6, 128.8, 127.1, 125.6, 124.3, 123.2, 122.5, 121.0, 116.9, 112.5, 109.1, 108.6 **(Figure A15)**. **HRMS** (ESI-TOF): (m/z) $[M+H]^+$ calcd for $C_{24}H_{17}N_3O_2$: 380.1321, found: 380.0142 **(Figure A16)**.

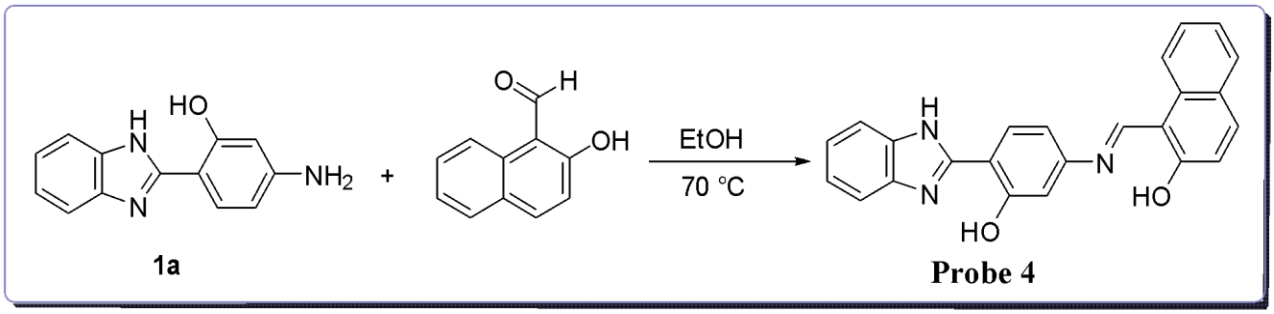

Scheme 3.8: Synthesis of probe 4.

3.3.3. Results and discussion

3.3.3.1. Photophysical properties of probe 4

Absorption and emission spectroscopy were used to examine the photophysical characteristics of probe **4**. Probe **4** (20 μM) showed an absorption peak at 335 nm and 340 nm in CH_3CN. After excitation at 340 nm, probe **4** displayed an emission band at 425 nm in CH_3CN with the Stokes shift of 85 nm. Furthermore, probe **4**'s absorption spectra showed negligible change in its maxima in most of the solvent but red shift from 340 nm to 355 nm was observed in the case of glycerol **(Figure 3.40a)**. The red shift in the absorption maxima in polar solvent can be attributed to the intramolecular charge transfer (ICT) phenomenon in the molecule from hydroxy naphthalene unit to benzimidazole unit. In low polarity solvents like cyclohexane, chloroform, and acetonitrile the emission maximum was found at 425 nm. In acetone and tetrahydrofuran, the emission maximum was red shifted to 440 nm. However, in highly polar solvents probe **4** showed large red shift to 610 nm and in glycerol the emission maximum was at 650 nm **(Figure 3.40b)**. Moreover, the Stokes shift value of probe **4** was also increased with the increase in the polarity of the solvent. The intramolecular charge transfer (ICT) process that takes place in the molecule between the hydroxy naphthalene unit and benzimidazole unit can be the cause of bathochromic shift in the emission intensity that is observed with solvent polarity.

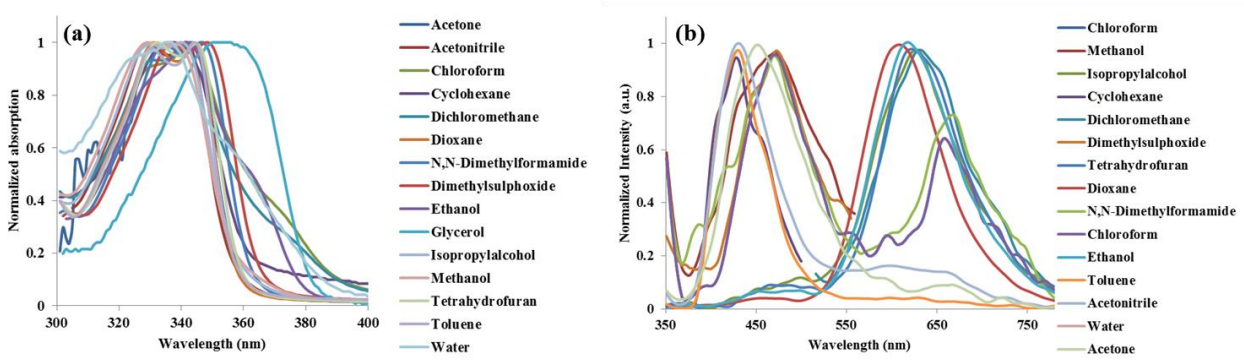

Figure 3.40: (a) Absorption and (b) emission spectra of probe 4 (20 µM) in different polarity solvents.

Table 3.12: Photophysical behaviour of probe 4 (20 µM).

S.No.	Solvent	λ_{max} (nm)	Molar absorptivity ε ($M^{-1}cm^{-1}$)	λ_{em} (nm)	Stokes shift Δν (cm^{-1})	Quantum yield (Φ)
1	Cyclohexane	335	11300	425	6320	0.44
2	CH_3CN	340	37650	425	5880	0.49
3	Toluene	345	35900	425	5460	0.51
4	$CHCl_3$	345	28600	425	5460	0.55
5	THF	345	35900	440	6260	0.53
6	Acetone	345	38500	440	6260	0.52
7	Dioxane	345	43200	460	7250	0.60
8	DMSO	350	41600	460	6830	0.48
9	DMF	350	41050	460	6830	0.53
10	IPA	345	37350	610	12600	0.52
11	Ethanol	345	38550	610	12600	0.51
12	Methanol	345	29350	610	12600	0.59
13	H_2O	335	8300	610	16340	0.65
14	Glycerol	355	6650	650	12790	0.59
Stokes shift = $1/(\lambda_{em} - \lambda_{max})$, Reference for QY = Quinine Sulphate						

3.3.3.2. Aggregation induced emission (AIE) study

Probe **4** has torsional flexibility with respect to C=N rotations at imine centre. So to confirm that experimentally we performed the Aggregation Induced Emission (AIE) studies. In order to study

the AIE property of probe **4**, absorption and emission spectra were recorded from CH_3CN to H_2O in varied ratio. Probe **4** (20 µM, CH_3CN) solution showed absorption band at 340 nm. The absorption of probe **4** at 340 nm decreased steadily with level-off tailing at 750 nm as the volume of water in the mixed solution of acetonitrile and water increased **(Figure 3.41a)**. The tailing of absorption spectra was proposed to be originated due to the formation of aggregates in the medium. The fluorescence of probe **4** enhanced at about 425 nm with the increasing content of H_2O in CH_3CN **(Figure 3.41b)**. Therefore, the emission at 425 nm in aggregated form would be due to restriction in intramolecular rotation around the C-N bond as the molecules are closely packed in aggregated form.

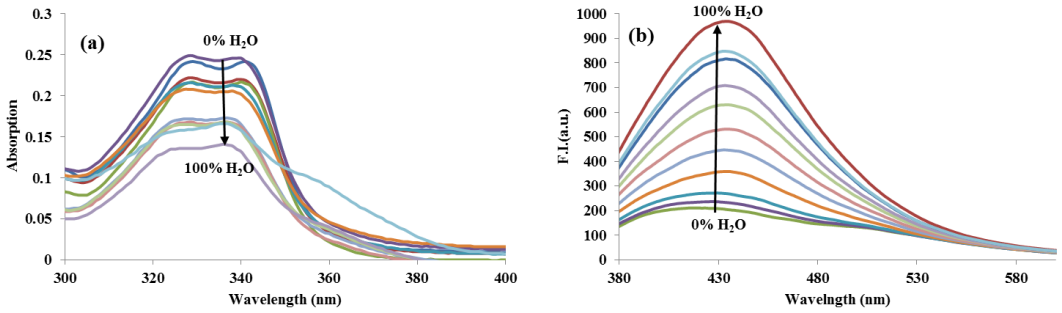

Figure 3.41: (a) Absorption spectra and (b) emission spectra of probe 4 upon increasing H_2O ratio in CH_3CN.

Further, DLS experiment supported aggregation formation and determined the size of probe **4** in different H_2O: CH_3CN ratios. In pure CH_3CN, the size was 20-150 nm with an average size of 50 nm with the PDI value of 0.4, while in 50% CH_3CN-H_2O; it was between 75-400 nm with average size of 150 nm and PDI value of 0.7. This hydrodynamic diameter increases to 1000 nm in pure H_2O with PDI value of 0.8 **(Figure 3.42)**. Similarly, FESEM images also showed aggregation upon increasing the H_2O ratio in CH_3CN **(Figure 3.43)**. The particle size of probe **4** in pure CH_3CN was found to be 44 nm and in 50% CH_3CN-H_2O the aggregates were formed with the average particle size of 95 nm while in pure H_2O the particle size of 150 nm. Both the DLS and FESEM results were in coherence.

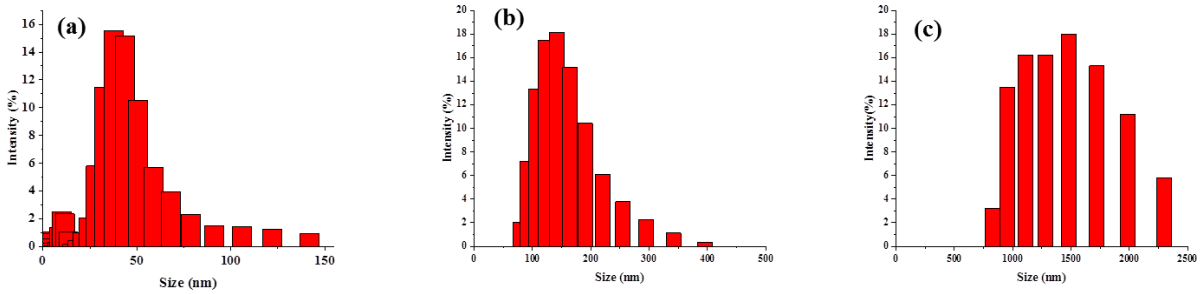

Figure 3.42: DLS of probe 4 (20 µM) in (a) CH_3CN, (b) 50% H_2O: CH_3CN and (c) H_2O.

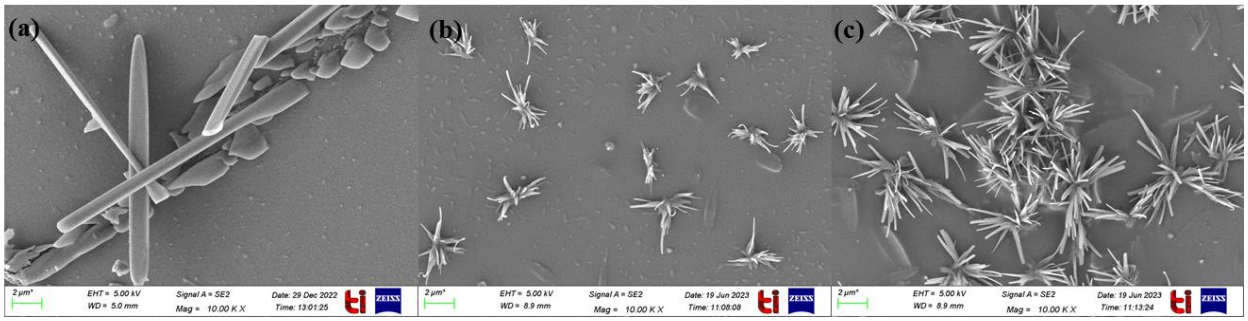

Figure 3.43: FESEM images of probe 4 in (a) CH_3CN, (b) 50% H_2O: CH_3CN and (c) H_2O.

3.3.3.3. Anion binding behavior of probe 4

One of the most important characteristics of a chemosensor is its selectivity for target ions, which improves the precision of analytical results. To identify the anions detected by probe **4** (20 µM) in H_2O:CH_3CN (1:9, v/v) solution, we chose common anions such as F^-, CN^-, Br^-, Cl^-, I^-, SCN^-, AcO^-, NO_3^-, $P_2O_7^{4-}$, $H_2PO_4^-$, HSO_4^- and SO_4^{2-} as their tetrabutylammonium salts. Probe **1** showed absorption maximum at 340 nm and the performance of the anions can be observed using the UV-Vis absorption spectra. The absorption spectra revealed that the other anions added under the same conditions did not result in an evident change in the absorption spectra, with the exception of CN^- ions **(Figure 3.44a)**. Using UV-Vis spectroscopy, a solution of probe **4** (20 µM) was titrated with CN^- ions in H_2O:CH_3CN (1:9, v/v). The absorption band at 350 nm was increased with the gradual addition of (0-30 µM) CN^- ions to the solution of probe **4 (Figure 3.44b)**.

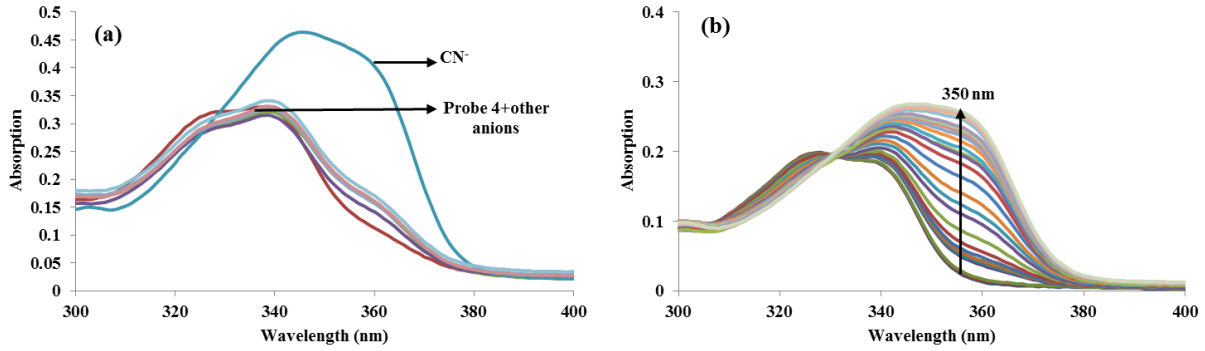

Figure 3.44: Absorption spectra of probe 4 (a) in the presence of different anions (1000 µM) and (b) with incremental addition of 0-30 µM) of CN^- ions in H_2O:CH_3CN (1:9, v/v).

The fluorescence spectra of probe **4** (20 µM) was recorded on excitation at 340 nm in H_2O:CH_3CN (1:9, v/v) solvent in order to study the fluorescence behavior of probe **4** towards previously examined anions. With the addition of CN^- ions to the solution of probe **4** the emission intensity at 425 nm was enhanced **(Figure 3.45a)**. The fluorescence spectra of probe **4** is unaffected by the presence of other anions. Gradual addition of (0-200 µM) CN^- ions to probe **4** (20 µM) caused a steady increase in the emission intensity, demonstrating turn-on fluorescent behavior **(Figure 3.45b)**. With the use of calibration curve generated by fluorescence titration, the limit of detection (LOD) for CN^- ion using probe **4** was calculated. The LOD for CN^- ions using probe **4** was found out to be 1.9×10^{-7} M.

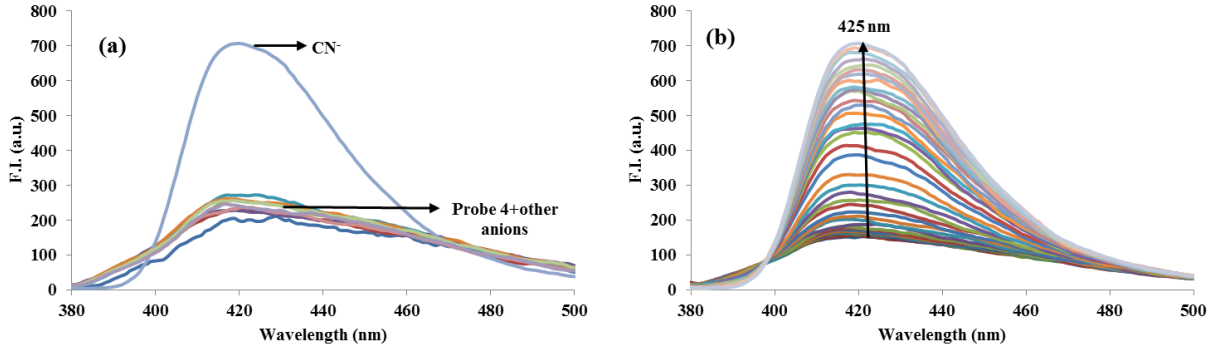

Figure 3.45: Emission spectra of probe 4 (a) in the presence of different anions (1000 µM) and (b) with incremental addition of 0-200 µM) of CN^- ions in H_2O:CH_3CN (1:9, v/v).

Using the job's plot technique, the stoichiometry of probe **4** and the CN^- ion was found. It demonstrated that the fluorescence intensity peaked at 0.5 mole fraction, indicating that probe **4** formed a 1:1 stoichiometry with CN^- ions **(Figure A18)**. The Benesi-Hildebrand equation was used to determine the binding constant between probe **4** and CN^- ions and the binding constant was calculated to be 1.8×10^4 M^{-1}. Additionally, in the presence of other anions, the selectivity of probe **4** towards CN^- ions was examined. The results demonstrated that there was no interference from any other anion in the complex of probe **4** and CN^- ions **(Figure 3.46)**.

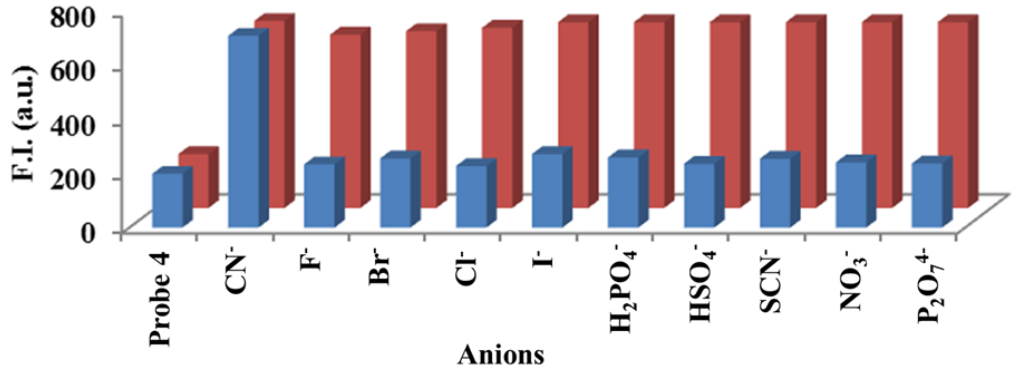

Figure 3.46: Relative emission intensity of probe 4 (20 µM) in H_2O: CH_3CN, 1:9 [v/v] (λ_{ex}= 340 nm) with different competing anions in the absence and presence of CN^- ions at λ_{em}= 425 nm, where blue bars represent the emission intensity change of probe 4 with different anions (1000 µM) and red bars represent probe 4+ CN^- in the presence of different relevant competing anions (1000 µM).

3.3.3.4. ^{1}H NMR Titration

Further, ^{1}H NMR titration experiment was performed in CD_3CN-d_3 to examine the sensing mechanism of probe **4** towards CN^- ions. The singlet at δ 8.39 ppm in ^{1}H NMR spectrum of probe **4** is attributed to the imine proton. The doublet at δ 7.05 ppm and a singlet at δ 7.03 ppm are due to the H_g and H_m protons respectively **(Figure 3.47)**. After the addition of 1.0 equiv. of CN^- ions the imine proton vanished and the signals due to H_g and H_m protons were shifted downfield. All the aromatic protons were also shifted downfield. A new signal at δ 6.17 ppm appeared which can be due to NH proton. All these spectral alterations confirmed that probe **4** and CN^- ions bind through Schiff base unit **(Scheme 3.9)**. Additionally, ^{1}H NMR results supported the 1:1 binding stoichiometry.

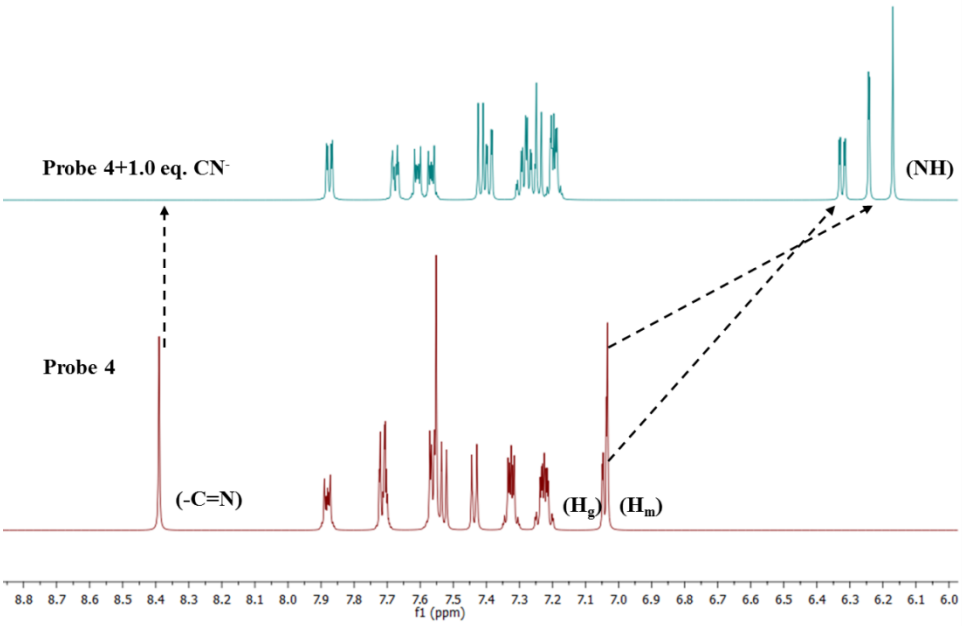

Figure 3.47: ^{1}H NMR titration of probe 4 with CN^- ions in CD_3CN-d_3.

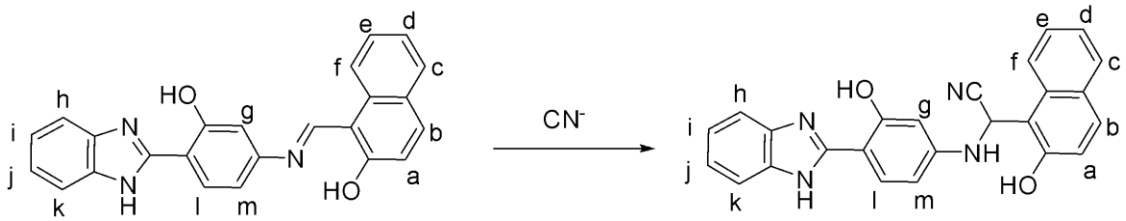

Scheme 3.9: Plausible binding mechanism for probe 4 and CN^- ions.

3.3.3.5. Time-correlated single photon counting (TCSPC) study

The fluorescence enhancement on binding with the anions has been supported by the results obtained from fluorescence decay measurement, using the TCSPC study **(Figure 3.48)**. The third exponential provides the best fit to the decay behavior of probe **4** and its CN^- ion complexes. Three components were identified by probe **4** having different lifetimes of 0.76 ns, 2.86 ns and 0.03 ns respectively. Each component's population was 28.75, 18.3 and 52.95%, respectively. Probe **4** has an average life time of 0.052 ns. When CN^- ions were added to probe **4**'s solution, three components with life time of 0.72 ns, 1.75 ns and 6.08 ns were obtained. The population of all the components was 19.51, 79.96 and 0.53%, respectively. The calculated average life time

was 1.38 ns. The increase in the average lifetime supports the fluorescence enhancement of probe **4** after the addition of CN^- ions.

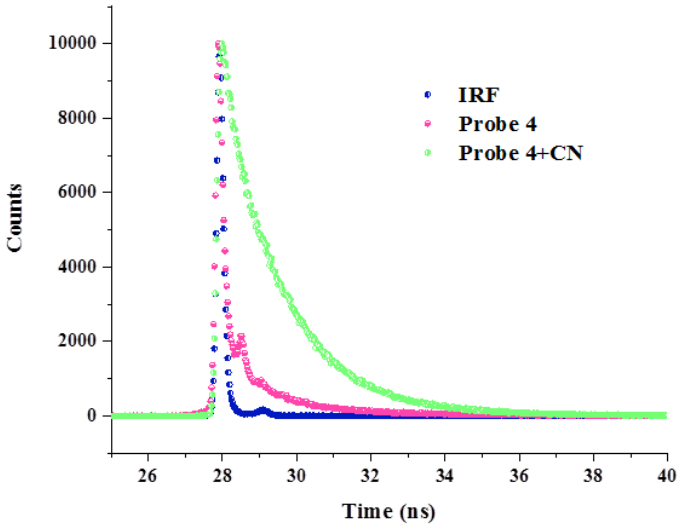

Figure 3.48: Time resolved fluorescence decay of probe 4 and its complexes with CN^- ions at λ_{em}= 425 nm in H_2O: CH_3CN (1:9, [v/v], 20 µM).

3.3.3.6. pH study

The charge distribution can be affected by the pH of the solution, which will change the probe **4**'s absorption and emission characteristics. As a result, we investigated the impact of pH on the fluorescent intensity of probe **4** and its complex with CN^- in H_2O: CH_3CN (1:9, [v/v]). The probe **4** was found stable in the pH range of 6.9-10.3. The absorption band at 340 nm increased as the pH of the solution was changed from 7.4- 2.8. Also in alkaline medium (7.4-11.1), the absorption intensity was not much changed. In the emission spectra as the pH of the solution of probe **4** was changed from 7.4-2.9 in the intensity at 425 nm was increased whereas in the alkaline medium the emission intensity at 425 nm showed negligible change. Moreover the complex of probe **4** and CN^- ions was stable in the pH range of 5.4-11.1 but in the acidic medium the fluorescence intensity decreases which could be due to the deprotonation of probe **4** and CN^- complex **(Figure 3.49)**.

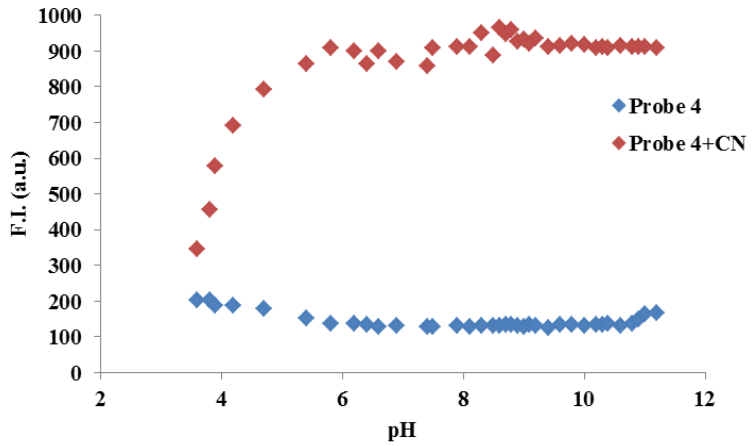

Figure 3.49: Effect of pH on probe 4 in H_2O:CH_3CN (1:9, v/v) at λ_{em}= 425 nm.

3.3.4. Conclusion

In summary, we successfully studied the role of conjugation on the ESIPT, ICT and AIE phenomenon and then on the sensing behavior of probe **3**. Probe **4** that showed the absorption and emission peaks at 340 nm and 425 nm, respectively. Probe **4** showed the "*turn-on*" behavior towards CN^- ions in mixed aqueous solution at 20 μM concentration with binding constant of 1.8×10^4 M^{-1} and detection limit of 1.9×10^{-7} M. Probe **4** also exhibited intramolecular charge transfer and aggregation induced emission phenomenon. The addition of CN^- ions to probe **4** prompted the formation of a 1:1 stoichiometry.

Summary of chapter 3

In conclusion, three benzimidazole based Schiff bases **(1, 3, and 4)** were synthesized and their photophysical characteristics have been examined using theoretical and experimental studies. All the probes have dual proton transfer sites one with hydroxy aryl benzimidazole and other with Schiff base unit and hydroxy unit. With the introduction of electron donating group, the intramolecular charge transfer occurs along with the ESIPT. The ESIPT and ICT phenomenon of all the three probes were investigated theoretically and experimentally. Theoretically calculated absorption and emission results matched closely to the experimental results. Further we checked the role of conjugation on the ESIPT, ICT and AIE phenomenon.

As expected, probes **1-4** showed ICT phenomenon with the introduction of electron donating group and with the increase in the conjugation. Further, probe **1-4** which is a Schiff base containing a imine linkage, showed weak emission in solution state due to limited flexibility and intramolecular motions. Probe **1** and **4** exhibited a strong aggregation induced emission (AIE) phenomenon compared to probe **3**, which had no AIE due to the presence of large $-NEt_2$ group which restricted the intramolecular rotation. These probes were also tested for their sensing properties towards anions.

Probe **1** detected Pb^{2+} and Al^{3+} ions in H_2O: CH_3CN (1: 9, v/v) with low detection limit whereas with the introduction of electron donating group ($-NEt_2$) the dipolar moment of the probe **3** increases which leads sensing in more polar solvent. Probe **3** detected Al^{3+} and HSO_4^- ions in H_2O: CH_3OH (1: 1, v/v). Further, the conjugation was increased in probe **4** that leads to increased polarity so the H_2O: CH_3CN (1: 9, v/v) system was used for the detection of CN^- ions.

Chapter 4

Investigation of excited state intramolecular proton transfer process and charge transfer process in hydroxy aryl benzothiazole based Schiff bases

1. Introduction

In context to chapter 3, we want to check the effect of heteroatom on the ESIPT phenomenon. The hydroxy benzothiazole derivatives are well known for excited state intramolecular proton transfer (ESIPT) process with very large Stokes shift value.[14, 47, 127-133] Heterocyclic benzothiazole derivatives are very good acceptors in D-π-A structures owing to their electron withdrawing property. This chapter covered the effect of heteroatom on the photophysical behavior of probe **5-7** containing unsymmetrical double proton, one with imine bond (-C=N-) and hydroxyl group (-OH), and the other with benzothiazole and hydroxyl group. The change in the hetero atom from NH to S (probe **5**) stabilizes the conjugated system and thus the absorption maximum can be increased. Further, molecular architecture was functionalized with electron donating substituents (probe **6**) and allowing their properties to be modulated. Also the effect of conjugation (probe **7**) on the ESIPT phenomenon and photophysical properties has been explored through theoretical and experimental studies. The fluorescent properties of these molecules can be altered for high Stokes shift and high quantum yield by incorporating electron donating group and by increasing the conjugation. The self-assembling properties of benzothiazole derivatives can be used to enhance their fluorescence and have application in bioimaging, optoelectronics and chemosensors. Benzothiazole moieties have three coordinating sites like O, S and N atom that make them potential sensors for ions and can also be responsible for aggregation induced emission (AIE) phenomenon. With the introduction of electron donating group and by increasing the conjugation on the molecule the intramolecular charge transfer can occur along with the ESIPT.

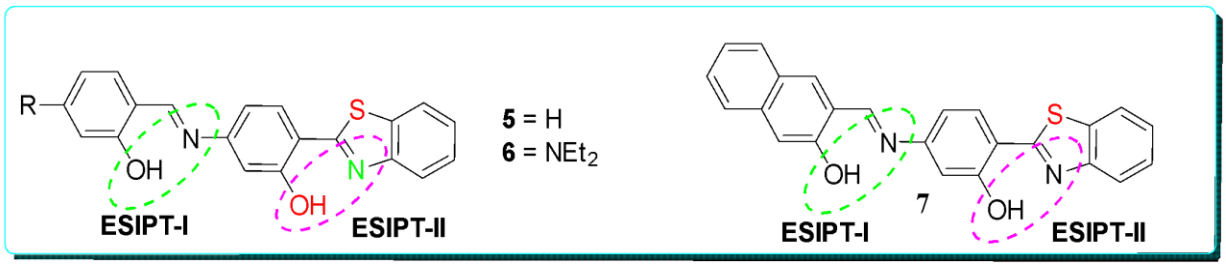

Figure 4.1: The different derivative of benzothiazole based Schiff base.

According to the examination of the experimental results, the substitution changed the photophysical characteristics and tuned excited state processes. Additionally, a summary of the substitution based investigations is provided in the following three sections:

4.1. Investigation of excited state intramolecular proton transfer process for hydroxy aryl benzothiazole based Schiff base**.**

4.2. Effect of electron donating group ($–NEt_2$) on excited state intramolecular proton transfer process of hydroxy aryl benzothiazole based Schiff base**.**

4.3. Effect of conjugation on excited state intramolecular proton transfer process in hydroxy aryl benzothiazole based Schiff base.

4.1.

Investigation of excited state intramolecular proton transfer process for hydroxy aryl benzothiazole based Schiff base

Abstract

As the benzothiazole based Schiff bases have two coordinating sites so they can be used as potential sensor for ions and may be responsible for aggregation induced emission (AIE) phenomenon. So, in this section a molecular system (probe **5)** containing imine moiety, benzothiazole moiety and appended hydroxyl unit through intramolecular H-bonding have been demonstrated for ESIPT phenomenon. The probe **5** have double excited state intramolecular proton transfer (ESIPT) sites in the form of basic N (imine group, benzothiazole group) and acidic OH (phenolic group) as hydrogen donor and acceptor units, respectively. Geometrical parameters, FTIR investigation were used to show that the intramolecular hydrogen bonding (IraHB) was initiated at the S_0 state and that it was strengthened at S_1 state. Potential energy curves were used to analyze the proton transfer and isomeric torsional conversion. The naked eye, UV-Visible, and fluorescence spectroscopy were used to investigate probe **5**'s interaction with various anions. Two absorption peaks were observed for probe **5** (20 µM; CH_3CN) at 290 nm and 360 nm and exhibit two emission bands, one at 415 nm the other at 540 nm upon excitation at 360 nm in CH_3CN. Probe **5** (20 µM; CH_3CN/H_2O (9:1, v/v)) developed a yellow color in the presence of F^- and $P_2O_7^{4-}$ ions. For both the ions, the corresponding UV-Vis measurements revealed a bathochromic shift of 85 nm. When complexed with anions, fluorescence emission changes clearly show that probe **5** behaves as "turn-on" sensor. The limit of detection (LOD) of probe **5** is calculated to be 41 and 23 nM for F^- and $P_2O_7^{4-}$ respectively. The ^1H NMR titration studies revealed more about their mode of binding with probe **5**.

4.1.2. Experimental section

4.1.2.1. Synthesis of compound 5a

The mixture of 4-aminosalicylic acid (500 mg, 3.3 mmol) and 2-aminothiophenol (408 mg, 3.3 mmol) in polyphosphoric acid (PPA) was stirred at 120 °C in 50 ml round bottom flask for 18 h **(Scheme 4.1)**. The reaction was monitored by TLC. After completion, the green coloured solid obtained by addition of water and ammonia solution, filtered and washed with water to get

compound **5a** in 90% yield. m.p.: 214-217 °C. ^{1}H NMR (DMSO-d_6, 400 MHz): δ (ppm) 7.66 (d, 1H, J = 8.4 Hz, ArH), 7.53 (dd, 2H, J_1 = 2.8 Hz, J_2 = 3.6 Hz, ArH), 7.20-7.16 (m, 2H, ArH), 6.21-6.13 (m, 2H, ArH). ^{13}C NMR (DMSO-d_6, 100 MHz): δ (ppm) 159.9, 153.1, 152.8, 127.7, 127.6, 122.8, 122.5, 106.9, 106.6, 100.7, 100.3.

4.1.2.2. Synthesis of probe 5

The compound **5a (**500 mg, 2.2 mmol) and salicylaldehyde (271 mg, 2.2 mmol) were mixed and stirred at 70 °C in ethanol for 6 h **(Scheme 4.1)**. On completion, reaction mixture was cooled and solid was filtered and washed with ethanol to get orange colored solid of probe **5** in 85% yields. m.p.: 243-245 °C. ^{1}H NMR (DMSO-d_6, 400MHz): δ (ppm) 11.58 (s, 1H, -OH), 8.71 (s, 1H, C=N), 7.96 (d, 1H, J = 10 Hz, ArH), 7.85 (d, 1H, J = 10 Hz, ArH), 7.76 (d, 1H, J = 10 Hz, ArH), 7.47-6.67 (m, 9H, ArH) **(Figure A19)**. ^{13}C NMR (DMSO-d_6, 100 MHz): δ (ppm) 192.3, 160.9, 159.9, 153.3, 152.8, 136.8, 133.9, 133.1, 129.7, 127.4, 122.3, 119.9, 119.4, 117.5, 116.9, 113.6, 109.5, 106.6, 101.1, 100.3 **(Figure A20)**. HRMS (ESI-TOF): (m/z) $[M+H]^+$ calcd for $C_{20}H_{15}N_2O_2S$: 347.0849, found: 347.0869 **(Figure A21)**.

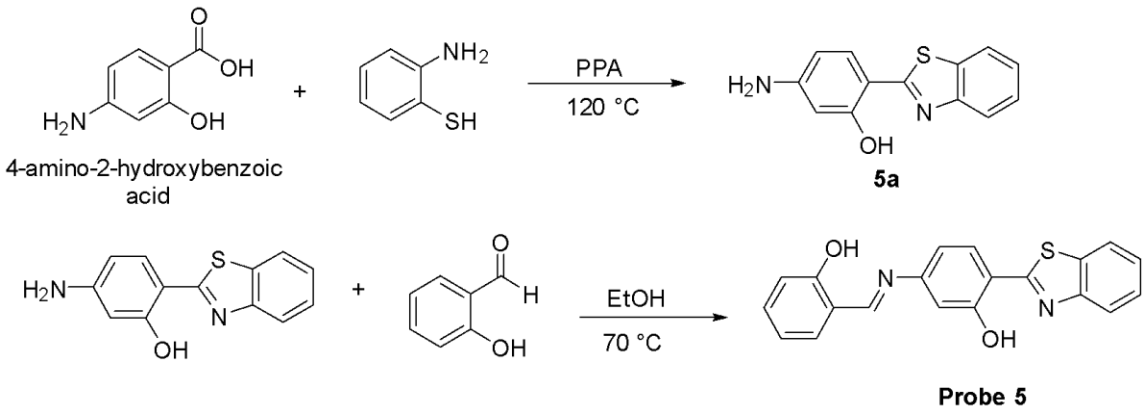

Scheme 4.1: Synthetic route for probe 5.

4.1.3. Results and Discussion

4.1.3.1. Photophysical properties

The absorption and emission measurements were used to examine the photophysical characteristics of probe **5**. Two absorption peaks were observed for probe **5** (20 μM; CH_3CN) at 290 nm and 360 nm in CH_3CN. The band at 290 nm can be due to π-π* transition within the

aromatic region and C=N group and the band at 360 nm is attributed to the intramolecular charge transfer (ICT) phenomenon. In CH_3CN probe **5** exhibit two emission bands, one at 415 nm with lower intensity accompanied by Stokes shift of 55 nm and the other at 540 nm with Stokes shift of 180 nm obtained upon excitation at 360 nm **(Figure 4.2)**. The high Stokes shift in the band can be due to ESIPT phenomenon occurring in the probe **5**. These two peaks are assigned as enolic with λ_{max} at 415 nm and keto with λ_{max} at 540 nm. It is observed that in an excited state intramolecular proton transfer (ESIPT), a molecule exhibits two bands, enol at lower wavelength and keto at higher wavelength.

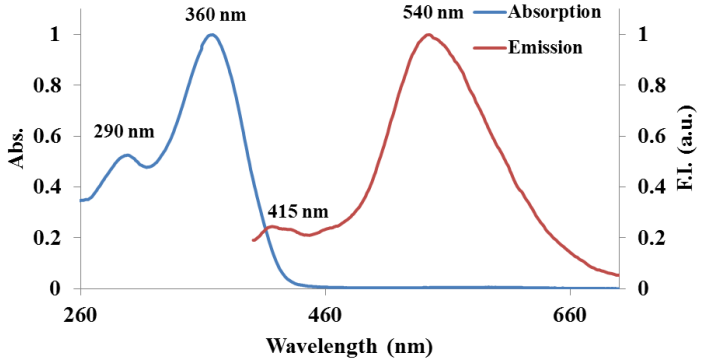

Figure 4.2: Normalized absorption and emission spectra of probe 5 (20 µM) in CH_3CN at λ_{ex}= 360nm.

4.1.3.2. Electronic spectra, electronic distribution and Intramolecular proton transfer

The presence of molecular flexibility leads to different geometrical configurations for probe **5**. Therefore, probe **5** was optimized at S_0 state and further; three low-lying excitations that correspond to S_0 geometry were calculated to investigate the origin of absorption spectra. For $S_0 \rightarrow S_1$ excitation determines 97 % orbital transition contribution from the HOMO (highest occupied molecular orbital) to LUMO (lowest unoccupied molecular orbital) with oscillation strength of 1.2806 at 377 nm, which is coherent with the experimental absorption peak at 360 nm. Additionally, the $S_0 \rightarrow S_2$ and $S_0 \rightarrow S_3$ excitations were determined at 334 nm and 309 nm with oscillation strength of 0.1742 and 0.0232, respectively. The $S_0 \rightarrow S_2$ and $S_0 \rightarrow S_3$ excitations were originated from HOMO-1→LUMO (98 %) and HOMO-2→LUMO (97 %) transition, respectively. Only $S_0 \rightarrow S_1$ excitation were considered for study because it has relatively strong oscillations strength. The electron density in the relevant molecular orbitals changed from the

benzothiazole unit (HOMO) to the Schiff base unit (LUMO) **(Figure 4.3)**, signifies the intramolecular charge transfer process.

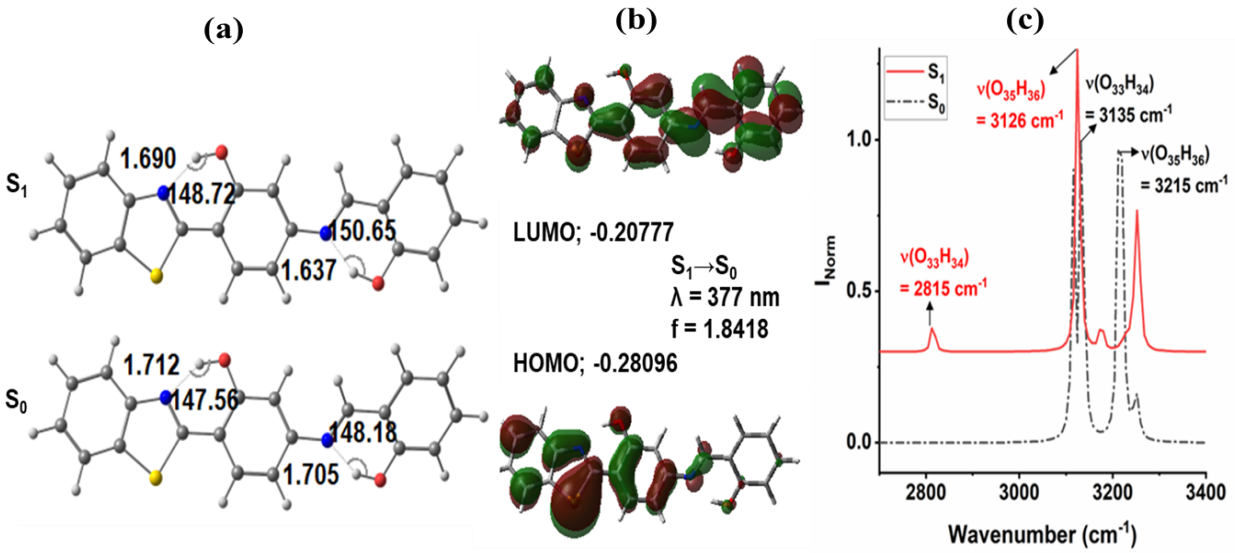

Figure 4.3: (a) Optimized structure of probe 5; (b) molecular orbitals of probe 5 and (c) FTIR spectra of probe 5, respectively at S_0 and S_1.

4.1.3.3. Intramolecular proton transfer

We established the necessary condition of intramolecular hydrogen bonding strengthening at the S_0 and S_1 state to understand the probe's behavior towards ESIPT process. $O_{33}H_{34}\cdots N_{21}$ and $O_{35}H_{36}\cdots N_{37}$, two types of asymmetrical intramolecular hydrogen bonding (IraHB) with short interaction distances and angles, were present in probe **5 (Figure 4.4)**. Further, $O_{33}H_{34}\cdots N_{21}$ IraHB exhibited a 319 cm^{-1} redshift from 3134 cm^{-1} to 2815 cm^{-1}; while $O_{35}H_{36}\cdots N_{37}$ IraHB exhibited 89 cm^{-1} redshifts from 3215 cm^{-1} to 3126 cm^{-1} on photoexcitation to S_1 state.

Furthermore, it could be noted that the atomic contribution for HOMO→LUMO at ESIPT sites i.e. O_{33} (ρ = 0.19816→ ρ = 1.64860), H_{34} (ρ = 0.02614→ ρ = 0.03942), N_{21} (ρ = 0.59962→ ρ = 11.01823), O_{35} (ρ = 1.78504→ ρ = 0.23729), H_{36} (ρ = 0.0005→ ρ = 0.00460), and N_{37} (ρ = 3.35351→ ρ = 1.43384) depicted that electronic density increases for N_{21}. The intramolecular charge transfer process at S_1 state signify the strengthening of $O_{33}H_{34}\cdots N_{21}$ IraHB that support the ESIPT process. These factors favor the excited state intramolecular proton transfer phenomenon. Therefore, the energies of tautomeric forms were calculated with zero-point energy

correction and established a relationship probe **5** (0 kcalmol^{-1}) < EK1 (1.96 kcalmol^{-1}) < EK2 (7.42 kcalmol^{-1}) < KK (8.98 kcalmol^{-1}) in S_0 state and probe **5** (64.82 kcalmol^{-1}) > EK1 (60.48 kcalmol^{-1}) < EK2 (66.25 kcalmol^{-1}) < KK (66.17 kcalmol^{-1}) in the S_1 state. Further, free energy change (ΔG=G(E)-G (K); where E and K are the standard enol and keto tautomeric forms) was used to predict the tautomeric conversion in S_0 and S_1 states. The negative ΔG for probe **5** (EE)→EK1 in S_1 state, indicated the possibility of ESIPT phenomenon. On the other hand, positive ΔG for probe **5** (EE)→EK2, EK1→KK and EK2→KK discommode the ESIPT process for second and double proton transfer. The potential energy curves (PECs) were calculated for EE→EK1 tautomeric conversion and an energy barrier of 1.65 kcalmol^{-1} was observed for forwarding proton transfer and 5.99 kcalmol^{-1} for reverse proton transfer in S_1 state. The determined low barrier for forwarding proton transfer facile the ESIPT pathway process. The results indicated that the ESIPT process is facile at imine and hydroxyl group.

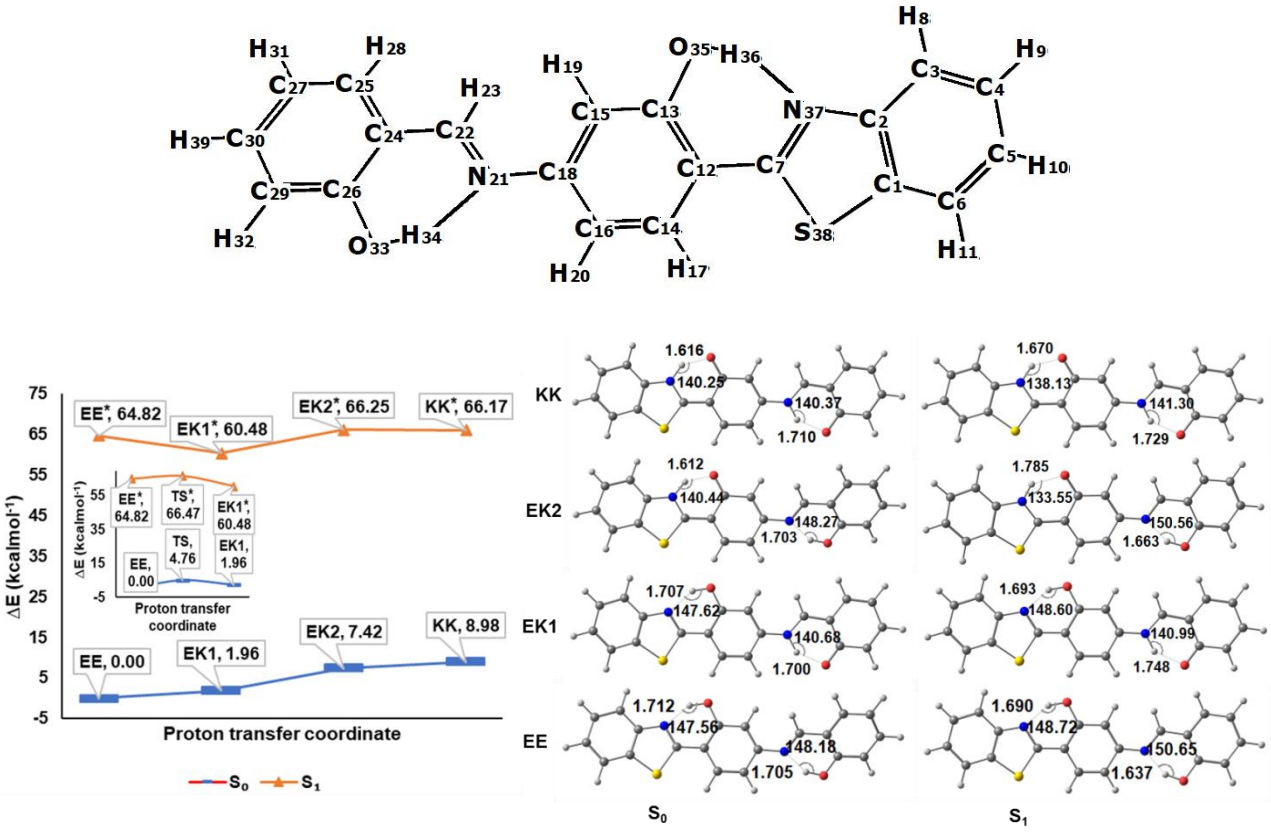

Figure 4.4: Energy profile of proton transfer of probe 5.

4.1.3.4. Aggregation induced emission enhancement (AIEE) characteristics of probe 5

Probe **5** has torsional flexibility with respect to C=N rotations at imine center. So to confirm that experimentally we performed the Aggregation Induced Emission (AIE) studies. AIE features of probe **5** were studied by absorption and emission spectra in less polar solvent (CH_3CN) with the incremental addition of highly polar solvent (H_2O). To confirm the AIEE phenomenon occurring in probe **5,** absorption and emission responses response was evaluated in CH_3CN-H_2O binary solvent system. **Figure 4.5** shows the results of altering the H_2O percentage in CH_3CN to examine the AIEE characteristic of probe **5**. It was observed that probe **5** aggregation starts in CH_3CN/H_2O mixture with higher water concentration (>30%). Probe **5** (20 μM) exhibits structured absorption spectra in dilute CH_3CN solution and a weak fluorescence emission at 465 nm on excitation at 360 nm. The fluorescence intensity of probe **5** remains unchanged while the volume of H_2O is increased from 0% to 30%. When $f_w \geq 40\%$ and the emission bands centred at 465 nm is rapidly turned on, the fluorescence intensity increases concominantly. The inset picture taken under UV irradiation clearly indicates that the solution changes colour from colorless to blue when 40-90% H_2O is added. Probe **5** appears to be AIEE active based on this examination.

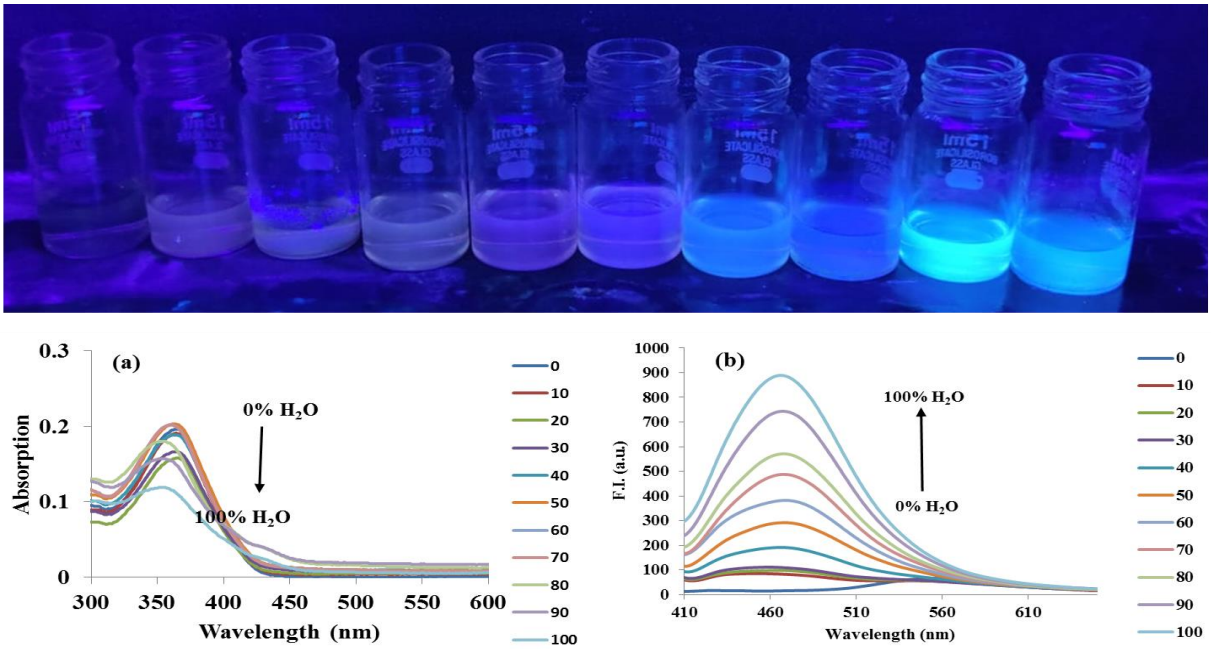

Figure 4.5: Effect of increasing H_2O ratio in CH_3CN under UV light, (a) Absorption and (b) emission spectra of probe 5 (20 µM) upon increasing the volume of H_2O in CH_3CN (λ_{ex}= 360 nm).

Dynamic light scattering (DLS) and field emission scanning electron microscopy (FESEM) were used to examine the aggregation behavior of probe **5**. The increase in particle size with the increase in the H_2O ratio was visible through the dynamic light scattering (DLS) experiment. The particle size in pure CH_3CN was between 0-150 nm with the average particle size of 40 nm and PDI value of 0.4. Further, with the increase in the H_2O ratio in CH_3CN the average particle size increases. In 50% H_2O/CH_3CN the particle size was between 75-400 nm and the average particle size was 150 nm with PDI value of 0.7. Similarly, in pure H_2O the average particle size was 1000 nm with PDI value of 0.8. The increase in the PDI value supported the homogeneity of the particles with the increase in the H_2O ratio. The homogeneity of the particles was further confirmed by FESEM images. In pure CH_3CN the rod like morphology of probe **5** was observed with average particle size of 52 nm. As the H_2O ratio was increased to 50% again rod like morphology with more homogenous particle size of 130 nm was observed. In pure H_2O flakes like morphology was observed with homogeneous particle size of 526 nm **(Figure 4.6)**.

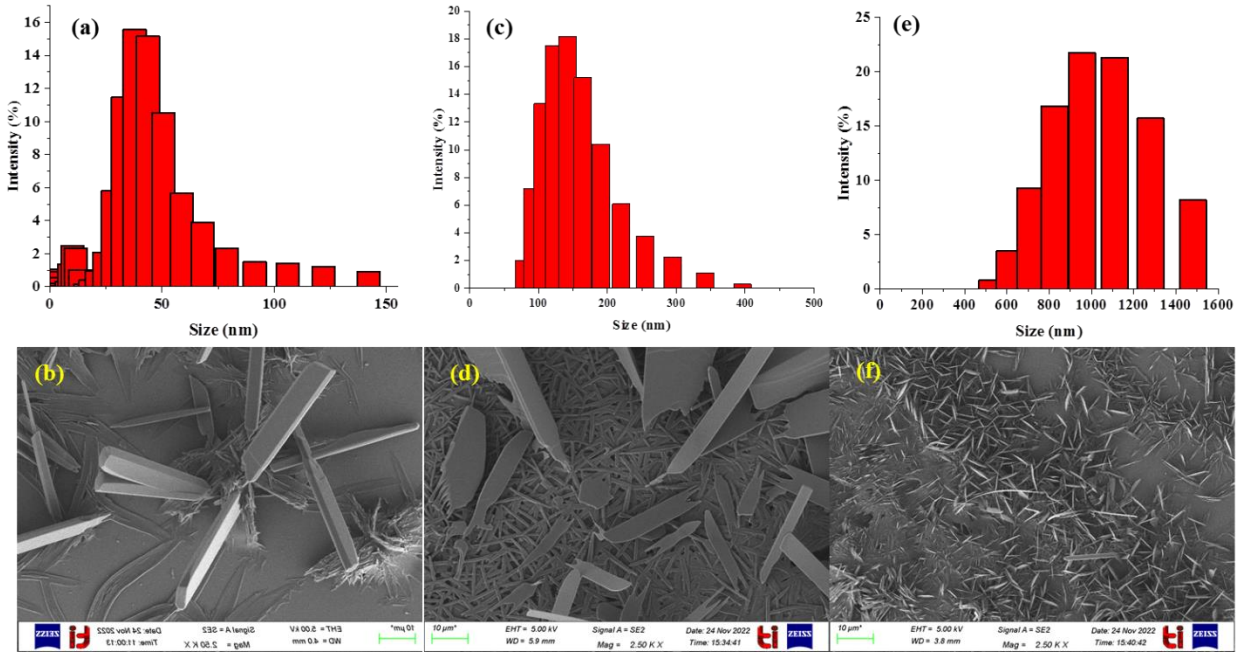

Figure 4.6: DLS and FESEM images of probe 5 in (a, b) pure CH_3CN, (c, d) 50% H_2O:CH_3CN and (e, f) pure H_2O.

4.1.3.5. Analytical performance of probe 5 towards anions

UV-Vis Absorption Study

The UV-Vis absorption spectral response of probe **5** (20 μM) towards different anions (F^-, CN^-, Br^-, I^-, SCN^-, AcO^-, NO_3^-, $P_2O_7^{4-}$, $H_2PO_4^-$, HSO_4^- and SO_4^{2-}) was recorded in CH_3CN:H_2O (9:1, [v/v], pH = 7.04). Probe **5** showed two absorption maximum at 290 and 365 nm. Interestingly, the spectral response of probe **5** to F^- and $P_2O_7^{4-}$ was associated with a sharp colour change of the solution from colourless to yellow, allowing the naked eye detection of both the ions. A titration experiment was carried out to obtain a quantitative understanding of the interaction between F^- and $P_2O_7^{4-}$ with probe **5**. The gradual addition of F^- and $P_2O_7^{4-}$ to probe **5** resulted in the systematic growth of a new absorbance band at 450 nm with simultaneously decrease in peak at 365 nm **(Figure 4.7)**. A distinct isosbestic point at 400 nm was observed, indicating intercoversion between the uncomplexed and complexed species.

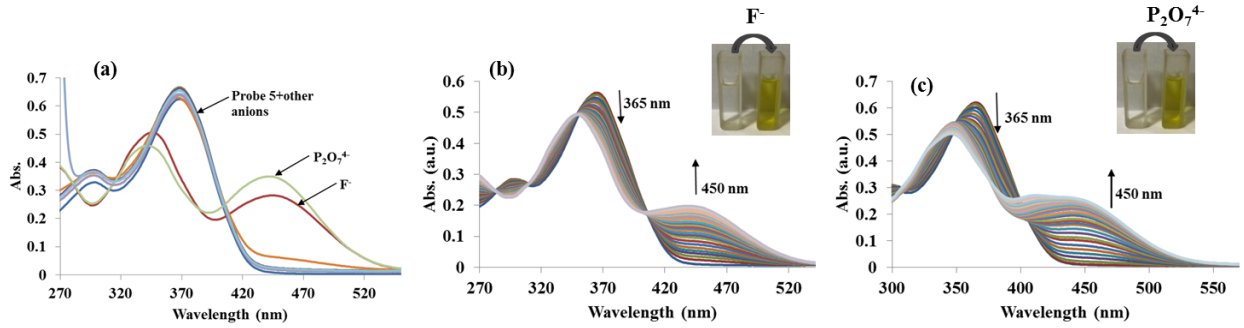

Figure 4.7: Absorption spectra of probe 5 (20 µM) in CH_3CN:H_2O (9:1, [v/v], pH=7.04) (a) in presence of different anions (1000 µM), (b) upon incremental addition of 0-100 µM of F^- ions, (c) upon incremental addition of 0-150 µM of $P_2O_7^{4-}$ ions.

Steady state emission studies

To investigate the sensing ability, the fluorescence response of probe **5** towards different anions (F^-, CN^-, Br^-, I^-, SCN^-, AcO^-, NO_3^-, $P_2O_7^{4-}$, $H_2PO_4^-$ and HSO_4^-) studies were performed in CH_3CN: H_2O (9:1, [v/v], pH=7.04) at 20 µM of concentration at room temperature. Probe **5** (20 µM) exhibited very weak emission band centred at 540 nm upon excitation at 365 nm. The excited state intramolecular proton transfer (ESIPT) caused by proton transfer from the oxygen atom of the hydroxyl group (-OH) proton-donor to the imine group (-C=N-) in presence of polar solvent is responsible for the weak fluorescence. No anion produced fluorescence upon addition to probe **5** except for F^- and $P_2O_7^{4-}$ ions, which give blue emission under UV light. Gradual addition of F^- to probe **5** (20 µM) resulted in a systematic increase in emission intensity associated with a 90 nm blue shift from 540 nm to 450 nm indicating a F^- ion induced turn-on fluorescent signaling behavior. A plateau in the fluorescence spectra was observed after the addition of 80 µM of F^- ions. Similar change was observed for $P_2O_7^{4-}$ ion where 80 nm of blue shift in the emission band from 540 nm to 460 nm was observed with the enhancement in the emission intensity. A plateau in the fluorescence spectra was observed after the addition of 100 µM of $P_2O_7^{4-}$ ions **(Figure 4.8)**.

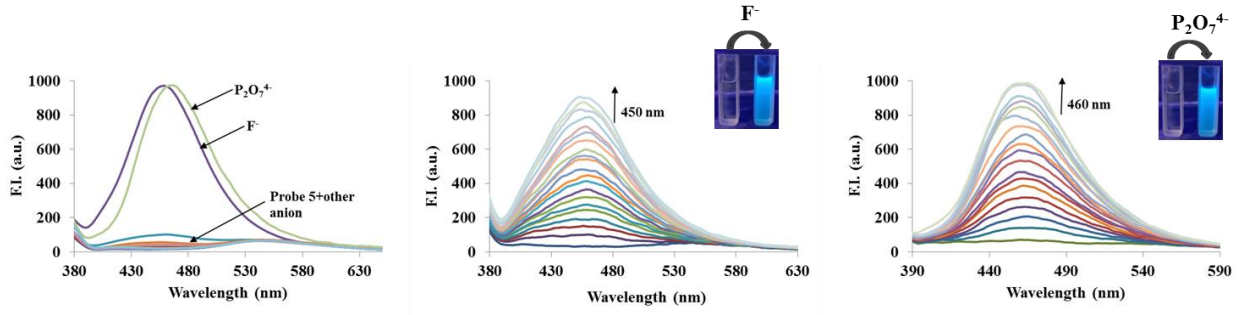

Figure 4.8: Emission spectra of probe 5 (20 µM) in CH_3CN:H_2O (9:1, [v/v], pH=7.04) (a) in presence of different anions (1000 µM), (b) upon incremental addition of 0-80 µM of F^- ions, (c) upon incremental addition of 0-100 µM of $P_2O_7^{4-}$ ions.

Furthermore, the sensing ability of probe **5** could be observed with the naked eye for selective turn on response of probe **5** towards F^-/ $P_2O_7^{4-}$ in CH_3CN: H_2O (9:1, [v/v]) in daylight and under UV irradiation to show a bright blue fluorescence in the presence of both the ions.

A conventional Job's plot experiment was performed to determine the stoichiometry of probe **5** with F^-/ $P_2O_7^{4-}$ ions. The intersection point was found to be at 0.5 mole fraction of $F^-/P_2O_7^-$, indicating that probe **5** coordinates with F^-/ $P_2O_7^{4-}$ ions in a 1:1 stoichiometric manner **(Figure A23)**. To further test that whether probe **5** can selectively detect F^-/ $P_2O_7^{4-}$ ions even in the presence of other anions, competitive anion experiment was carried out. Probe **5** was treated with other anions in the presence of F^-/ $P_2O_7^{4-}$ ions. The results indicated that the other ions do not lead to any significant change in the fluorescence intensity of probe **5** and F^-/ $P_2O_7^{4-}$ ions complex and showed the same spectral change even in the presence of other competitive anions indicating the selectivity of probe **5** towards F^-/ $P_2O_7^{4-}$ ions **(Figure 4.9)**.

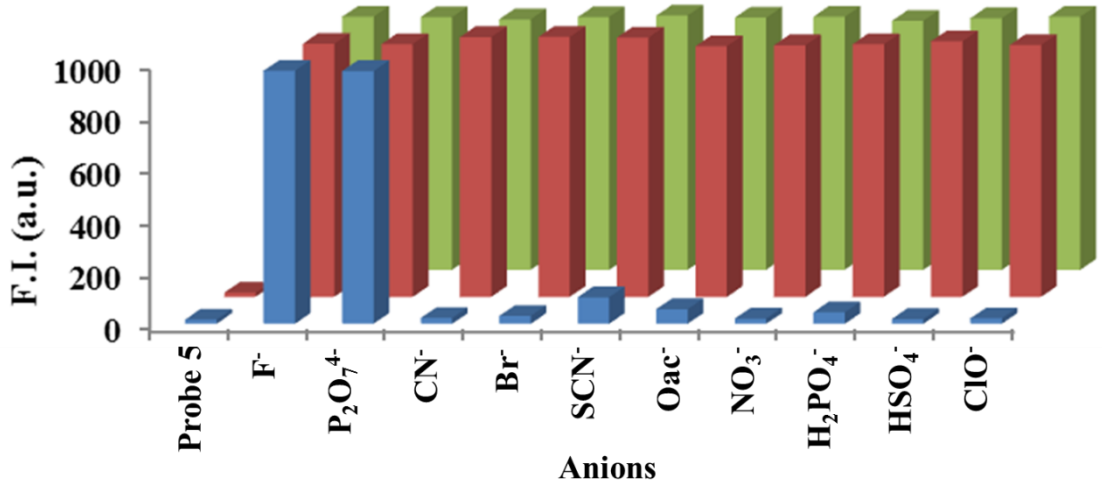

Figure 4.9: Relative emission intensity of probe 5 (20 µM) in CH_3CN:H_2O (9:1, [v/v], pH=7.04), (λ_{ex}= 365 nm) with different competing anions in the absence and presence of F^- and $P_2O_7^{4-}$ ions at λ_{em}= 460 nm, where blue bars represent the emission intensity change of probe 5 with different anions (1000 µM) and red bars represent probe 5 + F^- in the presence of different relevant competing anions (1000 µM), green bars represent probe 5 +$P_2O_7^{4-}$.

Detection limit and binding constant

The detection limit of probe **5** for the sensing of F^-/ $P_2O_7^{4-}$ was also an important parameter for the practical purposes. Probe **5** detects F^-/ $P_2O_7^{4-}$ *via* colorimetric response and the color change is visible to the naked eye. The detection limit as low as 41 nM and 23 nM was calculated using a good linear relationship between the relative fluorescence intensity and the concentration of F^- and $P_2O_7^{4-}$ respectively, which is well below the permissible level of F^- (1.5 µM) and $P_2O_7^{4-}$ (1.0 µM) in drinking water according to the United States Environmental Protection Agency (USEPA). As a result, our fluorescent probe **5** was extremely sensitive to F^- and $P_2O_7^{4-}$ ions.

We also determined the binding constant of the probe **5** with F^- and $P_2O_7^{4-}$ ions to confirm the selectivity. Assuming a 1:1 complex formation, the binding constant (K_a) was calculated from the probe **5**'s titration curve with F^- and $P_2O_7^{4-}$ using non-linear least square fitting of the emission intensity at 455 nm and 460 nm. The K_a value of probe **5**-F^- was estimated to be 1.8 $\times 10^4$ M^{-1} (R^2=0.9919) and for probe **5**- $P_2O_7^{4-}$ the binding constant was 3.5 $\times 10^4$ M^{-1} (R^2= 0.9818), demonstrating probe **5**'s strong binding affinity for both the ions.

4.1.3.6. pH dependence

It is well known that for various practical applications, whether the sensors are active or not at the appropriate pH conditions is critical for successful operation. As a result, we investigated the effect of the pH on fluorescence intensity of probe **5** in the presence and absence of F^- and $P_2O_7^{4-}$ ions. The emission intensity was nearly stable in the pH range 6.0-11.0, which makes it suitable for use in physiological pH conditions. The fluorescence intensity increases in the acidic (pH<6) region due to protonation of probe **5**'s imine nitrogen. As a result the hydrogen bonding between imine nitrogen and hydroxyl H gets disturbed. Again, increase in the emission intensity in the basic region (pH>11) has been attributed to the inhibition of ESIPT process. Hence, the emission intensity is stable over this pH range (6.0-11.0) and suitable for applications under physiological pH conditions **(Figure 4.10)**.

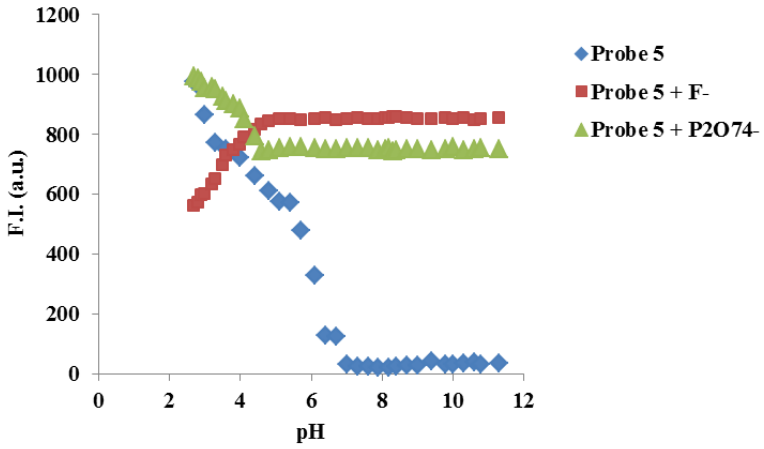

Figure 4.10: Effect of pH on probe 5and its complex with F^- and $P_2O_7^{4-}$ ions in CH_3CN:H_2O (9:1, [v/v] at λ_{em}= 460 nm.

4.1.3.7. ^{1}H NMR Titration of probe 5

^{1}H NMR titration experiment in CD_3CN-d_3 was carried out to gain insight into the mode of interaction between probe **5** and F^-/$P_2O_7^{4-}$ anions. The hydroxyl and imine protons were found to have proton at δ 11.58 (-OH) and 8.71 (-C=N) ppm in the ^{1}H NMR spectrum of probe **5** (5×10^{-3} M). Notably, when F^- anion (0-1.0 eq.) were sequentially added to the probe **5** solution, the proton resonating at δ 11.58 ppm due to OH group disappeared completely, indicating that the

hydroxyl proton was deprotonated in the presence of F^- anion. The simultaneous upfield chemical shifts for imine and aromatic protons from δ 6.5-8.0 ppm suggested a complete charge delocalization on the entire probe **5**. As a result, successive changes in ^1H NMR spectra clearly indicated an initial H-bond interaction between the probe **5** and F^- anion, which eventually resulted in the deprotonation **(Figure 4.11)**. Further, due to charge propagation from phenolic moiety to benzothiazole unit, the ESIPT inhibits and a significant colour change was observed due to extended conjugation. Scheme **4.2** depicts a plausible mechanism of interaction between probe **5** and F^- anion. Similar results were observed for $P_2O_7^{4-}$.

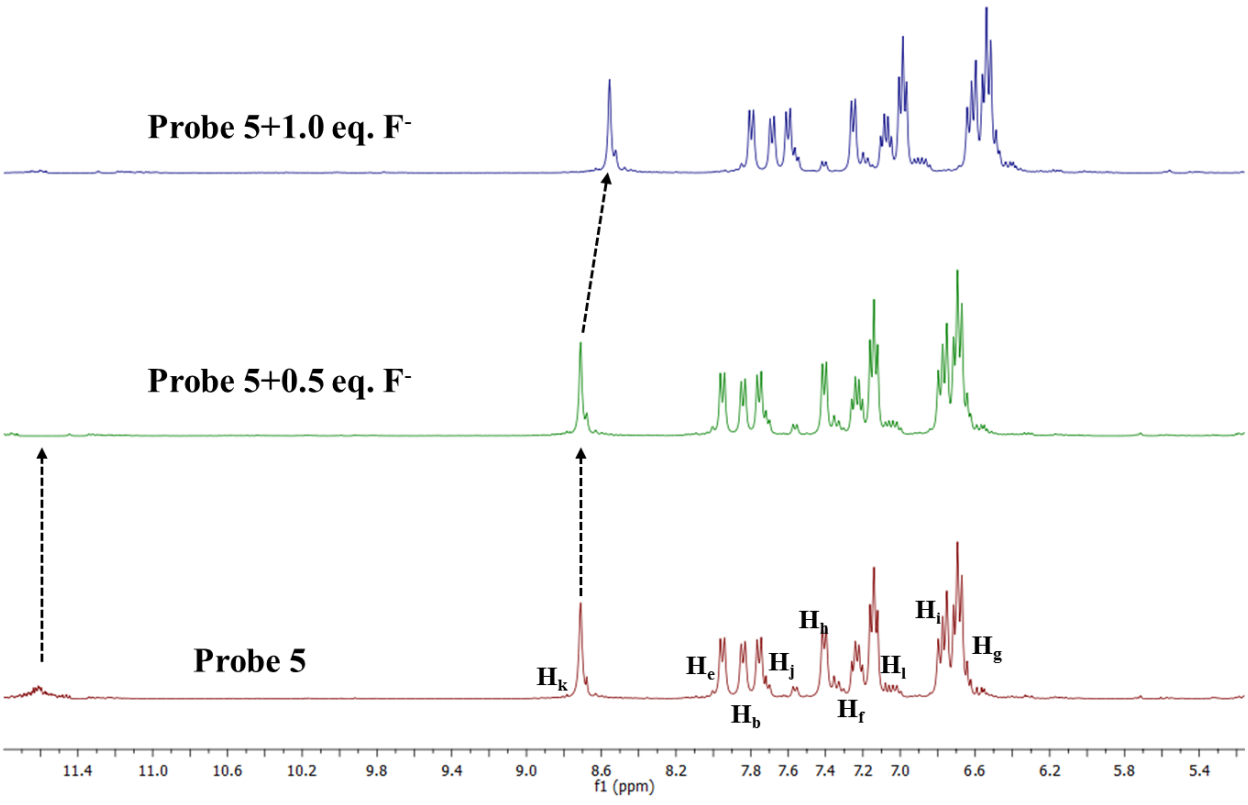

Figure 4.11: ^1H spectrum of probe 5 in the presence of F^- ion in CD_3CN-d_3.

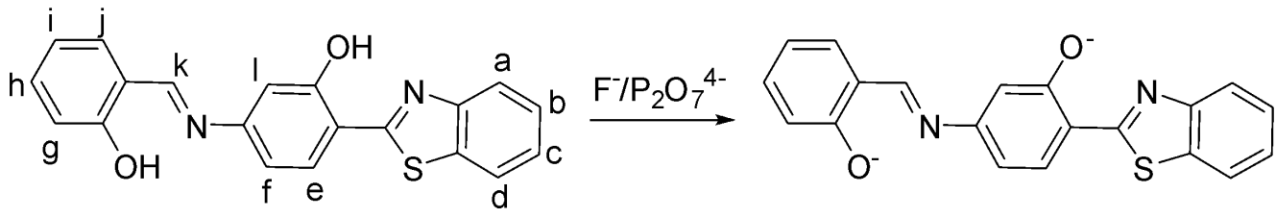

Scheme 4.2: Proposed mechanism for interaction between probe 5 and F^- and $P_2O_7^{4-}$ ion.

In order to explore further, the binding mechanism, DLS experiment was performed with probe **5** in presence and absence of F^- and $P_2O_7^{4-}$ ions. The probe **5** showed size of 75 nm in 10% H_2O-CH_3CN through DLS. However, upon addition of F^- and $P_2O_7^{4-}$ ions the size of the particles increases to 955 nm and 650 nm, respectively which support the formation of aggregates on binding with F^- and $P_2O_7^{4-}$ ions **(Figure 4.12)**. FESEM images showed change in morphology of probe **5** on addition of F^- and $P_2O_7^{4-}$ ions which confirmed the binding of probe **5** with F^- and $P_2O_7^{4-}$ ions **(Figure 4.13)**. Probe **5** showed particle size of 35 nm with flake like morphology that were distorted from edges and after the addition of F^- ions big cluster of size 947 nm were obtained having no specific morphology whereas after the addition of $P_2O_7^{4-}$ ions flake like morphology with particle size of 575 nm was obtained. Both the FESEM and DLS were in correlation with each other.

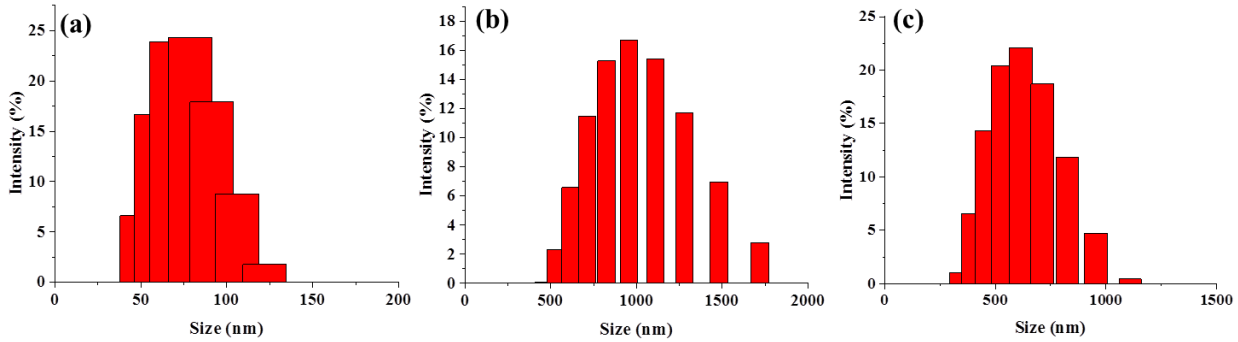

Figure 4.12: DLS profile of (a) probe 5 (20 µM), (b) after the addition of F^- ion and (c) after the addition of $P_2O_7^{4-}$ ions in CH_3CN: H_2O (9:1, [v/v]).

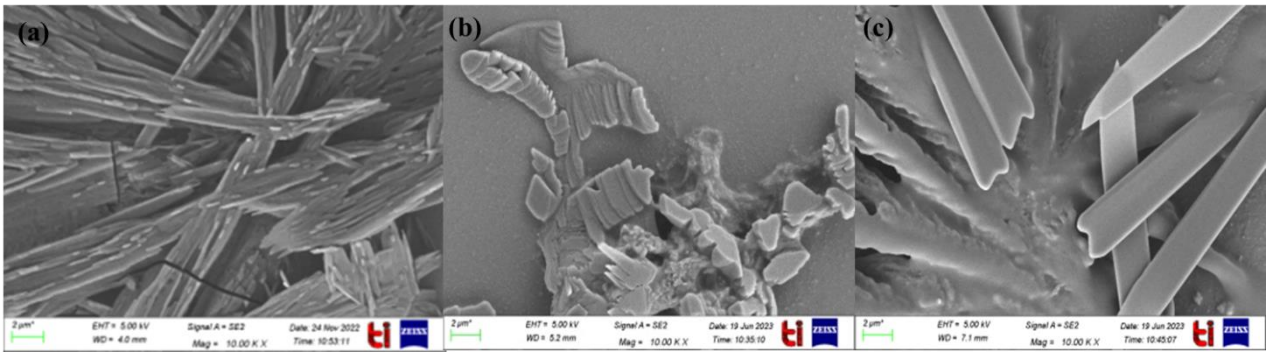

Figure 4.13: FESEM images of (a) probe 5, (b) after addition of F^- ion and (c) after addition of $P_2O_7^{4-}$ ions in CH_3CN: H_2O (9:1, [v/v]).

4.1.3.8. Detection of F^- ion in real samples

Probe **5** was used to detect F^- and $P_2O_7^{4-}$ in real water samples in order to investigate the practical applicability of the chemosensor and satisfactory results were achieved. F^- and $P_2O_7^{4-}$ sample solutions were prepared using tap water from laboratory. In this instance, known F^- and $P_2O_7^{4-}$ ion concentrations were directly spiked into tap water. The emission intensity was then measured at 450 nm after the samples were subjected to 20 µM of probe **5** in H_2O:CH_3CN (1:9, v/v) **(Figure 4.14)**. The favorable recoveries from tap water with varying F^- and $P_2O_7^{4-}$ ion concentration shows the practical applicability of probe **5** in everyday situations. Similarly, addition of toothpaste sample to the solution of probe **5** gave the same results and also good recoveries were obtained from toothpaste samples.

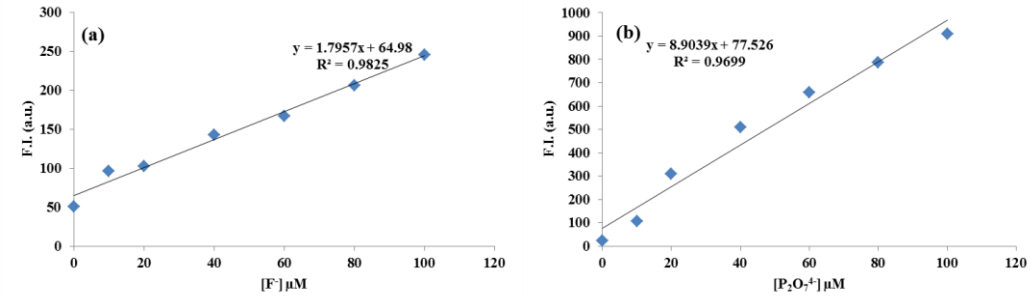

Figure 4.14: Emission spectra of probe 5 in the presence of different concentrations of spiked (a) F^- and (b) $P_2O_7^{4-}$ from 0 to 100 µM.

Table 4.1: Determination of F^- and $P_2O_7^{4-}$ ions in Tap water.

Ion	Sample	Ion Added (µM)	Ion Recovered (µM)	Recovery (%)
F^-	1	20	19.5	97.5
	2	40	39.7	99.3
$P_2O_7^{4-}$	1	20	20.1	100.5
	2	40	39.9	99.8

Table 4.2: Determination of F^- ion in toothpaste samples.

Sample	Sample	Added (µM)	Recovered (µM)	Recovery (%)
Toothpaste 1	1	20	20.5	102.5
	2	40	41.7	104.3
Toothpaste 2	1	20	21.1	105.5
	2	40	39.8	99.5

4.1.4. Conclusion

In this chapter, we looked into the untapped potential of a simple benzothiazole based Schiff base (probe **5**). The probe **5**'s ESIPT and AIE behavior has been rationalized. Probe **5** acts as a colorimetric and fluorescence turn-on chemosensor for F^- and $P_2O_7^{4-}$ ions. The variation of slight acidic and basic conditions makes probe **5** very useful in practical applications for pH range between 6.0-9.0. In comparison to other reports, the probe **5** is very sensitive for the detection of F^- and $P_2O_7^{4-}$ ions due to very low detection limit. Probe **5** was also used for the detection of F^- ions in real field samples.

4.2.

Effect of electron donating group ($–NEt_2$) on excited state intramolecular proton transfer process of hydroxy aryl benzothiazole based Schiff base

Abstract

In this study, the effect of $–NEt_2$ as an electron-donating group on photophysical properties of probe **6** was explored through experimental and theoretical studies. The introduction of $–NEt_2$ group will induce the inductive effect which will generate δ+ charge on carbon atom of imine bond, that can lead to hydrolysis by HOCl. HOCl/ClO^- is a physiologically essential component of reactive oxygen species (ROS) and plays a critical role in the human immune function system. With the low concentration, HOCl/ClO^- can kill invading germs and pathogens, mediate the physiological balance of the body, and induce oxidation of biomolecules such as proteins, lipids, and nucleic acid in biological cells, resulting in a variety of disorders. As a result, determining the concentration of HOCl/ClO^- in organisms is critical. In this study, we rationally designed Schiff base probe **6**, a ratiometric fluorescent probe for the detection of ClO^-. Probe **6** has good selectivity and sensitivity towards ClO^- detection. The emission maximum of probe **6** showed quenching with slight red shift in the emission band on the addition of ClO^- ions. The lowest detection limit of probe **6** for the detection of ClO^- ion was found out to be 5.5 μM. Further, probe **6** was successfully employed for the biological imaging with low cytotoxicity.

4.2.2. Experimental section

4.1.2.1. Synthesis of probe 6

The compound **5a** (200 mg, 0.8 mmol) and N, N-Diethylamino salicyladehyde (159 mg, 0.8 mmol) were refluxed in ethanol for 8 h **(Scheme 4.3)**. On completion the reaction mixture was cooled and solid was filtered and washed with ethanol to get yellowish green colored solid of probe **6** in 80% yields. m.p. 275-280 °C. ^{1}H NMR (DMSO-d_6, 400MHz): δ (ppm) 8.45 (s, 1H, ArH), 7.96 (d, 1H, J = 8 Hz, ArH), 7.89 (d, 1H, J = 8 Hz, ArH), 7.67 (d, 1H, J = 8 Hz, ArH), 7.51 (t, 1H, J = 16 Hz, ArH), 7.40 (t, 1H, J = 16 Hz, ArH), 7.17 (d, 1H, J = 8 Hz, ArH), 6.93 (d, 1H, J = 4 Hz, ArH), 6.85 (dd, 1H, J_1 = 8 Hz, J_2 = 12 Hz, ArH), 6.27 (dd, 1H, J_1 = 4 Hz, J_2 = 8 Hz, ArH), 6.18 (d, 1H, J = 4 Hz, ArH), 3.43 (q, 4H, eth-CH_2), 1.22 (t, 6H, eth-CH_3) **(Figure**

A24). ^{13}C NMR (DMSO-d_6, 100 MHz): δ (ppm) 159.9, 153.1, 152.8, 127.7, 127.6, 122.8, 122.5, 106.9, 106.6, 100.7, 100.3 **(Figure A25)**. ESI-MS: m/e 418.16 (M^++1) **(Figure A26)**.

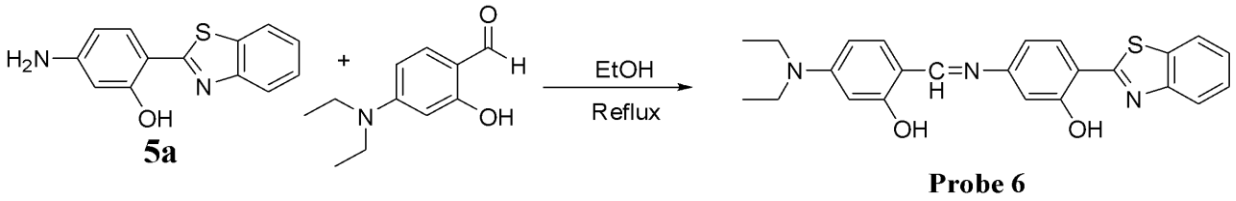

Scheme 4.3: Synthesis of probe 6.

4.2.3. Results and Discussion

4.2.3.1. Photophysical studies of probe 6

At ambient temperature, the UV-Vis and fluorescence spectra of probe **6** (20 μM) were recorded in different polar, nonpolar, protic and aprotic solvents. In all the solvents, probe **6** showed green color that was visible to the naked eye and an absorption band in the range of 380-450 nm. The significant absorbance of band in the range of 380-450 nm suggests that it may be a π-π* transition. The UV-Vis spectra of probe **6** showed red shift of 70 nm in the absorption intensity from 380 nm to 450 nm **(Figure 4.15a)**. The fluorescence spectra were taken in various solvents by exciting probe **6** at its absorption maximum of 435 nm. The probe **6** showed emission band in the range of 500-510 nm in all the solvents. As the polarity of the solvent is increased the fluorescence intensity also increases with slight red shift in the emission maximum from 500 nm to 510 nm **(Figure 4.15b)**. The slight variation in the emission band can be due to the differential stabilization of the emission band by different solvent in the excited state.

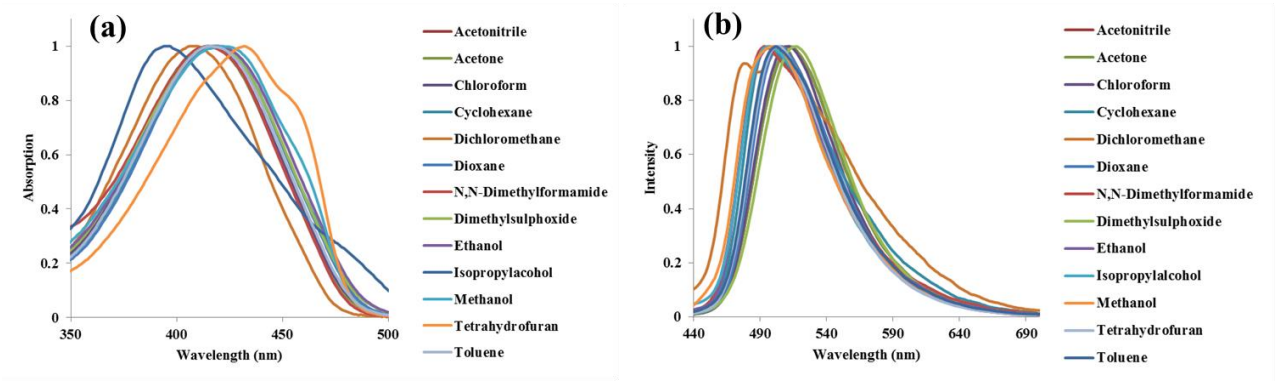

Figure 4.15: (a) Absorption and (b) emission spectra of probe 6 in different polarity solvents.

4.2.3.2. UV-Vis response of probe 6 towards anions

In order to determine the sensing ability of chromogenic detection of probe **6**, UV-Vis spectrum of probe **6** (20 μM) in the absence and presence of different anions (F^-, CN^-, Br^-, I^-, SCN^-, AcO^-, ClO^-, ClO_4^-, NO_3^-, $P_2O_7^-$, $H_2PO_4^-$, HSO_4^-, H_2O_2 and SO_4^{2-}) was recorded in CH_3OH:H_2O (9:1, [v/v], pH=7.04). Probe **6** showed its absorption maximum at 435 nm arising due to n-π* and π-π* transitions. Upon addition of ClO^- (1000 μM) to the solution of probe **6**, red shift along with the increase in the absorption maximum was observed **(Figure 4.16a)**. However, the absorption spectra with the other competing anions showed negligible change. With the gradual addition of ClO^- ions to probe **6** the absorption band at 450 nm increases **(Figure 4.16b)**.

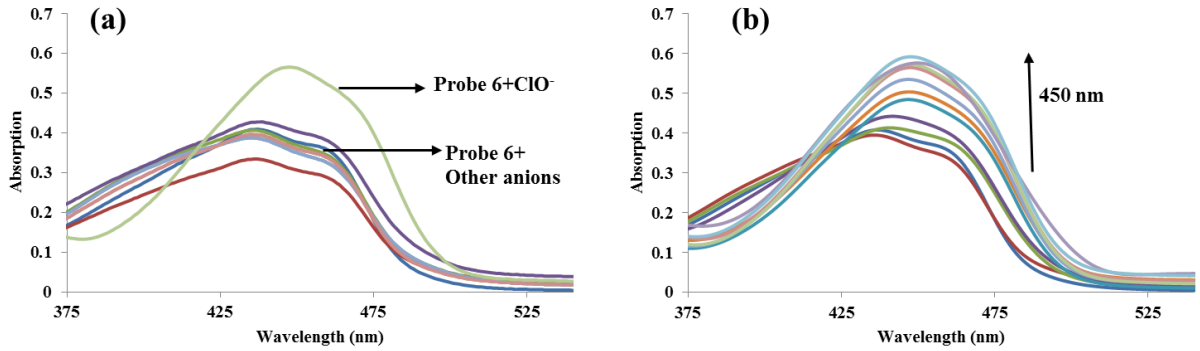

Figure 4.16: Absorption spectra of probe 6 (20μM CH_3OH: H_2O (9:1, [v/v], pH=7.04), (a) in presence of different anions (1000 μM) and (b) with incremental addition of 0- 200 μM of ClO^- ion.

4.2.3.3. Fluorescence response of probe 6 towards anions

To further investigate the sensing ability, the fluorescence response of probe **6** towards different anions (F^-, CN^-, Br^-, I^-, SCN^-, AcO^-, ClO^-, ClO_4^-, NO_3^-, $P_2O_7^-$, $H_2PO_4^-$, HSO_4^-, H_2O_2 and SO_4^{2-}) was examined in CH_3OH: H_2O (9:1, [v/v], pH=7.04) at 20 µM of concentration. The free probe **6** solution showed blue fluorescence at 500 nm on excitation at 435 nm **(Figure 4.17)**. The probe **6** showed fluorescence quenching behavior after the addition of ClO^- ion with bathochromic shift to 520 nm over the other tested anions **(Figure 4.18a)**. A plateau in the fluorescence spectra was observed after the addition of 20 µM of ClO^- ions **(Figure 4.18b)**. To further test that whether probe **6** can selectively detect ClO^- ion even in the presence of other anions, competitive ion experiment was carried out. Probe **6** was treated with other anions in the presence of ClO^- ion. The results indicated that the other ions do not lead to any significant change in the fluorescence intensity and ClO^- ion showed the same spectral change even in the presence of other competitive anions. The fluorescence response to the addition of ClO^- ion was not affected by the presence of other commonly coexisted anions, indicating the selectivity of probe **6** towards ClO^- ion **(Figure 4.19)**.

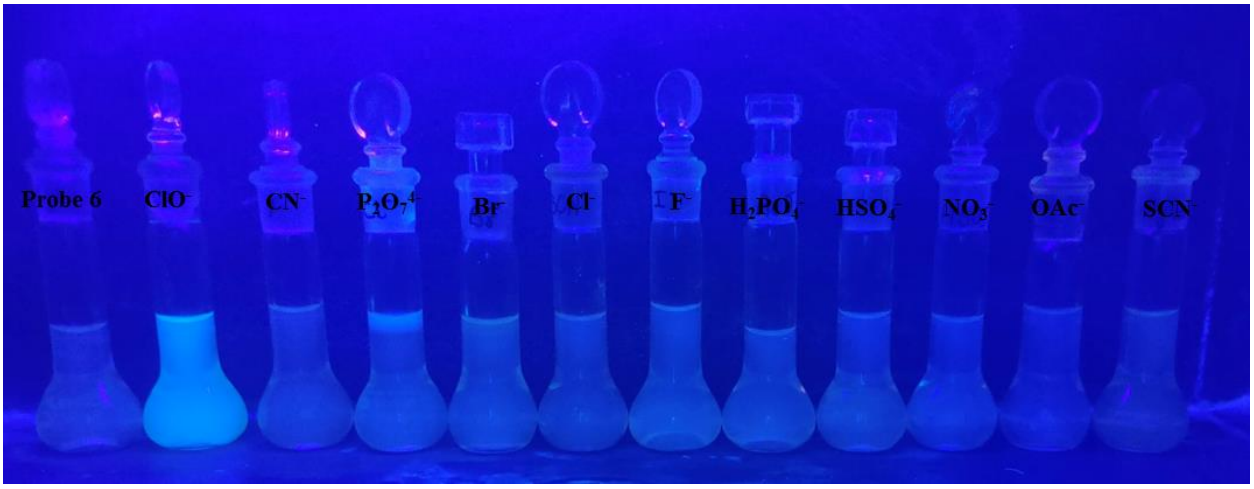

Figure 4.17: Effect of different anions on solution of probe 6 (20 µM, CH_3OH: H_2O (9:1, [v/v], pH=7.04) under UV light.

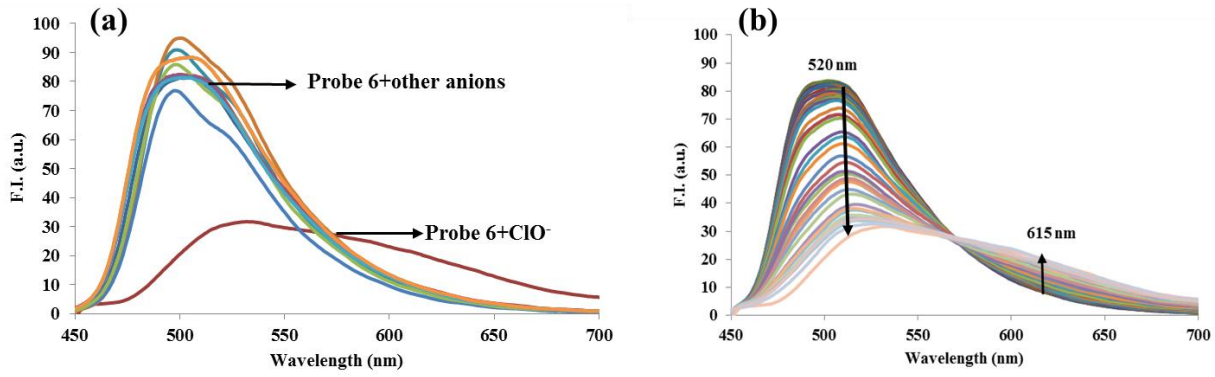

Figure 4.18: Emission spectra of probe 6 (20µM), CH_3OH: H_2O (9:1, [v/v], pH=7.04), (a) in presence of different anions (1000 µM) and (b) with incremental addition of 0-300 µM of ClO^- ion.

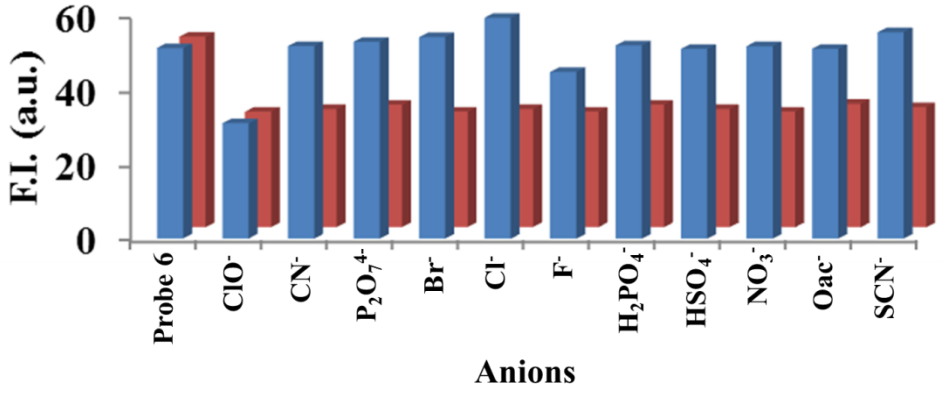

Figure 4.19: Relative emission intensity of probe 6 (20 µM, CH_3OH: H_2O (9:1, [v/v], pH=7.04) (λ_{ex}= 435 nm) with different competing anions in the absence and presence of ClO^- at λ_{em}= 520 nm, where blue bars represent the emission intensity change of probe 6 with different anions (1000 µM) and red bars represent probe 6 + ClO^- in the presence of different relevant competing anions (1000 µM).

4.2.3.4. Sensitivity of probe 6 towards ClO^- ions

To further check the sensitivity of probe **6** towards the ClO^- ions, we determined the binding constant of probe **6** with ClO^- ion. The binding constants for the complex was calculated by linear fitting of 1/ ($I-I_0$) to 1/ [ClO^-] according to the Benesi-Hildebrand equation. The binding constant for probe **6**- ClO^- complex was 2.7×10^3 M^{-1} with lowest detection of 5.5×10^{-6} M. Both fluorescence spectrum and UV-Vis spectrum were used to determine the stoichiometry between

probe **6** and ClO^-. The stoichiometry of probe **6** and ClO^- ions complex was found to be 1:1 **(Figure A28)**.

4.2.3.5. ^{1}H NMR titration experiment

In order to investigate the binding behavior of probe **6** towards ClO^- ion we performed the ^{1}H NMR titrations in CD_3OD-d_4. Upon addition of 1.0 eq. of ClO^- to the solution of probe **6** the spectra was not affected but after 24 hrs the imine peak at δ 9.56 ppm disappeared, which confirmed the hydrolysis of the Schiff base **(Figure 4.20)**. The aromatic protons also showed downfield shift upon addition of 1.0 eq. of ClO^- ion with slight splitting of the signals. The ^{1}H NMR titrations clearly showed that fluorescence quenching of probe **6** is due to the ClO^- prompted hydrolysis leading to the cleavage of imine bond to generate aldehyde and amine. The HRMS peak at 243.0593 due to amine and 194.1180 due to aldehyde also confirmed the hydrolysis mechanism **(Figure A29)**.

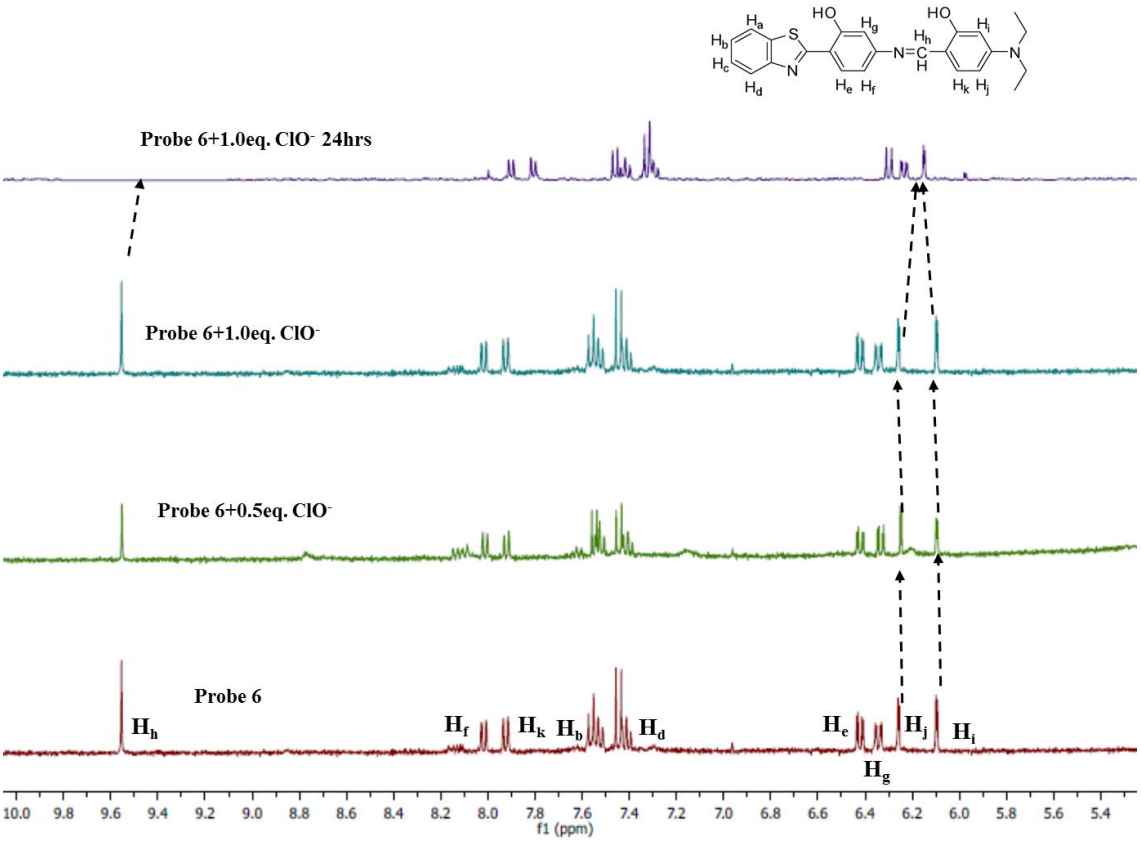

Figure 4.20: ^{1}H NMR spectra of probe 6 (5×10^{-3} M) upon addition of 1.0 equiv. of ClO^- ions in CD_3OD-d_4.

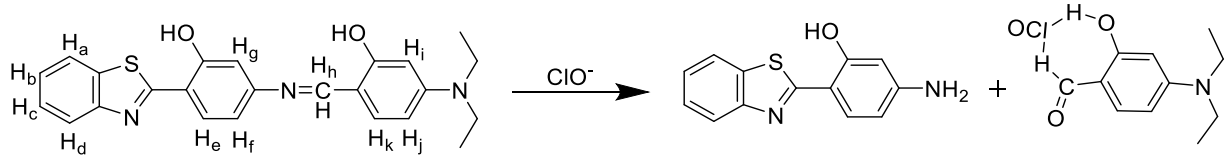

Scheme 4.4: Plausible sensing mechanism of ClO^- by probe 6.

4.2.3.6. ClO^- detection in solid state

Based on the above outcomes, we postulated that probe **6** in the presence of ClO^- ion in CH_3OH: H_2O (9:1, [v/v]) undergoes hydrolysis process. So, we predicted that on addition of ClO^- ion to probe **6**, it undergoes some morphological change in the solid state. The self-assemblies of probe **6** and probe **6**+ ClO^- mixture in CH_3OH: H_2O (9:1, [v/v]) were studied using microscopic techniques to any such impact on probe **6** in the solid state owing to the addition of ClO^- ion.

Field emission scanning electron microscopy (FESEM) images of thin coating on carbon tape prepared by drop cast method of probe **6** in CH_3OH: H_2O (9:1, [v/v]) revealed fibre-like aggregates all over the surface **(Figure 4.21a, b)**. These fibres like aggregates showed average size of 865 nm. On the other hand, the FESEM images of probe **6**+ ClO^- mixture in CH_3OH: H_2O (9:1, [v/v]) demonstrated flower shaped aggregate morphology with particle size of 955 nm **(Figure 4.21d, e)**.

Dynamic light scattering (DLS) technique further supported the increase in the particle size of probe **6** and probes **6**+ ClO^- mixtures. The DLS of probe **6** (20 μM) in CH_3OH: H_2O (9:1, [v/v]) showed that the average particle size is 500-1500 nm approximately **(Figure 4.21c)** whereas the average particle size of and probe **6**+ ClO^- mixture in CH_3OH: H_2O (9:1, [v/v]) is 200-2000 nm approximately **(Figure 4.21f)**.

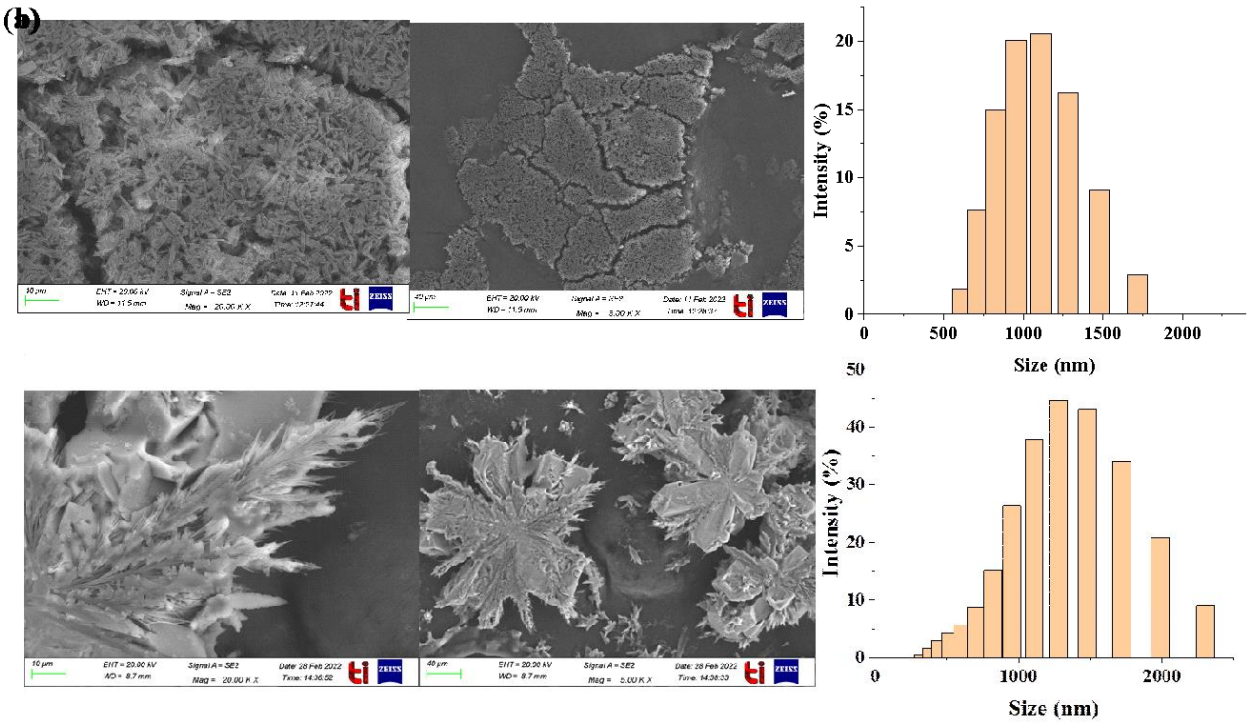

Figure 4.21: (a and b) SEM images for self-assembled fibre-like aggregates of probe 6 (20 µM) in $CH_3OH:H_2O$ (9 : 1); (c) DLS analysis of probe 6 (20 µM) in $CH_3OH:H_2O$ (9 : 1) solution; (d and e) SEM images of morphological changes in probe 6 (20 µM) after the addition of ClO^- ion in $CH_3OH:H_2O$ (9 : 1) solution; (f) DLS analysis of probe 6 (20 µM) after the addition of ClO^- ion in $CH_3OH:H_2O$ (9 : 1) solution.

4.2.3.7. Effect of pH on probe 6

We also checked the pH stability of probe **6** and its complex with the ClO^- ions. To check the pH stability we performed acid-base titration. From the acid-base titration it is clear that probe **6** was stable in the pH range from 5-10 at λ_{em} = 500 nm. The stability of probe **6** in the pH range 5-10 establishes its benefit for rapid monitoring in environmental and biological backgrounds **(Figure 4.22)**. The complex of probe **6** and ClO^- ions was also stable in pH range from 3-11 at λ_{em} = 520 nm, so the detection of these ions using probe **6** could be well performed in this pH range.

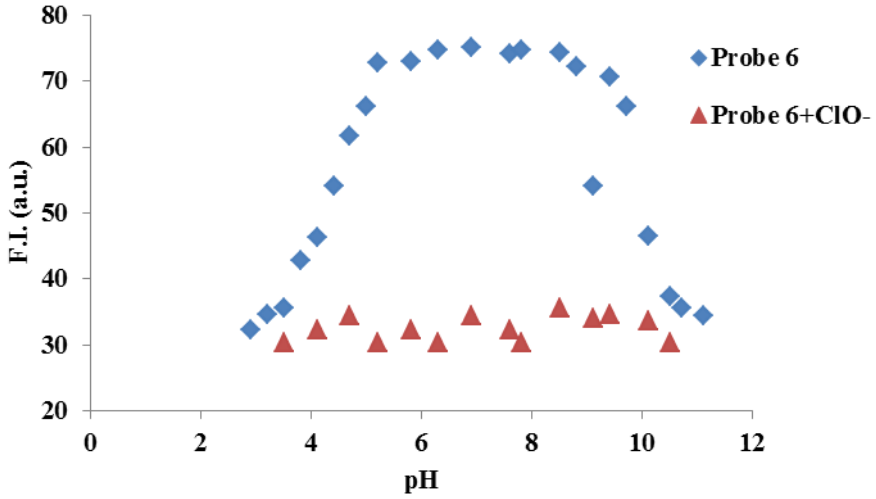

Figure 4.22: Effect of pH on emission spectra of probe 6 (20 µM) and its complex with ions in CH_3OH: H_2O (9:1, [v/v]) at 520 nm.

4.2.3.8. Time-correlated single photon counting (TCSPC) study

To further get insight of probe **6** behavior towards for ClO^- ion, we performed the time resolved fluorescence spectroscopy at 500 nm wavelength. The decay behavior of probe **6** and its ClO^- ion complexes is best fitted in third exponential function. The average decay time for probe **6** was found out to be 0.05 ns and has three life time components of 0.77 ns (~28.75 %), 2.86 ns (~18.3%) and 0.03 ns (~52.95%). After the addition of ClO^- ion the average life time increased to 0.71 ns with three life time components of 0.93 ns (~12.45 %), 1.61 ns (~83.77%) and 0.05 ns (~3.78%) **(Figure 4.23)**. The increase in the average life time of probe **6** after binding with ClO^- ion suggests the dynamic quenching behavior.

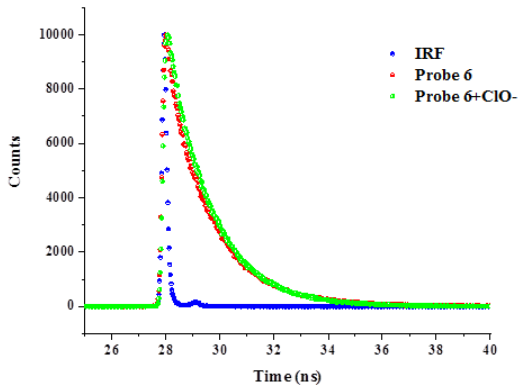

Figure 4.23: Time resolved fluorescence decay of probe 6 and probe 6+ ClO^-.

4.2.3.9. Cell Viability

We examined the in-vitro detection the ClO^- ions using cell based system in A549 lung cancer cell line for the possible biological applicability of probe **6** and to determine whether the probe **6** can specifically detect ClO^- ions under physiological conditions. We chose lung cancer cells (A549) since they are responsible for the greatest number of cancer related deaths. The cell viability experiment was performed to check the cytotoxicity of probe **6** on the cancer cell line. The cell viability assay results showed that probe **6** is statistically non-siginificant cytotoxic in nature. 0.6%, 4.2%, 6.1%, 6.5% and 8.9% lesser cell survival/ growth was found due to the treatment of 1, 5, 10, 25 and 50 µM concentrations of probe **6** respectively. Hypochlorite is known for its cytotoxic effect and showed up to a 17.6% loss of cell viability at the 100 µM hypochlorite concentration. Probe **6** was also checked for toxicity in combination with hypochlorite where different concentrations (5, 10, 25 and 50 µM) of hypochlorite were treated with 10, 25 and 50 µM concentrations of probe **6 (Figure 4.24)**. A slight decrement in the cell viability was observed where the viability of cells decreased from 91.5% to 76.1% with increasing hypochlorite concentration and 25 µM probe **6** concentrations. Similar trend was observed for probe **6** concentration 50 µM where viability of cells decreased from 98.6% to 77.5% with increasing hypochlorite (ClO^-) concentration.

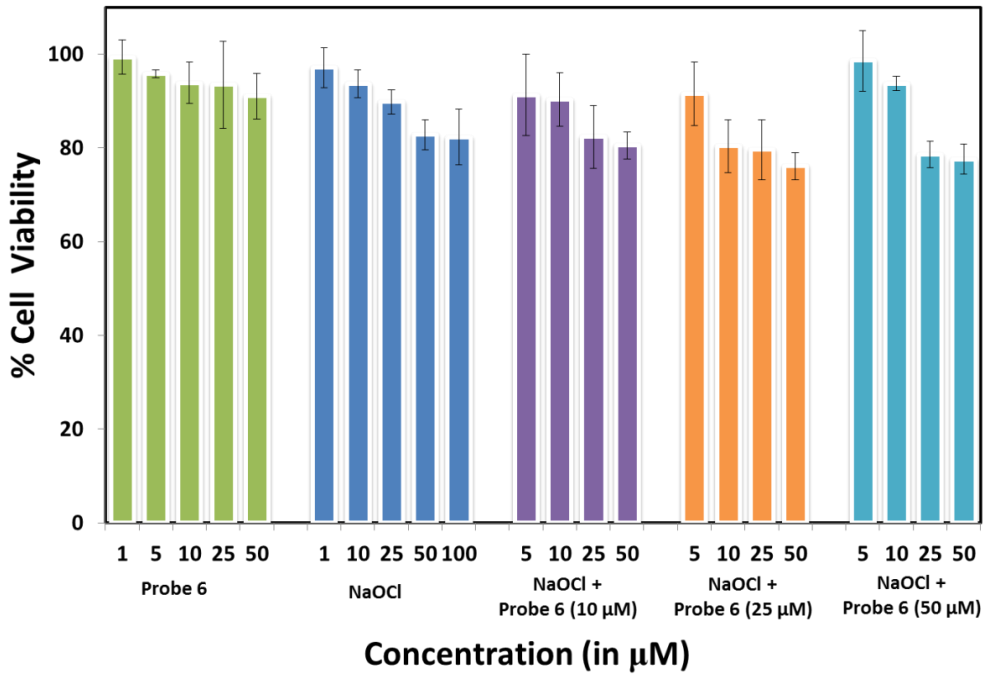

Figure 4.24: Biocompatibility of probe 6 and NaOCl.

4.2.3.10. *In-vitro* bioimaging

It has been observed that cancer cells have elevated levels of oxidative stress and hence have more ClO^- levels when compared with normal cells. Lung carcinoma epithelial cell line (A549) were used to study the effect of probe **6** where the cells were cultured till it reached a confluency of 70-80 % and then incubated with probe **6** (30 µM) and ClO^- (0-100 µM) for 3 h. Cellular imaging shows the good permeability of probe **6** with bluish-green fluorescence in the cytosol which is localized near the nucleus. Probe **6** showed bluish-green fluorescence with pixel intensity of 2.47 x 10^5 and very little red fluorescence with pixel intensity of 0.67 x 10^5 which was observed due to the presence of intrinsic hypochlorite (**Figure 4.25a**). On addition of extrinsic hypochlorite in the form of NaOCl, red fluorescence increased with maximum pixel intensity of 3.1 x 10^5 at ClO^- concentration of 100 µM and bluish-green fluorescence first increases with pixel intensity upto 4.0 x 10^5 at 5 µM ClO^- concentration and then decreases showing pixel intensity of 1.6 x 10^5 at 100 µM ClO^- concentration. The exponential increase in red fluorescence was observed with pixel intensity of 3.08 x 10^5 up to 10 µM ClO^- concentration and thereby saturation was observed (**Figure 4.25 b-i**).

Pixel intensity was measured for the bluish-green and red fluorescence which showed an increase in bluish-green fluorescence with increasing ClO^- concentration. After 5 µM, a decrease in intrinsic fluorescence was observed. On the other hand, an exponential increase in red fluorescence was observed up to 10 µM ClO- concentration after which saturation was observed (**Figure 4.25j)**. Minimum detection limit of hypochlorite was observed at 2.5 µM for 30 µM probe **5** concentration where quenching in green fluorescence was observed at 25 µM. The results clearly showed that probe **6** can detect ClO^- ions in A549 at concentrations as low as 2.5 µM.

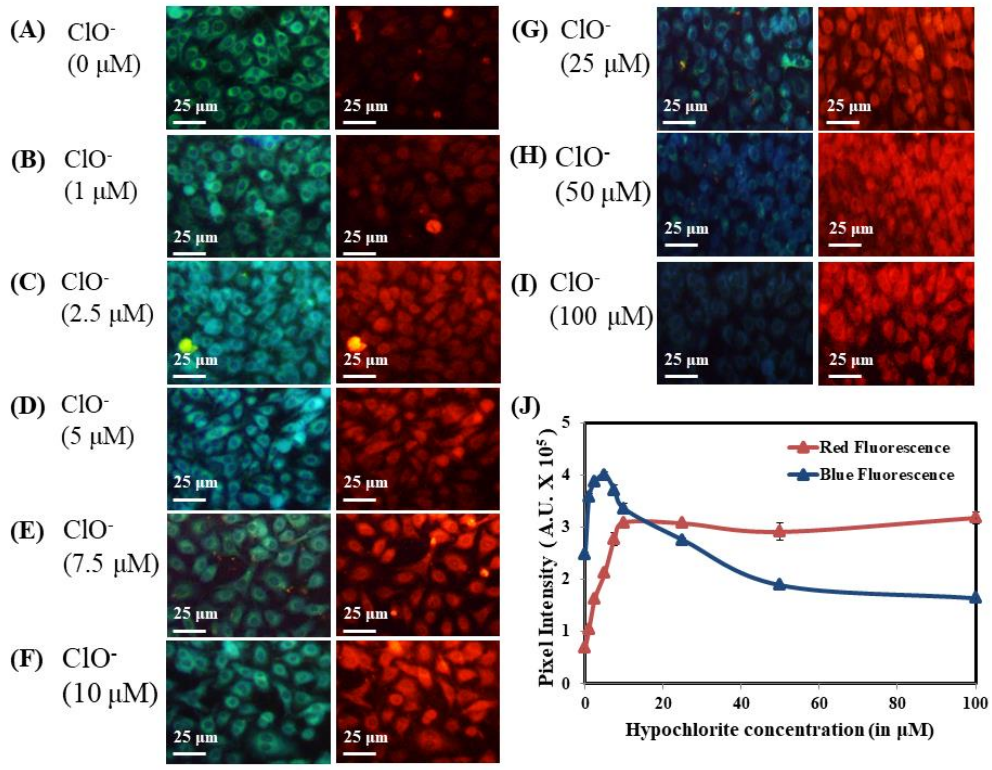

Figure 4.25: In-vitro bio-sensing of hypochlorite using probe 6.

4.2.4. Conclusion

In conclusion, we have designed and synthesized a Schiff base probe **6** for the detection of hypochlorite (ClO^-) ion with high selectivity and sensitivity in CH_3OH-H_2O solution. Probe **6** displayed absorption peak at 410 nm and weak emission peak at 500 nm. The absorption and emission band of probe **6** showed bathochromic shift after the addition of ClO^- ions. The lowest detection limit for ClO^- ions was calculated to be 5.5 µM with the binding constant of 1.8×10^3

M^{-1}. The probe **6** has good application in biological imaging with very low cytotoxicity. The sensing mechanism was investigated using ^{1}H NMR titrations.

4.3.

Effect of conjugation on excited state intramolecular proton transfer process in hydroxy aryl benzothiazole based Schiff base

Abstract

The photophysical properties of donor-π-acceptor chromophores can be improved by changing the donor or acceptor group and by enhancing the π-conjugation. The increase in conjugation induces restricted intramolecular rotations in molecule leading to the aggregation induced emission (AIE). In this study, the photophysical behavior of probe **7**, with high conjugation system was explored. A highly selective and sensitive fluorescent chemosensor was designed and developed for the detection of F^- and CN^- ions. Absorption and fluorescence techniques were used to evaluate the photophysical and sensing behavior of probe **7**. Interestingly, the probe **7** exhibits a ratiometric fluorescence "*turn-on*" response to both the anions in CH_3CN solvent. Probe **7** also exhibited intramolecular charge transfer phenomenon. The lowest detection limit for F^- and CN^- ions was 7.6×10^{-8} M and 1.1×10^{-7} M, respectively. The stoichiometry of probe **7** towards F^- and CN^- ions was determined using job's plot.

4.3.2. Experimental section

4.3.2.1. Synthesis of probe 7

The compound **5a** (200 mg, 0.8 mmol) and 2-hydroxy-1-naphthaldehyde (156 mg, 0.9 mmol) were stirred at 70 °C in ethanol for 3 h **(Scheme 4.5)**. The reaction mixture was cooled on completion and the solid was filtered and washed with ethanol to obtain orange coloured solid of probe **7** in 85% yield. m. p. 270-275 °C ^{1}H NMR (DMSO-d_6, 400MHz): δ (ppm) 9.63 (d, 1H, J = 8 Hz, -C=N), 8.48 (d, 1H, J = 8 Hz, ArH), 8.22 (d, 1H, J = 8 Hz, ArH), 8.13 (d, 1H, J = 8 Hz, ArH), 8.05 (d, 1H, J = 8 Hz, ArH), 7.92 (d, 1H, J = 12 Hz, ArH), 7.76 (dd, 1H, J_1 = 4 Hz, J_2 = 8 Hz, ArH), 7.54-7.50 (m, 2H, ArH), 7.44-7.42 (m, 1H, ArH), 7.34-7.30 (m, 2H, ArH), 7.24 (d, 1H, J = 4 Hz, ArH), 6.95 (d, 1H, J = 8 Hz, ArH) **(Figure A30)**. ^{13}C NMR (DMSO-d_6, 100 MHz): δ (ppm) 173.1, 165.4, 157.9, 155.4, 151.9, 147.1, 138.4, 134.5, 133.7, 130.3, 129.6, 128.8, 127.1, 125.6, 124.3, 123.2, 122.5, 121.0, 116.9, 112.5, 109.1, 108.6 **(Figure A31)**. HRMS (ESI-TOF): (m/z) $[M+H]^+$ calcd for $C_{24}H_{17}N_2O_2S$: 397.1007, found: 397.1015 **(Figure A32)**.

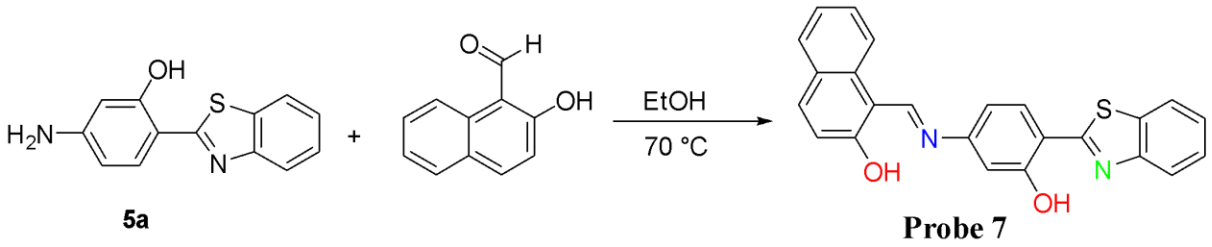

Scheme 4.5: Synthesis of probe 7.

4.3.3. Results and discussion

4.3.3.1. Synthesis and structural characterization

Probe **7** was synthesized in good yield by heating compound **5a** with 2-hydroxy-1-naphthaldehyde in ethanol. The desired probe **7** was then characterized using spectroscopic techniques such as ^{1}H NMR, ^{13}C NMR and HRMS. The ^{1}H NMR spectra of probe **7** showed characteristic doublet peak of imine (-C=N-) protons at δ 9.63 ppm. The doublet of imine proton can be due to the long range coupling with naphthaldehyde ring proton and the significant downfield shift indicated that the hydroxyl group and imine forms stable six-membered cyclic ring through intramolecular hydrogen bonding. It is important to note that the presence of intramolecular hydrogen bonds of the type O-H···N or O···H-N in probe **7** are favorable for the development of enol-imine and keto-amine type of tautomerism and the optical characteristic involves both ESIPT and ICT photophysical mechanisms.

4.3.3.2. Photophysical properties of probe 7

The Photophysical properties of probe **7** were studied using absorption and emission spectroscopy. Absorption spectrum of probe **7** (20 μM) in CH_3CN showed one high energy transition band at 400 nm in CH_3CN and two low energy transition bands at 445 nm and 475 nm. Also, probe **7** (20 μM) exhibited emission band at 505 nm after being excited at 400 nm with Stokes shift of 105 nm. Since, probe **7** contains electron donor and acceptor units, the intramolecular charge transfer (ICT) process may be enabled. Various solvents of different polarity were used to gain insight into how intramolecular charge transfer affects the steady state absorption and emission spectra. In non-polar solvents the absorption peak was at 400 nm but as we increased the polarity of the solvents the absorption maximum showed red shift to 475 nm with enhancement in the shoulder band at 535 nm **(Figure 4.26a)**. The red shift in the absorption

maximum can be attributed to intramolecular charge transfer in the molecule from hydroxy naphthalene unit to benzothiazole unit. Similarly, in most of the solvents the emission maxima was at 505 nm but in methanol and H_2O the emission maxima shifts to 535 nm and 560 nm respectively **(Figure 4.26b)**. The shift in the emission maximum also suggested the intramolecular charge transfer. Probe **7** also showed visible color changes from light yellow to orange as the polarity of the solvents was increased **(Figure 4.26c)**.

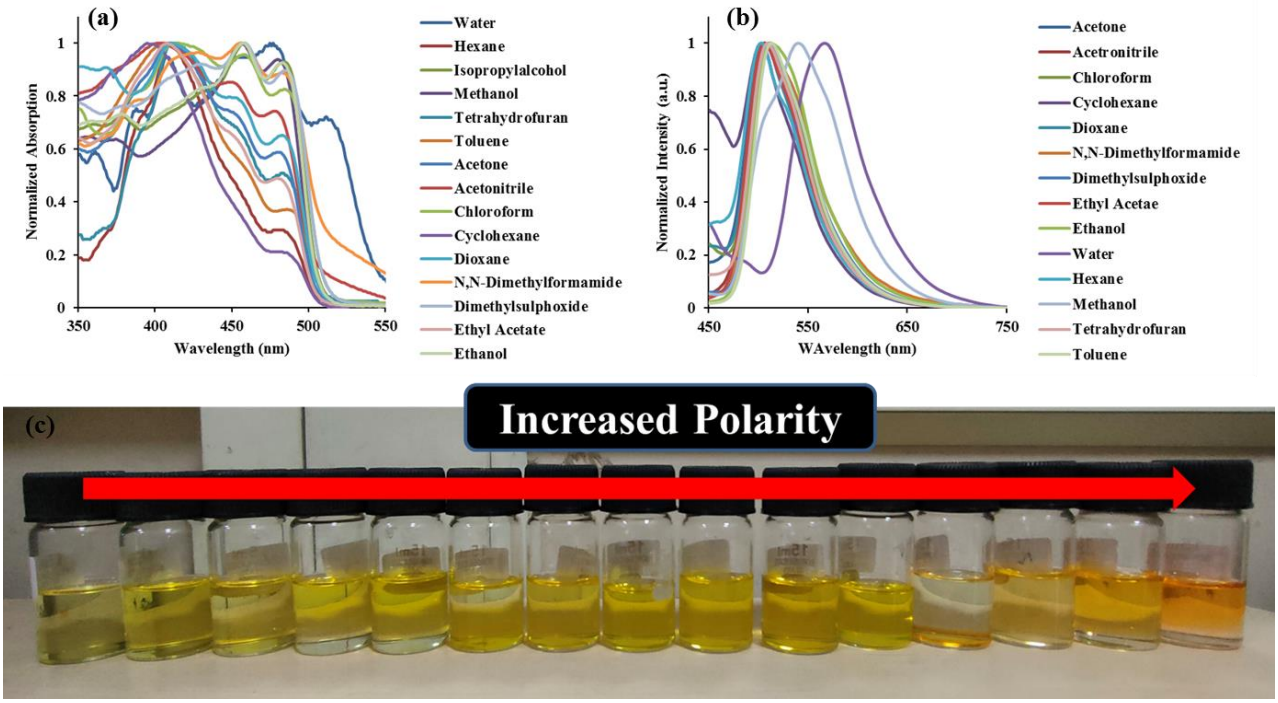

Figure 4.26: (a) absorption spectra and (b) emission spectra of probe 7 in solvents of different polarity, and (c) colorimetric response of probe 7 (20 µM) upon increasing polarity of the solvent.

Table 4.3: Photophysical properties of probe 7.

S.No.	Solvent	λ_{max} (nm)	Molar absorptivity ε ($M^{-1}cm^{-1}$)	λ_{em} (nm)	Stokes shift Δν (cm^{-1})	Quantum yield (Φ)
1	Hexane	405	6050	505	4890	0.49
2	Cyclohexane	405	16300	505	4890	0.45
3	Toluene	405	19500	505	4890	0.51
4	Chloroform	405	14900	505	4890	0.59

5	Tetrahydrofuran	405	5300	505	4890	0.53
6	Acetone	405	15550	505	4890	0.55
7	Dioxane	405	15700	505	4890	0.55
8	Ethyl acetate	405	19550	505	4890	0.56
9	Dimethylsulphoxide	455	17550	505	2180	0.48
10	N,N-Dimethylformamide	455	15300	505	2180	0.54
11	Acetonitrile	405	16900	505	4890	0.72
12	Isopropylalcohol	475	15400	505	1250	0.75
13	Ethanol	455	18350	505	2180	0.58
14	Methanol	475	16100	535	2360	0.65
15	Water	475	5300	560	3190	0.69
Stokes shift = $1/(\lambda_{em}- \lambda_{max})$, Reference for QY = Quinine Sulphate						

4.3.3.3. Aggregation Induced Emission (AIE) studies

Aggregation induced emission (AIE) characteristics are frequently seen in organic fluorophores with rotors. We looked into the AIE impact of naphthalene rotor in probe **7**. As a result, AIE experiment was carried out in CH_3CN/H_2O with continuously changing H_2O content. The absorption spectra of probe **7** showed blue shift from 400 nm to 355 nm as the H_2O percentage was increased from 0 to 50%. However, as H_2O fractions increased from 60 % to 100 %, the absorption intensity progressively increased with noticeable red shift from 355 nm to 480 nm and an apparent leveling off tail in the absorption band was observed **(Figure 4.27a)**. The visible color change of probe **7** solution upon increasing the H_2O ratio was observed. The level off tailing can be due to the Mie scattering and aggregation of probe **7** upon increasing the H_2O ratio. The development of J-type aggregates is correlated with the bathochromic shift. Further, by changing the H_2O percentage in CH_3CN solution from 0-100% variation in the emission spectra of probe **7** was also seen. With the increase in the H_2O fraction the emission intensity was also increased **(Figure 4.27b)**. This enhancement in the emission intensity is assigned to the aggregation induced emission process in probe **7**.

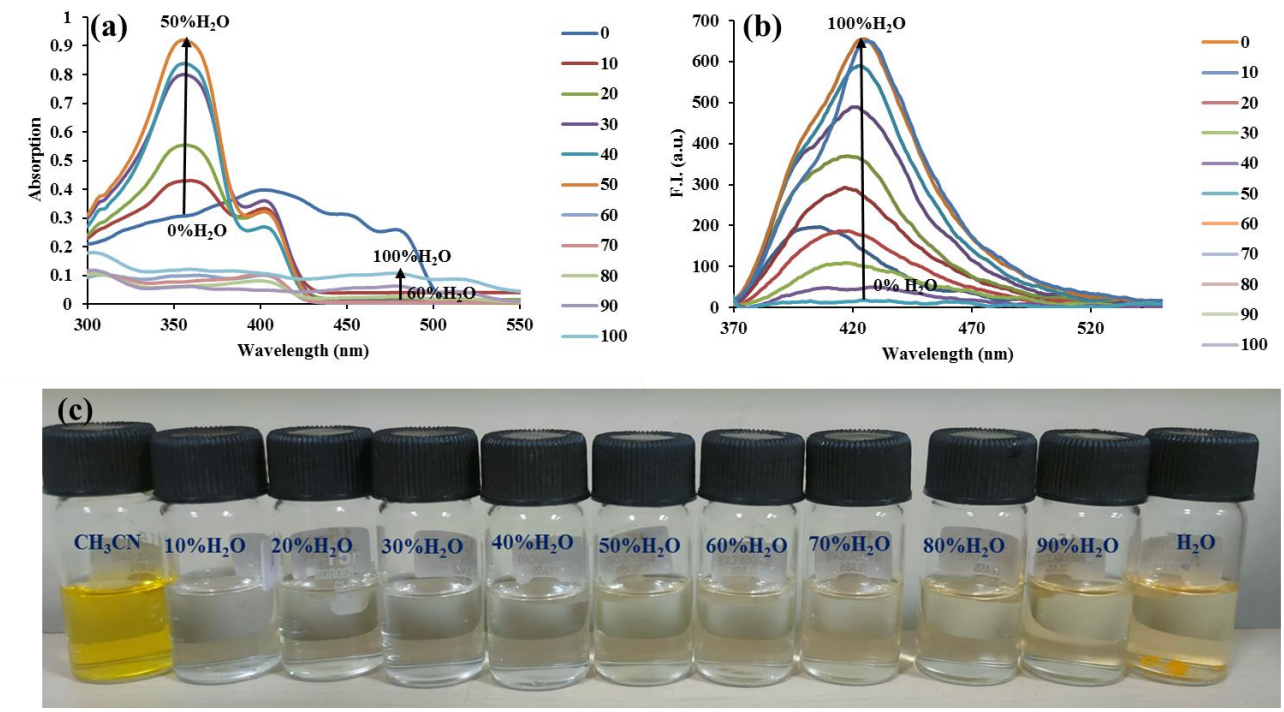

Figure 4.27: (a) Absorption spectra and (b) emission spectra of probe 7 with increasing H_2O ratio in CH_3CN. Image: Colorimetric response of probe 7 upon increasing H_2O content in CH_3CN.

To investigate the aggregation behavior of probe **7** dynamic light scattering (DLS) experiment was performed. DLS experiment supported aggregation formation and determined the size of probe **7** in different H_2O: CH_3CN ratios. In pure CH_3CN, the size was 20-100 nm with an average size of 50 nm with PDI value of 0.3, while in 50% CH_3CN-H_2O; it was between 100-500 nm with average size of 250 nm with PDI value of 0.6. This hydrodynamic diameter increases to 1250 nm in pure H_2O with PDI value of 0.8 **(Figure 4.28)**. The particle size of probe **7** in pure CH3CN through FESEM was found to be 20 nm and in 50% CH_3CN-H_2O the particle size increased to 150 nm whereas in pure H_2O the particle size was found to be 993 nm **(Figure 4.29)**. The DLS and FESEM results were in coherence.

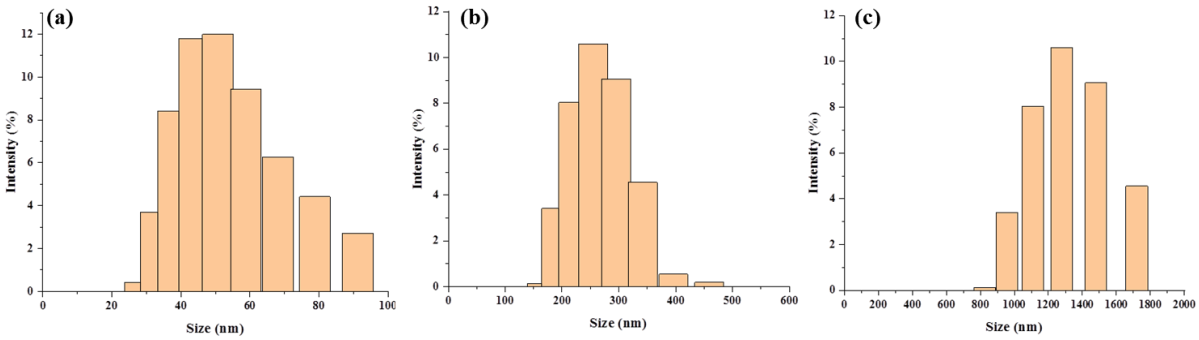

Figure 4.28: DLS of probe 7 in (a) CH_3CN, (b) 50% H_2O:CH_3CN and (c) H_2O.

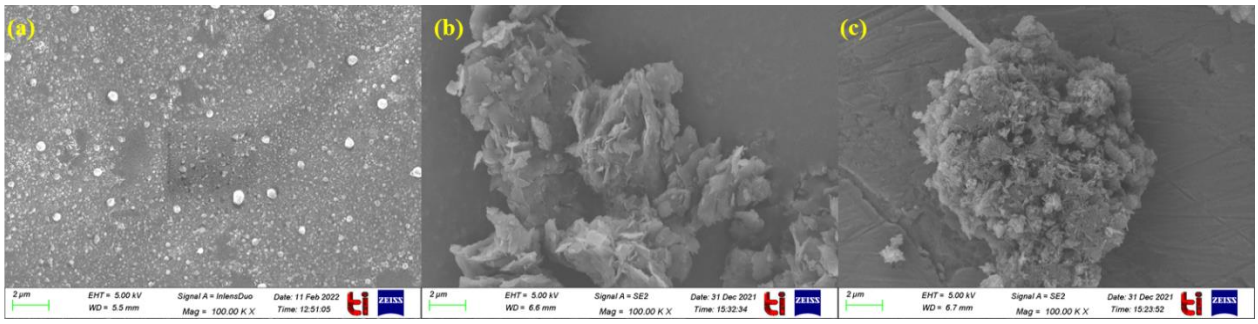

Figure 4.29: FESEM images of probe 7 in (a) CH_3CN, (b) 50% H_2O:CH_3CN and (c) H_2O.

4.3.3.4. Anion binding behavior of probe 7

The binding behavior of probe **7** (20 µM) towards various anions was studied in CH_3CN. As discussed earlier, probe **7** showed one high energy transition band at 400 nm and two low energy transition bands at 445 nm and 475 nm. A weak intensity emission band at 505 nm was observed upon excitation at 400 nm. The anion binding affinity of probe **7** was examined in the presence and absence of different anions *viz* F^-, Cl^-, Br^-, I^-, $H_2PO_4^-$, NO_3^-, AcO^-, ClO^-, SO_4^{2-}, $P_2O_7^{4-}$, CN^-, SCN^- by using absorption and emission spectroscopy. Probe **7** displayed strong affinity for F^- and CN^- anions. For both F^- and CN^- anion, an absorption band at 475 nm was enhanced and the band at 400 nm and 445 nm disappeared **(Figure 4.30a)**. Additionally, probe **7** showed a good colorimetric response, changing the solution's light yellow color to orange and dark yellow color with F^- and CN^- anion, respectively. Similarly, in the fluorescence spectra the emission maxima of probe **7** at 505 nm showed blue shift to 450 nm upon interaction with F^- and CN^- anions **(Figure 4.30b)**.

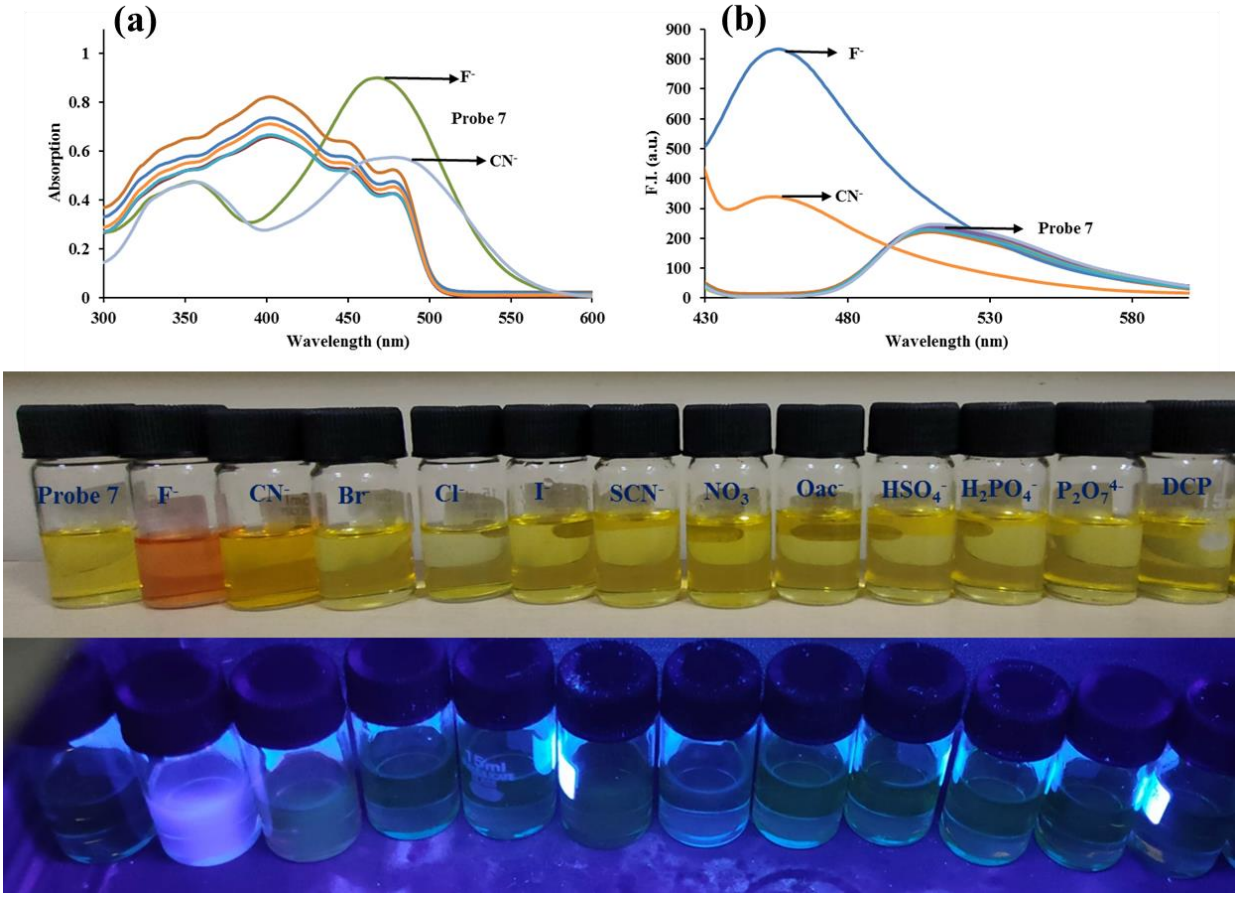

Figure 4.30: (a) Absorption and (b) emission spectra of probe 7 (20 µM) upon interaction of different anions (1000 µM) in CH_3CN. Images: Colorimetric and fluorogenic responses of probe 7 (20 µM) upon interaction with different anions in CH_3CN.

Titration assays were used to investigate the binding affinities of probe **7** for F^- and CN^-. The absorption band centred at 405 nm decreased with slight blue shift to 390 nm and the band at 475 nm was enhanced upon incremental addition of F^- (0-100 µM). Also the absorption band at 330 nm was slightly enhanced and the band at 295 nm was decreased with the formation of two isosbestic points at 435 nm and 355 nm. Formation of two isosbestic points indicated the presence of equilibrium between multiple species **(Figure 4.31a)**. Similar to this, when the emission titration experiment was carried out by the sequential addition of F^- ions (0-360 µM), intensity of emission band at 450 nm was enhanced **(Figure 4.31b)**. The emission spectrum with different mole fractions of F^- ions was taken in order to assess the reaction stoichiometry between probe **7** and F^- ions. For the interaction between probe **7** and F^-, the maxima at a mole

fraction of 0.5 indicated 1:1 stoichiometry **(Figure A34a)**. From the emission titration, using the Benesi-Hildebrand equation, the binding constant for probe **7** and F^- ion was found out to be 2.9×10^5 M^{-1}. The lowest detection limit for F^- ions was calculated to be 7.6×10^{-8} M.

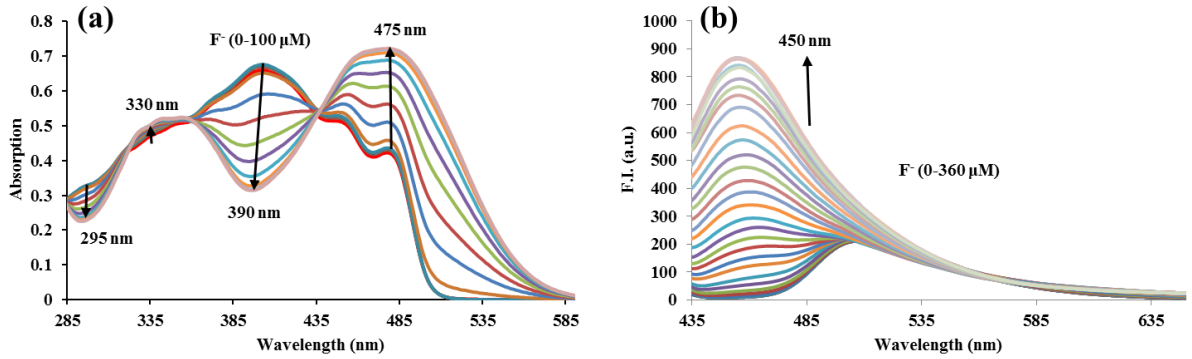

Figure 4.31: (a) Absorption spectra of probe 7 upon incremental addition of 0-100 µM of F^- ions and (b) emission spectra of probe 7 upon incremental addition of 0-360 µM of F^- ions.

Furthermore, similar results were obtained for CN^- ion. In the absorption titration, band at 475 nm increased while the band at 405 nm decreased with slight blue shift to 390 nm **(Figure 4.32a)**. The formation of two isosbestic points indicated the equilibrium between multiple species. Similarly, in emission titration the band at 505 nm decreased with simultaneous increase in the emission intensity at 450 nm **(Figure 4.32b)**. The binding constant for CN^- ion was found out to be 7.5×10^3 M^{-1} with lowest detection limit of 1.1×10^{-7} M **(Table 4.4)**. The job's plot indicated the 1:1 stoichiometry for probe **7** and CN^- ions **(Figure A34b)**. We also performed interference study to understand the selectivity of probe **7** towards F^- and CN^- ions. Insignificant changes in the emission spectrum of probe **7**+F^- and probe **7**+CN^- were noticed after the addition of excess of the competitive anions (1000 µM) **(Figure 4.33)**. This indicated that probe **7** has relatively high selectivity for both F^- and CN^- anions.

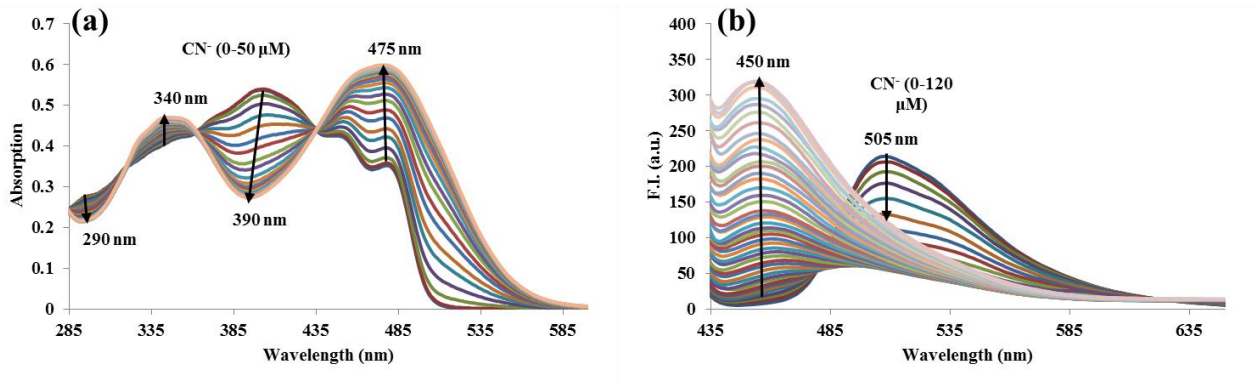

Figure 4.32: (a) Absorption spectra of probe 7 upon incremental addition of 0-50 µM of CN^- ions and (b) emission spectra of probe 7 upon sequential addition of 0-120 µM of CN^- ions.

Table 4.4: Binding constant ad detection limit of probe 7 for F^- and CN^- ions.

	Binding Constant	LOD
Probe 7 + F^-	2.9×10^5 M^{-1}	7.6×10^{-8} M
Probe 7 + CN^-	7.5×10^3 M^{-1}	1.1×10^{-7} M

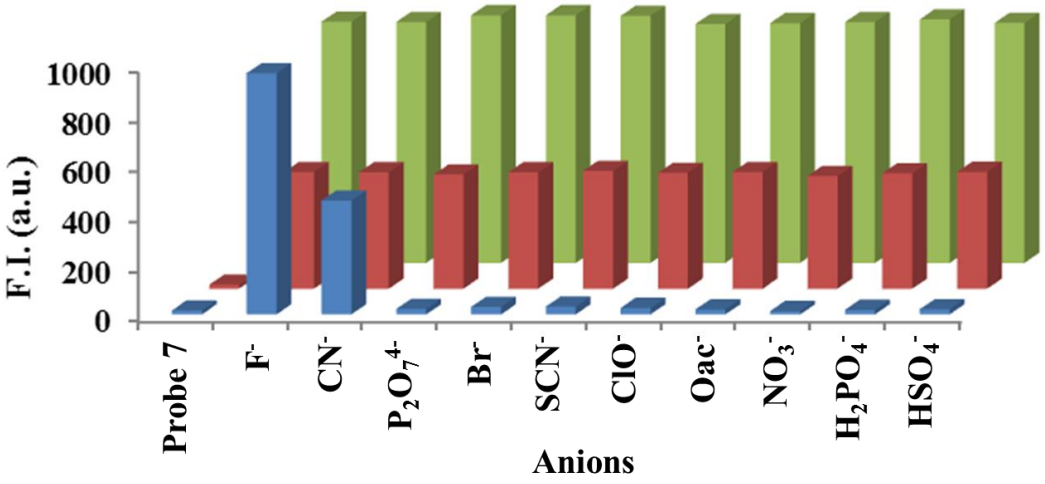

Figure 4.33: Relative emission intensity of probe 7 (20 µM) in CH_3CN (λ_{ex}= 390 nm) with different competing anions in the absence and presence of F^- and CN^- ions at λ_{em}= 450 nm, where blue bars represent the emission intensity change of probe 5 with different anions (1000 µM) and red bars represent probe 7 + CN^- in the presence of different relevant competing anions (1000 µM), green bars represent probe 7 + F^-.

4.3.3.5. Time-correlated single photon counting (TCSPC) study

The fluorescence enhancement behavior of probe **7** upon binding with F^- and CN^- ions was confirmed from results of TCSPC study. The decay behavior of probe **7** and its complexes is best fitted in third exponential function **(Figure 4.34)**. Probe **7** showed three components having lifetimes of 1.12 ns, 6.90 ns and 0.07 ns respectively. The population of all the components was 7.32, 8.45 and 84.23%, respectively. The average life time for probe **7** comes out to be 0.09 ns. Upon the addition of F^- ions to the solution of probe **7**, again three components were obtained with life time of 1.43 ns, 1.53 ns and 2.44 ns. The population of all the components was 27.85, 39.02 and 33.14%, respectively. The average life time was calculated to be 1.71 ns. Similarly, after the addition of CN^- ions the average life time were 2.12 ns **(Table 4.5)**. The increase in the average life time supported the fluorescence enhancement after the addition of both the anions.

Table 4.5: Fluorescence lifetime measurements for Probe 7 and its anion complexes in CH_3CN.

CH_3CN	τ_1 (ns)	τ_2 (ns)	τ_3 (ns)	α_1	α_2	α_3	χ^2	τ_{av} (ns)
Probe **7**	1.12	6.90	0.07	7.32	8.45	84.23	1.12	0.09
Probe **7**+ F^-	1.43	1.53	2.44	27.85	39.02	33.14	1.18	1.71
Probe **7**+CN^-	1.76	9.52	2.36	35.42	0.94	63.64	1.07	2.12

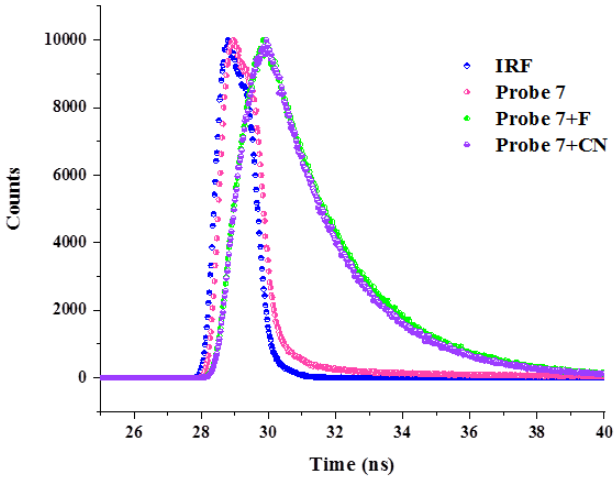

Figure 4.34: Time resolved fluorescence decay of probe 7 and probe 7 with F^- and CN^- ions.

4.3.3.6. ^1H NMR of probe 7 with F^- and CN^- ions

To find the possible binding mechanism of F^- and CN^- ions with probe **7** ^1H NMR titrations were performed in CD_3CN-d_3. Probe **7** showed hydroxyl protons at δ 11.33 ppm which upon the addition of 1.0 equiv. of F^- ions disappeared. Also the imine proton at δ 10.23 ppm showed downfield shift to δ 9.63 ppm **(Figure 4.35)**. The disappearance of hydroxyl proton suggested the H-binding of F^- ion with naphtholic hydrogen. Further with the addition of F^- ions to the solution of probe **7** the upfield shift in the aromatic protons at δ 6.63 ppm due to phenolic protons was observed which can be due to charge delocalization on probe **7** after binding to F^- ions. Moreover, the protons at δ 7.53-7.26 ppm due to naphthalene ring were also shifted upfield indicating the change in the charge distribution after deprotonation.

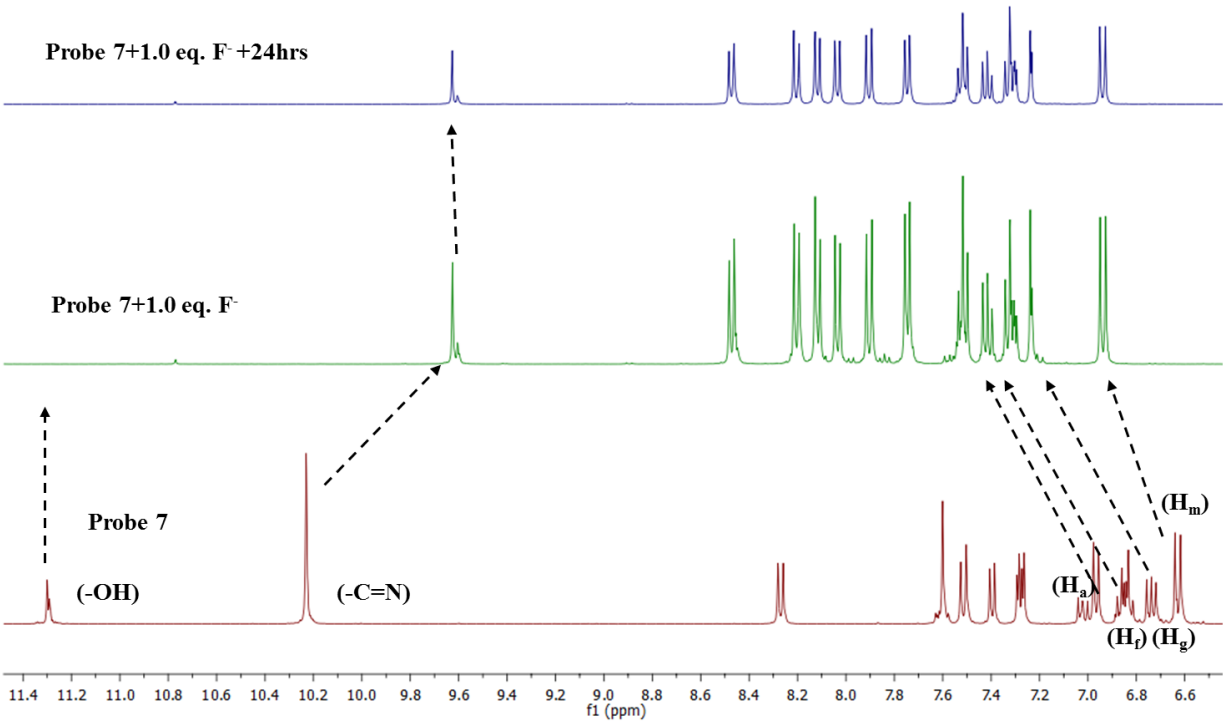

Figure 4.35: ^1H NMR spectra of probe 7 with F^- ions in CD_3CN-d_3.

Similarly, the addition of 1.0 equiv. of CN^- ions to probe **7** resulted in a considerable alteration in the protons. The hydroxyl protons (-OH) at δ 11.33 ppm disappeared with the addition of CN^- ions whilst the imine proton (-C=N) at δ 10.21 ppm shifted downfield to δ 9.65 ppm **(Figure 4.36)**. The observed upfield changes corresponding to the aromatic protons clearly supported

both deprotonation and charge propagation throughout the molecule. This implied that deprotonation of the –OH proton and nucleophilic addition of the CN^- ions to probe **7**. The imine proton vanished completely and new signal at δ 8.06 ppm appeared owing to a stable H-bonding interaction with the negatively charged oxygen atom of probe **7**.

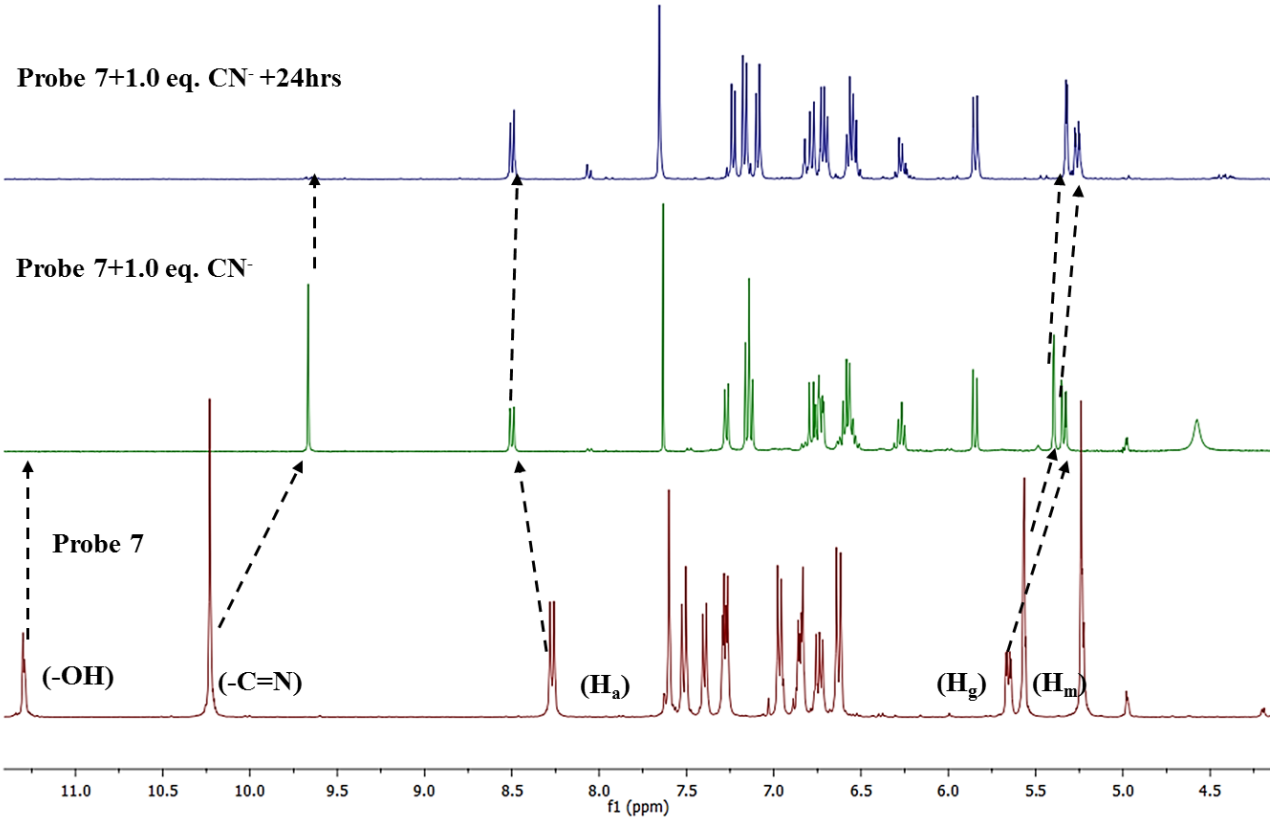

Figure 4.36: ^{1}H NMR spectra of probe 7 with CN^- ions in CD_3CN-d_3.

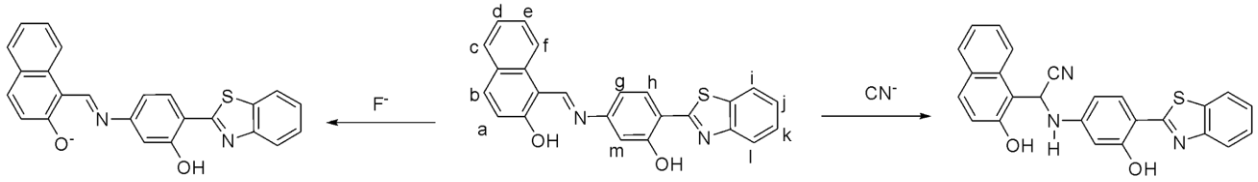

Scheme 4.6: Possible binding mechanism of probe 7 with F^- and CN^- ions.

4.3.4. Conclusion

In conclusion, an effective chemosensor probe **7** was synthesized and its phoyophysical behavior was investigated in several solvent systems. Probe **7** also exhibited AIE phenomenon. Probe **7** was used for the detection of F^- and CN^- ions with high selectivity and sensitivity in CH_3CN solvent system. The F^- and CN^- ions were detected by probe **7** with naked eye. Probe **7** can detect F^- and CN^- ions with lowest detection limit of 7.6×10^{-8} M and 1.1×10^{-7} M, respectively. Both the F^- and CN^- ions bind to probe **7** through different mechanisms.

Summary of chapter 4

To summarize, the study involved the synthesis and evaluation of three Schiff base compounds **(5-7)** that are based on benzothiazole unit. The Photophysical properties of these compounds were analyzed using experimental and theoretical calculations. The compounds contain unsymmetrical double proton transfer sites, one with imine bond (-C=N-) and hydroxyl group (-OH), and the other with benzothiazole and hydroxyl groups positioned in close proximity, allowing for intramolecular O-H···N hydrogen bonding. The para position of the hydrogen acceptor sites was modified with substituents that have the ability to donate electron or increase conjugation. The introduction of the $–NEt_2$ unit in probe **6** caused the electron density to shift towards the core of the molecule. Additionally, the presence of electron donating unit reduced the acidity of the –OH unit, which hindered the ESIPT and allowed the ICT phenomenon to dominate.

As expected, probes **5-7** showed ICT phenomenon with the introduction of electron donating group and with the increase in the conjugation. Further, probe **5-7** which is a Schiff base containing a imine linkage, showed weak emission in solution state due to limited flexibility and intramolecular motions. Probe **5** and **7** exhibited a strong aggregation induced emission (AIE) phenomenon compared to probe **6**, which had no AIE due to the presence of large $–NEt_2$ group which restricted the intramolecular rotation, as discussed in chapter **3**. These probes were also tested for their sensing properties towards anions.

Probe **5** detected F^- and $P_2O_7^{4-}$ ions in CH_3CN: H_2O (9: 1, v/v) with low detection limit whereas with the introduction of electron donating group ($–NEt_2$) the dipolar moment of the probe **6** increases which leads sensing in more polar solvent. Probe **6** detected ClO^- ions in CH_3OH: H_2O (9: 1, v/v). Further, the conjugation was increased in probe **7** that leads to increased polarity so the CH_3CN system was used for the detection of F^- and CN^- ions through H-bonding.

Chapter 5

Study of excited state intramolecular proton and charge transfer in 8-hydroxyquinoline Schiff bases and application as sensor

Previously we have studied the effect of heteroatom on the hydroxyaryl benzazole ring, herein; we want to explore the effect of heteroaromatic ring on the ESIPT phenomenon. The 8-hydroxyquinoline moiety has been extensively used fluorophore for the sensing. Numerous areas of material science and pharmaceutics have made substantial use of 8-hydroxyquinoline and its derivatives.[134-138] The extensive use of 8-hydroxyquinoline and its derivatives is mostly due to its known metal chelation capabilities.[139-143] 8-Hydroxyquinoline acts as second most important chelating agent after EDTA and binds through N and O atoms. In this regard, 8-hydroxyquinoline and its derivatives have been applied to industrial and analytical applications for the separation and detection of metal ions.[144-148] 8-Hydroxyquinoline derivatives are well known as fluorogenic sensor for metal ions. When complexed with different metal ions, the fluorescence properties of 8-hydroxyquinoline allows it to be used as optoelectronic materials. The aluminium complex of 8-hydroxyquinoline has been used in the optoelectronics and solar cells.[149-157] Enol and imine groups in hydroxyquinoline change their relative acidity and basicity upon photoexcitation to the first excited singlet state, shifting equilibrium with new pK_a value in the excited state and causing excited state proton transfer (ESPT).[158-161] Each species has distinctive lifespan and emission wavelength. 8-Hydroxyquinoline based Schiff bases are widely used as sensors and have different applications.

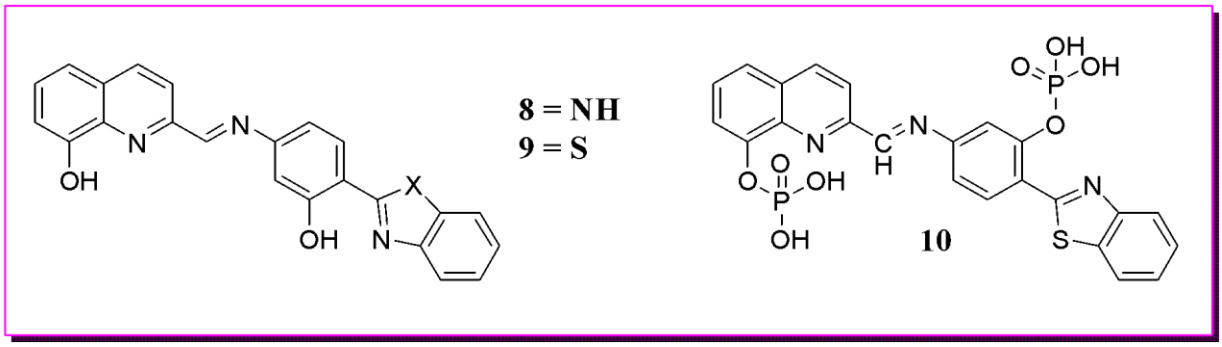

Figure 5.1: The different derivatives of 8-hydroxyquinoline Schiff base.

Here, the effects of 8-hydroxyquinoline moiety as Schiff base on hydroxyl aryl benzazole is evaluated and was further used for evaluation its behavior towards common ions. This chapter has been separated into three sections based on the types of substituents.

5.1. Study of excited state intramolecular proton transfer process for 8-hydroxyquinoline-benzimidazole Schiff base.

5.2. Study of excited state intramolecular proton transfer process for 8-hydroxyquinoline-benzthiazole Schiff base.

5.3. Protection and deprotection of excited state intramolecular proton transfer process in 8-hydroxyquinoline-benzthiazole Schiff base for enzyme sensing.

5.1.

Study of excited state intramolecular proton transfer process for 8-hydroxyquinoline-benzimidazole Schiff base

5.1.1. Abstract

In this chapter we studied the effect of heteroaromatic ring on the photophysical behavior of probe **8**. Further, the importance of benzimidazole in co-ordination chemistry has piqued the interest in development of transition metal complexes. Aside from benzimidazole, quinoline based Schiff base derivatives are also essential physiologically. This section covered the study of ESIPT phenomenon on the molecular systems containing double intramolecular hydrogen bonding sites. The synthesized probe **8** displayed an absorption peak at 370 nm. Upon excitation at 370 nm, probe **8** displayed emission peak at 535 nm with significant Stokes shift of ~165 nm. Indeed, probe **8** exhibited ESIPT phenomenon from an acidic ―OH (phenolic group) hydrogen donor to basic -C═N― (imine group) hydrogen acceptor units. Further, probe **8** was established as chromo-fluorescent sensor towards DCP ions in H_2O: CH_3CN (1:1, v/v, pH=7.1). The appearance of new absorption peaks at 435 nm in the presence of DCP ions confirms the complex formation. The probe **8**.DCP displayed "turn-on" emission at 540 nm. The detection limit of probe **8** towards DCP ions was determined to be 1.5×10^{-7} M.

5.1.2. Experimental section

5.1.2.1. Synthesis of compound 8a

Compound **8a** was synthesized by using reported method.[162] 8-hydroxy-2-methyl-quinoline (500 mg, 3 mmol) was added to selenium oxide (1 gm, 9 mmol) in dioxane (20 mL) under inert atmosphere of N_2 gas. The reaction mixture was refluxed for 21 hrs at 90 °C. After the completion of reaction the mixture was filtered. The obtained solid was purified using silica column chromatography to give yellow colored compound **8a** in 55% yield. m.p.: 92-97 °C. ^{1}H NMR ($CDCl_3$-*d*, 400MHz): δ (ppm) 9.93 (s, 1H, -CHO), 8.34 (d, 1H, *J* = 8 Hz), 7.33-7.27 (m, 3H), 6.97-6.93 (m, 1H). ^{13}C NMR (DMSO-d_6, 100 MHz): δ (ppm) 193.2, 159.4, 152.2, 139.1, 137.6, 136.4, 128.9, 125.8, 120.9, 115.7.

5.1.2.2. Synthesis of probe 8

The compound **8a** and **1a** were stirred at 70 °C in ethanol for 6 h **(Scheme 5.1)**. The reaction mixture was cooled on completion of reaction and the separated solid was filtered and washed with ethanol to obtain orange coloured solid of probe **8** in 73 % yield. m.p. 250-260 °C ^{1}H NMR (DMSO-d_6, 400MHz): δ (ppm) 8.86 (s, 1H, -C=N), 8.60 (dd, 1H, J_1 = 4 Hz, J_2 = 8 Hz, ArH), 8.14 (d, 1H, J = 4 Hz, ArH), 8.01-7.98 (m, 2H, ArH), 7.83 (d, 1H, J = 4 Hz, ArH), 7.66-7.59 (m, 4H, ArH), 7.47-7.42 (m, 2H, ArH), 7.21 (dd, 1H, J = 4 Hz, ArH) **(Figure A35).** ^{13}C NMR (DMSO-d_6, 100 MHz): δ (ppm) 161.2, 156.6, 155.1, 153.6, 151.0, 150.8, 136.8, 136.6, 135.7, 132.4, 130.3, 129.6, 126.1, 122.7, 122.4, 118.1, 117.6, 114.2, 113.3, 112.8, 110.2, 107.4 **(Figure A36)**. **HRMS** (ESI-TOF): (m/z) $[M+H]^+$ calcd for $C_{23}H_{16}N_4O_2$: 380.1413, found: 380.0142 **(Figure A37)**.

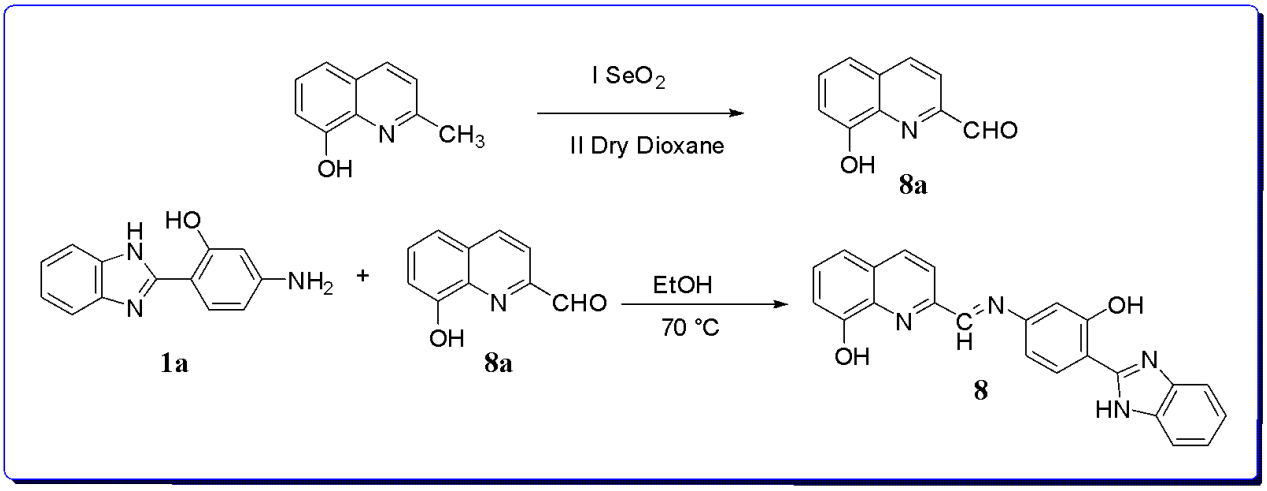

Scheme 5.1: Synthesis of probe 8.

5.1.3. Results and Discussion

5.1.3.1. Photophysical properties of probe 8

Absorption and emission spectroscopic methods were used to observe the photophysical behavior of probe **8**. Absorption spectrum of probe **8** (20 μM, CH_3CN) displayed absorption maxima at 370 nm. Probe **8** (20 μM, CH_3CN) showed weak emission band at 535 nm upon excitation at 370 nm, accomplished by Stokes shift of 165 nm. Probe **8** contains functional diversity in terms of hydrogen donor units and hydrogen acceptor units, which may lead to excited state intramolecular proton transfer and intramolecular charge transfer phenomenon. We examined the absorption and emission spectra in various polarity mediums to gain understanding into the above mentioned mechanism. The absorption maximum for probe **8** in non-polar

solvents like hexane, cyclohexane was at 370 nm. As the polarity of the solvent was increased the absorption maximum showed red shift from 370 nm to 380 nm whereas in H_2O probe **8** showed absorption maxima at 410 nm. The red shift observed in the absorption spectra with increase in the polarity of the solvent can be due to enhanced intramolecular charge transfer process taking place in probe **8** **(Figure 5.2a)**. Similar findings were made incase of emission spectra, where probe **8** showed the emission maximum at 420 nm and 425 nm in non-polar medium but as the polarity of the solvents was increased the emission maximum was red shifted to 525 nm and 535 nm. The red shift of 115 nm can be due to intramolecular charge transfer phenomenon occurring in the molecule. Further in H_2O the emission maxima showed blue shift to 428 nm which can be the result of protic solvent interaction with basic imine nitrogen **(Figure 5.2b)**.

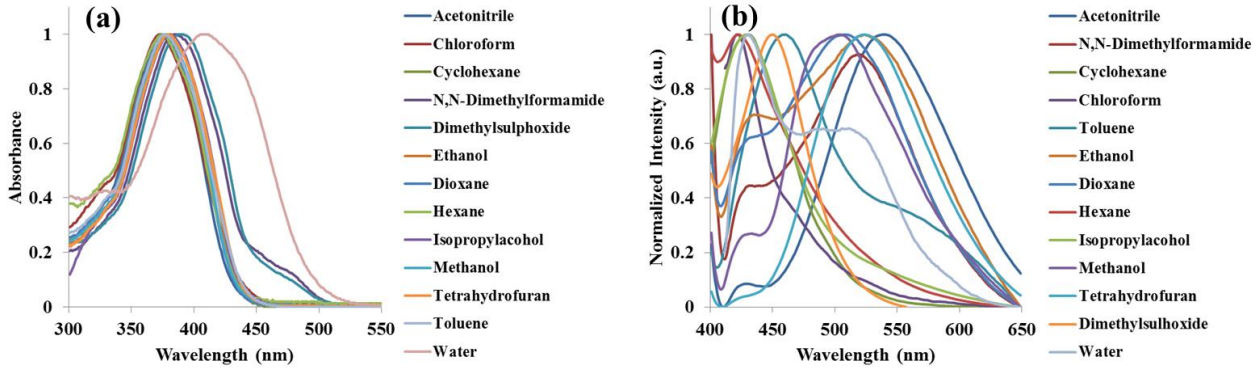

Figure 5.2: Normalized (a) absorption spectra and (b) emission spectra of probe 8 in different solvents.

Table 5.1: Photophysical properties of probe 8.

S.No.	Solvent	λ_{max} (nm)	Molar absorptivity ε ($M^{-1}cm^{-1}$)	λ_{em} (nm)	Stokes shift Δν (cm^{-1})	Quantum yield (Φ)
1	Hexane	370	7650	420	3200	0.35
2	Cyclohexane	370	7900	425	3500	0.33
3	Toluene	370	12600	455	5030	0.39
4	Chloroform	370	13350	420	3200	0.41
5	Tetrahydrofuran	370	11850	425	3500	0.40
6	Acetonitrile	370	14600	535	8310	0.44

7	Dioxane	380	15600	510	7400	0.50
8	Dimethylslphoxide	380	14500	515	6900	0.55
9	N,N-Dimethylsulphoxide	380	13500	525	7300	0.51
10	Isopropylalcohol	380	14650	525	7300	0.57
11	Ethanol	380	14150	525	7300	0.54
12	Methanol	380	13900	500	6300	0.52
13	Water	410	9850	428	1100	0.51
Stokes shift = $1/(\lambda_{em}- \lambda_{max})$, Reference for QY = Quinine Sulphate						

5.1.3.2. Spectral characteristics of probe 8

The UV-Vis absorption spectra and fluorescence spectra in H_2O: CH_3CN (1:1, v/v, pH=7.1) following addition of various anions at 20 µM concentration were monitored for the anion recognition. Probe **8** revealed strong absorption maximum at 375 nm in H_2O: CH_3CN (1:1, v/v, pH=7.1). Among different anions tested, probe **8** displayed selectivity only for diethyl chlorophosphate (DCP) ions in H_2O: CH_3CN (1:1, v/v, pH=7.1) at 20 µM. Only DCP ions showed bathochromic shift and shifted the absorption band at 435 nm when probe **8** interacted with the various anions, whereas no meaningful change in the absorption spectra was observed on interaction with the other anions *viz.*, F^-, Cl^-, Br^-, I^-, $H_2PO_4^-$, NO_3^-, AcO^-, ClO^-, SO_4^{2-}, $P_2O_7^{4-}$, CN^-, SCN^-, Triethylphosphate (TEP), Tributylphosphate (TBP) **(Figure 5.3a)**. The absorption band at 435 nm was increased with a bathochromic shift while the band at 375 nm was decreased as concentration of the DCP ions was gradually increased up to 380 µM **(Figure 5.3b)**.

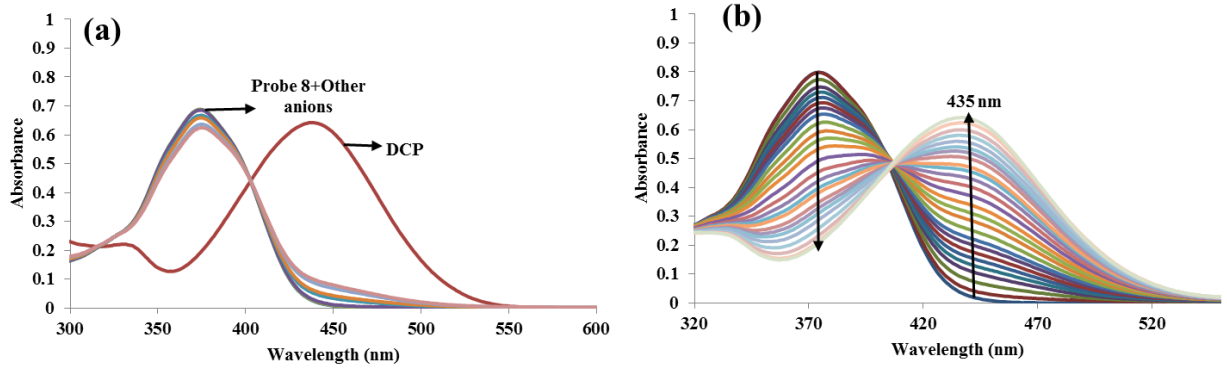

Figure 5.3: Absorption spectra of probe 8 (20 µM) in H_2O:CH_3CN (1:1, [v/v], pH=7.1) (a) in presence of different anions (1000 µM), and (b) upon incremental addition of 0-380 µM of DCP ions.

The fluorescence spectra of probe **8** in H_2O: CH_3CN (1:1, v/v, pH=7.1) at 20 µM concentration was recorded to observe the fluorescence properties of probe **8** towards DCP ions. Upon excitation at 370 nm the emission maximum was observed at 520 nm. Probe **8** demonstrated selectivity for DCP ions among the different anions **(Figure 5.4a)**. Probe **8** showed increase in emission intensity following interaction with DCP ions at 540 nm, whereas all other anions showed no change in emission intensity of probe **8**. After interacting with DCP ions, probe **8** formed more widespread π-conjugation systems, resulting in an increase in emission intensity.

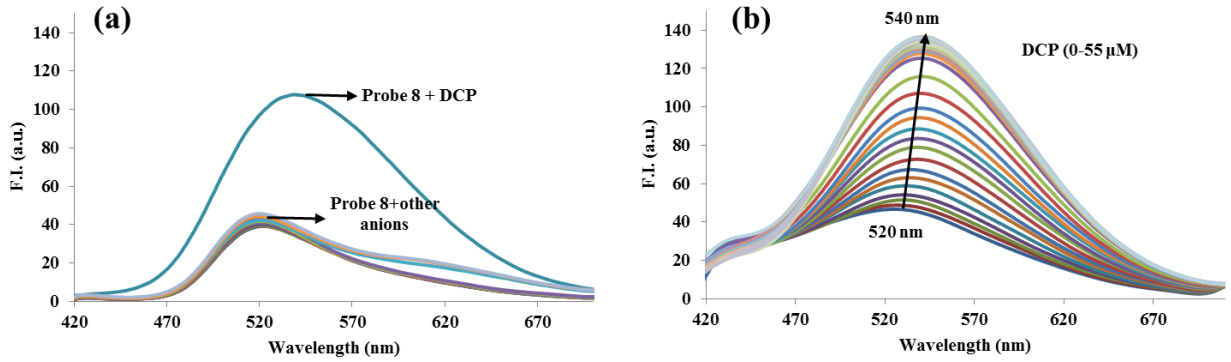

Figure 5.4: Emission spectra of probe 8 (20 µM) in H_2O:CH_3CN (1:1, [v/v], pH=7.1) (a) in presence of different anions (1000 µM), and (b) upon incremental addition of 0-55 µM of DCP ions.

After the addition of 55 µM of DCP ions, a plateau in the fluorescence spectra was achieved **(Figure 5.4b)**. A competitive experiment was performed to further examine whether probe **8** can detect DCP ions selectively even in the presence of other anions. To further test that whether probe **8** can selectively sense DCP ion even in the presence of other anions, competitive experiment was carried out. Probe **8** was treated with other anions in the presence of DCP ions. The results demonstrated that the presence of other ions did not significantly alter the fluorescence intensity of probe **8** in the presence of DCP ions **(Figure 5.5)**. These results indicated that the presence of other anions had no effect on the selectivity of probe **8** towards DCP ions.

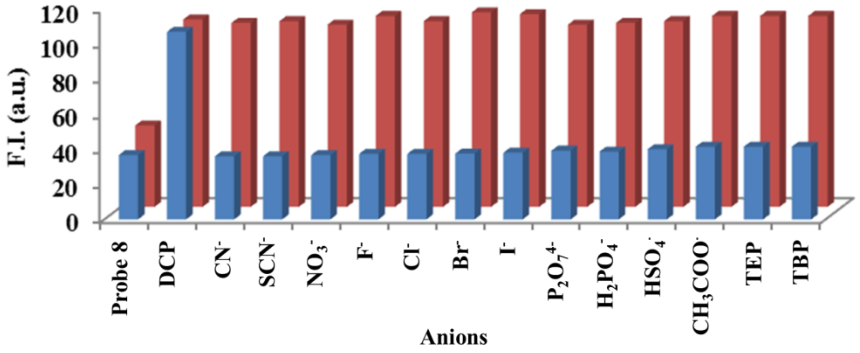

Figure 5.5: Relative emission intensity of probe 8 (20 µM) in H_2O: CH_3CN, 1:1 [v/v], pH=7.1 (λ_{ex}= 370 nm) with different competing anions in the absence and presence of DCP ions at λ_{em}= 540 nm, where blue bars represent the emission intensity change of probe 8 with different anions (1000 µM) and red bars represent probe 8+ DCP in the presence of different relevant competing anions (1000 µM).

Based on fluorescence titration, the detection limit of probe **8** for DCP ions ion was determined. The calibration curve for the determination of DCP ions was drawn. The lowest detection limit for DCP ion was determined to be 1.5×10^{-7} M. Additionally, the Benesi-Hildebrand equation was used to determine the binding constant between probe **8** and DCP ions. The measured fluorescence intensity $1/ [I-I_0]$ was changed as a function of 1/ [DCP] in a linear relationship with R^2 = 0.9925, indicating the 1:1 stoichiometry between probe **8** and DCP ions. The binding constant was determined from the fluorescence titration data and was found out to be 1.5×10^4 M^{-1}. Job's plot analysis was carried out to establish the stoichiometry between probe **8** and DCP ion. The maximum fluorescence intensity was found out to be at 0.5, indicating the formation of 1:1 stoichiometry **(Figure A39)**.

5.1.3.3. Effect of pH on probe 8

pH titration of probe **8** and it's complex with the DCP ion were carried out to examine the practical applicability in a wide pH range. The presence of aldimine (-C=N-) and hydroxyl group (-OH) can lead to the protonation or deprotonation of probe **8** under acidic or basic medium. In H_2O: CH_3CN (1:1, v/v), the effect of pH on probe **8** was observed. The probe **8** was stable in the pH range of 6.4-11.1 **(Figure 5.6)**. The fluorescence intensity in the pH range 6.4-11.1 showed negligible change. An increase in fluorescence intensity at 520 nm was seen below pH 6, which may have been caused by the protonation of the hydroxyl O and imine N atoms blocking the

ESIPT process. Further, the complex of probe **8** + DCP was stable in the pH range of 5-11, so the detection of DCP using probe **8** could be well performed in this pH range.

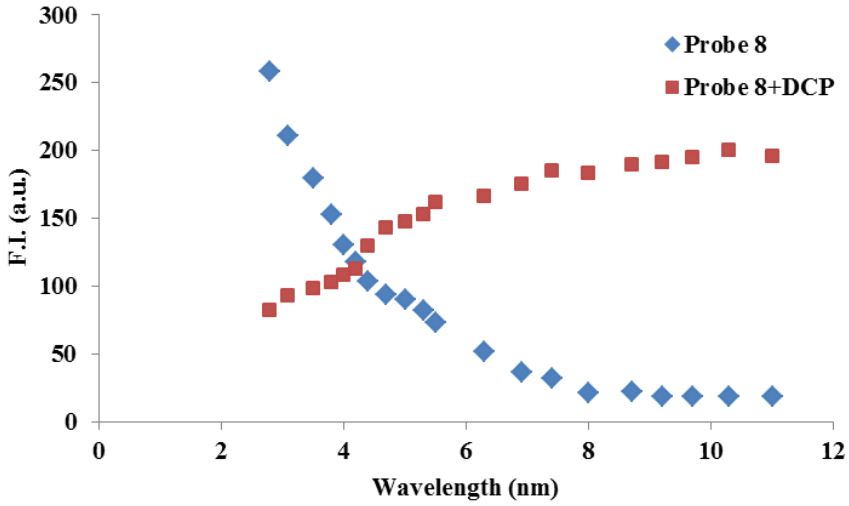

Figure 5.6: Effect of pH on probe 8 in H_2O: CH_3CN, 1:1 [v/v] at λ_{em}= 540 nm.

5.1.3.4. Time-correlated single photon counting (TCSPC) study

The results of fluorescence decay measurement using the TCSPC study have established that the fluorescence is increased upon interaction with DCP **(Figure 5.7)**. The tri-exponential function provides the best fit to decay behavior of probe **8** and its DCP complex. Probe **8** has three components with lifetime values of 1.65 ns, 6.26 and 0.15 ns and population of the components was 32.03 %, 56.38% and 11.58%, respectively. The average life time for probe **8** was found to be 0.97 ns. Upon adding DCP ions to the solution of probe **8**, three components were obtained with lifetime of 2.02, 5.88 and 0.22 ns with a population of 42.36%, 51.19% and 6.46%, respectively. The average lifetime was calculated to be 1.69 ns **(Table 5.2)**. The increase in average life time supports the fluorescence enhancement of probe **8** after binding with DCP ions.

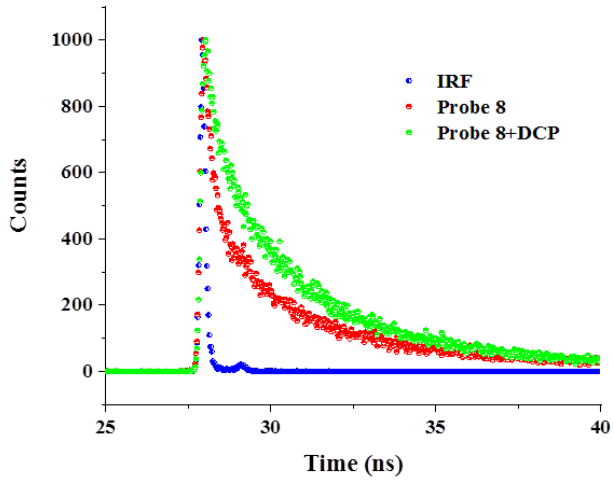

Figure 5.7: Time resolved fluorescence decay of probe 8 and its complex with DCP ions at λ_{em}= 540 nm in H_2O: CH_3CN (20 µM, 1:1, [v/v], pH=7.1).

Table 5.2: Fluorescence lifetime measurements for probe 8 and complex with DCP in H_2O: CH_3CN (1:1, [v/v], 20 µM).

H_2O:CH_3CN (1:1, [v/v])	τ_1 (ns)	τ_2 (ns)	τ_3 (ns)	α_1	α_2	α_3	χ^2	τ_{av} (ns)
Probe 8	1.65	6.26	0.15	32.03	56.38	11.58	1.08	0.97
Probe 8+DCP	2.02	5.88	0.22	42.36	51.19	6.46	1.07	1.69

5.1.3.5. Plausible Sensing Mechanism

To find the binding mechanism of probe **8** towards DCP ions ^{1}H NMR titrations were carried out in CD_3CN-d_3 **(Figure 5.8)**. The singlet at 8.86 ppm corresponds to H_h proton due to imine protons of probe **8** experienced a slight downfield shift to 8.93 ppm. The double doublet at 8.59 ppm and 8.14 ppm owing to H_j and H_i protons of 8-hydroxyquinoline shifted downfield to 8.76 ppm and 8.14 ppm respectively. The protons at 8.00 ppm due to H_a and H_b protons of benzimidazole ring were shifted downfield to 8.14 ppm and 8.04 ppm. Further, the protons at 7.47 ppm and at 7.44 ppm due to H_e and H_g protons of phenyl ring shifted to 7.69 ppm and 7.67 ppm. The protons at 7.23 ppm due to H_m proton were also slightly shifted. The protons of 8-hydroxyquinoline ring were not affected much which indicated that there is no change in the electronic configuration in 8-hydroxyquinoline ring after the addition of DCP. These results

showed that DCP did not bind with –OH group of 8-hydroxyquinoline ring. The change in the ^{1}H NMR spectra suggested the binding of DCP through OH group of the phenyl ring **(Scheme 5.2)**.

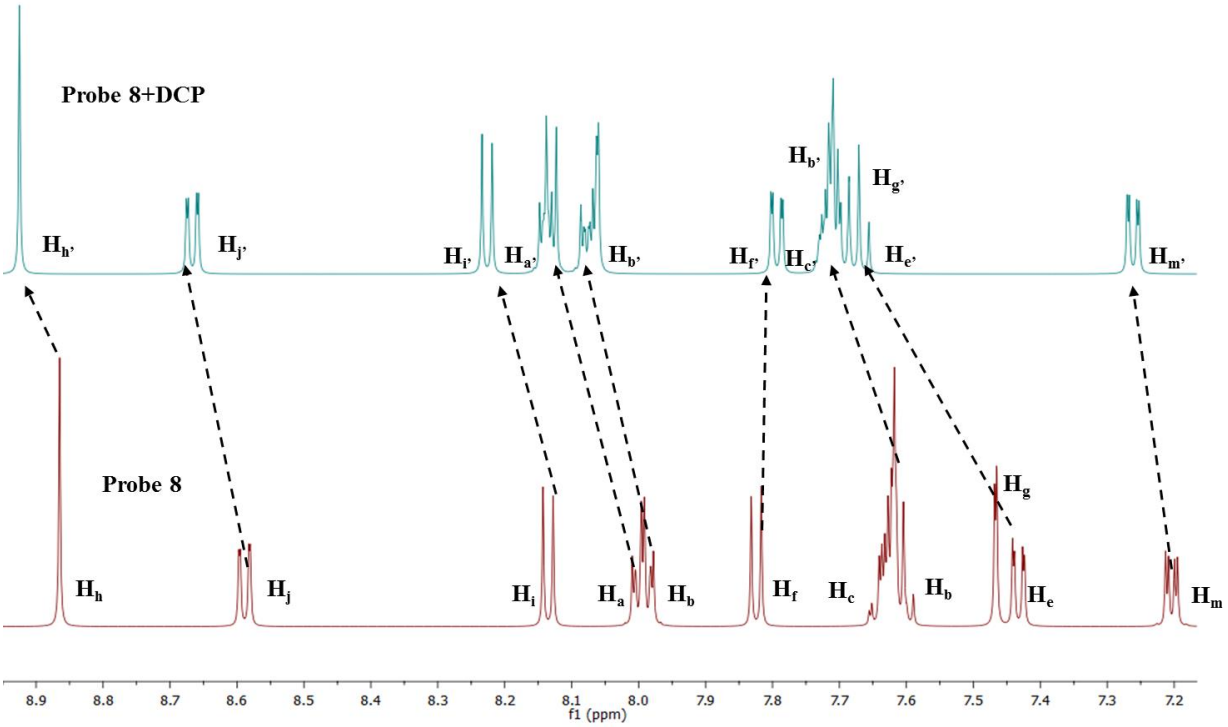

Figure 5.8: ^{1}H NMR spectra of probe 8 (5× 10^{-3} M) upon addition of 1.0 equiv. of DCP ions in CD_3CN-d_3.

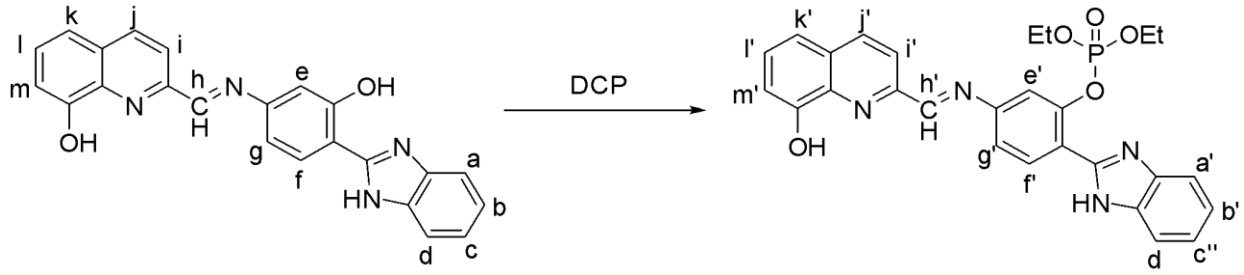

Scheme 5.2: Plausible mechanism for probe 8 and DCP binding.

5.1.4. Conclusion

In summary, the fluorescent properties of probe **8** towards DCP ions in H_2O: CH_3CN (1:1; v/v, pH = 7.1) were studied. Upon addition of DCP ions, absorption band of probe **8** at 435 nm was enhanced ratiometrically with respect to absorption band at 370 nm. Likewise, probe **6**.DCP

displayed emission enhancement response at 540 nm with respect to probe **8**'s emission at 520 nm in H_2O: CH_3CN (1:1; v/v, pH=7.1). The limit of detection of probe **8** towards DCP ions was measured to be 1.5×10^{-7}.

5.2.

Study of excited state intramolecular proton transfer process for 8-hydroxyquinoline-benzthiazole Schiff base

5.2.1. Abstract

This chapter covered the photophysical behavior of dual ESIPT based Schiff base and the effect of hetero-atom on the ESIPT phenomenon was studied. 8-Hydroxyquinoline-benzthiazole based Schiff base has been studied as quinoline moiety acts as a fluorophore and binding unit whereas with the introduction of benzothiazole moiety the weak fluorescent properties of 8-hydroxyquinoline can be modified. Probe **9** was found to be selective towards CN^- and $P_2O_7^{4-}$ ions through absorption and emission responses. Probe **9** displayed a ratiometric rise of peaks at 445 nm and 450 nm through absorption and emission spectra, respectively. The appearance of new absorption peaks confirmed the complex formation. The determined limits of detection of probe **9** towards CN^- and $P_2O_7^{4-}$ ions were 41 nM and 49 nM, respectively. Probe **9** also showed intramolecular charge transfer (ICT) phenomenon along with ESIPT.

5.2.2. Experimental section

5.2.2.1. Synthesis of probe 9

The compound **5a** and **8a** were stirred at 70 °C in ethanol for 9 h **(Scheme 5.3)**. The reaction mixture was cooled on completion of reaction and the solid was filtered and washed with ethanol to obtain orange coloured solid of probe **9** in 78 % yield. m.p. 285-290 °C; ^{1}H NMR (DMSO-d_6, 400MHz): δ (ppm) 8.50 (s, 1H, -C=N), 8.23 (dd, 1H, J_1 = 4 Hz, J_2 = 8 Hz, ArH), 8.07-8.02 (m, 2H, ArH), 7.78 (d, 1H, J = 4 Hz, ArH), 8.11 (s, 1H, ArH), 7.55 (d, 1H, J = 4 Hz, ArH), 7.49 (q, 2H, J = 8 Hz, ArH), 7.27-7.23 (m, 2H, ArH), 7.09-7.06 (m, 2H, ArH), 6.85 (dd, 1H, J_1 = 2 Hz, J_2 = 8 Hz, ArH) **(Figure A40)**. ^{13}C NMR (DMSO-d_6, 100 MHz): δ (ppm) 162.4, 161.6, 160.4, 158.5, 155.6, 153.5, 152.7, 137.7, 137.3, 134.4, 132.6, 131.5, 127.9, 126.5, 124.7, 124.4, 123.7, 121.0, 119.9, 115.3, 114.8, 109.9 **(Figure A41)**. **HRMS** (ESI-TOF): (m/z) $[M]^+$ calcd for $C_{23}H_{15}N_3O_2S$: 397.0885, found: 397.2060 **(Figure A42)**.

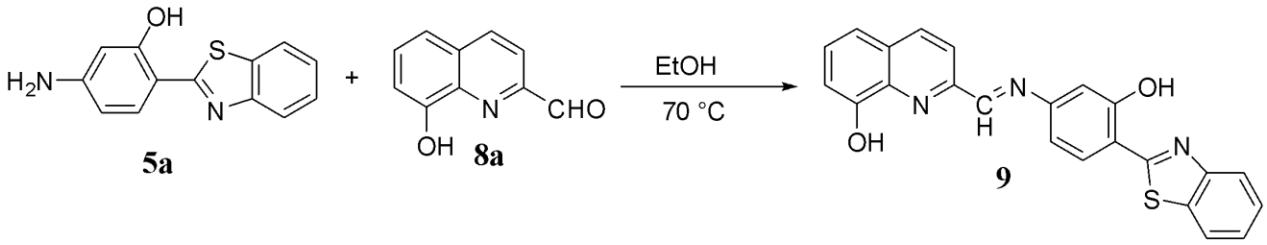

Scheme 5.3: Synthesis of probe 9.

5.2.3. Results and discussion

5.2.3.1. Photophysical properties of probe 9

The absorption and emission spectra of probe **9** was recorded in various solvents to check the effect of solvent polarity on the optical properties of the probe **9**. Solvent polarity typically affects the ground or excited state of fluorescent probe, which caused the absorption and emission spectra to shift bathochromically or hypsochromically. The probe **9** (20 μM) showed absorption peak at 360 nm in CH_3CN. Probe **9** exhibited two emission bands at 400 nm and 535 nm upon photoexcitation at 360 nm, accomplished by Stokes shift of 85 nm. Additionally, the absorption spectra of probe **9**, in different solvents displayed peak around 360 nm and showed weak dependency on the solvent environment **(Figure 5.9c)** whereas emission in low polarity environments such as cyclohexane, chloroform, acetonitrile, dioxane, tetrahydrofuran, and ethyl acetate showed peak around 400 nm. However, in polar environments, emission moves towards the longer wavelength. It is noteworthy that the intensity ratio of low and high Stokes shifted emission increases with the polarity of the environment **(Figure 5.9d)**. The bathochromic shift observed in the emission intensity with the polarity of the solvent can be due to the intramolecular charge transfer (ICT) phenomenon occurring in the molecule.

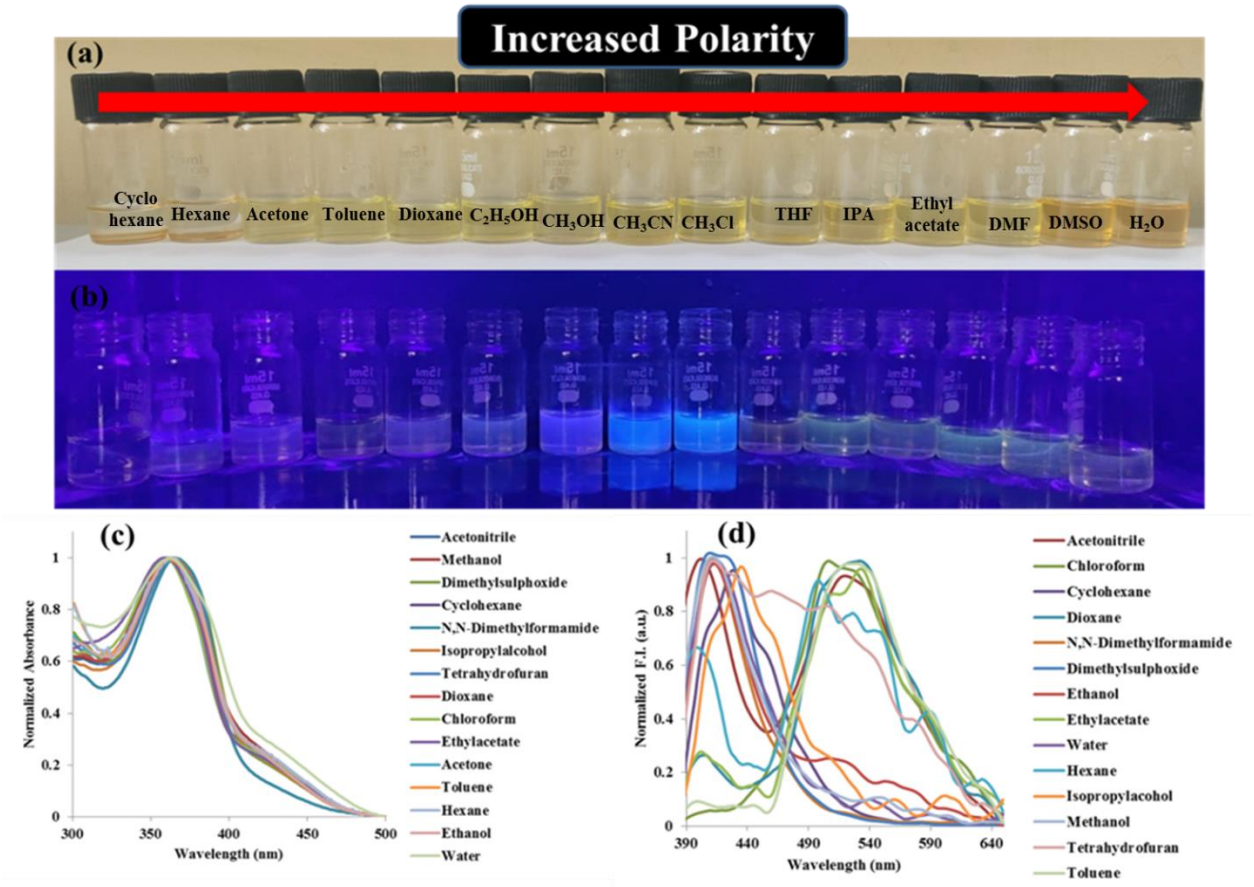

Figure 5.9: Effect of different solvents on probe 9 (a) under visible, (b) UV light of 365 nm, (c) absorption spectra and (d) emission spectra.

Table 5.3: Photophysical properties of probe 9.

S.No.	Solvent	λ_{max} (nm)	Molar absorptivity ε ($M^{-1}cm^{-1}$)	λ_{em} (nm)	Stokes shift Δν (cm^{-1})	Quantum yield (Φ)
1	Hexane	360	5550	400	2800	0.24
2	Cyclohexane	360	3300	400	2800	0.25
3	Toluene	360	30650	540	9300	0.41
4	Chloroform	360	29400	540	9300	0.44
5	Tetrahydrofuran	360	31250	400	2800	0.33
6	Acetonitrile	360	28900	535	8400	0.48
7	Dioxane	360	31200	540	9300	0.43

8	Dimethylsulphoxide	360	26800	415	3700	0.55
9	N,N-Dimethylformamide	360	35200	420	4000	0.51
10	Isopropylacohol	360	32400	430	4600	0.48
11	Ethanol	360	47000	420	4000	0.53
12	Methanol	360	28650	400	2800	0.49
13	Water	360	27000	410	3400	0.46
Stokes shift = $1/(\lambda_{em} - \lambda_{max})$, Reference for QY = Quinine Sulphate						

5.2.3.2. Absorption and Fluorescence studies of probe 9 towards anions

Probe **9** showed absorption band at 375 nm in CH_3CN:CH_3OH (9:1, v/v), which can be due to π-π* transitions. The recognition behavior of probe **9** towards anions *viz.* CN^-, I^-, Br^-, Cl^-, F^-, ClO^-, SCN^-, CH_3COO^-, $H_2PO_4^-$, NO_3^-, HSO_4^-, and $P_2O_7^{4-}$ was investigated using absorption and emission spectroscopy. Probe **9** showed selectivity towards CN^- and $P_2O_7^{4-}$ ions. Except for the CN^- and $P_2O_7^{4-}$ ions, the absorption spectrum of other anions added under the same conditions showed no change **(Figure 5.10a)**. The addition of CN^- ions to probe **9** (20 µM) in CH_3CN:CH_3OH (9:1, v/v) decreased the absorption intensity at 375 nm and a new absorption band appeared at 435 nm. Similarly, for $P_2O_7^{4-}$ ions, the absorption intensity at 375 nm decreased with the appearance of new band at 435 nm. A solution of probe **9** (20 µM) in CH_3CN:CH_3OH (9:1, v/v) was quantitatively titrated with CN^- and $P_2O_7^{4-}$ ions using absorption spectroscopy. A plateau was observed after the addition of 80 µM of CN^- ions to probe **9** and the absorption intensity at 375 nm was decreased with simultaneous increase in the intensity at 445 nm **(Figure 5.10b)**. Similar results were observed for the $P_2O_7^{4-}$ ions as the plateau was obtained after the incremental addition of 0-240 µM of $P_2O_7^{4-}$ ions **(Figure 5.10c)**.

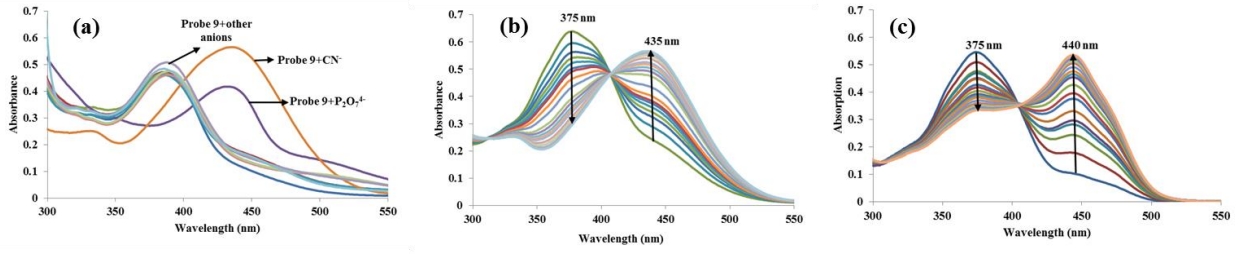

Figure 5.10: Absorption spectra of probe 9 (20 µM) in CH_3CN:CH_3OH (9:1, v/v) (a) in presence of different anions (1000 µM), (b) upon incremental addition of 0-80 µM of CN^- ions, (c) upon incremental addition of 0-

240 µM of $P_2O_7^{4-}$ ions.

Further, on excitation at 375 nm, probe **9** (20 µM) in CH_3CN:CH_3OH (9:1, v/v) showed two emission bands at 400 nm and 535 nm. The fluorescence of probe **9** was enhanced for both the CN^- and $P_2O_7^{4-}$ ions while the emission intensity with other anions remained unchanged **(Figure 5.11a)**. Furthermore, as CN^- ions were gradually added to probe **9**, the emission intensity at 455 nm was increased while the intensity at 535 nm was decreased. After the addition of 0-100 µM of CN^- ions, a plateau was achieved **(Figure 5.11b)**. Similar results were observed for $P_2O_7^{4-}$ ions a plateau was observed after the addition of 0-140 µM **(Figure 5.11c)**.

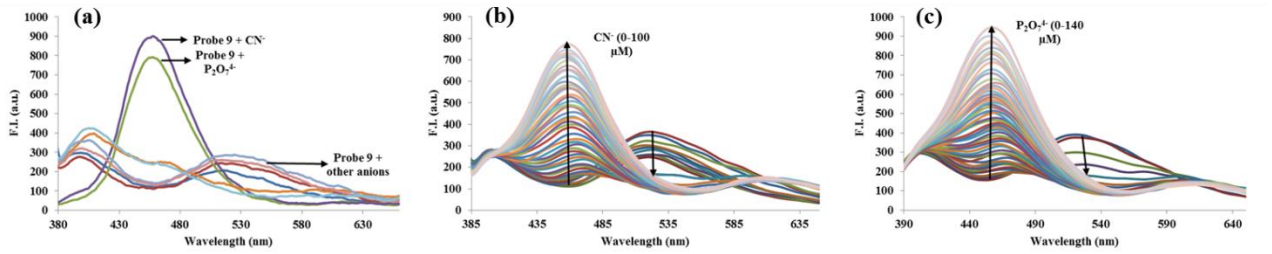

Figure 5.11: Emission spectra of probe 9 (20 µM) in CH_3CN:CH_3OH (9:1, v/v) (a) in presence of different anions (1000 µM), (b) upon incremental addition of 0-100 µM of CN^- ions, (c) upon incremental addition of 0-140 µM of $P_2O_7^{4-}$ ions.

Based on fluorescence titration data, the detection limit of probe **9** for CN^- ions was calculated to be 41 nM which is much lower than the maximum contaminant level permitted in drinking water (1.9 µM). The binding constant of probe **9** for CN^- ions was determined by Benesi-Hildebrand equation and was found out to be 1.2×10^4 M^{-1}. Similarly for $P_2O_7^{4-}$ ions the binding constant was calculated to be 6.3×10^3 M^{-1} with the lowest detection limit of 49 nM

Further, due to the high sensitivity of the probe **9** in detecting CN^- and $P_2O_7^{4-}$ ions, the preferential selectivity of probe **9** was examined in the presence of various anions. To perform this, the probe **9** (20 µM) in CH_3CN:CH_3OH (9:1, v/v) was treated with CN^- and $P_2O_7^{4-}$ ions in the presence of other competitive anions. The presence of other anions had no interference in the detection of CN^- and $P_2O_7^{4-}$ ions at 450 nm. Hence, the probe **9** revealed a good practical ability to recognize CN^- and $P_2O_7^{4-}$ ions in the presence of other anions **(Figure 5.12)**.

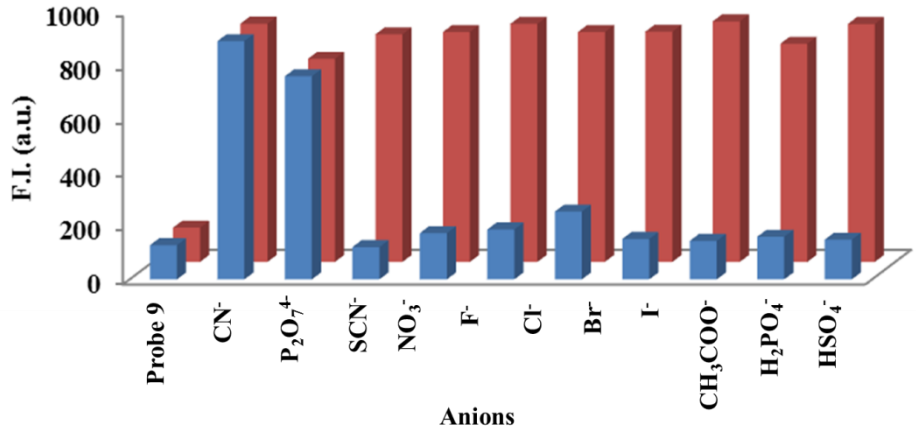

Figure 5.12: Relative emission intensity of probe 9 (20 µM) in CH_3CN:CH_3OH (9:1, v/v) (λ_{ex}= 375 nm) with different competing anions in the absence and presence of CN^- and $P_2O_7^{4-}$ ions at λ_{em}= 450 nm, where blue bars represent the emission intensity change of probe 9 with different anions (1000 µM) and red bars represent probe 9 + CN^- and $P_2O_7^{4-}$ ions in the presence of different relevant competing anions (1000 µM).

5.2.3.3. NMR titration

^1H NMR titrations were performed to find the binding mechanism of probe **9** with CN^- and $P_2O_7^{4-}$ ions. The ^1H NMR titrations were carried out in CD_3CN-d_3 at 5 mM of concentration **(Figure 5.13)**. The singlet at 8.91 ppm due to imine proton of probe **9** disappears and a new peak emerges at 5.32 ppm after the addition of 1.0 eq. of CN^- ions. The protons at 7.65 ppm and 7.45 ppm due to H_f and H_g protons of hydroxyquinoline ring showed downfield shift indicating the change in the electronic configuration of probe **9** after the addition of CN^- ions. The results indicated the nucleophilic addition of CN^- ions at imine centre of probe **9**. Whereas, the singlet at 8.91 ppm due to imine proton of probe **9**, on addition of $P_2O_7^{4-}$ ions did not show any change. Howover, the aromatic protons at 7.95 ppm and 7.84 ppm due to H_e and H_c protons were also merged and a new signal at 7.91 ppm was observed that indicated the change in the electron density upon the addition of $P_2O_7^{4-}$ ions. The results indicated the H-bonding after the addition of $P_2O_7^{4-}$ ions **(Scheme 5.4)**.

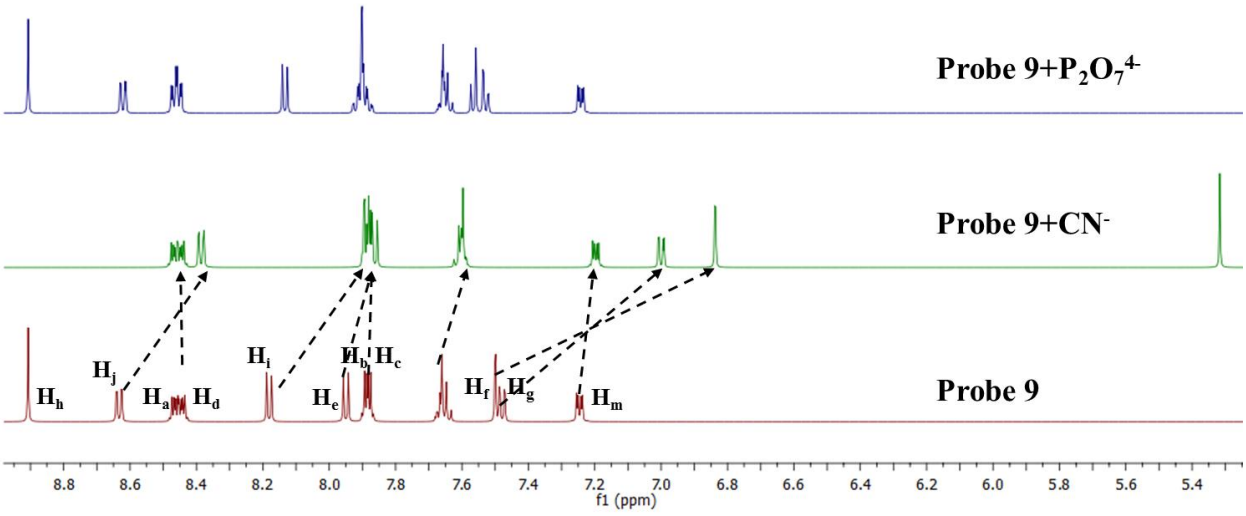

Figure 5.13: ^{1}H NMR spectra of probe 9 (5× 10^{-3} M) upon addition of 1.0 equiv. of CN^- and $P_2O_7^{4-}$ ions in CH_3CN-*d*$_3$.

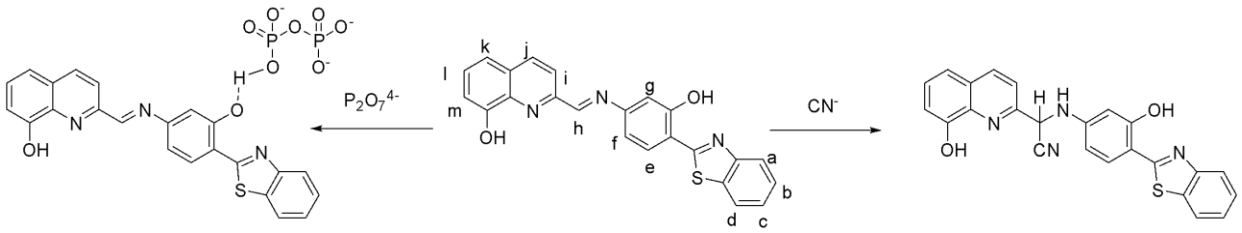

Scheme 5.4: Plausible binding mechanism of probe 9 with CN^- and $P_2O_7^{4-}$ ions.

5.2.3.4. Time-Correlated Single Photon Counting (TCSPC) study

To further get insight of the behavior of probe **9** towards CN^- and $P_2O_7^{4-}$ ions, we have performed the time-resolved fluorescence spectroscopy at two emission bands of 400 nm and 515 nm **(Figure 5.14)**. At 400 nm, the decay time for probe **9** has been found to be 0.96 ns with three life time components of 0.95 ns (~50.06%), 0.95 (~49.54%) and 2.27 ns (~0.4%). After binding with CN^- ions, the decay time of complex was changed to 1.68 ns with three life time components of 0.67 ns (~7.42%), 1.72 (~79.64%) and 6.06 ns (~12.94%). The significant increase in lifetime of probe **9** after coordinating with CN^- signifies the electron transfer. Similarly at 515 nm, the average lifetime value of probe **9** was found out to be 0.89 ns whereas

after binding to CN^- ions the average lifetime was increased to 5.48 ns indicating fluorescence enhancement. Similar results were obtained after the addition of $P_2O_7^{4-}$ ions **(Table 5.4)**.

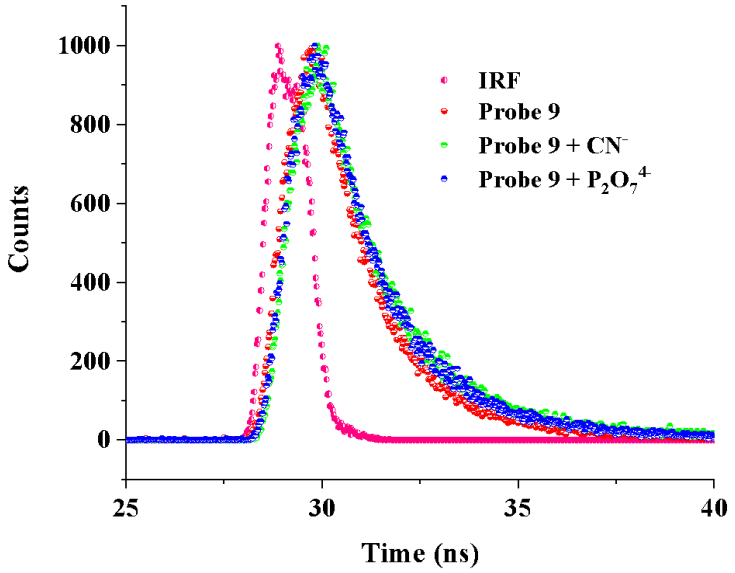

Figure 5.14: Time resolved fluorescence decay of probe 9 and its complex with CN^- and $P_2O_7^{4-}$ ions in CH_3CN:CH_3OH (9:1, v/v) at 20 µM.

Table 5.4: Fluorescence lifetime measurements for probe 8 and complex with CN^- and $P_2O_7^{4-}$ ions in CH_3CN:CH_3OH (9:1, v/v).

CH_3CN:CH_3OH (9:1, v/v)	Wavelength (nm)	τ_1 (ns)	τ_2 (ns)	τ_3 (ns)	α_1	α_2	α_3	χ^2	τ_{av} (ns)
Probe 9	400 nm	0.95	0.95	2.27	50.06	49.54	0.4	0.94	0.96
	535 nm	1.62	4.65	0.47	30.27	29.25	40.48	1.00	0.89
Probe 9 + CN^-	400 nm	0.67	1.72	6.06	7.42	79.64	12.94	1.03	1.68
	535 nm	2.03	5.52	5.50	0.29	49.77	49.94	1.04	5.48
Probe 9 + $P_2O_7^{4-}$	400 nm	1.06	2.04	6.56	31.15	64.15	4.7	1.05	1.62
	535 nm	0.07	1.99	3.16	3.64	65.27	31.1	1.05	1.03

5.2.4. Conclusion

In conclusion, probe **9** based on 8-hydroxyquinoline and benzothiazole has been designed and synthesized. The probe **9** was used as a ratiometric probe for selective detection of CN^- and $P_2O_7^{4-}$ ions without the interference from other anions. Probe **9** showed two emission bands at 400 nm and 535 nm due to ESIPT process occurring in the molecule and ESIPT process was inhibited when probe **9** binds to CN^- and $P_2O_7^{4-}$ ions with the formation of new band at 450 nm for both the ions. Probe **9** also exhibited intramolecular charge transfer phenomenon. The binding behavior of probe **9** with CN^- and $P_2O_7^{4-}$ ions was examined through job's plot method and ^1H NMR titration method.

5.3.

Protection and deprotection of excited state intramolecular proton transfer process in 8-hydroxyquinoline-benzthiazole Schiff base for enzyme sensing

5.3.1. Abstract

This section covered the ESIPT "off-on" based fluorescent probe **10** for the detection of ALP enzyme. The phosphate group in probe **10** acts as both an ESIPT blocker and an ALP responsive moiety. Probe **10** was synthesized for the detection of alkaline phosphatase (ALP) enzyme. The increase in the serum levels of ALP activity cause critical illnesses. In medical diagnostics, ALP activity is frequently regarded as a significant biomarker. Since endogenic ALP secreted by cancer cells has the catalytic ability to remove the phosphoryl group, which can then be localized for in situ imaging of ALP. ALP is present in variety of cancer cells in large amount. Although the probes always exhibit great selectivity and sensitivity, they are typically influenced by factors. Ratiometric fluorescence techniques, which benefits from the reduced background noise, would effectively overcome the problems and result in improved sensing performance. As a result, an ESIPT based ratiometric probe **10** for the detection of ALP activity was developed using phosphorylated benzothiazole derivative. Therefore, it is anticipated that probe **10** will solve the diffusion issue and can be appropriate for in situ enzyme activity measurements in living cells. Probe **10** could detect ALP with the lowest detection limit of 47 nM. The ^{1}H NMR titration experiment was performed for the detection mechanism.

5.3.2. Experimental Section

5.3.2.1. Synthesis of probe 10

Probe **9** (200 mg, 0.5 mmol) was dissolved in DCM (20 mL) and stirred at 0 °C. Then $POCl_3$ (0.2 mL) and pyridine (0.3 mL) were added **(Scheme 5.5)**. After that, the reaction solution was stirred at room temperature for 1 h. Then, ice water (50 mL) was added, and the reaction solution was extracted with DCM. The combined organic phase was dried with Na_2SO_4, and concentrated under reduced pressure. Probe **10** was obtained as a white solid with 40% yield. ^{1}H NMR (DMSO-d_6, 400MHz): δ (ppm) 9.81 (s, 1H, C=N), 8.94 (dd, 1H, J_1 = 4 Hz, J_2 = 8 Hz, ArH), 8.54 (dd, 1H, J_1 = 2 Hz, J_2 = 8 Hz, ArH), 8.26 (d, 1H, J = 4 Hz, ArH), 8.21 (d, 1H, J = 8 Hz, ArH), 8.13 (d, 1H, J = 4 Hz, ArH), 8.09 (d, 1H, J = 2 Hz, ArH), 8.02-7.99 (m, 1H, ArH), 7.93 (d, 1H, J = 8 Hz, ArH), 7.72-7.69 (m, 1H, ArH), 7.66-7.62 (m, 1H, ArH), 7.59-7.51 (m, 2H, ArH)

(Figure A45). ^{13}C NMR (DMSO-d_6, 100 MHz): δ (ppm) 160.7, 160.5, 160.4, 159.7, 159.6, 159.5, 157.4, 144.6, 144.5, 144.4, 144.3, 144.2, 144.2, 141.2, 141.2, 141.1, 141.0, 141.0, 138.8, 138.7, 137.2, 137.1, 135.6, 135.6, 131.9, 131.1, 131.0, 130.4, 128.6, 127.6, 127.1, 127.0, 120.7, 118.6, 117.9, 92.0, 91.4 **(Figure A46)**. **HRMS** (ESI-TOF): (m/z) $[M]^+$ calcd for $C_{23}H_{17}N_3O_8P_2S$: 557.0212, found: 557.2421 **(Figure A47)**.

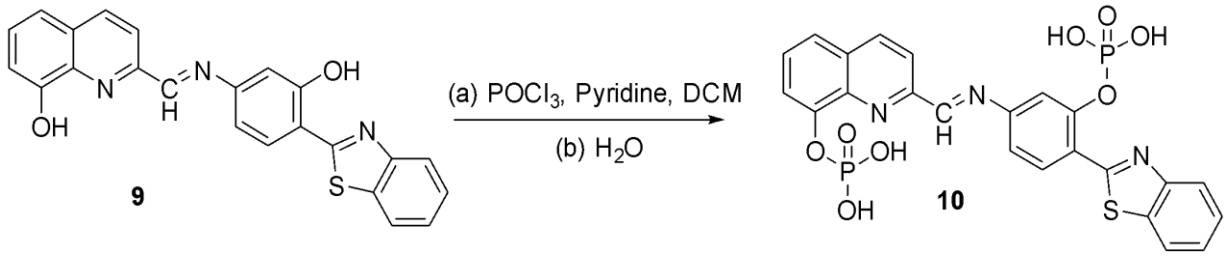

Scheme 5.5: Synthesis of probe 10.

5.3.3. Results and discussion

5.3.3.1. Photophysical properties of probe 10

The Photophysical properties of probe **10** were studied using absorption and emission spectroscopy. Probe **10** showed absorption maximum at 325 nm in CH_3CN at 20 μM of concentration and on excitation at 325 nm the emission maximum for probe **10** was observed at 415 nm. Further, we checked the effect of solvent polarity on the absorption and emission spectrum of probe **10**. The absorption maximum of probe **10** in hexane and acetone was observed at 325 nm whereas in medium and highly polar solvents like acetonitrile, toluene and H_2O the absorption maxima shift to 330 nm **(Figure 5.15a)**. The slight red shift in the absorption maxima can be due to intramolecular charge transfer mechanism. Similarly, the emission maximum of probe **10** in non-polar solvents was at 395 nm and as the polarity of the solvents was increased the emission maxima shifts from 395 nm to 485 nm and 535 nm **(Figure 5.15b)**. These results suggested the intramoecular charge transfer phenomenon occurring in probe **10**.

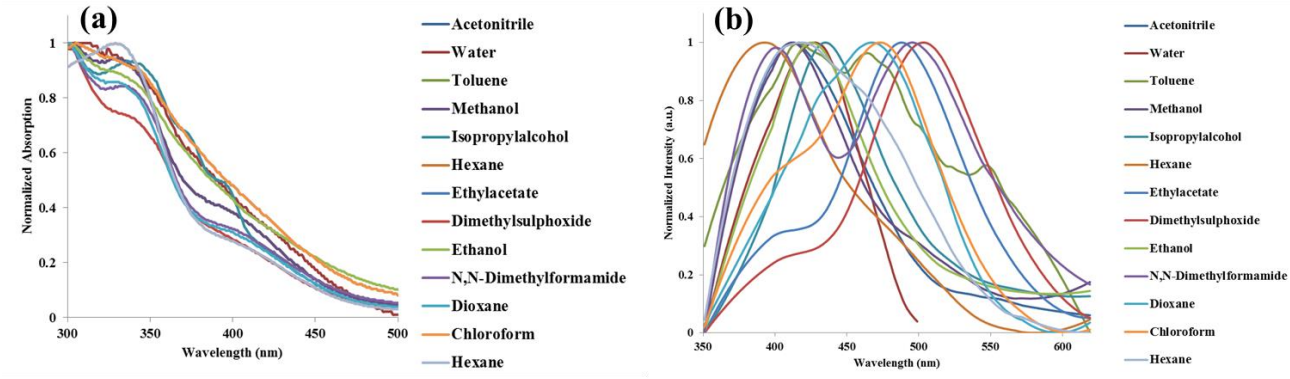

Figure 5.15: Normalized (a) absorption spectra and (b) emission spectra of probe 10 in different solvents.

Table 5.5: Photophysical behaviour of probe 10.

S. No.	Solvent	λ_{max} (nm)	Molar absorptivity ε ($M^{-1}cm^{-1}$)	λ_{em} (nm)	Stokes shift $\Delta\nu$ (cm^{-1})	Quantum yield (Φ)
1	Hexane	325	550	390	5100	0.23
2	Cyclohexane	325	12000	410	6400	0.26
3	Chloroform	325	8000	470	9500	0.21
4	Acetonitrile	325	10150	415	6400	0.19
5	Toluene	325	10350	460	9000	0.22
6	Isopropylalcohol	325	9600	415	6700	0.24
7	Ethylacetate	325	14700	485	10100	0.13
8	Dimethysulphoxide	325	9100	535	10800	0.11
9	N,N-Dimethylformamide	325	10000	535	10100	0.17
10	Dioxane	325	8700	535	6700	0.12
11	Ethanol	325	11300	425	7300	0.19
12	Methanol	325	7400	430	7500	0.16
13	Water	325	9250	425	7300	0.14
Stokes shift = $1/(\lambda_{em} - \lambda_{max})$, Reference for QY = Quinine Sulphate						

5.3.3.2. Design of probe 10

We have designed a fluorescent probe **10** for ALP activity by derivatizing the probe **9**, with large Stokes shift and might be utilized as a bio-imaging agent. A phosphoryl group which replaces the hydroxyl group in probe **9** was used as both a particular substrate of the ALP and ESIPT site. The addition of ALP caused hydrolytic cleavage of the phosphoryl moiety in probe **10** turning ESIPT on. Probe **9** showed a two emission bands at 410 nm due to enol form and at 535 nm due to keto form on excitation at 325 nm. The fluorescence of probe **10** was quenched at 535 nm and the only band at 435 nm was observed after the phosphorylation of probe **9** in CH_3CN **(Figure 5.16)**.

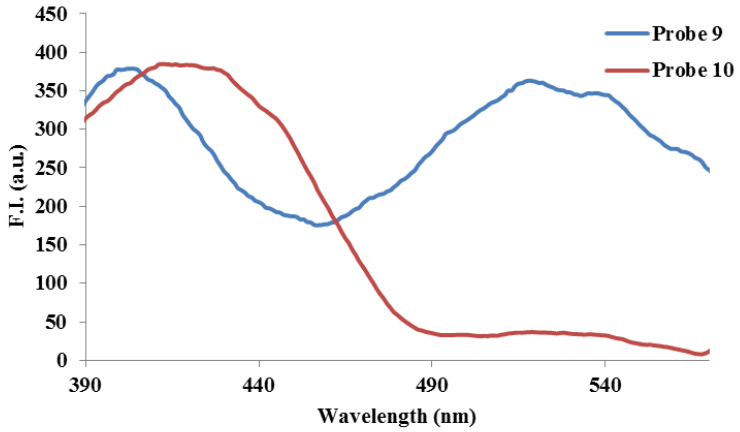

Figure 5.16: Emission spectra of probe 9 and probe 10.

5.3.3.3. Absorption and fluorescence behavior

The absorption and emission properties of probe **10** were measured in CH_3CN at 20 μM concentration. In the CH_3CN, probe **10** exhibited absorption maximum at 325 nm. The sensing ability of the probe **10** for ALP was examined in CH_3CN. The absorption intensity of probe **10** did not show any change in the absorption intensity after the addition of ALP. The probe **10** exhibits an emission band at 435 nm on excitation at 325 nm. The phosphate group acts as both an ESIPT blocker and an ALP responsive site in probe **10**. We anticipate that the phosphate group protecting the hydroxyl group in probe **10** will inhibit ESIPT and cause the tautomer emission to be quenched and the addition of ALP cleaves the phosphate group and transforms the probe **10** back into probe **9**, which correspondingly restores ESIPT and recovers the strong

tautomer emission. Addition of ALP produced a slight decrease in the emission intensity at 435 nm and a new band at 530 nm was also observed **(Figure 5.17a)**. With the incremental addition of 0-40 µM of ALP to the probe **10** the fluorescent intensity at 415 nm decreased with simultaneous increase in intensity at 530 nm **(Figure 5.17b)**. The binding constant for probe **10** and ALP was calculated using Benesi-Hildebrand equation and it comes out to be 2.3×10^5 M. Similarly the lowest detection limit for the ALP detection by probe **10** was found out to be 47 nM using the calibrate line. The stoichiometry of probe **10** and ALP was found to be 1:1 by Jobs plot method.

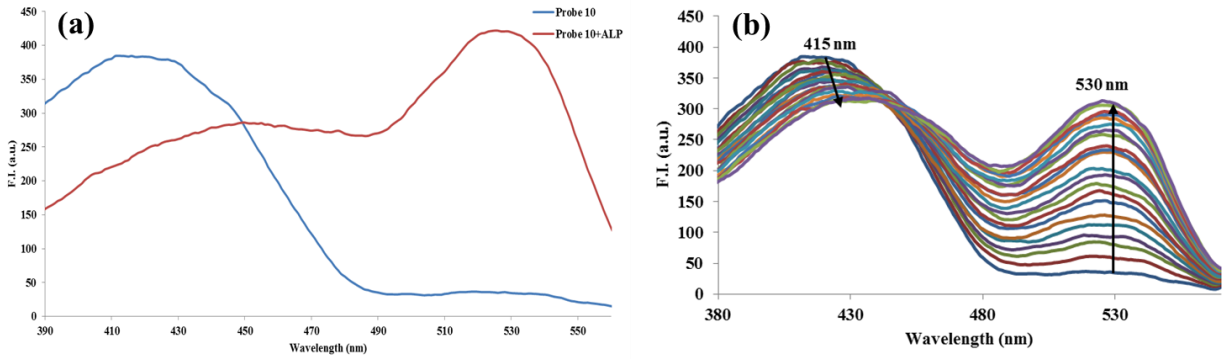

Figure 5.17: Emission spectra of probe 10 (20 µM) in CH_3CN (a) in presence of ALP (1000 µM), and (b) upon incremental addition of 0-400 µM of ALP.

5.3.3.4. NMR titrations

The ^1H NMR titrations were carried out in CD_3CN-d_3 at 5 mM of concentration to find the binding mechanism of probe **10** with ALP **(Figure 5.18)**. The doublet at 8.66 ppm due to H_j proton of probe **10** shifted upfield to 8.35 ppm after the addition of 1.0 eq. of ALP. The protons at 8.15 ppm and 8.05 ppm due to H_f and H_e protons of phenyl ring showed upfield shift to 7.75 ppm and 7.63 ppm, respectively indicating the change in the electronic configuration of probe **10** after the addition of ALP. Also, the other aromatic protons of hydroxyquinoline ring experienced upfield shifting. These results showed that the addition of ALP cleaves the phosphate group and inorganic phosphatase was also released **(Scheme 5.6)**.[163, 164]

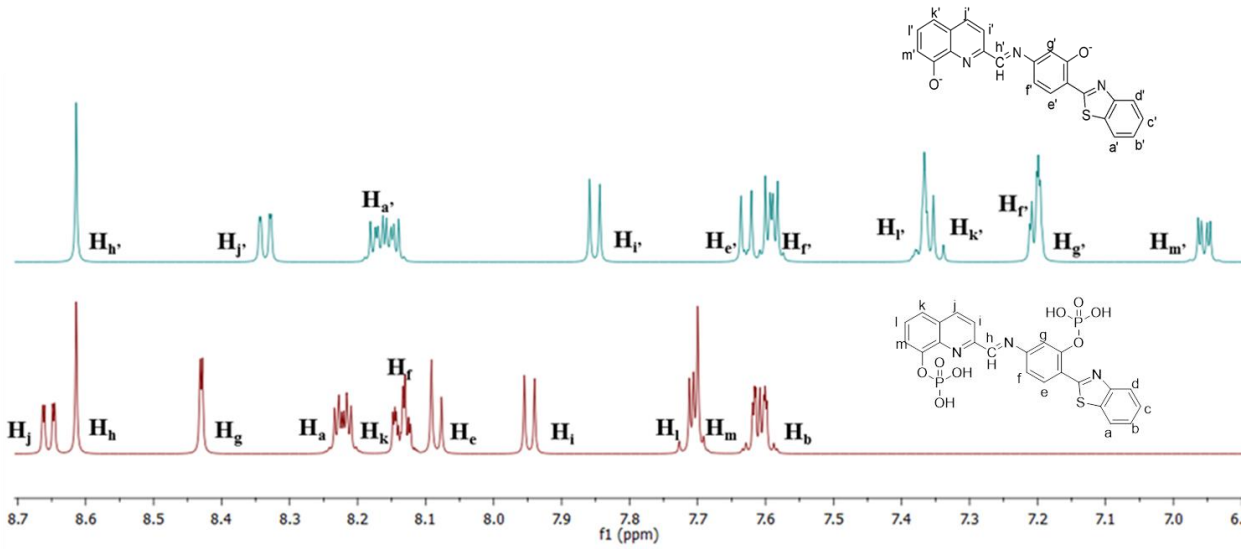

Figure 5.18: ^{1}H NMR of probe 10 with ALP in CD_3CN-d_3.

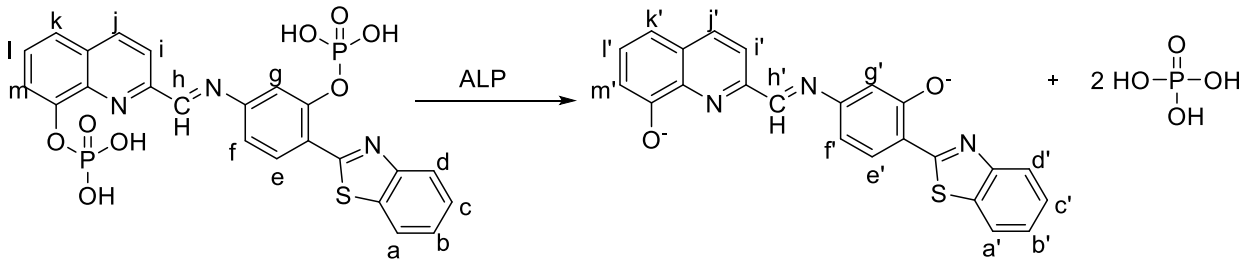

Scheme 5.6: The binding behavior of probes 10 towards ALP enzyme.

5.3.3.5. Time-Correlated Single Photon Counting (TCSPC) study

The results of fluorescence decay measurement using the TCSPC study have established that the fluorescence is increased upon interaction with ALP **(Figure 5.19)**. The tri-exponential function provides the best fit to decay behavior of probe **10** and after the addition of ALP enzyme. Probe **10** has three components with lifetime values of 3.93 ns, 7.24 and 0.90 ns and population of the components was 33.46 %, 60.44 % and 6.1 %, respectively. The average life time for probe **10** was found to be 4.23 ns. Upon adding ALP to the solution of probe **10**, three components were obtained with lifetime of 4.00, 7.18 and 1.06 ns with a population of 30.49 %, 61.97 % and 7.55 %, respectively. The average lifetime was calculated to be 4.29 ns **(Table 5.6)**. The average

lifetime of probe **10** before and after the addition of ALP remained almost constant indicating that the probe **10** binds with ALP in static manner.

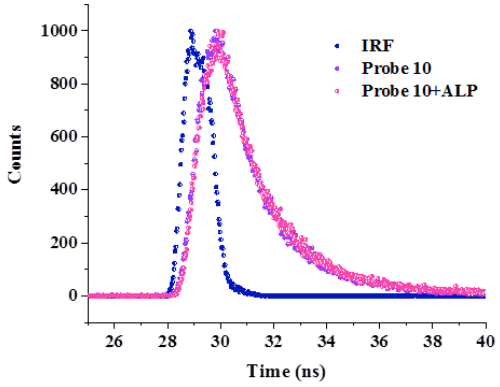

Figure 5.19: Time resolved fluorescence decay of probe 10 and its complex with ALP enzyme at λ_{em}= 435 nm in CH_3CN at 20 µM.

Table 5.6: Fluorescence lifetime measurements for probe 10 and with ALP in CH_3CN λ_{em}= 435 nm.

CH_3CN	τ_1 (ns)	τ_2 (ns)	τ_3 (ns)	α_1	α_2	α_3	χ^2	τ_{av} (ns)
Probe 10	3.93	7.24	0.90	33.46	60.44	6.1	1.09	4.23
Probe 10+ALP	4.00	7.18	1.06	30.49	61.97	7.55	1.11	4.29

5.2.4. Conclusion

In conclusion, a novel ALP targeted fluorescent probe **10** was synthesized. Probe **10** could detect ALP based on the modulation of ESIPT process via hydroxyl group protection and deprotection. Probe **10** was used for the detection of ALP enzyme through ESIPT "OFF-ON" mechanism and it could detect ALP with lowest detection limit of 47 nM.

Summary of chapter 5

This chapter examined the photophysical behavior of asymmetrical systems with intramolecular hydrogen bonds. The fluorescent probes **8-10** with large Stokes shift values were designed and synthesized. The solvatochromic behavior of all the three probes was investigated in order to understand the sensitivity of probes towards solvents of different polarity. The solvents studies revealed that the probes **8-10** exhibited the intramolecular charge transfer (ICT) phenomenon. Probe **8** having benzimidazole moiety detected DCP ions and by changing the hteroatom from N to S the probe **9** detected CN^- and $P_2O_7^{4-}$ ions. Further, probe **10** detected the ALP enzyme by the phosphorylation of OH group of probe **9**.

The probe **8** displayed absorption band at 370 nm and upon excitation at 370 nm an emission peak at 535 nm was observed with the Stokes shift value of 165 nm. Probe **8** displayed a ratiometric rise of peaks at 375 nm and 540 nm through absorption and emission spectra, respectively. The appearance of new absorption peaks confirmed the complex formation. The determined limit of detection of probe **8** towards DCP ions was 1.5×10^{-7} M with the binding constant value of 1.5×10^{4} M^{-1}.

The second section covered the chromo-fluorescent properties of probe **9** towards CN^- and $P_2O_7^{4-}$ ions in CH_3CN:CH_3OH (9:1, v/v). Upon addition of CN^- and $P_2O_7^{4-}$ ions, absorption band of probe **9** at 445 nm and 435 nm, respectively, was enhanced ratiometrically with respect to absorption band at 375 nm. Further, probe **9** displayed ratiometric emission response at 450 nm with respect to emission of probe **9** at 400 nm and 530 nm in CH_3CN:CH_3OH (9:1, v/v). The detection of CN^- and $P_2O_7^{4-}$ ions was followed up by inhibition of ESIPT. The limit of detection of probe **9** towards CN^- and $P_2O_7^{4-}$ ions were measured to be 41 nM and 49 nM, respectively. Further, probe **10** was used for the detection of ALP enzyme through ESIPT "OFF-ON" mechanism.

Summary and scope of the thesis

Summary

The excited state intramolecular proton transfer phenomenon as well as photophysical processes of different molecular architecture were investigated in this thesis, and the results are summarized below:

1. Three benzimidalole based Schiff bases as probe **1, 3** and **4** have been synthesized and studied for ESIPT or ICT phenomenon.

i. Probe **1** displayed weak emission due to the ESIPT process and it also exhibited AIE phenomenon due to intramolecular rotation around C=N bond. Also probe **1** showed selectivity towards Pb^{2+} ions and Al^{3+} ions with very low detection limit.

ii. The presence of electron-donating $-NEt_2$ group in probe **3** inhibits the ESIPT process and showed ICT phenomenon. The presence of $-NEt_2$ group restricted the intramolecular rotations and thus no AIE was observed. Probe **3** could detect Al^{3+} ions and HSO_4^- ions selectively with low detection limit.

iii. The extended conjugation in probe **4** ease the charge transfer and thus, it displayed ICT process along with AIE. Probe **4** selectively detected CN^- ions through fluorescence turn-on behavior.

2. The heteroatoms of probe **5-7** provide the platform for coordination to anions and thus, resulted in tuned sensing

i. Probe **1** displayed weak emission due to the ESIPT process and it also exhibited AIE phenomenon due to intramolecular rotation around C=N bond. Probe **5** selectively detected F^- and $P_2O_7^{4-}$ ions through ratiometric absorption and *turn-on* emission response in CH3CN: H2O (9: 1, v/v) with very low detection limit.

ii. The presence of electron-donating $-NEt_2$ group in probe **3** inhibits the ESIPT process and showed ICT phenomenon. The presence of $-NEt_2$ group restricted the intramolecular rotations

and thus no AIE was observed. Probe **6** detected ClO^- ions in mixed aqueous solution with a detection limit of 5.5 µM.

iii. The extended conjugation in probe **4** ease the charge transfer and thus, it displayed ICT process along with AIE. Probe **7** selectively detected F^- and CN^- ions through emission *turn-on* response, respectively. The detection limits towards F^- and CN^- ion were 76 nM and 1.1×10^{-7} M, respectively.

3. Asymmetrical molecular systems were synthesized and studied for photophysical behavior

i. 8-Hydroxyquinoline-benzimidazole based probe **8** displayed significant Stokes shift and showed emission enhancement with DCP.

ii. 8-Hydroxyquinoline-benzothiazole based probe **9** displayed dual emission and significant Stokes shift. Probe **9** acts as a ratiometric probe for CN^- and $P_2O_7^{4-}$ ions.

iii. 8-Hydroxyquinoline-benzothiazole based probe **10** with ESIPT "OFF-ON" mechanism was synthesized for ALP enzyme.

S.No.	Probe	Analyte	Solvent	Detection Limit	Phenomenon
1	Probe **1**	Pb^{2+} and Al^{3+}	H_2O: CH_3CN (1:9 [v/v])	2.7 nM and 33 nM	ICT and AIE
2	Probe **3**	Al^{3+} and HSO_4^-	H_2O: CH_3OH (1:1, v/v)	33 nM and 23 nM	ICT
3	Probe **4**	CN^-	H_2O:CH_3CN (1:9, v/v)	1.9 10^{-7} M	ICT and AIE
4	Probe **5**	F^- and $P_2O_7^{4-}$	CH_3CN:H_2O (9:1, [v/v], pH = 7.04)	41 nM and 23 nM	AIE
5	Probe **6**	ClO^-	CH_3OH: H_2O (9:1, [v/v], pH=7.04)	5.5 µM	ICT and AIE
6	Probe **7**	F^- and CN^-	CH_3CN	76 nM and 1.1 $\times10^{-7}$ M	ICT and AIE

7	Probe **8**	DCP	H_2O: CH_3CN (1:1, v/v, pH=7.1)	1.5×10^{-7} M	ESIPT
8	Probe **9**	F^- and $P_2O_7^{4-}$	CH_3CN:CH_3OH (9:1, v/v)	41 nM and 49 nM	ICT
9	Probe **10**	ALP	CH_3CN	47 nM	ESIPT "OFF-ON" and ICT

Scope

The ESIPT based fluorophores has been extensively studied due to their strong fluorescence, high quantum yield and large Stokes shift. Till now different ESIPT based fluorophore moieties have explored having a single site for ESIPT (single pair of proton donor and acceptor). Further with the introduction of another proton transfer site to the single ESIPT moieties the fluorescence, quantum yield and Stokes shift can be enhanced. Only a very few reports are available in literature where double sites (double pair of proton donor and acceptor) for ESIPT phenomenon are available on single platform. In the present thesis, ESIPT process was explored on different molecular architecture with diverse functionality. We synthesized different hydroxyl aryl benzimidazole/benzothiazole based Schiff bases with dual ESIPT sites. The torsional flexibility at imine centre C=N restrict the intramolecular rotaion in the probes inducing aggregation induced emission phenomenon. Furthermore, incorporation of ESIPT phenomenon on AIE active moieties to have two phenomena on single platform displayed wide spectral window. Such systems have the advantage of high emission with large Stokes' shift even at higher concentration. Moreover the introduction of electron donating group in probe cause excited state intramolecular charge transfer phenomenon (ESICT).

References

1. N. Amdursky, Y. Lin, N. Aho and G. Groenhof, *Proceedings of the National Academy of Sciences*, 2019, **116**, 2443-2451.
2. D. R. Weinberg, C. J. Gagliardi, J. F. Hull, C. F. Murphy, C. A. Kent, B. C. Westlake, A. Paul, D. H. Ess, D. G. McCafferty and T. J. Meyer, *Chemical Reviews*, 2012, **112**, 4016-4093.
3. S. Park, J. E. Kwon and S. Y. Park, *Physical Chemistry Chemical Physics*, 2012, **14**, 8878-8884.
4. P. J. Tonge and S. R. Meech, *Journal of Photochemistry and Photobiology A: Chemistry*, 2009, **205**, 1-11.
5. H. Mishra, V. Misra, M. Mehata, T. Pant and H. Tripathi, *The Journal of Physical Chemistry A*, 2004, **108**, 2346-2352.
6. H.-W. Tseng, J.-Q. Liu, Y.-A. Chen, C.-M. Chao, K.-M. Liu, C.-L. Chen, T.-C. Lin, C.-H. Hung, Y.-L. Chou and T.-C. Lin, *The Journal of Physical Chemistry Letters*, 2015, **6**, 1477-1486.
7. V. Misra and H. Mishra, *The Journal of chemical physics*, 2008, **128**, 244701.
8. L. Chen, J.-W. Ye, H.-P. Wang, M. Pan, S.-Y. Yin, Z.-W. Wei, L.-Y. Zhang, K. Wu, Y.-N. Fan and C.-Y. Su, *Nature Communications*, 2017, **8**, 15985.
9. A. Acuna, F. Amat-Guerri, A. Costela, A. Douhal, J. Figuera, F. Florido and R. Sastre, *Chemical physics letters*, 1991, **187**, 98-102.
10. C.-C. Yan, X.-D. Wang and L.-S. Liao, *ACS Photonics*, 2020, **7**, 1355-1366.
11. Y. Tsutsui, W. Zhang, S. Ghosh, T. Sakurai, H. Yoshida, M. Ozaki, T. Akutagawa and S. Seki, *Advanced Optical Materials*, 2020, **8**, 2070056.
12. J. Catalan, F. Fabero, M. Soledad Guijarro, R. M. Claramunt, M. D. Santa Maria, M. d. l. C. Foces-Foces, F. Hernandez Cano, J. Elguero and R. Sastre, *Journal of the American Chemical Society*, 1990, **112**, 747-759.
13. C.-C. Hsieh, C.-M. Jiang and P.-T. Chou, *Accounts of chemical research*, 2010, **43**, 1364-1374.
14. A. C. Sedgwick, L. Wu, H.-H. Han, S. D. Bull, X.-P. He, T. D. James, J. L. Sessler, B. Z. Tang, H. Tian and J. Yoon, *Chemical Society Reviews*, 2018, **47**, 8842-8880.

15. A. P. Demchenko, K.-C. Tang and P.-T. Chou, *Chemical Society Reviews*, 2013, **42**, 1379-1408.
16. Y. Long, M. Mamada, C. Li, P. L. Dos Santos, M. Colella, A. Danos, C. Adachi and A. Monkman, *The Journal of Physical Chemistry Letters*, 2020, **11**, 3305-3312.
17. G. Jiang, F. Li, J. Fan, Y. Song, C.-K. Wang and L. Lin, *Journal of Materials Chemistry C*, 2020, **8**, 98-108.
18. N. Suzuki, K. Suda, D. Yokogawa, H. Kitoh-Nishioka, S. Irle, A. Ando, L. M. Abegao, K. Kamada, A. Fukazawa and S. Yamaguchi, *Chemical science*, 2018, **9**, 2666-2673.
19. H.-W. Zheng, Y. Kang, M. Wu, Q.-F. Liang, J.-Q. Zheng, X.-J. Zheng and L.-P. Jin, *Dalton Transactions*, 2021, **50**, 3916-3922.
20. L. Chen, P. Y. Fu, H. P. Wang and M. Pan, *Advanced Optical Materials*, 2021, **9**, 2170097.
21. L. Chen, D. Wu, J.-M. Kim and J. Yoon, *Analytical chemistry*, 2017, **89**, 12596-12601.
22. K.-C. Tang, M.-J. Chang, T.-Y. Lin, H.-A. Pan, T.-C. Fang, K.-Y. Chen, W.-Y. Hung, Y.-H. Hsu and P.-T. Chou, *Journal of the American Chemical Society*, 2011, **133**, 17738-17745.
23. L. G. Arnaut and S. J. Formosinho, *Journal of Photochemistry and Photobiology A: Chemistry*, 1993, **75**, 1-20.
24. M. HeeáLee and J. SeungáKim, *Chemical Society Reviews*, 2015, **44**, 4185-4191.
25. L. Peng, S. Xu, X. Zheng, X. Cheng, R. Zhang, J. Liu, B. Liu and A. Tong, *Analytical chemistry*, 2017, **89**, 3162-3168.
26. J. Massue, D. Jacquemin and G. Ulrich, *Chemistry Letters*, 2018, **47**, 1083-1089.
27. L. Cui, Y. Baek, S. Lee, N. Kwon and J. Yoon, *Journal of Materials Chemistry C*, 2016, **4**, 2909-2914.
28. M. Dommett, M. Rivera and R. Crespo-Otero, *The Journal of Physical Chemistry Letters*, 2017, **8**, 6148-6153.
29. V. S. Padalkar and S. Seki, *Chemical Society Reviews*, 2016, **45**, 169-202.
30. P. M. Vérité, C. A. Guido and D. Jacquemin, *Physical Chemistry Chemical Physics*, 2019, **21**, 2307-2317.
31. X. Zhang, L. Guo, F.-Y. Wu and Y.-B. Jiang, *Organic letters*, 2003, **5**, 2667-2670.

32. V. S. Patil, V. S. Padalkar, A. B. Tathe and N. Sekar, *Dyes and Pigments*, 2013, **98**, 507-517.
33. V. S. Patil, V. S. Padalkar, K. R. Phatangare, V. D. Gupta, P. G. Umape and N. Sekar, *The Journal of Physical Chemistry A*, 2012, **116**, 536-545.
34. Y. Li, D. Dahal, C. S. Abeywickrama and Y. Pang, *ACS omega*, 2021, **6**, 6547-6553.
35. F. Han, W. Liu and C. Fang, *Chemical Physics*, 2013, **422**, 204-219.
36. J. Zhao, S. Ji, Y. Chen, H. Guo and P. Yang, *Physical Chemistry Chemical Physics*, 2012, **14**, 8803-8817.
37. H. Hu, X. Cheng, Z. Ma, R. P. Sijbesma and Z. Ma, *Journal of the American Chemical Society*, 2022, **144**, 9971-9979.
38. Z. Zhang, Y.-A. Chen, W.-Y. Hung, W.-F. Tang, Y.-H. Hsu, C.-L. Chen, F.-Y. Meng and P.-T. Chou, *Chemistry of Materials*, 2016, **28**, 8815-8824.
39. A. C. Sedgwick, W.-T. Dou, J.-B. Jiao, L. Wu, G. T. Williams, A. T. A. Jenkins, S. D. Bull, J. L. Sessler, X.-P. He and T. D. James, *Journal of the American Chemical Society*, 2018, **140**, 14267-14271.
40. A. L. Sobolewski, *Physical Chemistry Chemical Physics*, 2008, **10**, 1243-1247.
41. L. Wu, H.-H. Han, L. Liu, J. E. Gardiner, A. C. Sedgwick, C. Huang, S. D. Bull, X.-P. He and T. D. James, *Chemical Communications*, 2018, **54**, 11336-11339.
42. S.-J. Lim, J. Seo and S. Y. Park, *Journal of the American Chemical Society*, 2006, **128**, 14542-14547.
43. M. M. Henary, Y. Wu and C. J. Fahrni, *Chemistry–A European Journal*, 2004, **10**, 3015-3025.
44. J. Waluk, *Polish Journal of Chemistry*, 2008, **82**, 947.
45. L. Xian-Lin and H. Wei, *Chinese Journal of Analytical Chemistry*, 2021, **49**, 184-196.
46. H. C. Joshi and L. Antonov, *Molecules*, 2021, **26**, 1475.
47. P. Zhou and K. Han, *Aggregate*, 2022, **3**, e160.
48. P. Kundu and N. Chattopadhyay, *Journal of Photochemistry and Photobiology A: Chemistry*, 2023, **435**, 114296.
49. X. Li, Q. Wang, L. Song, J. Zhao and B. Jin, *Spectrochimica Acta Part A: Molecular and Biomolecular Spectroscopy*, 2022, **279**, 121377.

50. M. Durko, G. Ulrich, D. Jacquemin, J. Mysliwiec and J. Massue, *Physical Chemistry Chemical Physics*, 2023.
51. D. Wang, S.-J. Li, W. Cao, Z. Wang and Y. Ma, *ACS omega*, 2022, **7**, 18017-18026.
52. N. Singh, N. Kaur, R. C. Mulrooney and J. F. Callan, *Tetrahedron Letters*, 2008, **49**, 6690-6692.
53. A. Santra, S. Mishra, S. K. Panda and A. K. Singh, *Inorganica Chimica Acta*, 2022, **537**, 120933.
54. V. Bhardwaj, K. Bhardwaj and S. K. Sahoo, *Journal of Fluorescence*, 2023, 1-8.
55. J. Y. Yang, J. H. Han, Z. B. Shang, Y. Wang and S. M. Shuang, *Journal of Luminescence*, 2022, **249**, 119017.
56. S. M. Kumar, S. Munusamy, D. Jothi, S. Enbanathan and S. K. I. Iyer, *Journal of Molecular Liquids*, 2023, **373**, 121235.
57. H. Liu, B. Zhang, C. Tan, F. Liu, J. Cao, Y. Tan and Y. Jiang, *Talanta*, 2016, **161**, 309-319.
58. R. Behura, P. P. Dash, P. Mohanty, S. Behera, M. Mohanty, R. Dinda, S. K. Behera, A. K. Barick and B. R. Jali, *Journal of Molecular Structure*, 2022, **1264**, 133310.
59. B. Kaur, A. Gupta and N. Kaur, *Journal of Photochemistry and Photobiology A: Chemistry*, 2020, **389**, 112140.
60. S. Li, D. Cao, X. Meng, Z. Hu, Z. Li, C. Yuan, T. Zhou, X. Han and W. Ma, *Journal of Photochemistry and Photobiology A: Chemistry*, 2020, **392**, 112427.
61. W. Pan, X. Yang, Y. Wang, L. Wu, N. Liang and L. Zhao, *Journal of Photochemistry and Photobiology A: Chemistry*, 2021, **420**, 113506.
62. X. Guo, C. Guo, Y. Xing, Y. Liu, K. Wei, M. Kang, X. Yang, M. Pei and G. Zhang, *Journal of Photochemistry and Photobiology A: Chemistry*, 2022, **430**, 113990.
63. Q. Su, Q. Niu, T. Sun and T. Li, *Tetrahedron Letters*, 2016, **57**, 4297-4301.
64. M. Tajbakhsh, G. B. Chalmardi, A. Bekhradnia, R. Hosseinzadeh, N. Hasani and M. A. Amiri, *Spectrochimica Acta Part A: Molecular and Biomolecular Spectroscopy*, 2018, **189**, 22-31.
65. W. Zhu, L. Yang, M. Fang, Z. Wu, Q. Zhang, F. Yin, Q. Huang and C. Li, *Journal of Luminescence*, 2015, **158**, 38-43.

66. J. Fu, B. Li, H. Mei, Y. Chang and K. Xu, *Spectrochimica Acta Part A: Molecular and Biomolecular Spectroscopy*, 2020, **227**, 117678.
67. C. Patra, C. Sen, A. D. Mahapatra, D. Chattopadhyay, A. Mahapatra and C. Sinha, *Journal of Photochemistry and Photobiology A: Chemistry*, 2017, **341**, 97-107.
68. Y.-Y. Huang, F.-X. Wang, S.-Y. Mu, X. Sun, Q.-Z. Li, C.-Z. Xie and H.-B. Liu, *Spectrochimica Acta Part A: Molecular and Biomolecular Spectroscopy*, 2020, **243**, 118754.
69. B. Naskar, R. Modak, Y. Sikdar, D. K. Maiti, A. Bauzá, A. Frontera, A. Katarkar, K. Chaudhuri and S. Goswami, *Sensors and Actuators B: Chemical*, 2017, **239**, 1194-1204.
70. P. Singh, H. Singh, V. Vanita, R. Sharma, G. Bhargava and S. Kumar, *ChemistrySelect*, 2016, **1**, 6880-6887.
71. H. Peng, Y. Han, N. Lin and H. Liu, *Optical Materials*, 2019, **95**, 109210.
72. S. Paul and P. Banerjee, *Sensors and Actuators B: Chemical*, 2021, **329**, 129172.
73. N. H. Kim, J. Lee, S. Park, J. Jung and D. Kim, *Sensors*, 2019, **19**, 2500.
74. L. Yan, H. Yang, N. Liu, F. Meng and S. Zhang, *Spectrochimica Acta Part A: Molecular and Biomolecular Spectroscopy*, 2022, **275**, 121116.
75. S. Zhang, Y. Wang and H. Xu, *Spectrochimica Acta Part A: Molecular and Biomolecular Spectroscopy*, 2022, **275**, 121193.
76. C. Bai, J. Zhang, Y. Qin, H. Huang, Z. Xia, Q. Zheng, H. Dai, P. Lu, H. Miao and C. Qu, *Chemical Engineering Journal*, 2022, **443**, 136445.
77. J. Shu, T. Ni, X. Liu, B. Xu, L. Liu, W. Chu, K. Zhang and W. Jiang, *Dyes and Pigments*, 2021, **195**, 109708.
78. Y. Xie, L. Yan, Y. Tang, M. Tang, S. Wang, L. Bi, W. Sun and J. Li, *Journal of Fluorescence*, 2019, **29**, 399-406.
79. R. Ali, R. C. Gupta, S. K. Dwivedi and A. Misra, *New Journal of Chemistry*, 2018, **42**, 11746-11754.
80. B. Nakwanich, A. Koonwong, A. Suramitr, P. Prompinit, R. P. Poo-arporn, S. Hannongbua and S. Suramitr, *Journal of Molecular Structure*, 2021, **1245**, 131132.
81. S. Ghosh, S. Paul, S. Halder, M. Shit, A. Karmakar, J. B. Nandi, K. Jana and C. Sinha, *Journal of the Indian Chemical Society*, 2023, **100**, 100957.
82. R. C. Gupta, S. K. Dwivedi, R. Ali and A. Misra, *ChemistrySelect*, 2018, **3**, 2025-2031.

83. A. Helal, N. T. T. Thao, S. W. Lee and H.-S. Kim, *Journal of Inclusion Phenomena and Macrocyclic Chemistry*, 2010, **66**, 87-94.
84. Y. Pan and Y. Han, *Tetrahedron Letters*, 2017, **58**, 1301-1304.
85. D. Gil, B. Suh and C. Kim, *Journal of Fluorescence*, 2021, **31**, 1675-1682.
86. A. Bhattacharyya, S. C. Makhal and N. Guchhait, *Journal of Photochemistry and Photobiology A: Chemistry*, 2020, **388**, 112177.
87. N. Tohora, M. Mahato, T. Sultana, S. Ahamed, S. Ghanta and S. K. Das, *Journal of Photochemistry and Photobiology A: Chemistry*, 2023, **442**, 114807.
88. S. Kamali, R. Arabahmadi, M. Orojloo and S. Amani, *Microchemical Journal*, 2023, **184**, 108204.
89. J. Li, A. Gong, G. Shi and C. Chai, *RSC advances*, 2019, **9**, 30943-30951.
90. P. Alam, V. Kachwal and I. R. Laskar, *Sensors and Actuators B: Chemical*, 2016, **228**, 539-550.
91. L. Chen, S. J. Park, D. Wu, H. M. Kim and J. Yoon, *Dyes and Pigments*, 2018, **158**, 526-532.
92. A. Manna and S. Goswami, *New Journal of Chemistry*, 2015, **39**, 4424-4429.
93. C. Chang, F. Wang, J. Qiang, Z. Zhang, Y. Chen, W. Zhang, Y. Wang and X. Chen, *Sensors and Actuators B: Chemical*, 2017, **243**, 22-28.
94. S. Goswami, A. Manna, S. Paul, A. K. Das, K. Aich and P. K. Nandi, *Chemical communications*, 2013, **49**, 2912-2914.
95. M. K. Bera, C. Chakraborty, P. K. Singh, C. Sahu, K. Sen, S. Maji, A. K. Das and S. Malik, *Journal of Materials Chemistry B*, 2014, **2**, 4733-4739.
96. C. Liang and S. Jiang, *Analyst*, 2017, **142**, 4825-4833.
97. A. Pundi, J. Chen, C.-J. Chang, S.-R. Hsieh, M.-C. Lee, C.-H. Chou and T.-D. Way, *Spectrochimica Acta Part A: Molecular and Biomolecular Spectroscopy*, 2021, **262**, 120139.
98. S. Liu, L. Zhang, P. Zhou, Y. Yang and W. Wu, *Sensors and Actuators B: Chemical*, 2018, **255**, 401-407.
99. J. Wang, H. Li, H. Qin, Z. Su, G. Liu and S. Hou, *Journal of Molecular Structure*, 2023, **1274**, 134416.

100. M. E. Sidqi, A. A. A. Aziz, A. E. Abolehasan and M. A. Sayed, *Journal of Photochemistry and Photobiology A: Chemistry*, 2022, **424**, 113616.
101. G. Suman, S. Bubbly, S. Gudennavar and V. Gayathri, *Journal of Photochemistry and Photobiology A: Chemistry*, 2019, **382**, 111947.
102. P. Puri, G. Kumar, K. Paul and V. Luxami, *New Journal of Chemistry*, 2018, **42**, 18550-18558.
103. H. Sun, Y. Jiang, J. Nie, J. Wei, B. Miao, Y. Zhao, L. Zhang and Z. Ni, *Materials Chemistry Frontiers*, 2021, **5**, 347-354.
104. X. Zhang, L.-Y. Shen, Q.-L. Zhang, X.-J. Yang, Y.-L. Huang, C. Redshaw and H. Xu, *Molecules*, 2021, **26**, 1233.
105. H. W. Liu, K. Li, X. X. Hu, L. Zhu, Q. Rong, Y. Liu, X. B. Zhang, J. Hasserodt, F. L. Qu and W. Tan, *Angewandte Chemie International Edition*, 2017, **56**, 11788-11792.
106. W. Yang, X. Zhao, J. Zhang, Y. Zhou, S. Fan, H. Sheng, Y. Cao and Y. Hu, *Dyes and Pigments*, 2018, **156**, 100-107.
107. H. Sheng, Y. Hu, Y. Zhou, S. Fan, Y. Cao, X. Zhao and W. Yang, *Dyes and Pigments*, 2019, **160**, 48-57.
108. H. Sheng, Y. Hu, Y. Zhou, S. Fan, Y. Cao, X. Zhao and W. Yang, *Journal of Photochemistry and Photobiology A: Chemistry*, 2018, **364**, 750-757.
109. Y. Yu, H. Xu, W. Zhang, B. Wang and Y. Jiang, *Talanta*, 2018, **176**, 151-155.
110. B. Liu, J. Wang, G. Zhang, R. Bai and Y. Pang, *ACS applied materials & interfaces*, 2014, **6**, 4402-4407.
111. L. Tang, J. Shi, Z. Huang, X. Yan, Q. Zhang, K. Zhong, S. Hou and Y. Bian, *Tetrahedron Letters*, 2016, **57**, 5227-5231.
112. M. Tian, J. Sun, Y. Tang, B. Dong and W. Lin, *Analytical chemistry*, 2018, **90**, 998-1005.
113. Q. Hu, F. Zeng, C. Yu and S. Wu, *Sensors and Actuators B: Chemical*, 2015, **220**, 720-726.
114. F. Zhang, T. Du, L. Jiang, L. Zhu and D. Tian, *Bioorganic Chemistry*, 2022, **128**, 106026.
115. P. Zhang, C. Fu, Q. Zhang, S. Li and C. Ding, *Analytical chemistry*, 2019, **91**, 12377-12383.
116. L. Peng, M. Gao, X. Cai, R. Zhang, K. Li, G. Feng, A. Tong and B. Liu, *Journal of Materials Chemistry B*, 2015, **3**, 9168-9172.

117. H. Tian, W. Lin, X.-L. Hu, J.-B. Wang, M.-Y. Zhang, Y. Zang, X.-Y. Wu, J. Li, T. D. James and X.-P. He, *Organic Chemistry Frontiers*, 2023.
118. F. S. Santos, E. Ramasamy, V. Ramamurthy and F. S. Rodembusch, *Photochemical & Photobiological Sciences*, 2017, **16**, 840-844.
119. F. S. Santos, E. Ramasamy, V. Ramamurthy and F. S. Rodembusch, *Journal of Photochemistry and Photobiology A: Chemistry*, 2016, **317**, 175-185.
120. L. s. G. TA Duarte, F. S. Rodembusch, T. D. Atvars and R. G. Weiss, *The Journal of Physical Chemistry A*, 2019, **124**, 288-299.
121. S. S. Sun, Z. Wang, X. W. Wu, J. H. Zhang, C. J. Li, S. Y. Yin, L. Chen, M. Pan and C. Y. Su, *Chemistry–A European Journal*, 2018, **24**, 10091-10098.
122. Y. Wu, X. Peng, J. Fan, S. Gao, M. Tian, J. Zhao and S. Sun, *The Journal of organic chemistry*, 2007, **72**, 62-70.
123. H. Li, Z. Wei, Y. Ma, W. Zhang, D. Wang, X. Wang and G. Jin, *Chemical Physics*, 2020, **529**, 110553.
124. X. Wang, T. Xu and H. Duan, *Sensors and Actuators B: Chemical*, 2015, **214**, 138-143.
125. E. Horak, P. Kassal, M. Hranjec and I. M. Steinberg, *Sensors and Actuators B: Chemical*, 2018, **258**, 415-423.
126. G. Liu, M. Yang, L. Wang, J. Zheng, H. Zhou, J. Wu and Y. Tian, *Journal of Materials Chemistry C*, 2014, **2**, 2684-2691.
127. D. Wu, A. C. Sedgwick, T. Gunnlaugsson, E. U. Akkaya, J. Yoon and T. D. James, *Chemical Society Reviews*, 2017, **46**, 7105-7123.
128. B. Valeur and I. Leray, *Coordination Chemistry Reviews*, 2000, **205**, 3-40.
129. J. S. Kim and D. T. Quang, *Chemical Reviews*, 2007, **107**, 3780-3799.
130. R. Martinez-Manez and F. Sancenon, *Chemical reviews*, 2003, **103**, 4419-4476.
131. X.-L. Hu, H.-Q. Gan, F.-D. Meng, H.-H. Han, D.-T. Shi, S. Zhang, L. Zou, X.-P. He and T. D. James, *Frontiers of Chemical Science and Engineering*, 2022, **16**, 1425-1437.
132. P. D. Beer and P. A. Gale, *Angewandte Chemie International Edition*, 2001, **40**, 486-516.
133. T. Stoerkler, T. Pariat, A. D. Laurent, D. Jacquemin, G. Ulrich and J. Massue, *Molecules*, 2022, **27**, 2443.
134. C. Nuñez, J. Fernandez-Lodeiro, M. Dinis, M. Larguinho, J. L. Capelo and C. Lodeiro, *Inorganic Chemistry Communications*, 2011, **14**, 831-835.

135. X.-h. Jiang, B.-d. Wang, Z.-y. Yang, Y.-c. Liu, T.-r. Li and Z.-c. Liu, *Inorganic Chemistry Communications*, 2011, **14**, 1224-1227.
136. Y.-W. Liu, M. X. Kao and A.-T. Wu, *Sensors and Actuators B: Chemical*, 2015, **208**, 429-435.
137. M.-H. Kao, T.-Y. Chen, Y.-R. Cai, C.-H. Hu, Y.-W. Liu, Y. Jhong and A.-T. Wu, *Journal of Luminescence*, 2016, **169**, 156-160.
138. Y. Liu, H. Cui, K. Wei, M. Kang, P. Liu, X. Yang, M. Pei and G. Zhang, *Spectrochimica Acta Part A: Molecular and Biomolecular Spectroscopy*, 2023, 122376.
139. Rohini, K. Paul and V. Luxami, *The Chemical Record*, 2020, **20**, 1430-1473.
140. J.-T. Wang, Y.-Y. Pei, S.-F. Ren, M.-Y. Yan, W. Luo, B. Zhang and Q.-F. Li, *Spectrochimica Acta Part A: Molecular and Biomolecular Spectroscopy*, 2020, **229**, 117956.
141. N. Ribeiro, P. F. Farinha, J. O. Pinho, H. Luiz, J. P. Mészáros, A. M. Galvão, J. Costa Pessoa, É. A. Enyedy, C. P. Reis and I. Correia, *Pharmaceutics*, 2022, **14**, 2583.
142. S. Khan, X. Chen, A. Almahri, E. S. Allehyani, F. A. Alhumaydhi, M. M. Ibrahim and S. Ali, *Journal of Environmental Chemical Engineering*, 2021, **9**, 106381.
143. A. G. Erturk, *Journal of Molecular Structure*, 2020, **1202**, 127299.
144. H. Jiang, D. Tang, Z. Li, J. Li, H. Liu, Q. Meng, Q. Han and X. Liu, *Spectrochimica Acta Part A: Molecular and Biomolecular Spectroscopy*, 2020, **243**, 118784.
145. A. R. U. Parambil, P. Kavyashree, A. Silswal and A. L. Koner, *RSC advances*, 2022, **12**, 13950-13970.
146. N. Roy, S. Nath, A. Dutta, P. Mondal, P. C. Paul and T. S. Singh, *RSC advances*, 2016, **6**, 63837-63847.
147. S. Mukherjee and S. Talukder, *Journal of fluorescence*, 2016, **26**, 1021-1028.
148. P. Karimi, *Journal of Molecular Structure*, 2019, **1182**, 266-270.
149. Z.-J. Jiang, H.-S. Lv, J. Zhu and B.-X. Zhao, *Synthetic metals*, 2012, **162**, 2112-2116.
150. D. Wang, S.-M. Li, J.-Q. Zheng, D.-Y. Kong, X.-J. Zheng, D.-C. Fang and L.-P. Jin, *Inorganic chemistry*, 2017, **56**, 984-990.
151. Z. Li, W. Zhang, X. Liu, C. Liu, M. Yu and L. Wei, *RSC Advances*, 2015, **5**, 25229-25235.

152. C. Zhou, Y. Song, N. Xiao, Y. Li and J. Xu, *Journal of fluorescence*, 2014, **24**, 1331-1336.
153. L. Feng, H. Li, Y. Lv and Y. Guan, *Analyst*, 2012, **137**, 5829-5833.
154. D. Singh, V. Nishal, S. Bhagwan, R. K. Saini and I. Singh, *Materials & Design*, 2018, **156**, 215-228.
155. V. Oliveri and G. Vecchio, *European journal of medicinal chemistry*, 2016, **120**, 252-274.
156. V. Oliveri, *ChemistryOpen*, 2015, **4**, 792-795.
157. M. Albrecht, M. Fiege and O. Osetska, *Coordination Chemistry Reviews*, 2008, **252**, 812-824.
158. E. Bardez, I. Devol, B. Larrey and B. Valeur, *The Journal of Physical Chemistry B*, 1997, **101**, 7786-7793.
159. C. Chen, *Chem. Rev*, 1998, **171**, 161.
160. F. Launay, V. Alain, É. Destandau, N. Ramos, É. Bardez, P. Baret and J.-L. Pierre, *New Journal of Chemistry*, 2001, **25**, 1269-1280.
161. P. L. Jones, A. J. Amoroso, J. C. Jeffery, J. A. McCleverty, E. Psillakis, L. H. Rees and M. D. Ward, *Inorganic Chemistry*, 1997, **36**, 10-18.
162. N. A. C. Dos Santos, M. Natali, E. Badetti, K. Wurst, G. Licini and C. Zonta, *Dalton Transactions*, 2017, **46**, 16455-16464.
163. P. Zhang, C. Fu, Q. Zhang, S. Li and C. Ding, *Analytical chemistry*, 2019, **91**, 12377-12383.
164. Z. Song, R. T. Kwok, E. Zhao, Z. He, Y. Hong, J. W. Lam, B. Liu and B. Z. Tang, *ACS Applied Materials & Interfaces*, 2014, **6**, 17245-17254.

List of Publications

1. **Aastha Palta,** Gulshan Kumar and Vijay Luxami, Journal of Photochemistry and Photobiology A: Chemistry, (2022) 114198; Excited state double proton transfer efficient probe: Theoretical investigation and sensing ability towards Pb^{2+} and Al^{3+} ions.
2. **Aastha Palta,** Gulshan Kumar and Vijay Luxami, Spectrochimica Acta Part A: Molecular and Biomolecular Spectroscopy 300 (2023) 122873; Dual hydrogen bonding containing intramolecular charge transfer efficient "*turn-on*" fluorescent probe for Al^{3+} and HSO_4^- ions: Real-time application in water samples and molecular keypad lock.
3. Iqubal Singh, Gulshan Kumar, **Aastha Palta,** Kamaldeep Paul and Vijay Luxami, Inorganica Chimica Acta 557 (2023) 121684; Naphthalimide-Benzimidazole Conjugate for Selective "Turn-on" sensor for Hg^{2+} in aqueous media.
4. **Aastha Palta,** Dinesh Singla, Kamaldeep Paul and Vijay Luxami, Chemistryselect, 2023; Coumarin-pyrazole based Fluorescent Sensor for Selective Detection of Dopamine in Aqueous Medium.
5. **Aastha Palta,** Gulshan Kumar and Vijay Luxami, Highly selective colorimetric and fluorescent probe for F^- and $P_2O_7^{4-}$ based on AIEE and dual ESIPT **(Under Revision)**.
6. **Aastha Palta,** Sunidhi Sharma, Diptiman Choudhury and Vijay Luxami, Highly specific benzothiazole based Schiff base for the ratiometric detection of hypochlorite (ClO^-) ion in aqueous system: a real application in biological imaging **(Under Preparation)**.
7. **Aastha Palta,** Gulshan Kumar, Iqubal Singh, Kamaldeep Paul and Vijay Luxami, Cinnamonitrile-linked Naphthalimide-Benzimidazole Conjugate: A Selective Fluorescent Turn-off Probe for Cyanide Ion Detection with Aggregation-Induced Emission **(Under Preparation)**.
8. **Aastha Palta,** Priya Thakur, Priya Vashisht and Vijay Luxami, A highly selective 1,10-phenanthroline based Schiff base for the fluorescent detection of nerve agent stimulants **(Under Preparation)**.
9. **Aastha Palta,** Priya Vashisht and Vijay Luxami, Synthesis and spectroscopic investigation of novel Ru (II) complexes of 1,10-phenanthroline based Schiff bases with ct-DNA **(Under Preparation)**.
10. **Aastha Palta,** and Vijay Luxami, Fluorescent "*turn-on*" benzimidazole conjugates for the detection of CN^- ion in mixed aqueous medium **(Under Preparation)**.

11. **Aastha Palta,** and Vijay Luxami, Excited state intramolecular proto transfer based ratiometric fluorescent sensor for F^- and CN^- ions **(Under Preparation)**.
12. **Aastha Palta,** and Vijay Luxami, ESIPT efficient sensor for the detection of DCP ions and application as molecular logic gate and paper strips **(Under Preparation)**.
13. **Aastha Palta,** and Vijay Luxami, 8-hyroxyquinoline based ratiometric sensor for the detection of CN^- and $P_2O_7^{4-}$ ions and its application in enzyme sensing **(Under Preparation)**.

Conferences and Workshops

1. National Conference on "**Chemical and Environmental Sciences: Advanced Innovations-2020"** at Punjabi University, Patiala.

2. International Symposium on **"Recent advances in Self assembled Materials and Supramolecular Chemistry"** at GNDU, Amritsar.

3. **CRSI-ACS National Symposium** in Chemistry at IISER, Mohali.

4. Webinar on **"Managing Research Literature using Mendeley"** at Thapar Institute of Engineering and Technology, Patiala.

5. **CRSI-ACS National Symposium** in Chemistry at JNU, Delhi.

APPENDIX

Chapter 3

Investigation of excited state intramolecular proton transfer process and charge transfer process in hydroxy aryl benzimidazole based Schiff bases

Chapter 3.1. Investigation of excited state intramolecular proton transfer process for hydroxy aryl benzimidazole based Schiff base

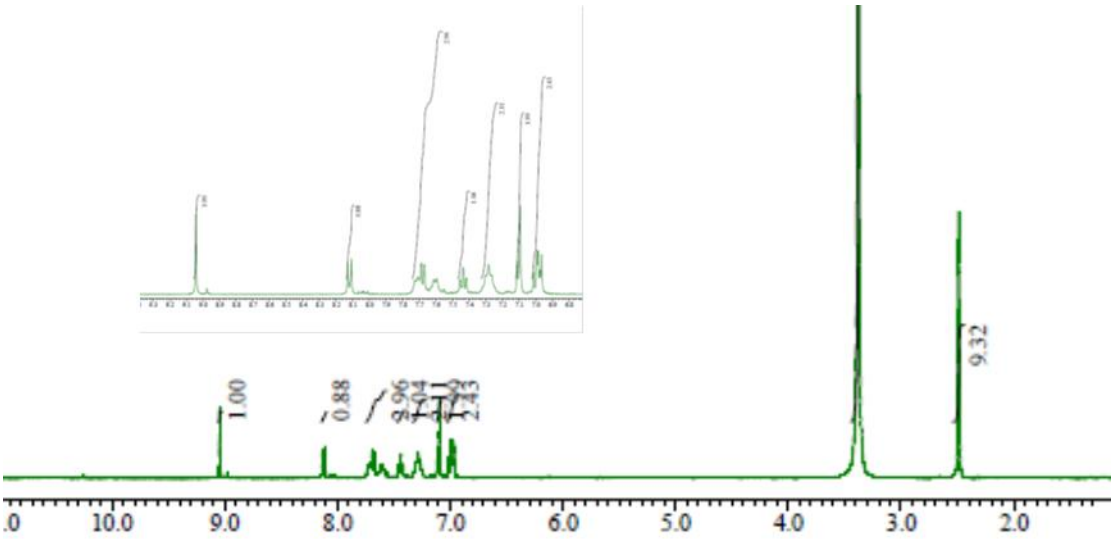

Figure A1: ^{1}H NMR spectrum of probe **1**.

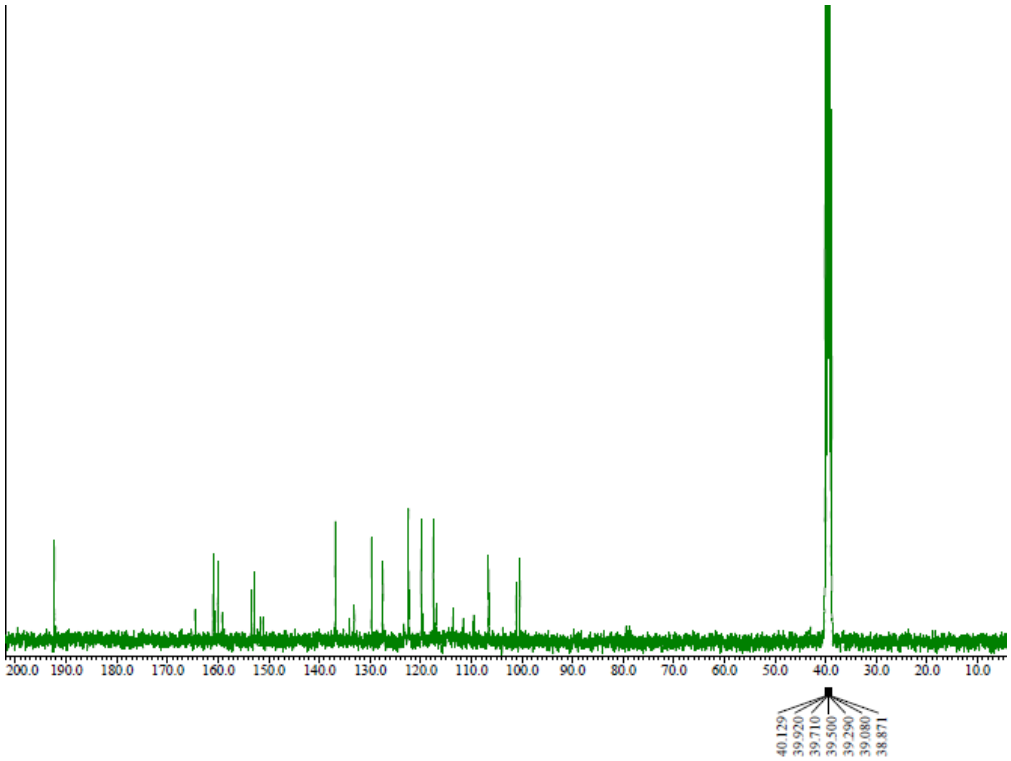

Figure A2: ^{13}C NMR of probe **1.**

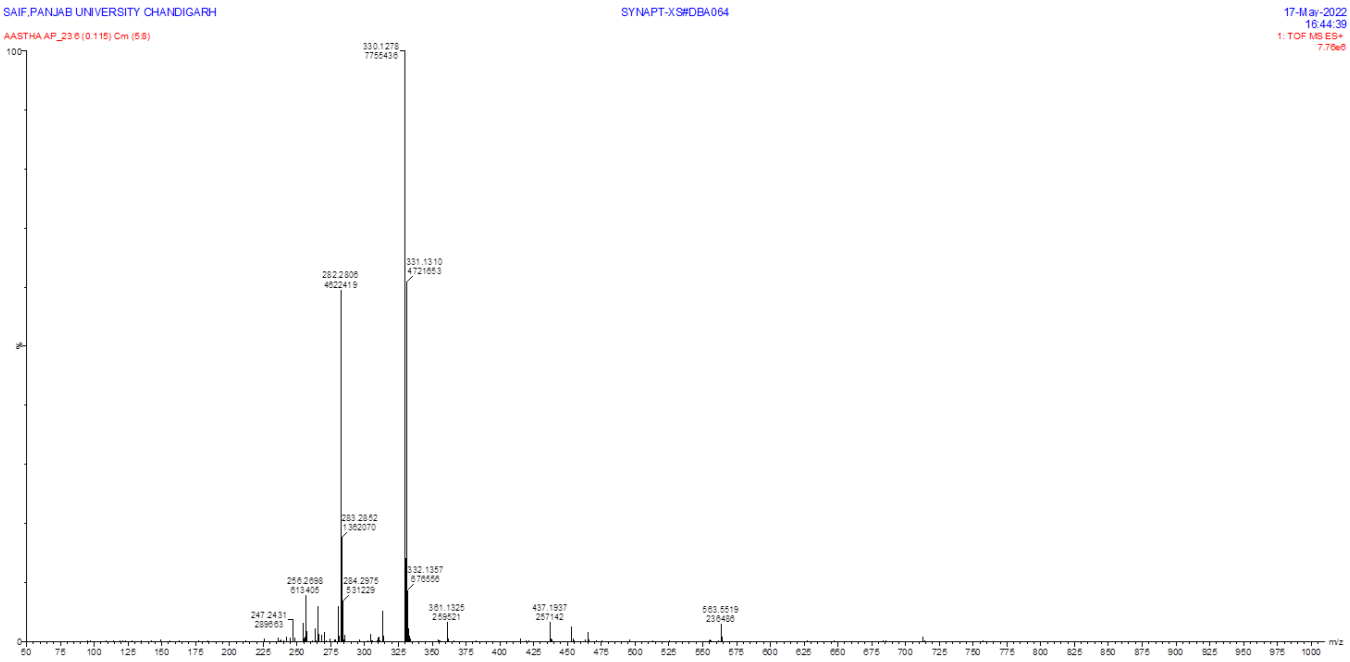

Figure A3: HRMS spectrum of probe **1.**

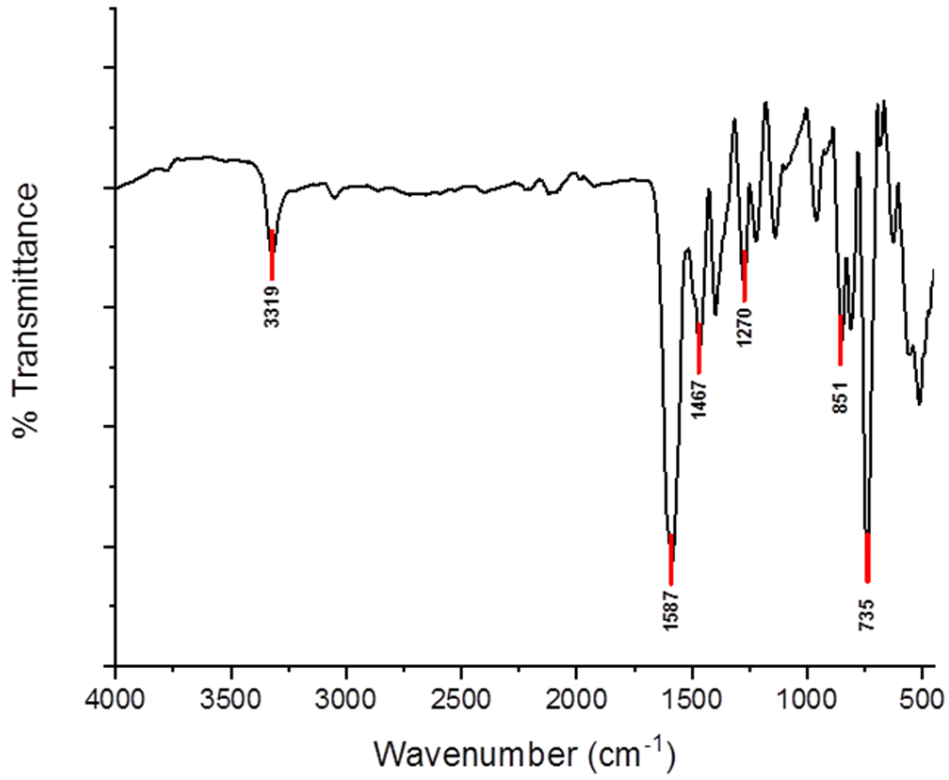

Figure A4: FTIR spectrum of probe **1.**

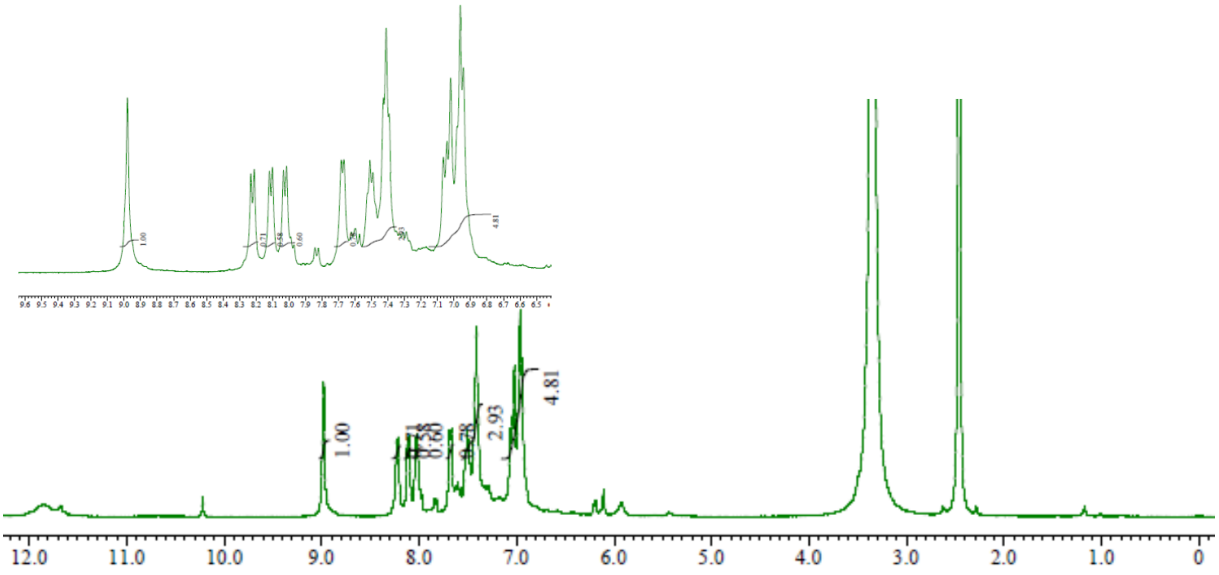

Figure A5: ^{1}H NMR of probe **2.**

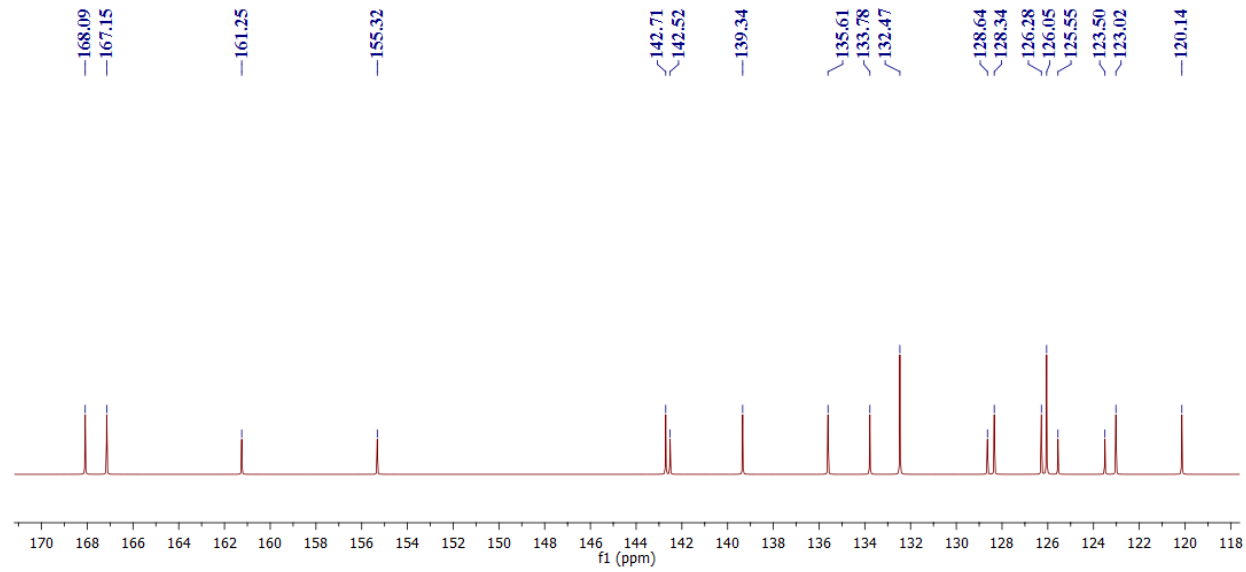

Figure A6: ^{13}C NMR of probe **2.**

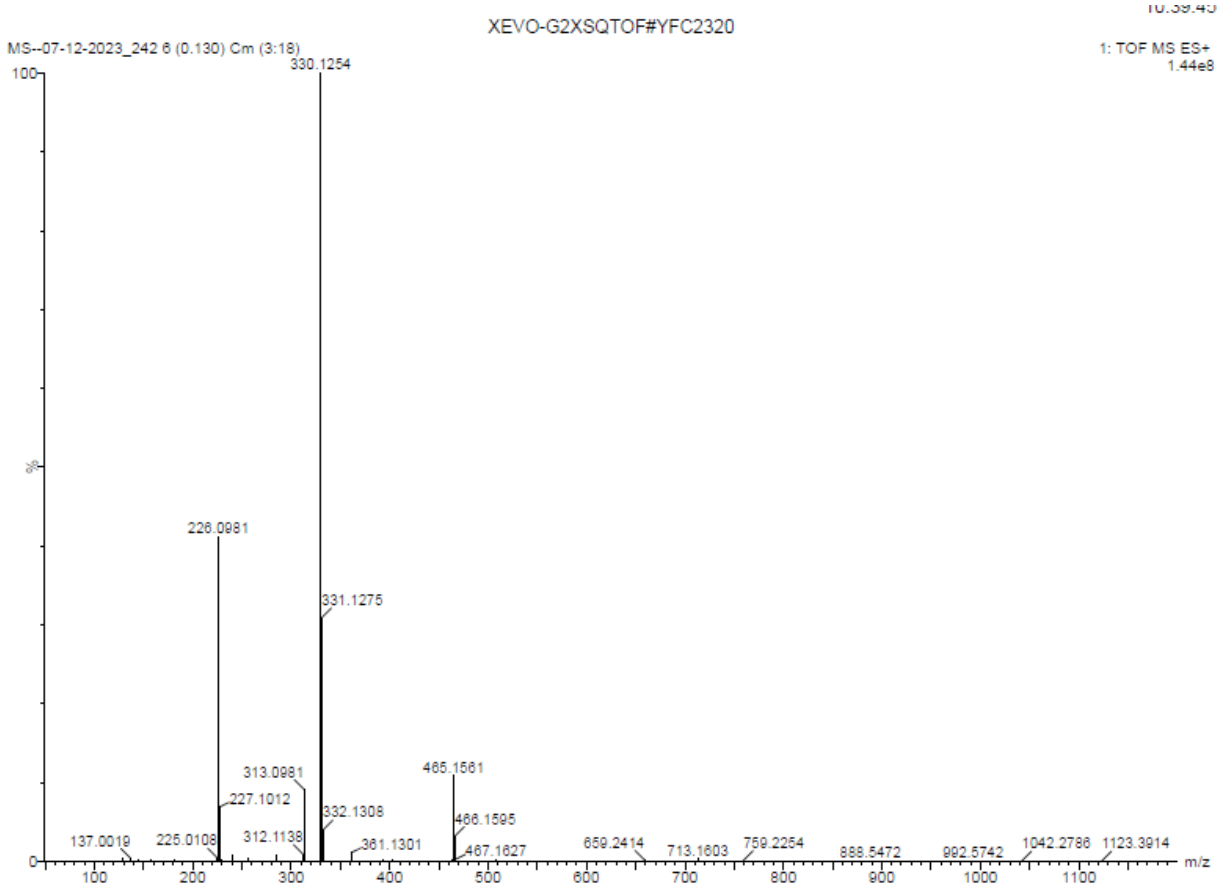

Figure A7: HRMS spectrum of probe **2.**

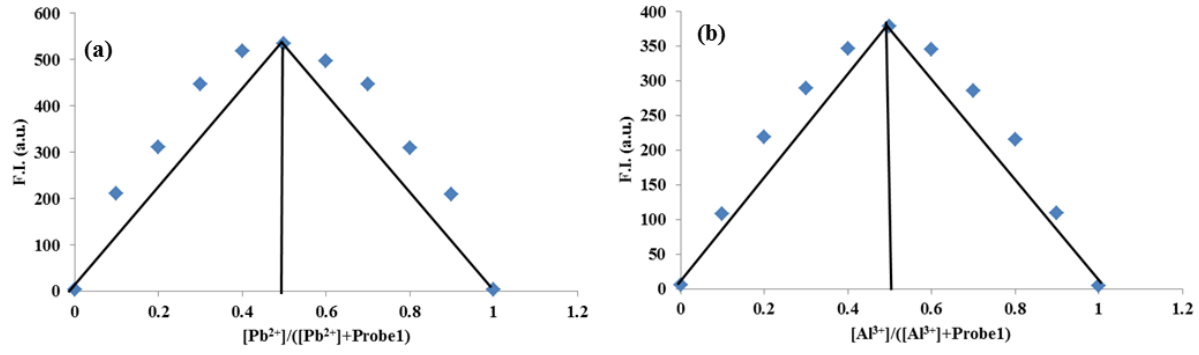

Figure A8: Job's Plot for probe **1**(20 μM) binding with (a) Pb^{2+} (20 μM) and (b) Al^{3+} (20 μM) in H_2O: CH_3CN (1:9, [v/v]).

Chapter 3.2. Effect of electron donating group ($-NEt_2$) on excited state intramolecular proton transfer process of benzimidazole based Schiff base

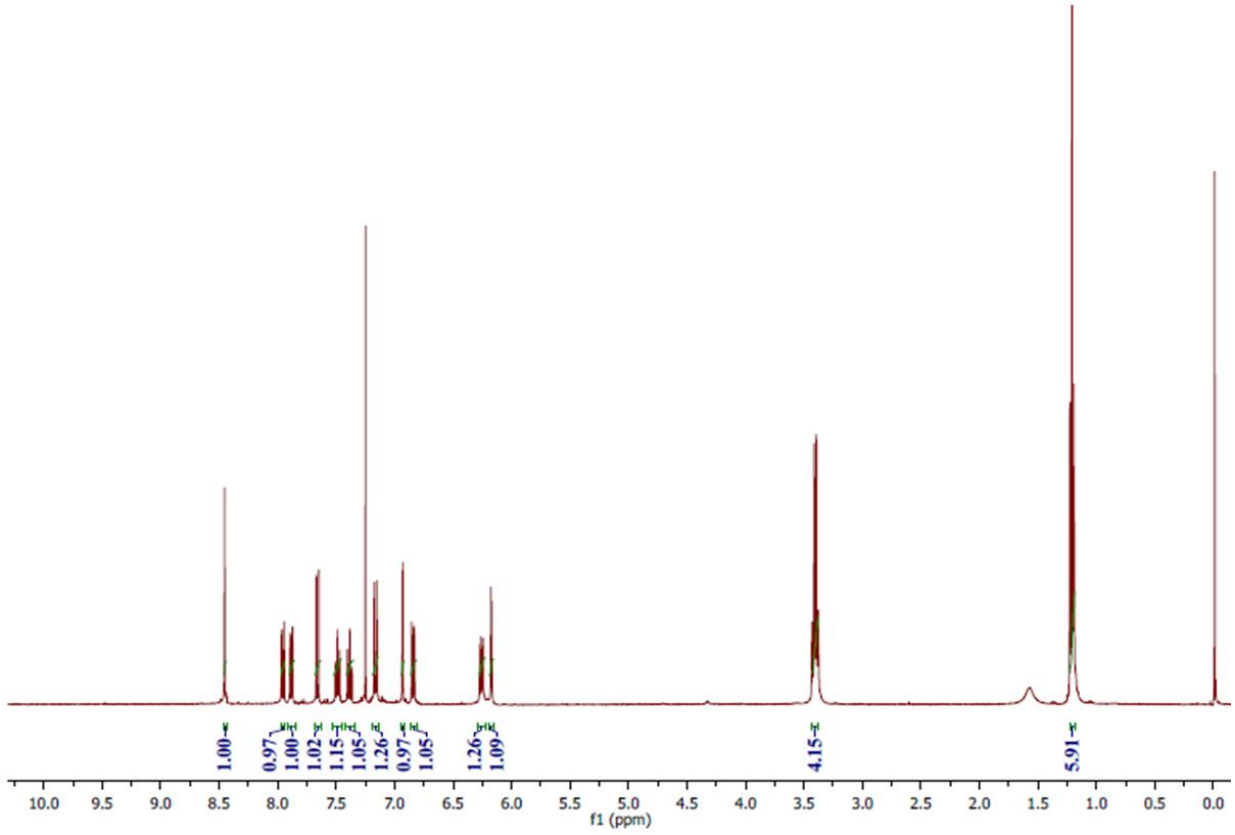

Figure A9: ^{1}H NMR spectrum of probe **3.**

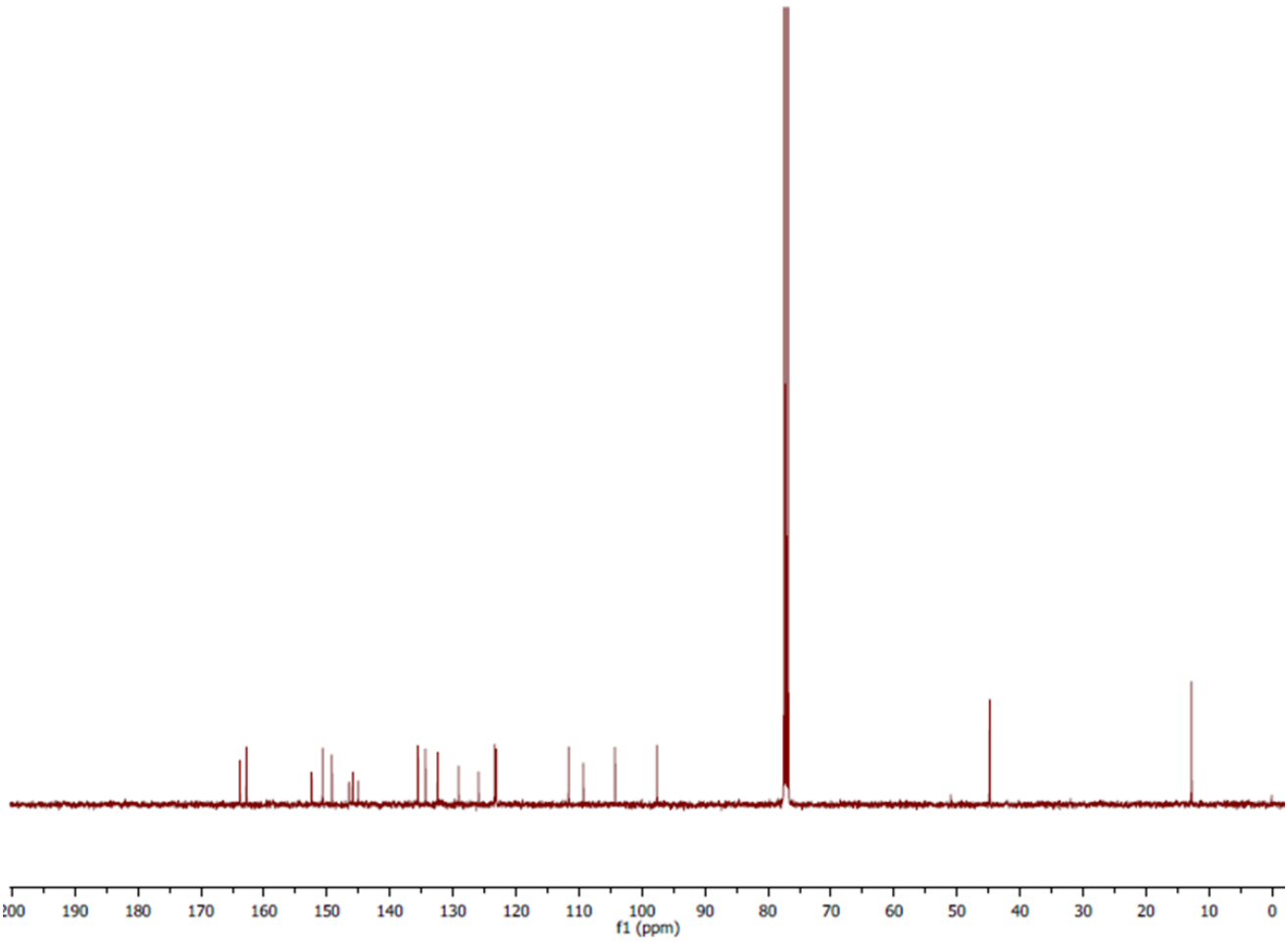

Figure A10: ^{13}C NMR of probe **3.**

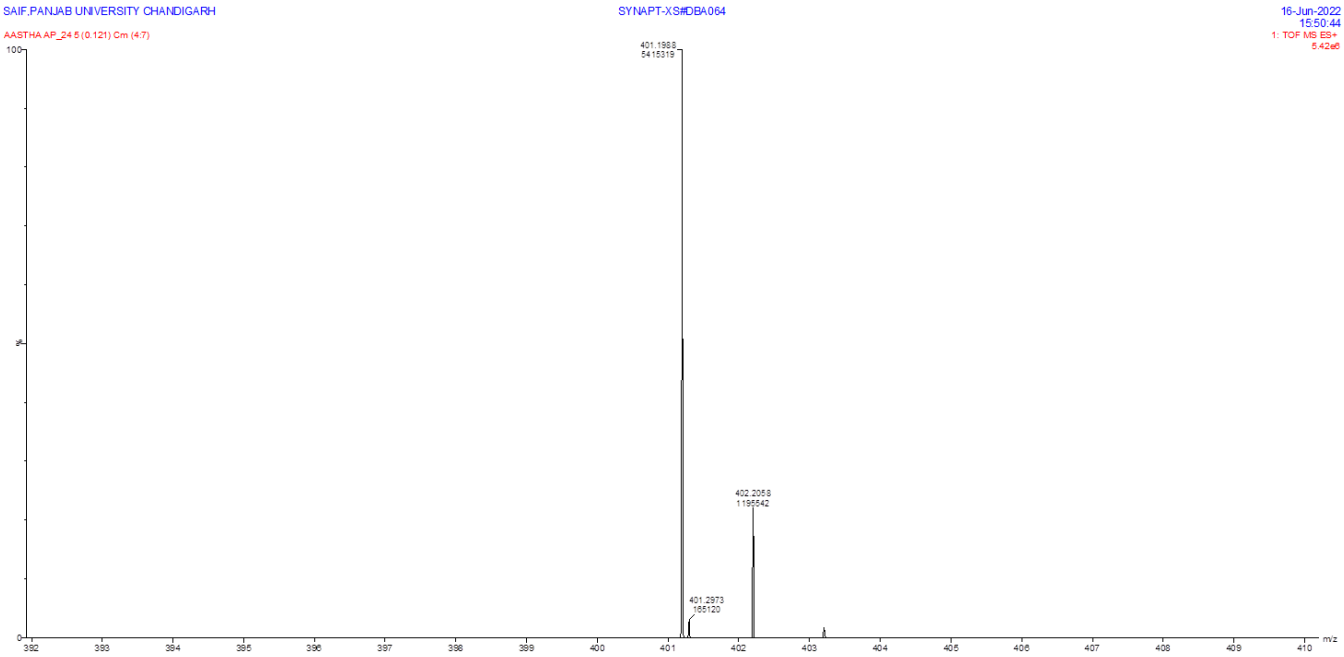

Figure A11: HRMS spectrum of probe **3.**

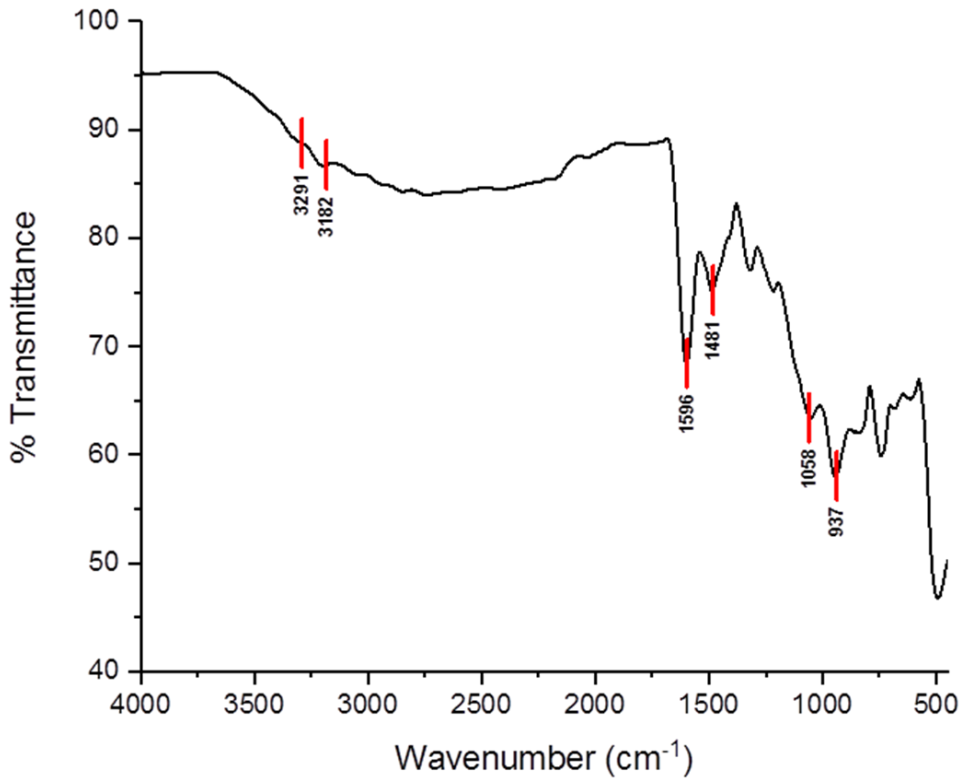

Figure A12: FTIR spectrum of probe **3.**

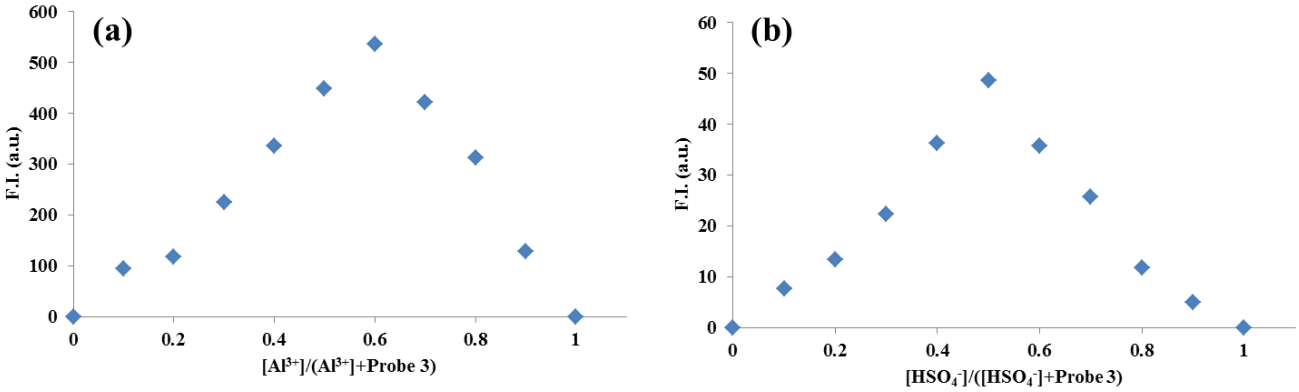

Figure A13: Job's Plot of probe **3** (20μM), H_2O: CH_3OH (1:1, [v/v]), (a) Al^{3+} (10μM) and (b) HSO_4^-.

Chapter 3.3. Effect of conjugation on excited state intramolecular proton transfer process in hydroxy aryl benzimidazole based Schiff base

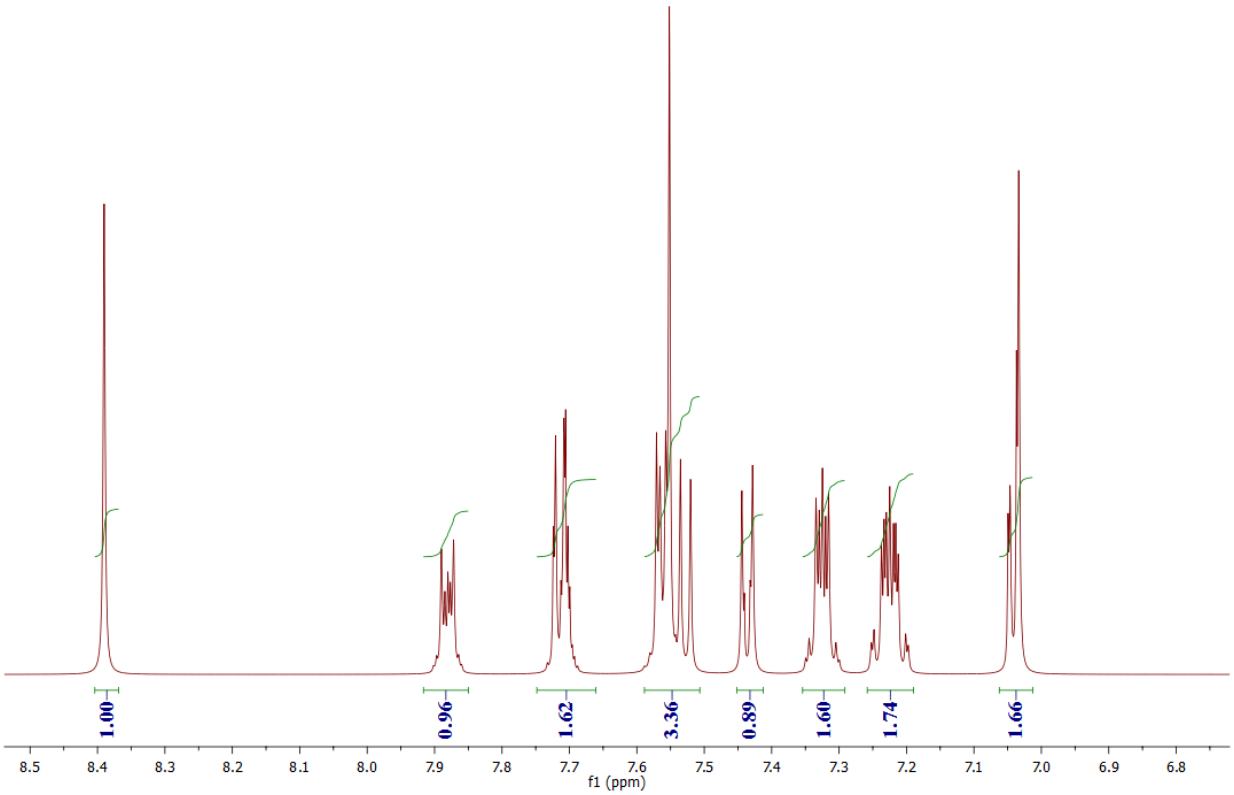

Figure A14: ^{1}H NMR spectrum of probe **4.**

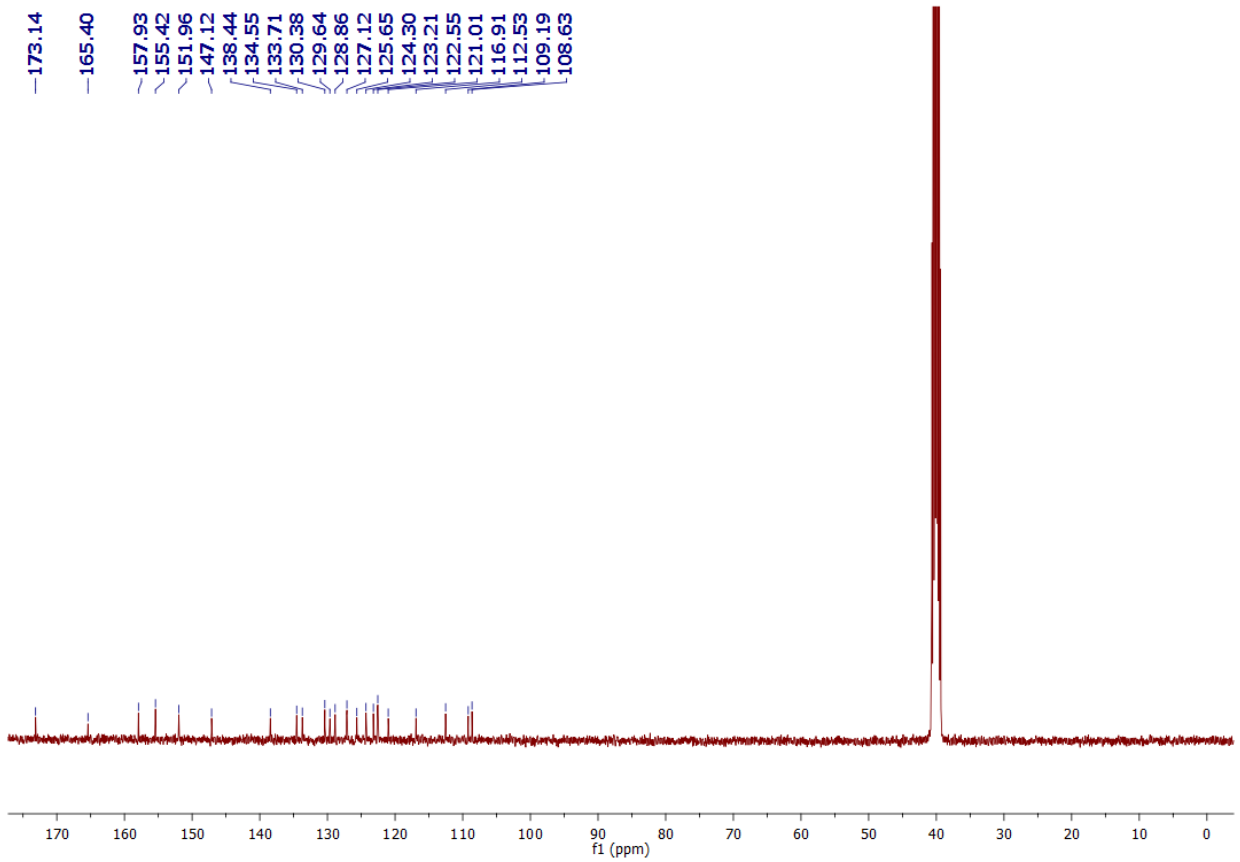

Figure A15: ^{13}C NMR of probe **4.**

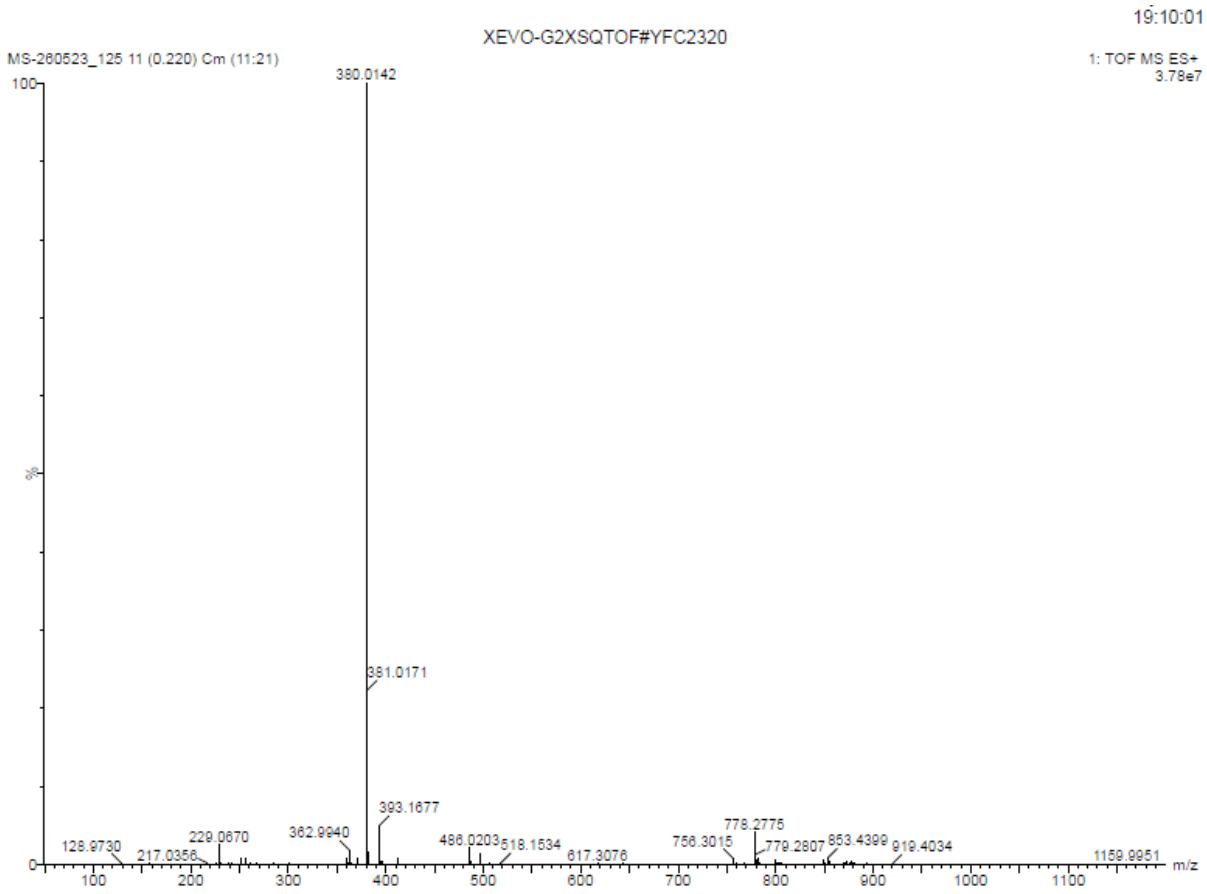

Figure A16: HRMS spectrum of probe **4.**

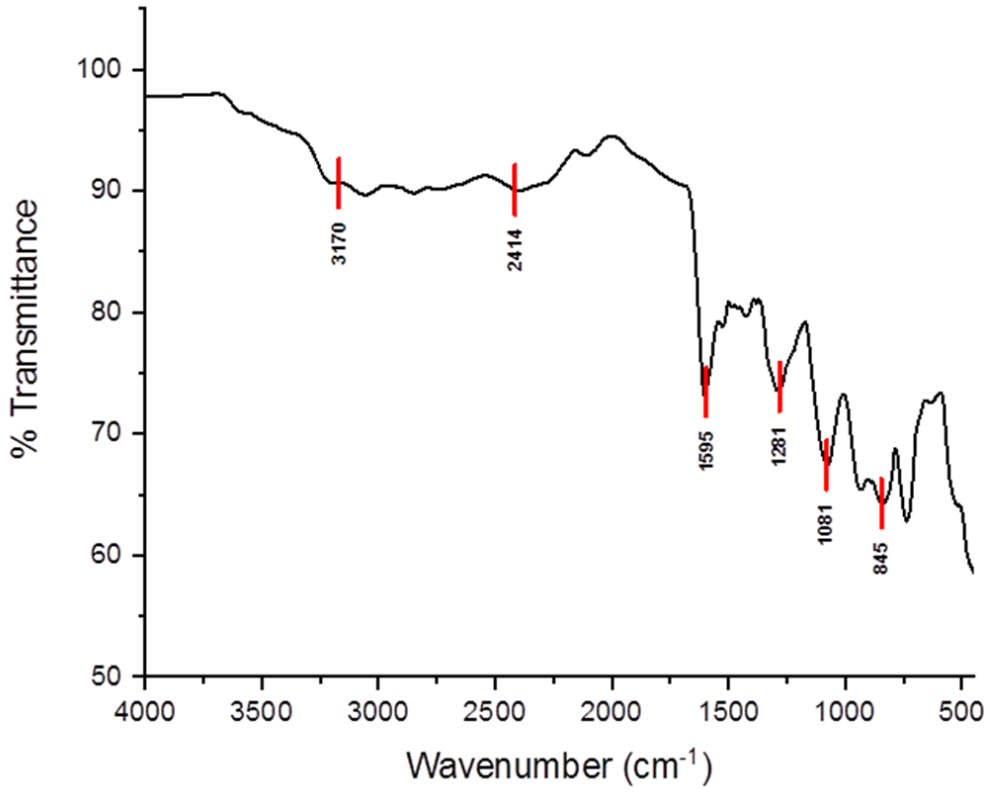

Figure A17: FTIR spectrum of probe **4.**

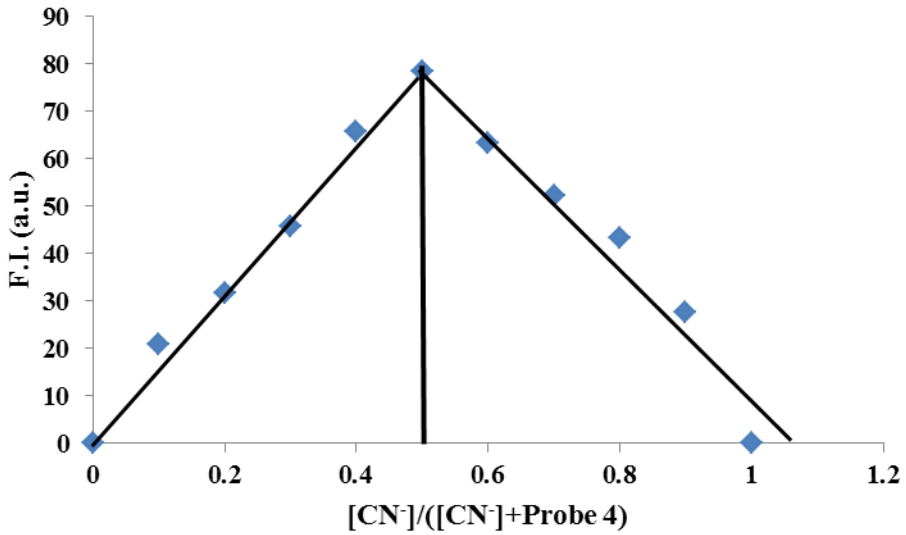

Figure A18: Job's Plot for probe **4** (20 μM) binding with CN^- (20 μM) in H_2O: CH_3CN, 1:9 [v/v].

Chapter 4

Investigation of excited state intramolecular proton transfer process and charge transfer process in hydroxy aryl benzothiazole based Schiff bases

Chapter 4.1. Investigation of excited state intramolecular proton transfer process for hydroxy aryl benzothiazole based Schiff base

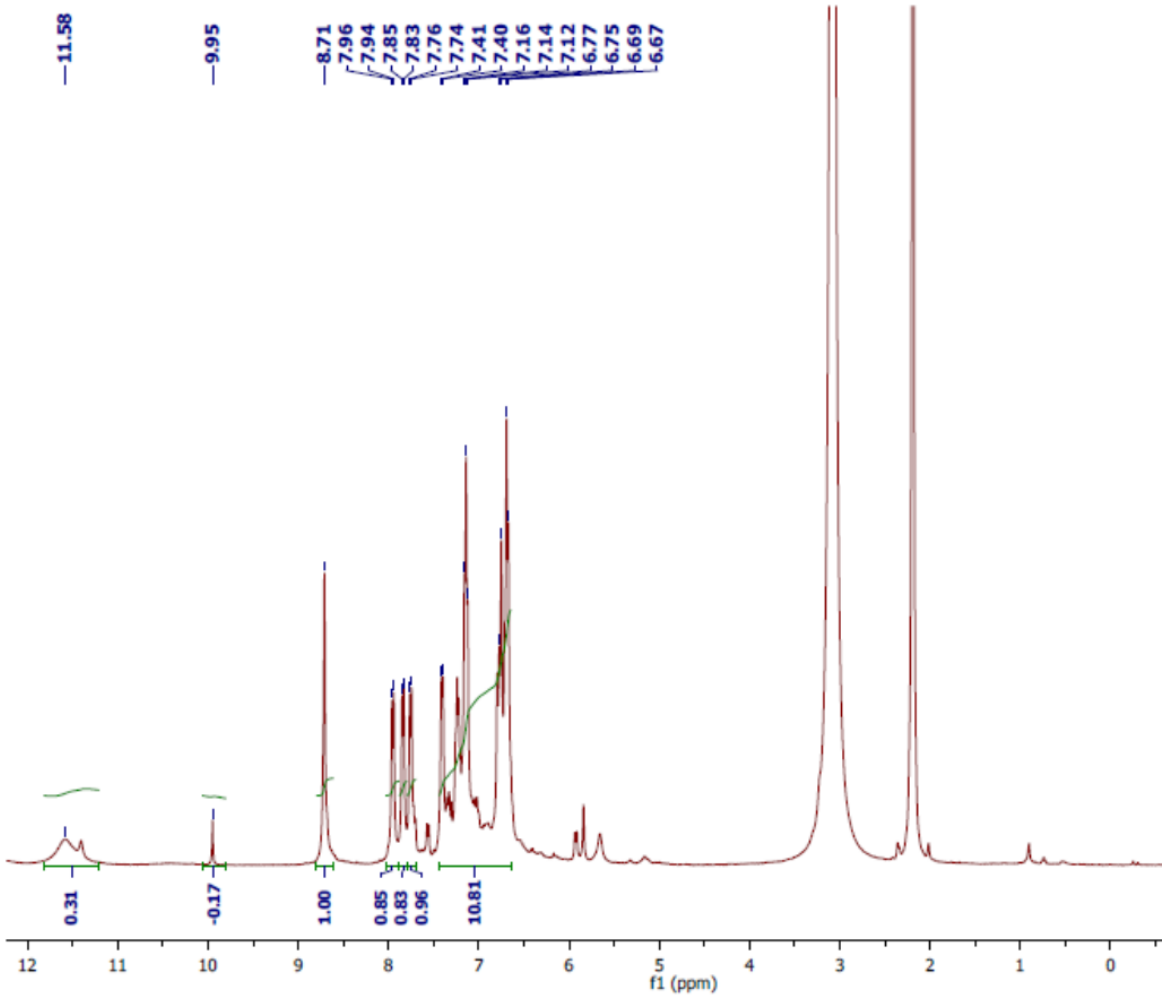

Figure A19: ^{1}H NMR of probe **5**.

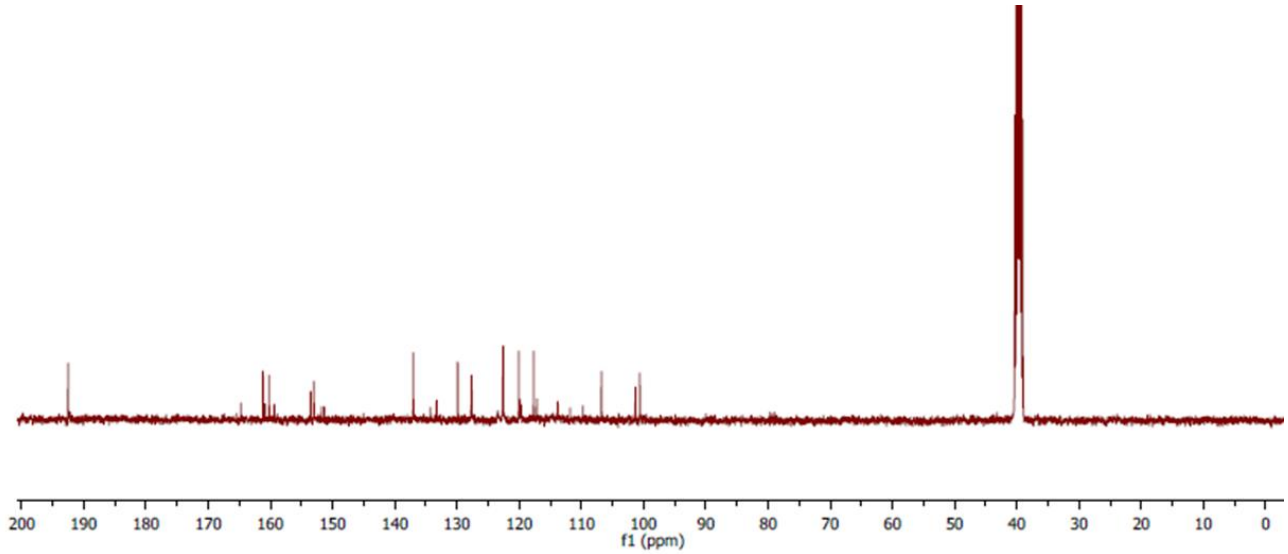

Figure A20: ^{13}C NMR of probe **5**.

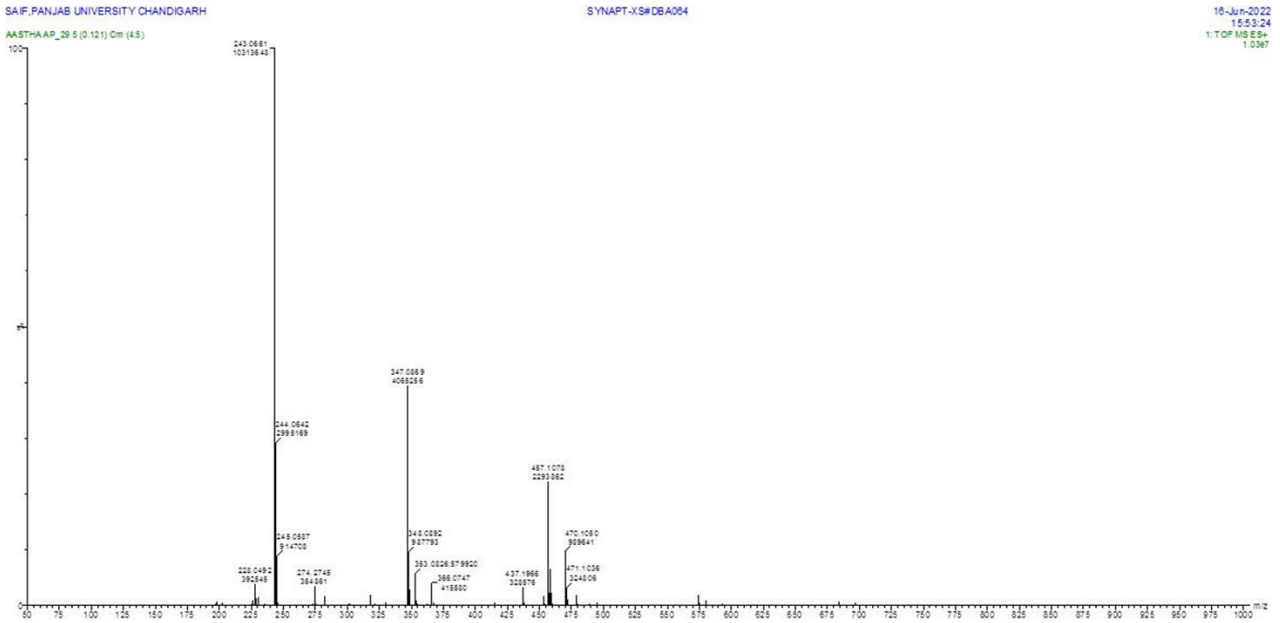

Figure A21: HRMS spectrum of probe **5**.

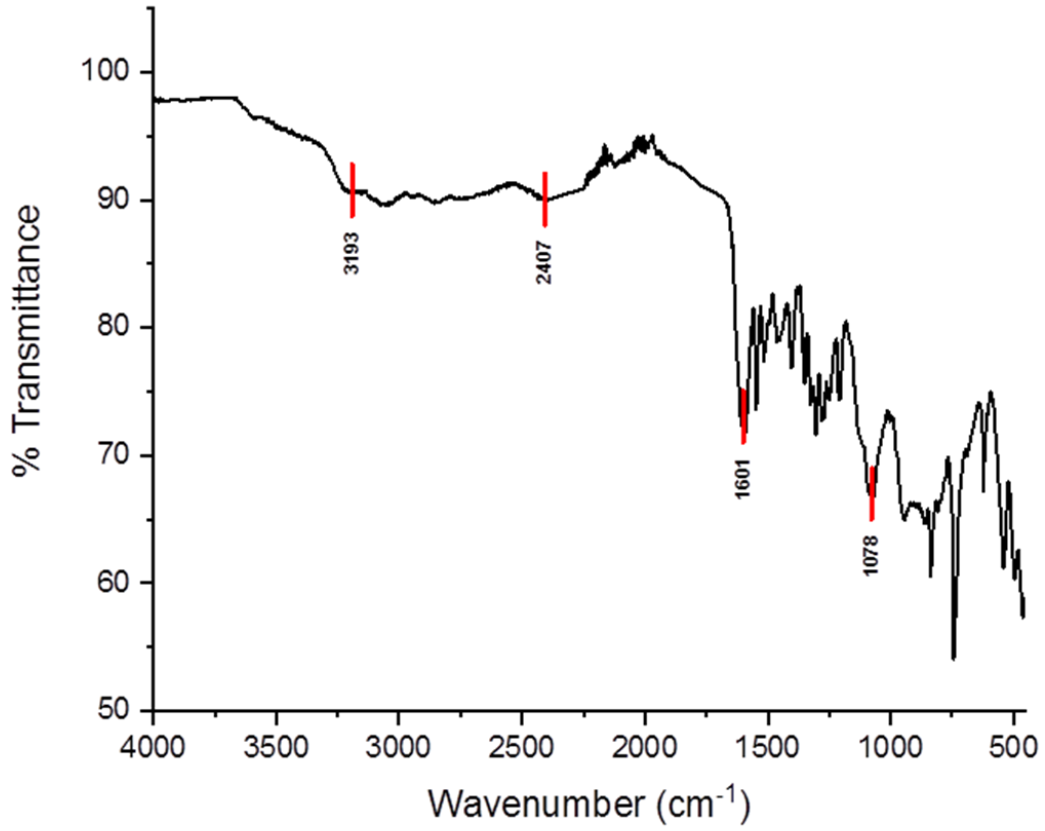

Figure A22: FTIR spectrum of probe **5.**

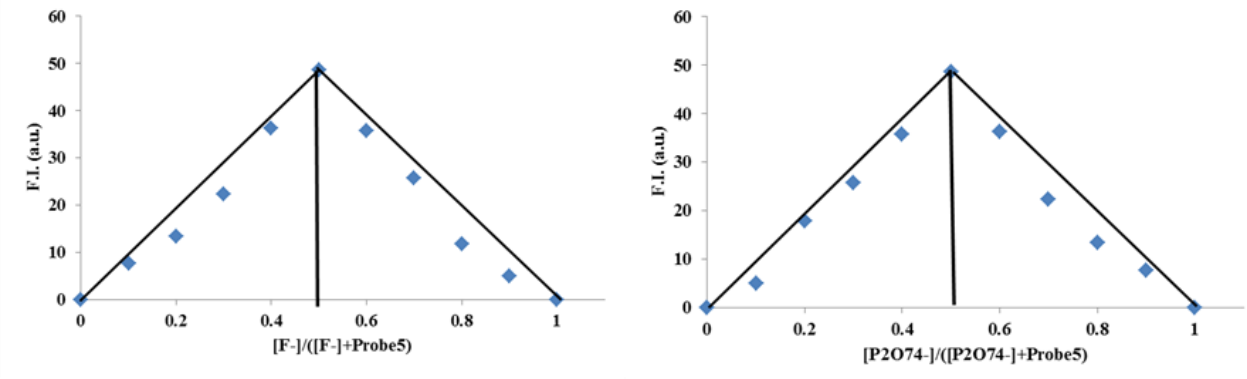

Figure A23: Job's Plot of probe **5** (20µM), CH_3CN: H_2O (1:1, [v/v], (a) F^- (20µM) and (b) $P_2O_7^{4-}$ (20 µM).

Chapter 4.2. Effect of electron donating group $-NEt_2$ on excited state intramolecular proton transfer process of benzothiazole based Schiff base

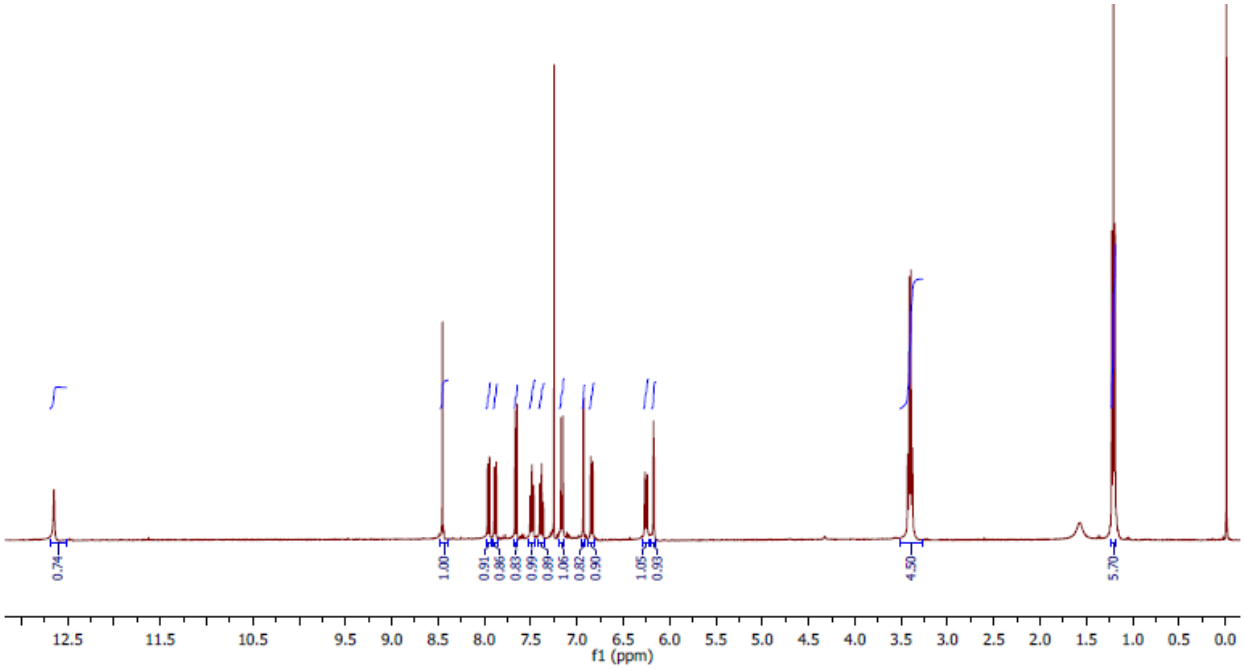

Figure A24: ^{1}H NMR spectrum of probe **6.**

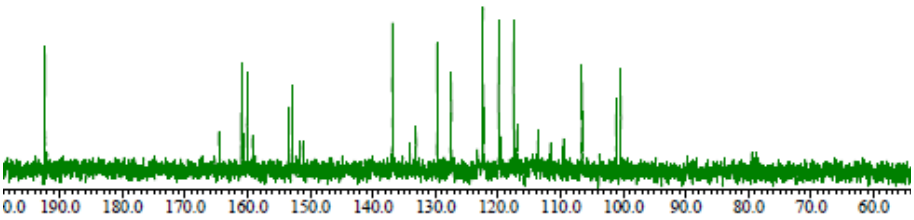

Figure A25: ^{13}C NMR of probe **6.**

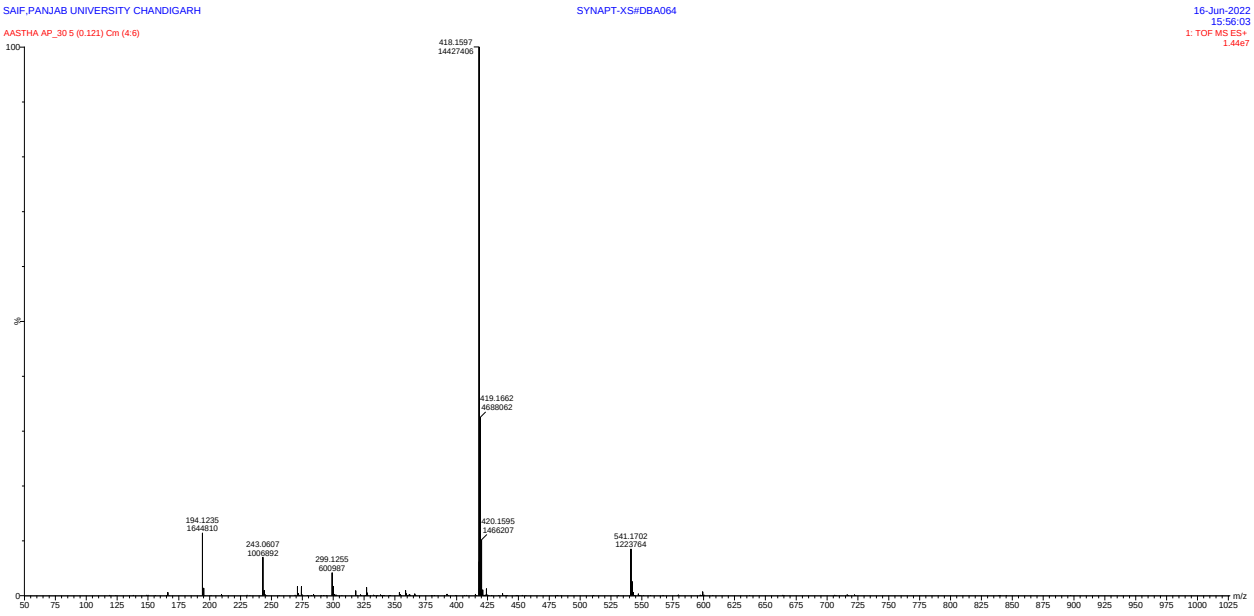

Figure A26: HRMS spectrum of probe **6**.

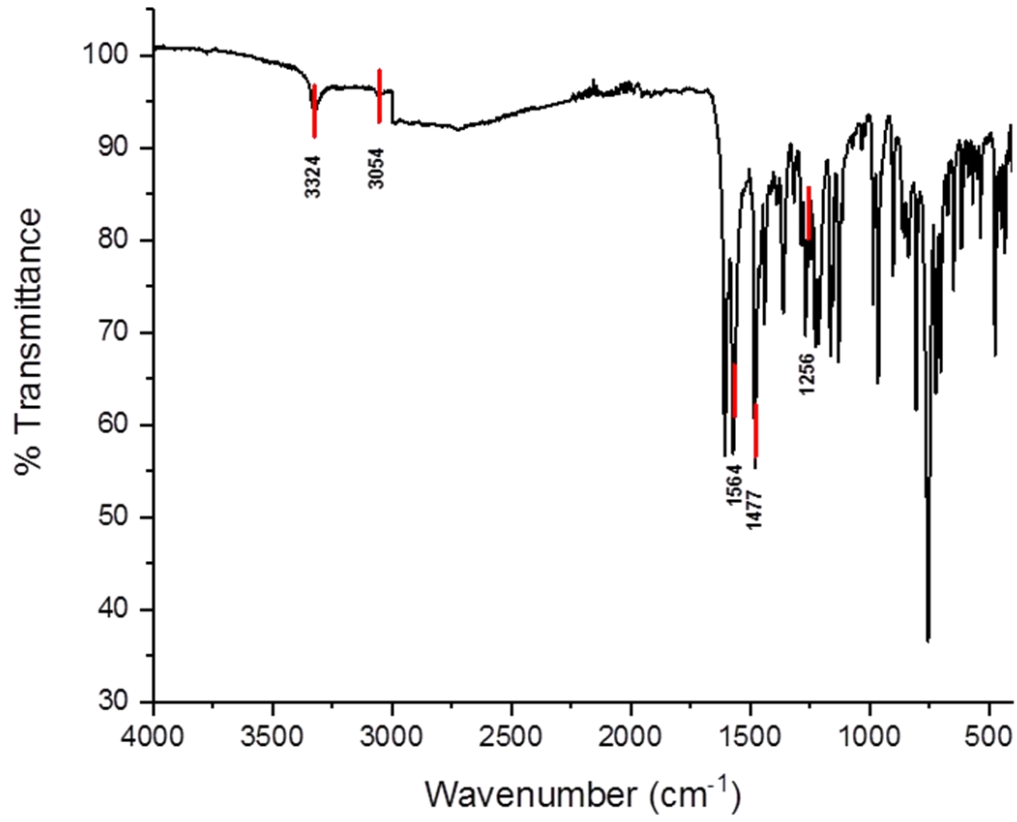

Figure A27: FTIR spectrum of probe **6.**

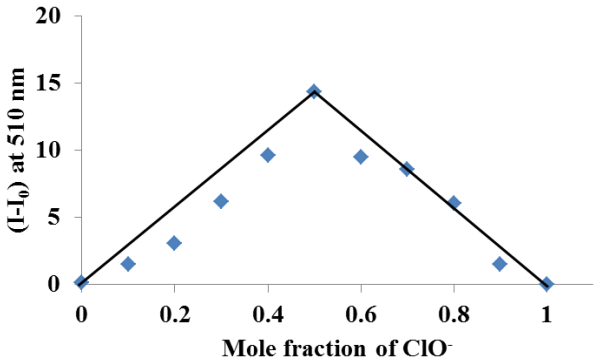

Figure A28: Job's Plot for probe **6** (20 μM) binding with ClO^- (20 μM) in CH_3OH: H_2O (9:1, [v/v], pH=7.04).

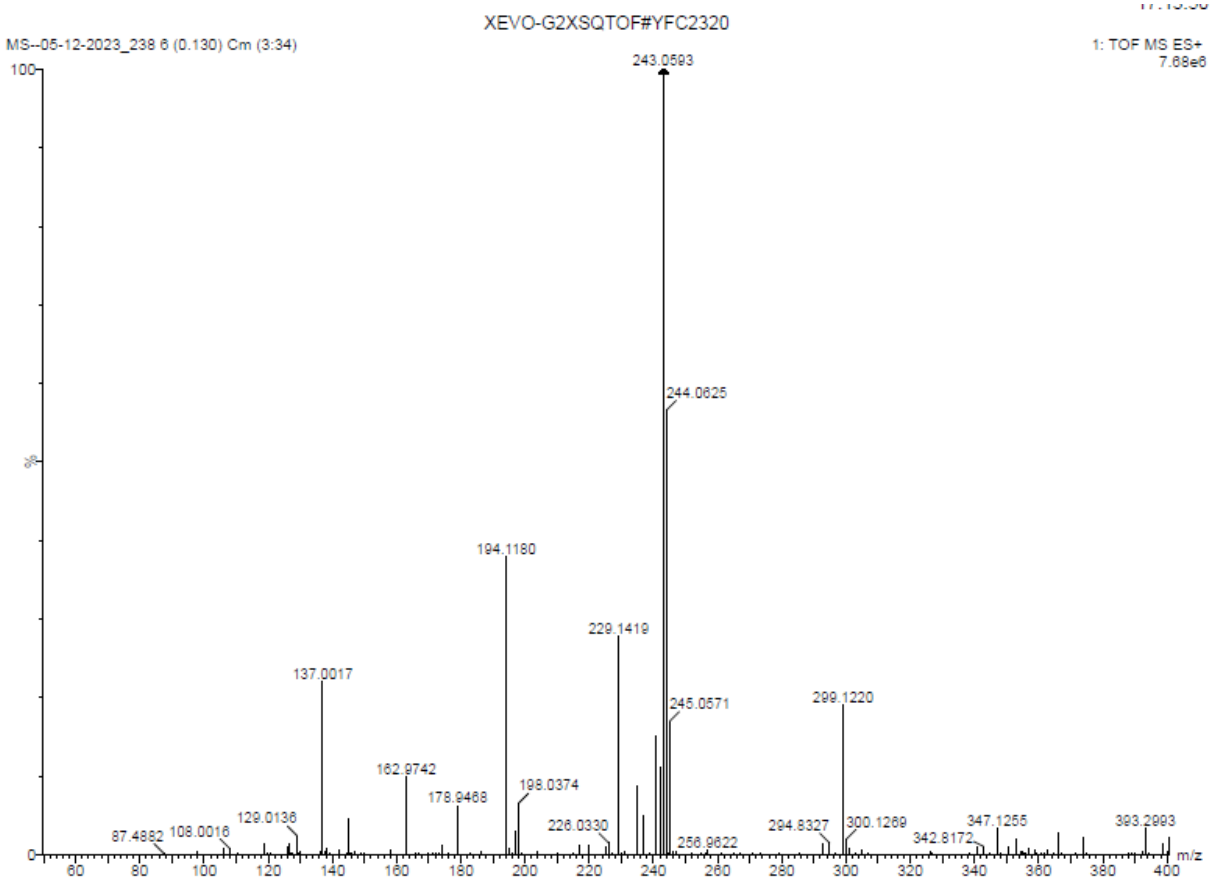

Figure A29: HRMS spectrum of probe **6**+ClO^- complex.

Chapter 4.3. Effect of conjugation on excited state intramolecular proton transfer process in hydroxy aryl benzothiazole based Schiff base

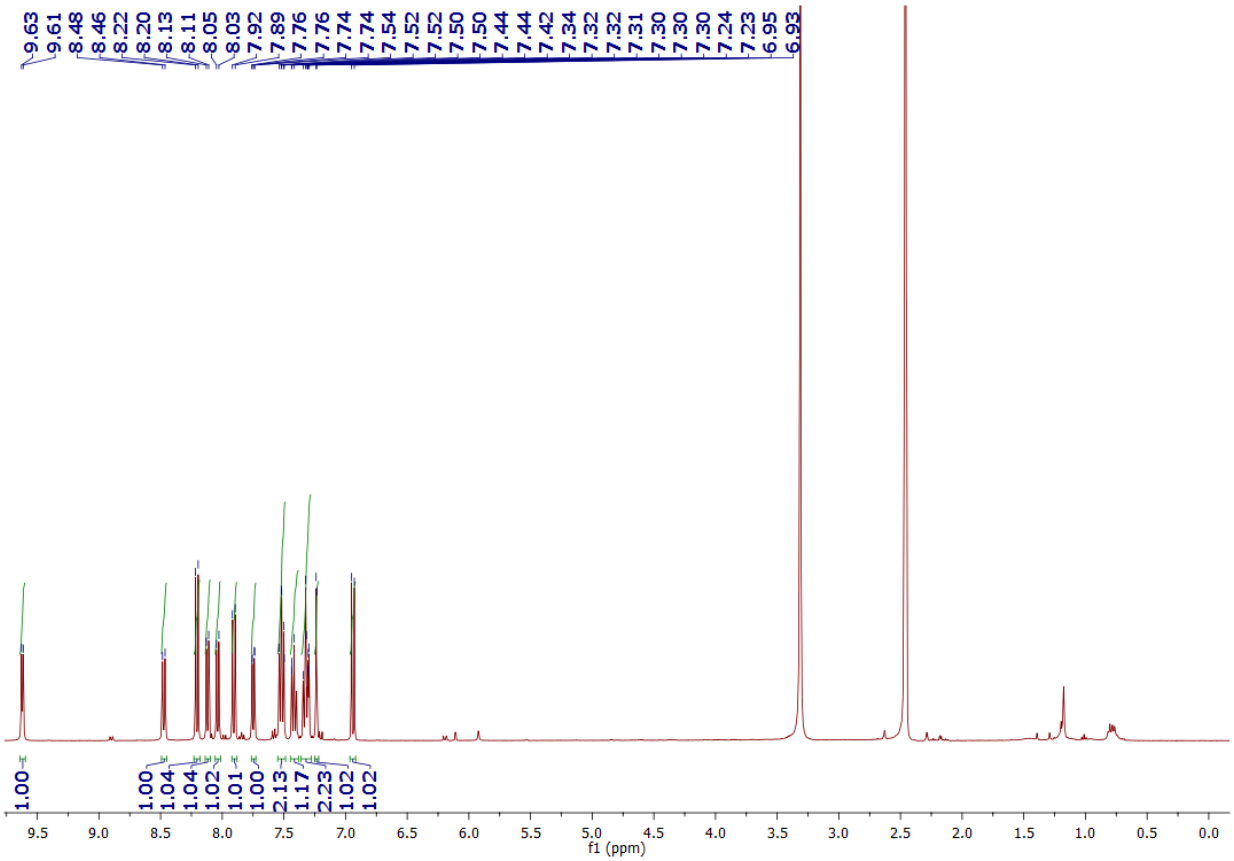

Figure A30: ^{1}H NMR spectrum of probe **7.**

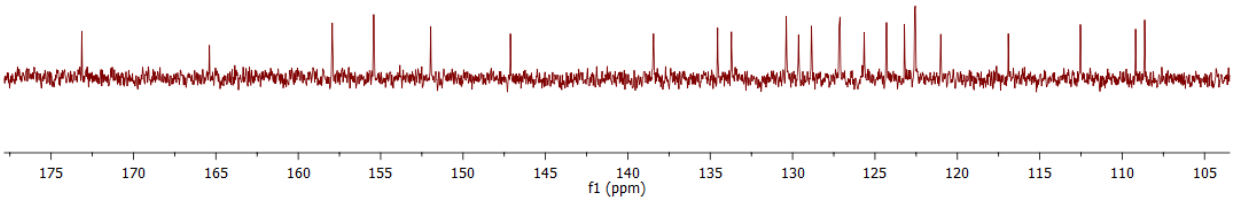

Figure A31: ^{13}C NMR of probe **7.**

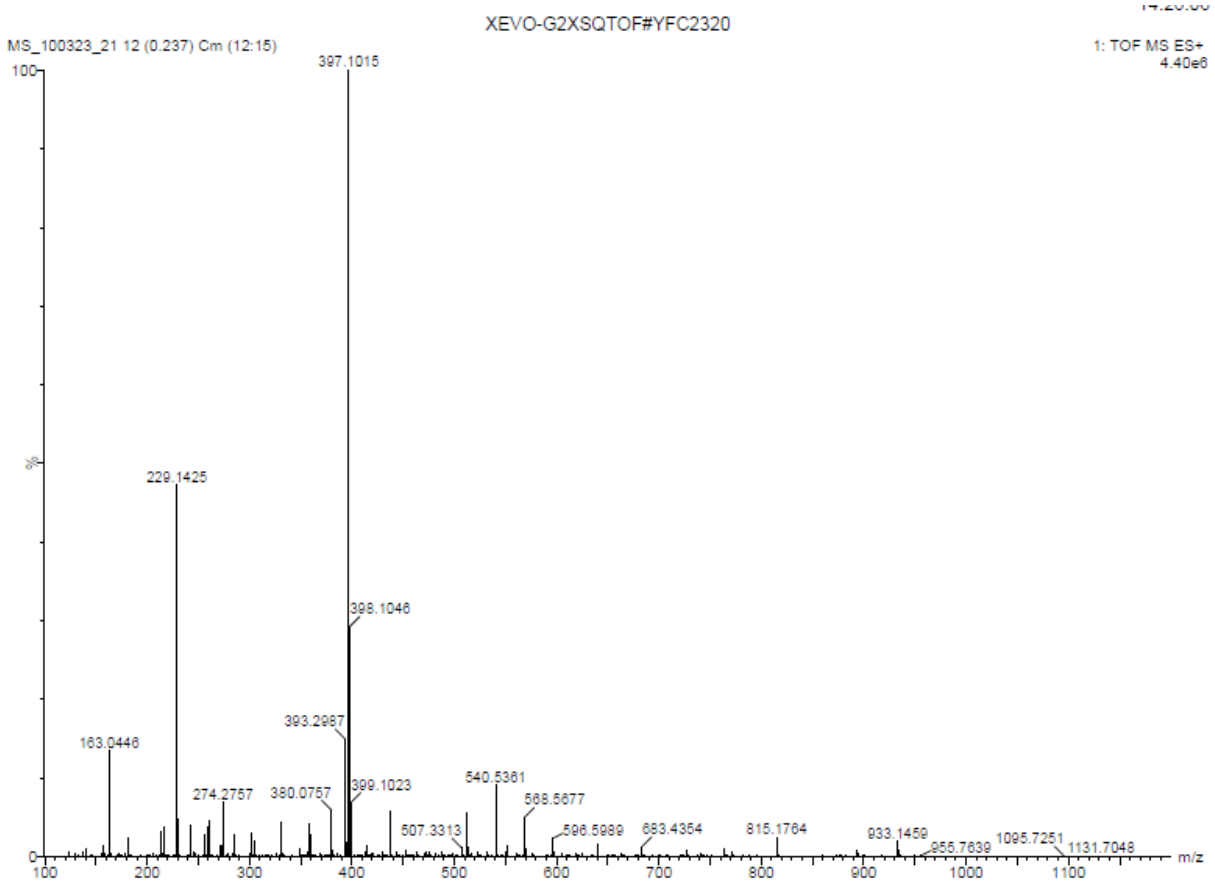

Figure A32: HRMS spectrum of probe **7**.

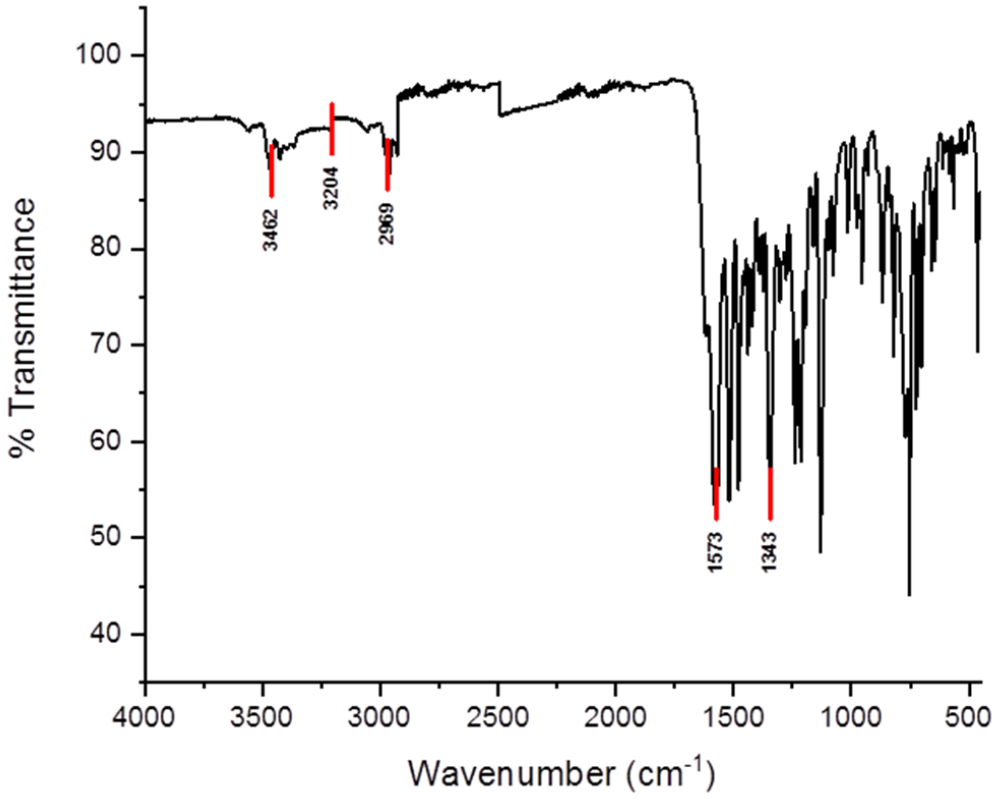

Figure A33: FTIR spectrum of probe **7.**

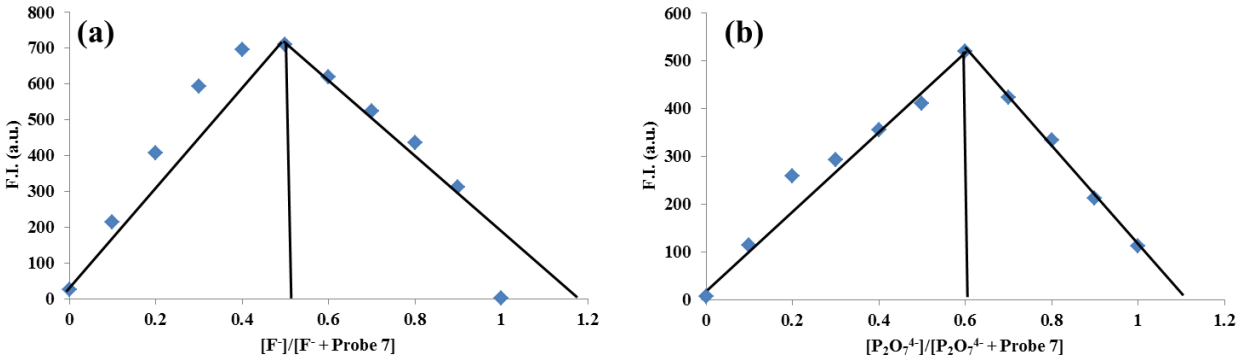

Figure A34: Job's Plot of probe **7** (20µM), CH_3CN (a) F^- (20µM) and (b) CN^- (20 µM).

Chapter 5

Study of excited state intramolecular proton and charge transfer in 8-hydroxyquinoline Schiff bases and application as sensor

Chapter 5.1. Study of excited state intramolecular proton transfer process for 8-hydroxyquinoline-benzimidazole Schiff base

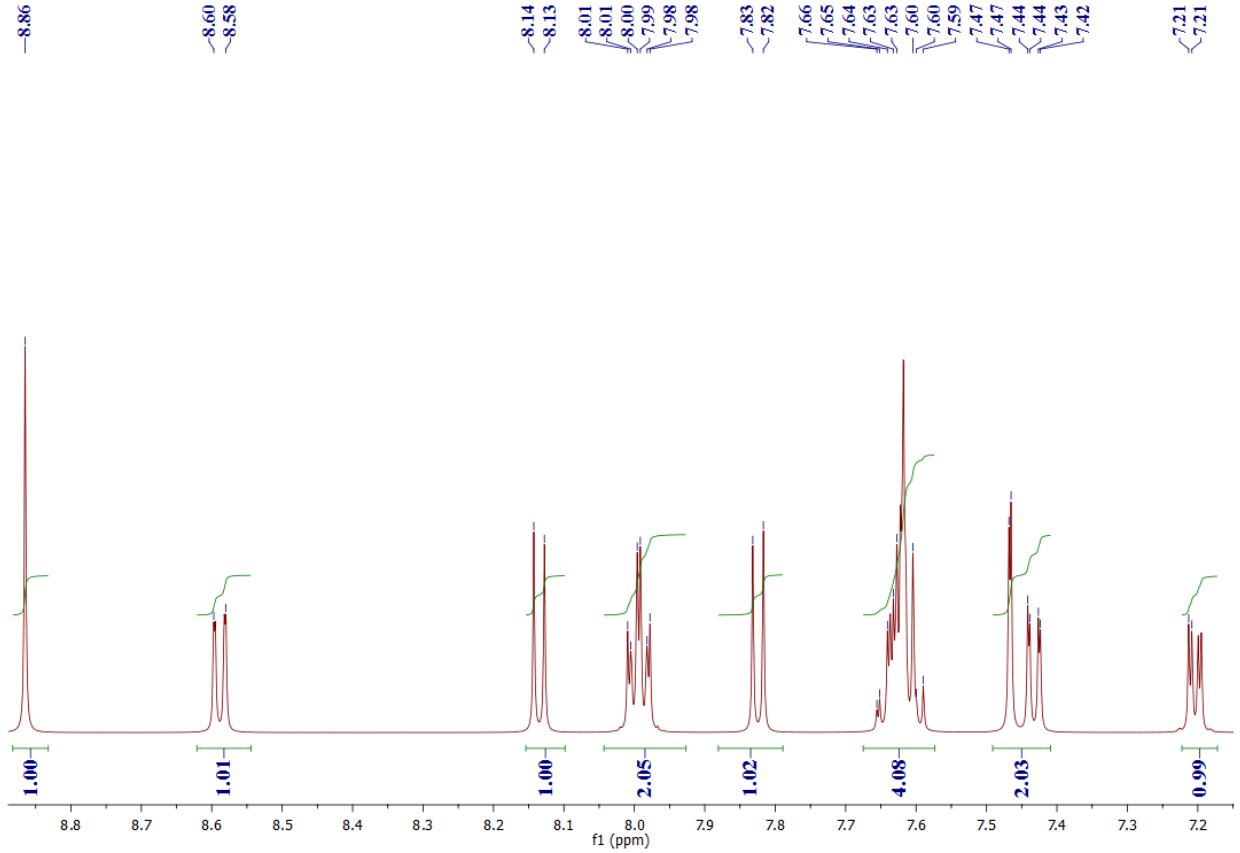

Figure A35: ^{1}H NMR of probe **8**.

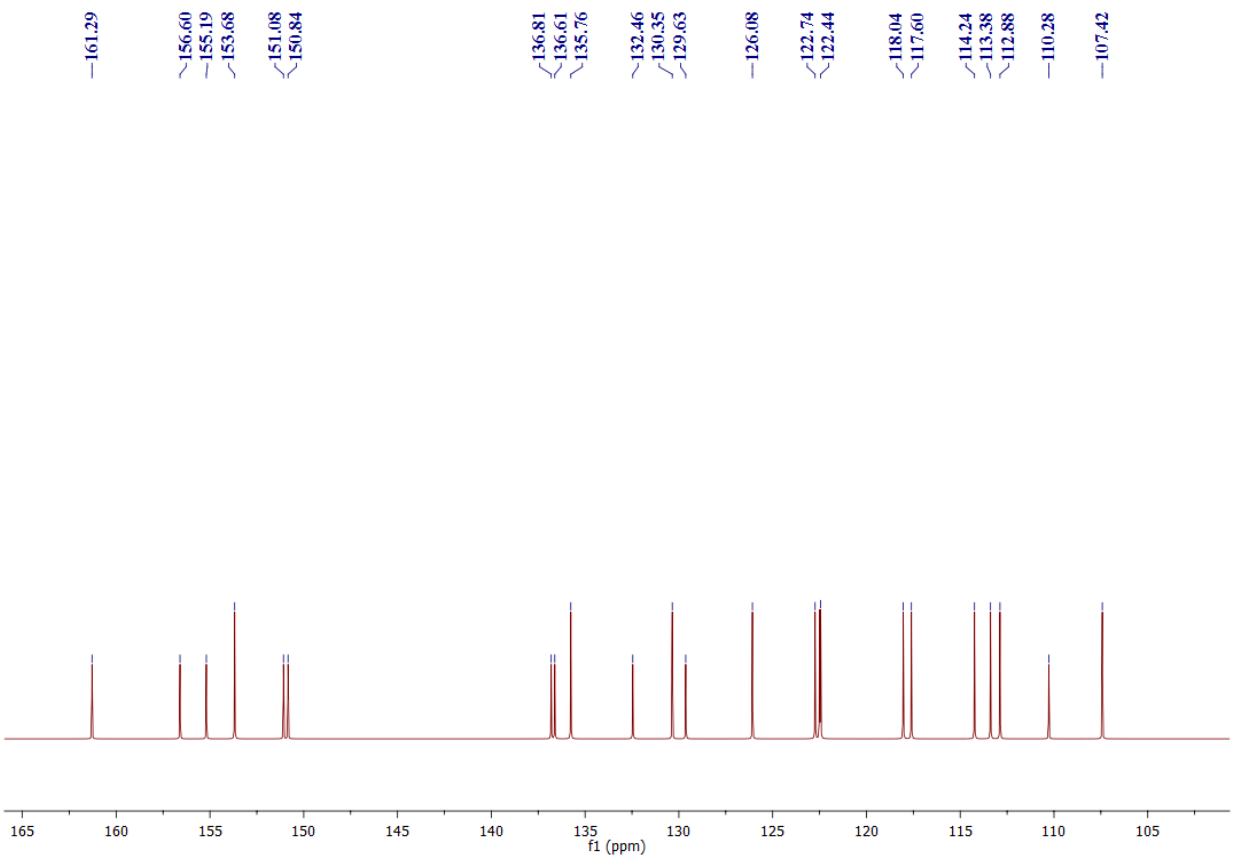

Figure A36: ^{13}C NMR of probe **8**.

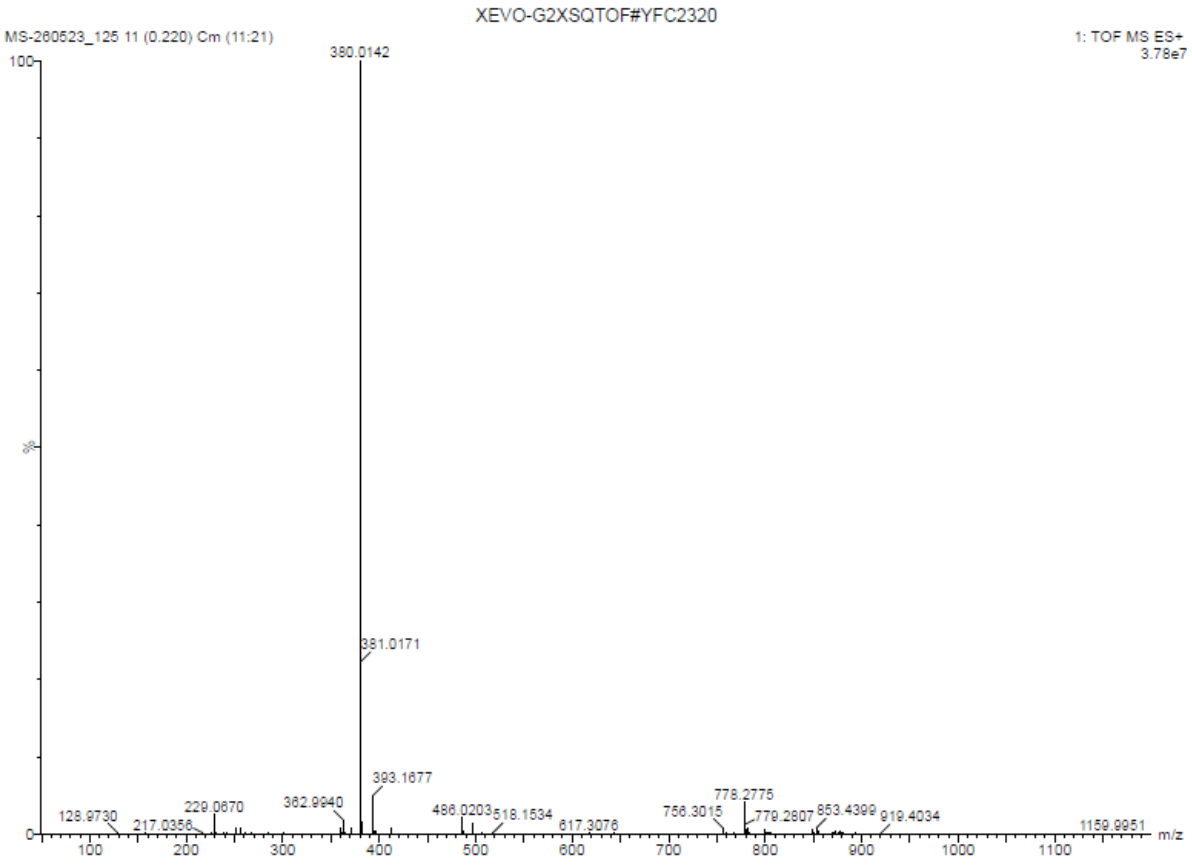

Figure A37: HRMS spectrum of probe **8**.

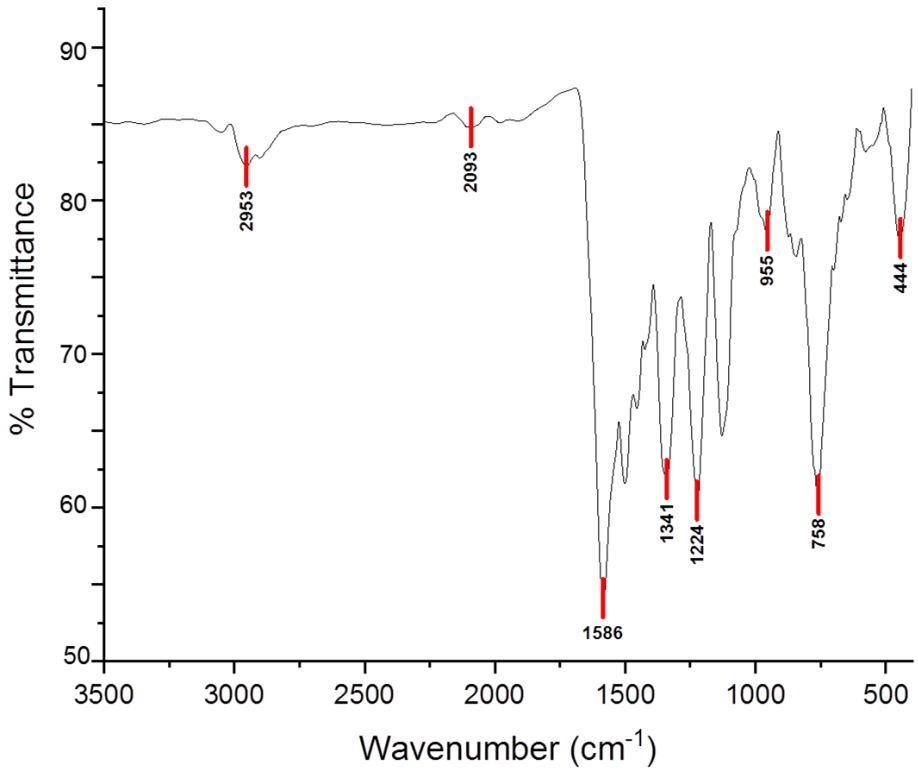

Figure A38: FTIR spectrum of probe **8.**

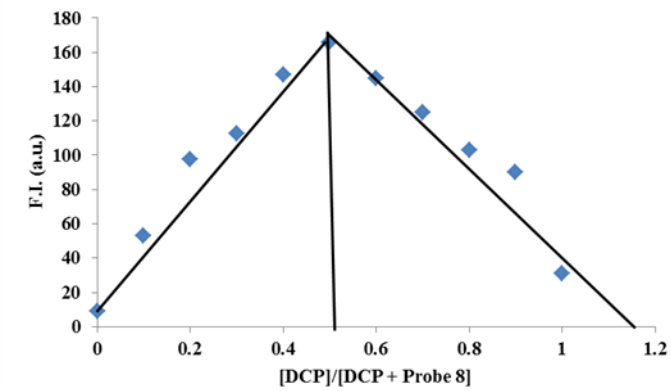

Figure A39: Job's Plot for probe **8** (20 μM) binding with DCP (20 μM) in H_2O: CH_3CN, 1:1 [v/v].

Chapter 5.2. Study of excited state intramolecular proton transfer process for 8-hydroxyquinoline-benzthiazole Schiff base

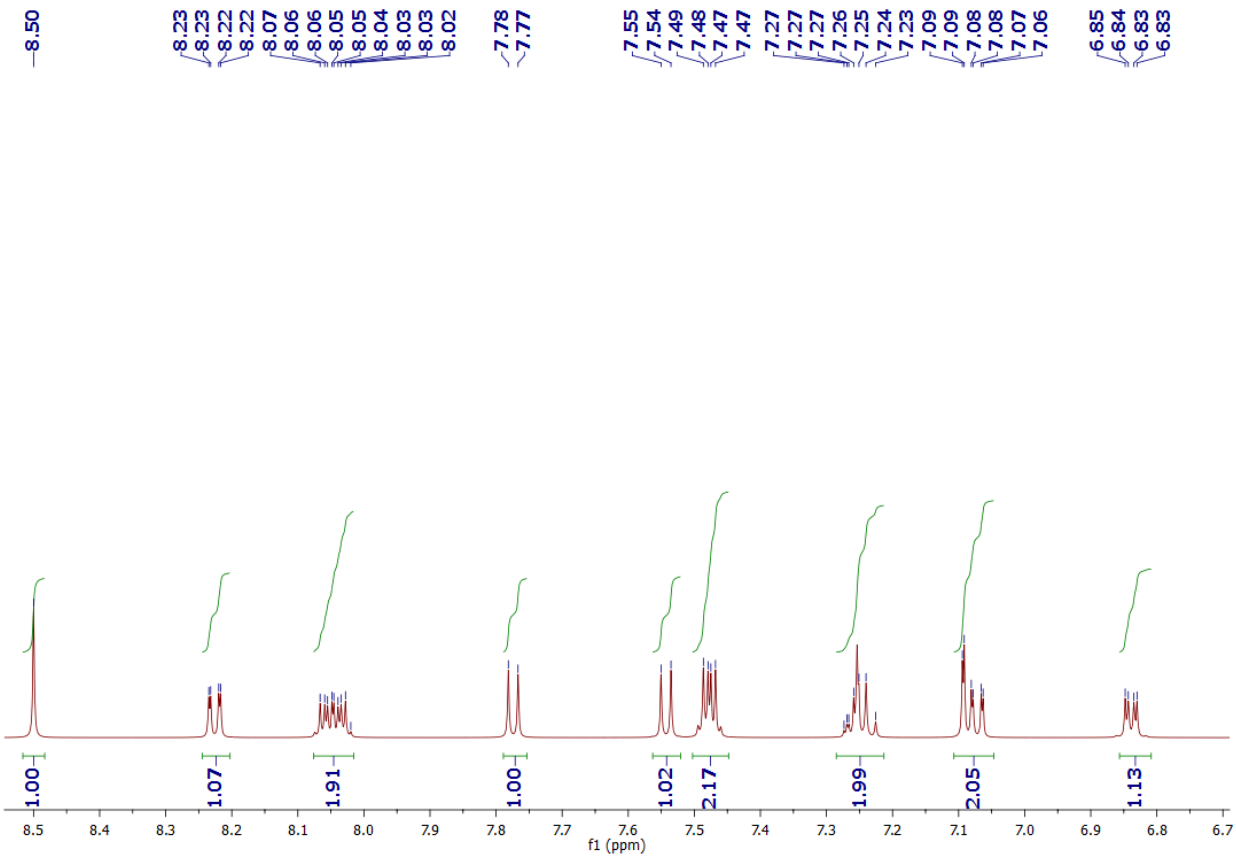

Figure A40: ^{1}H NMR of probe **9**.

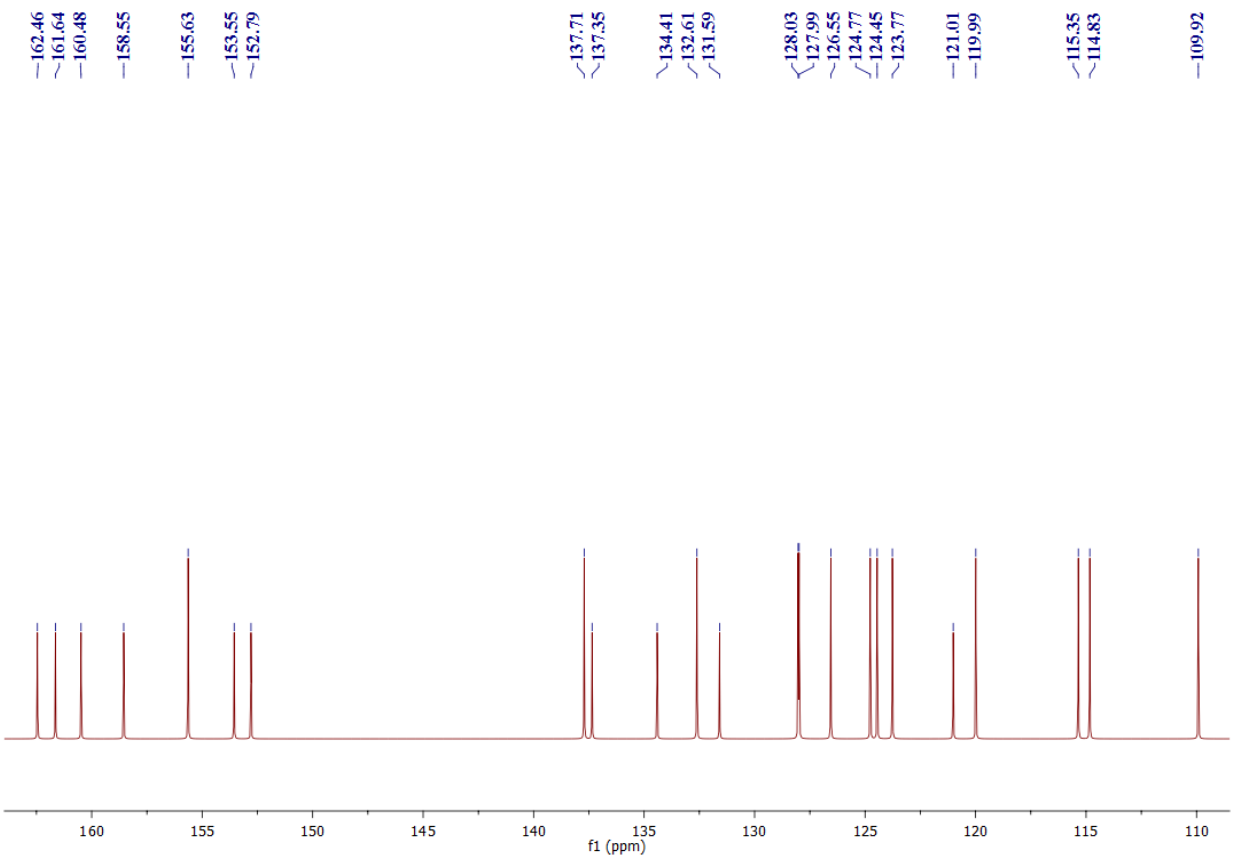

Figure A41: ^{13}C NMR of probe **9**.

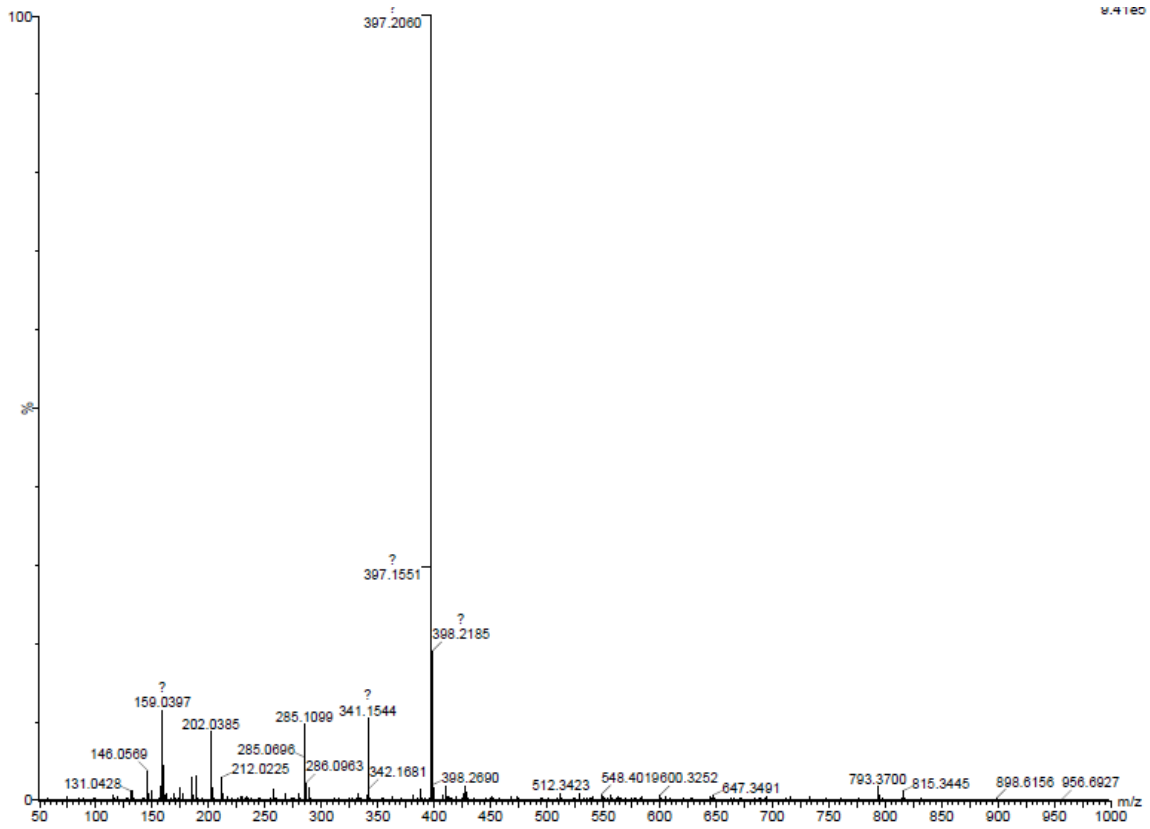

Figure A42: HRMS spectrum of probe **9**.

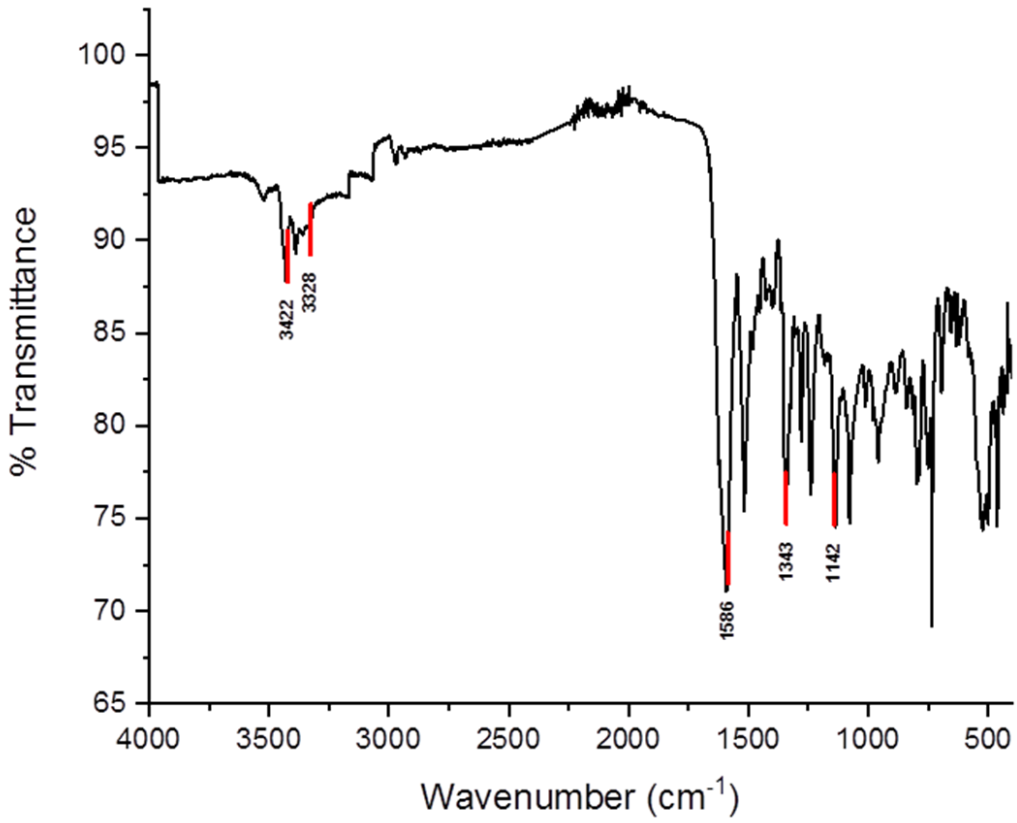

Figure A43: FTIR spectrum of probe **9.**

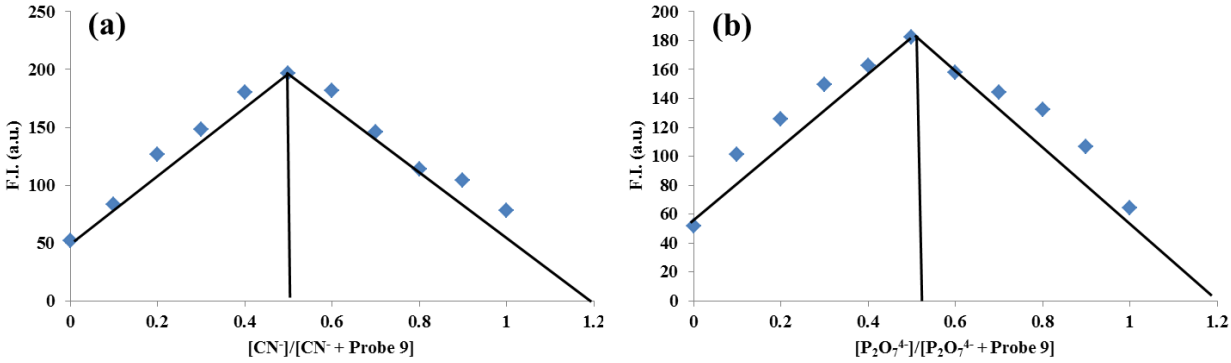

Figure A44: Job's Plot of probe **9** (20µM) CH_3CN:CH_3OH (9:1, v/v) (a) CN^- (20µM) and (b) $P_2O_7^{4-}$ (20 µM).

Chapter 5.3. Protection and deprotection of excited state intramolecular proton transfer process in 8-hydroxyquinoline-benzthiazole Schiff base for enzyme sensing

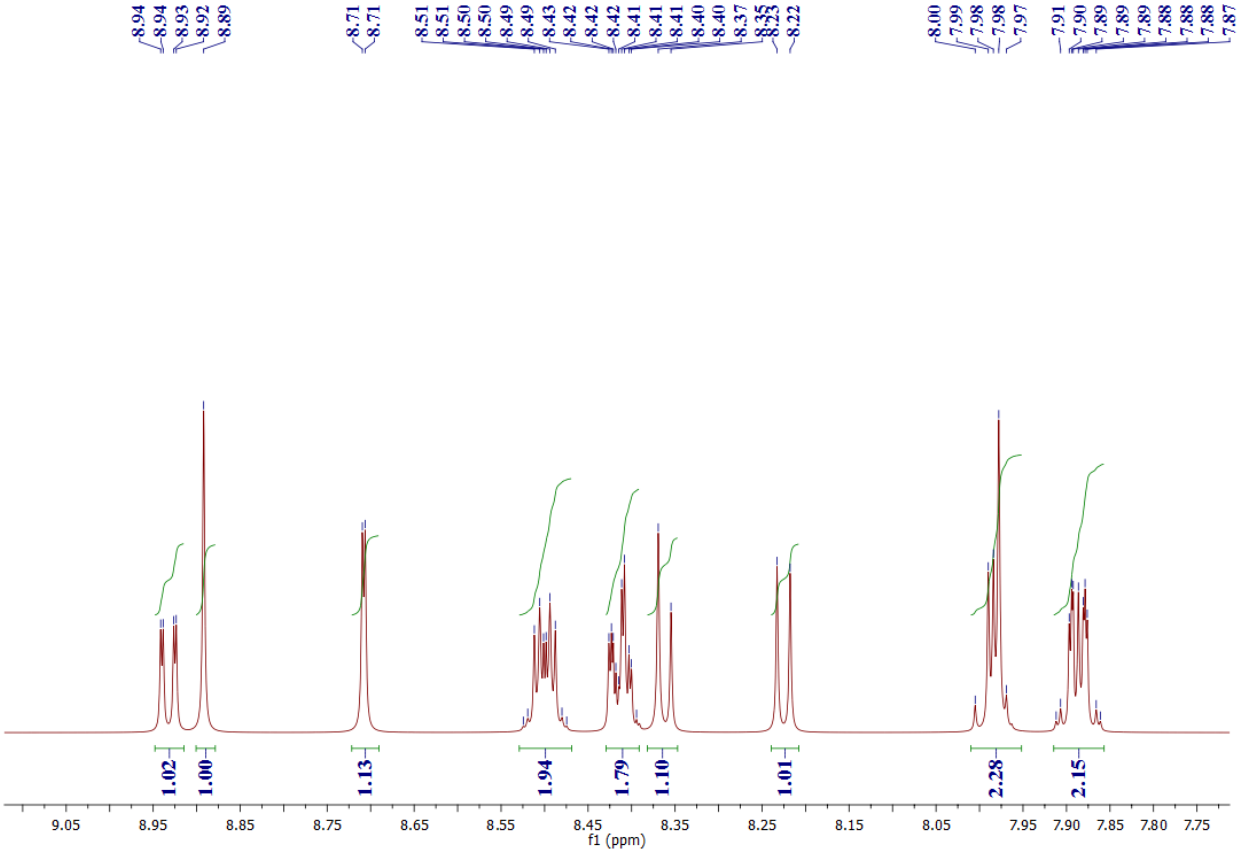

Figure A45: ^{1}H NMR of probe **10**.

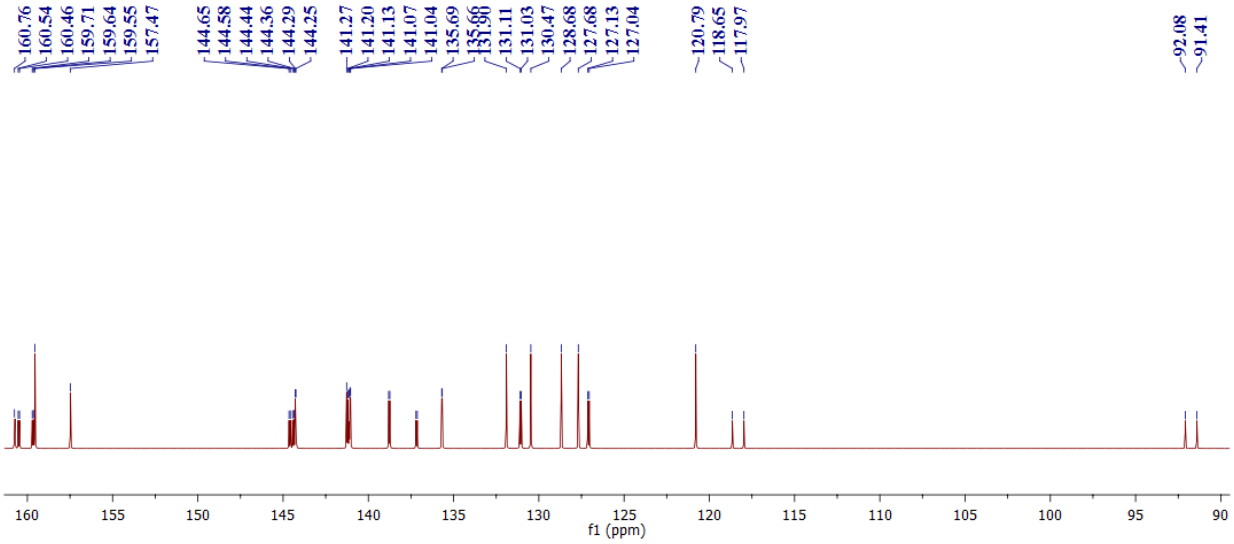

Figure A46: ^{13}C NMR of probe **10**.

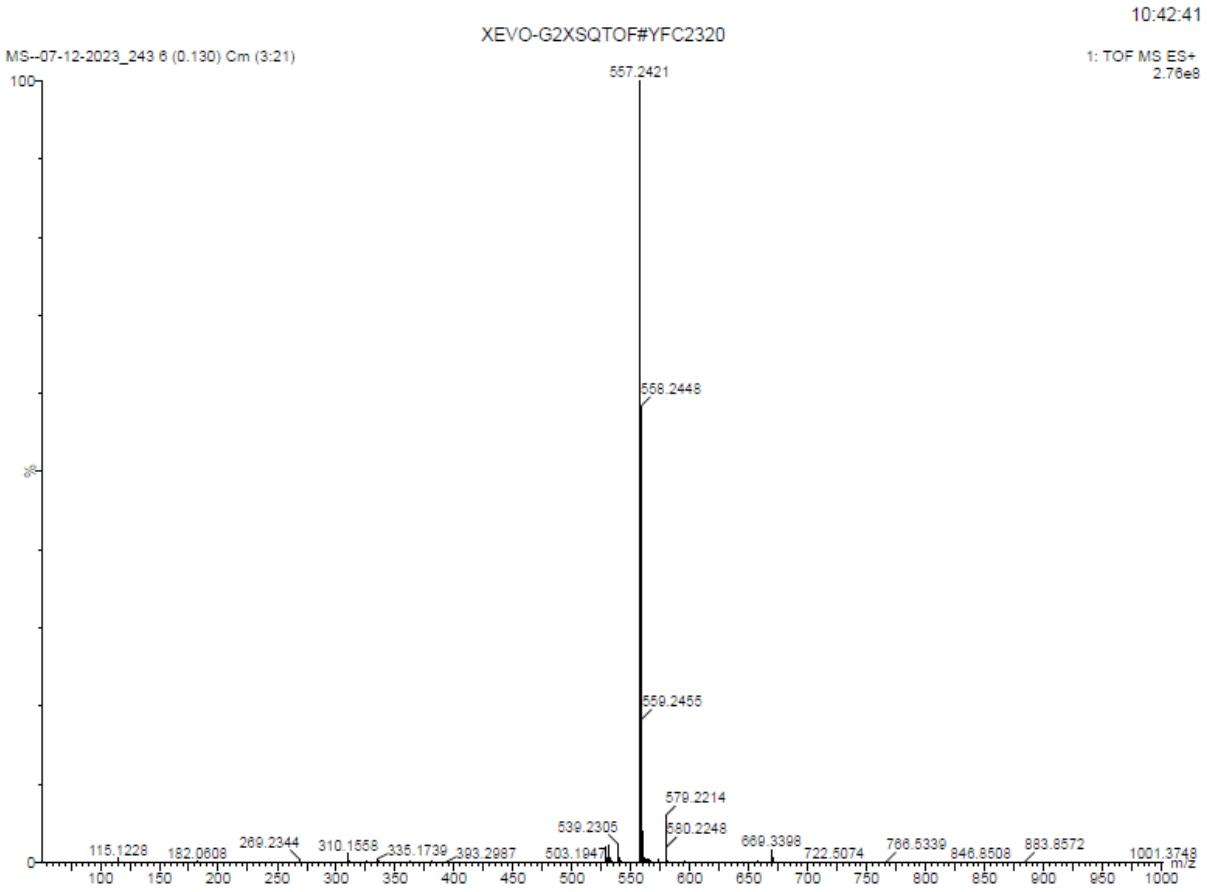

Figure A47: HRMS of probe **10**.